EFFECT OF PRECIOUS METAL PARTICLE SIZE AND SUPPORT TYPE ON CATALYTIC ACTIVITY AS REVEALED BY X-RAY METHODS

Donato Decarolis

Department of Chemistry

University College London

Thesis submitted for the degree of Doctor of Philosophy

Declaration

I, Donato Decarolis, confirm that the work presented in this thesis is my own.

Where information has been derived from other sources, I can confirm that this has been indicated in the thesis.

……

Abstract

For supported nanoparticulate catalysts, the effect of their properties, such as size and interaction with support, on a catalytic process is still in debate. This is partially caused by the limited control that typical nanoparticle preparation methods offer which may lead to the presence of nanoparticles possessing a range of sizes and shapes, leading to a lack of clarity in the correlation between properties and catalysis. The work presented in this thesis focuses on producing size-selected monometallic supported nanoparticles and their detailed characterisation, both ex situ and in situ (under reaction conditions) mainly through the application of the technique of X-ray absorption spectroscopy (XAFS).

Chapter 3 of this thesis focuses on understanding the mechanism of formation of Au nanoparticles produced by reverse micelle encapsulation, through a combination of various techniques (transmission electron microscopy, dynamic light scattering, UV-vis, combined small angle X-ray scattering/XAFS). From the combined data, it is possible to rationalise the synthesis process, which can be divided into three steps: fast reduction of Au (III) species to Au (I), slow reduction and agglomeration of Au atoms in sub-nanometric clusters and a final agglomeration to form the nanoparticles.

Chapter 4 and 5 focus on the application of monometallic nanoparticles to the catalytic hydrogenation of 1,3-butadiene, used as a model reaction, using in situ XAFS to correlate size and support effect with their catalytic activities. For Au nanoparticles (chapter 4) it appears that a restructuring process takes places under reaction conditions. Depending on the sample, this process can be favourable (Au/SiO_2) or detrimental (Au/Al_2O_3) and is highly dependent on particle size. For Pd nanoparticles (chapter 5) it was possible to identify the active species necessary (Pd^0), and detrimental (PdH and PdC) for the selective hydrogenation of 1,3-butadiene in Pd as well as the role of support and size in promoting the presence of each phase.

Impact Statement

The knowledge acquired from the data presented in this thesis would improve the understanding of the hydrogenation of 1,3-butadiene to butenes, an important chemical reaction which is paramount in reducing the amount of waste caused by the presence of 1,3-butadiene in industrial feeds. Understanding the behaviour of Pd catalysts would help to reduce the amount of catalysts needed and reuse the one already present. The possibility of Au catalysts, despite their high cost, would further reduce waste by improving the selectivity. Furthermore, the improvement brought to the synthesis of nanoparticles, thanks to the information obtained by the combination of both ex situ (DLS, TEM) and in situ techniques (XAFS,SAXS), would help to move forward toward the ability to produce monodisperse nanoparticles, which would be helpful both for academic and industrial purpose. Having monodisperse nanoparticles would help academics to correlate structure and activity, which in turn would help the catalysts development toward a greener economy.

Acknowledgements

I would like to thank my supervisor, Professor Andrew Beale, for the opportunity to work on this project. He helped me to grow both as a scientist but most importantly as a man, always motivating me to do my best and to not lose focus. I would like also to thank him for all the time he spent looking after me and for being always present when needed.

I would also like to thank friends I made during the course of my PhD, especially Diego Gianolio, Michele Guastamacchia and Giulio Crevatin for being always there when I needed someone to speak to.

I would also like to thank the PhD students I had the pleasure to spend my time with, from the "old guard", Miren Agote-Aran, Antonios Vamvakeros, Scott Rogers, Wilm Jones, Alex O'Malley to cite a few, to the new students, Emma Campbell, Daniela Farmer, Andrea Zachariou, Dorota Matras and all the others for raising my moral when I was down.

I would also like to thank Ines Lezcano Gonzales, Yaroslav Odarchenko, David Martin for all the help they have given me during my PhD.

A large thank to my family in Italy, especially my parents Pietro Decarolis and Giovanna Sciarrino, for their continuous support and encouragement

But the most special acknowledgement should be given to my partner, Simona Oliveri, for all the moral support she gave me during the course of my PhD. Without her I would be half the man I am now.

This PhD thesis is dedicated to her.

TABLE OF CONTENTS

1 Introduction

1.1 Introduction to catalysis

Catalysis is the science and technology of influencing the rates of chemical reactions [1]. An acceleration of the reaction rate and a reduction of the energy expenditure, paired with an increase in selectivity, results in a decrease of the costs, both in term of energy and materials, necessary to obtain the same amount of product.

This improves not only the profit generated by the industry but also reduces the amount of waste towards resulting in a eco-friendlier approach to synthesis. It is also a key technology in emissions abatement.

"Catalysis" is a term introduced by Berzelius in 1836, in order to identify and classify chemical reactions whose progress is affected by additional substances which are not part of the reaction (be it either as reagent or product) [2].

Considering a simple chemical reaction, such as:

$$A \leftrightarrow B + C \qquad \text{Eq. 1.1}$$

as written, this equation represents a reaction where a species A transform to give species B and C. The energetics of the process, if thought as a exothermic process ($\Delta H < 0$) can be described in the schematic in figure 1.1.1

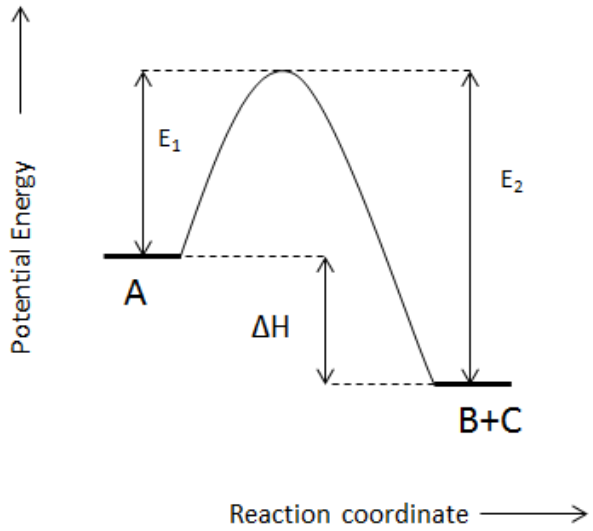

Figure 1.1.1. Energetics of a possible reaction A → B + C

In order to for the species A to transform into the products it must form an activated state, also called transition state, A* which then decomposes to form the product, as expressed in the equation

$$A \rightarrow A^* \rightarrow B + C \qquad \text{Eq. 1.2}$$

The energy required for the formation of the transition state is E_1, which is well above the average thermal energy of A molecules. The same concept can be applied for the reverse reaction, where B and C can form an activated state B-C* and transform back in A, with an energy requirement which is expressed by E_2.

Considering the situation when A decomposes in the presence of a solid surface which would adsorb A. The equation will then change to the following

$$A \rightarrow A^{ads} \rightarrow A^* \rightarrow B^{ads} + C^{ads} \rightarrow B + C \qquad \text{Eq. 1.3}$$

If the energy required for the various process (adsorption, activation, desorption) is lower than the energy reaction, as shown in figure 1.1.2, the process can be said to be catalysed.

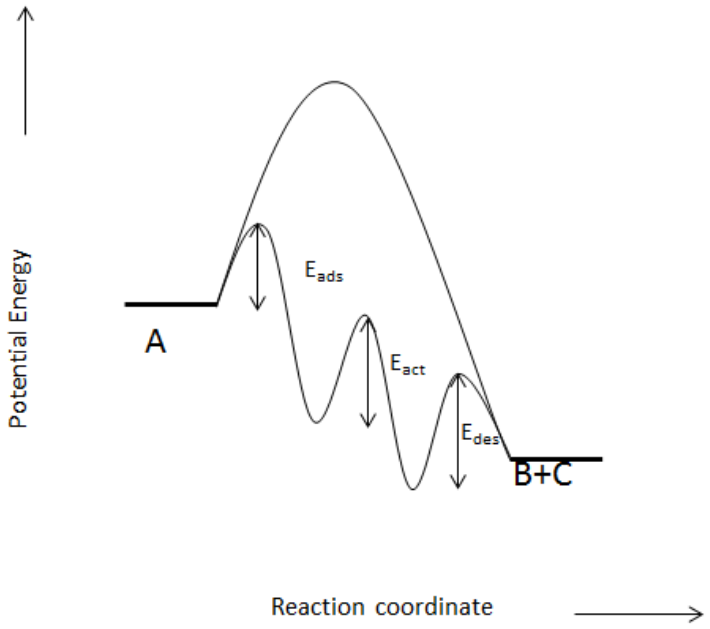

Figure 1.1.2 Schematic diagram of the energy profile for a reaction A → B+C with and without a catalyst.

Lowering the activation energy is only one of the advantages of using a catalyst. Catalysts also have a very significant effect on the selectivity of a process. Taking as example two hypothetic reactions:

$$A + B \leftrightarrow C \qquad \text{Eq. 1.4}$$

$$A + B \leftrightarrow D \qquad \text{Eq. 1.5}$$

where two reagents A and B can react to give two different product, C and D whose schematic are represented in figure 1.1.3

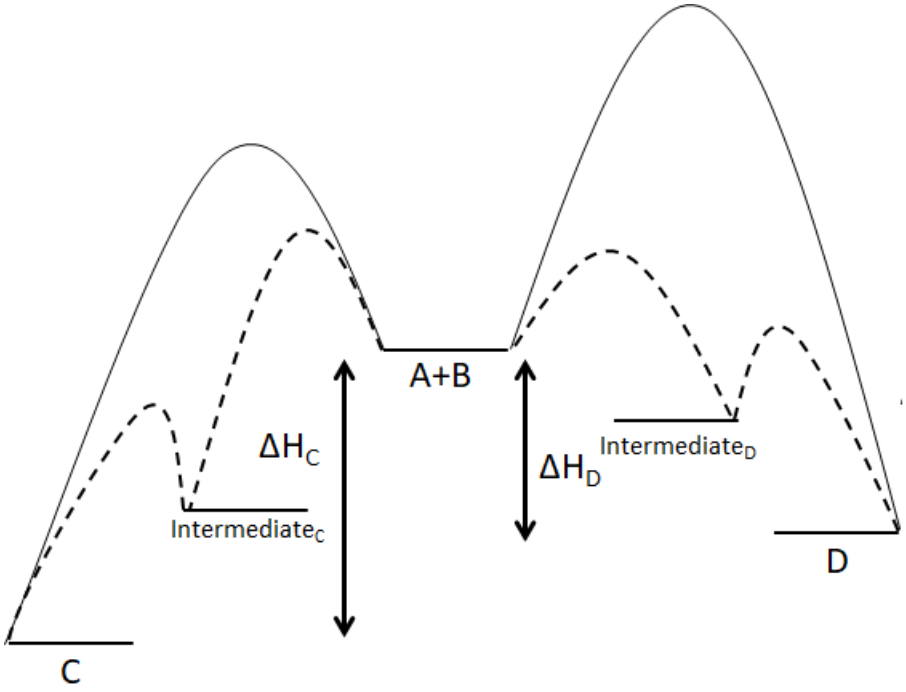

Figure 1.1.3. Energy profile for the reaction A + B → C (on the left) and A + B → D (on the right). The dotted lines represent the catalysed reactions.

The rates of production of C and D, in an uncatalysed reaction, are only dependent on the activation energies, E_1^C and E_1^D assuming no significant difference in the Arrhenius constant *A* of the Arrhenius equation

$$k = Ae^{\frac{-E_1}{T}} \qquad \text{Eq. 1.6}$$

The Arrhenius equation (eq 1.6) then determines the rate of reaction according to

$$\frac{\mathrm{d}[C]}{\mathrm{d}t} = k[\mathrm{A}][\mathrm{B}] \qquad \text{Eq.1.7}$$

Where [A] and [B] are the concentration of the reactant in a A+B ↔ C reaction, [C] the product and t the time of reaction.

As the ΔH_C is higher than ΔH_D, the product C is more thermodynamically favoured ($E_1^C < E_1^D$), and therefore will be the product that is formed selectively. If the catalyst is introduced, allowing the formation of an intermediate for the product D with a lower activation energy compared to the one formed for product C, the rate of reaction for D therefore increases and D is therefore selectively produced. Thus, catalysts are able to change the selectivity toward the products by providing different reaction energetic paths.

In order to simplify the comparison between catalysts the turnover number (TON) or turnover frequency (TOF) are used. The TON is the number of times *n* that the reaction takes places per catalytic site for a fixed set of reaction condition (temperature, concentration or pressure among others) as expressed by equation 1.8

$$TON = \frac{p}{S} \qquad \text{Eq. 1.8}$$

Where p is the number of molecules of a given product and S the number of active sites. If to eq. 1.8 the time factor (t in eq. 1.9) is added TOF is obtained

$$TOF = \frac{1}{S}\frac{\mathrm{d}p}{\mathrm{d}t} \qquad \text{Eq. 1.9}$$

However, there are some limitation in this approach, whereas for some catalysts is possible to accurately determine the number of active sites, for other, such as nanoparticles, it is much more complex.

Early examples of catalytic reactions include the production of sulfuric acid, through vanadium-assisted oxidation of SO_2 to SO_3 (Contact process [3]), ammonia synthesis (the Haber-Bosch process using an iron (+ chromium) catalyst [4]) and oxidation (the Ostwald process using platinum as catalyst [5]). A major advantage of catalysis is the ability to use less reagents to obtain the same amount of product as an uncatalysed reaction, or completely alter the procedure required for the synthesis of a particular chemical. These properties make catalysis an important asset in *green chemistry* studies. *Green chemistry* is a branch of chemistry which focus on the efficient use of raw materials, preferably renewable, eliminating waste and avoid the use of toxic and/or hazardous reagents and solvents in the manufacture and application of chemical products [6]. The principles of *green chemistry*, defined by Anastans [6], are the following:

1. Waste prevention instead of remediation
2. Atom efficiency
3. Less hazardous/toxic chemicals
4. Safer product by design
5. Innocuous solvents and auxiliaries
6. Energy efficient by design
7. Preferably renewable raw materials
8. Shorter synthesis

9. Catalytic rather than stoichiometric reagents
10. Design product for degradation
11. Analytical methodologies for pollution prevention
12. Inherently safer process

In order to define the potential environmental acceptability of chemicals process two parameters are taken in account: the E factor, which is defined are mass ratio of waste to desired product, and atom efficiency, calculated by dividing the molecular weight of the desired product by the sum of the molecular weights of all the substance produced in the stoichiometric reaction [6].

Catalysis can be delineated into three main categories: homogeneous, heterogeneous and bio-catalysis. In homogeneous catalysis, the catalyst is in the same physical phase as the reagents (e.g. the catalyst/reagents are dissolved into the reaction media). Metallocenes, such as Ziegler-Natta catalysts, are a class of homogenous catalysts widely used, usually in the form of Cp_2MX ($Cp= \eta^5\text{-}C_5H_4R$, M= Ti, Zr, Hf, X= Me, Cl), for polymerization of 1-alkenes [7]. In bio-catalysis, the role of the catalysts is taken by the enzymes, highly optimized catalysts necessary in biological systems to allow chemical transformations necessary to the life to take place [8]. These catalysts are capable of accepting a wide array of molecules and are extremely selective, catalysing reaction with unparalleled enantio- and regio- selectivity [9].

Heterogeneous catalysis concerns different physical states, usually a liquid or gas reagent typically reacting with a solid catalyst. Heterogeneous catalysis offers various advantages compared to homogeneous and bio catalysts, such as ease of recycling and separation from the products. [10]. Nowadays heterogeneous catalysis has become overwhelmingly important in our society, with more than 90 % of the chemical manufacturing process using as a mean to obtain their product throughout the world, in various processes from food to medicine to fuels [11]. But is not only industry which is interested, academia is also interested by the challenge of the ability to rationally design new catalyst, and improve the performances [11]. However, there is still much debate regarding the importance of the physico-chemical properties of the catalyst and the effect this has on a reaction. For example, the nature of the exposed surface may influence on the adsorption of reactant species, for example in the adsorption of methane over MgO catalysts [12]. Moreover, the atomic structure of the metal oxide or a crystal face may also play a role in influencing the activity, due to example defects

on surfaces [12], [13]. Another parameter influencing the activity of the catalyst is their surface area [14]. The rate of product formation is often a function of the available surface area accessible to the reactants, so the larger the amount of surface area available to the reactants, the greater the conversion [15]. One way to increase the amount of surface area would be introducing porosity, such as in the case of zeolites or metal-organic frameworks [16]–[18]. If the pores of the catalysts are sufficiently wide not to impede the passage of the reactant or products, and the internal surface is homogenous, the conversion rate is directly proportional to the catalytic surface area. Another way to improve the catalytic activity is to reduce the size, as shown in figure 1.1.4-5. As the catalyst particle size decreases linearly, the area exposed increases exponentially, thus making the catalyst sites more available for the reactant. When the subdivision is taken to an extreme, i.e. down to the nm scale, the catalyst become a nanoparticle, which results in a change in its properties. It is this aspect that renders them so appealing for study and application as heterogeneous catalysts.

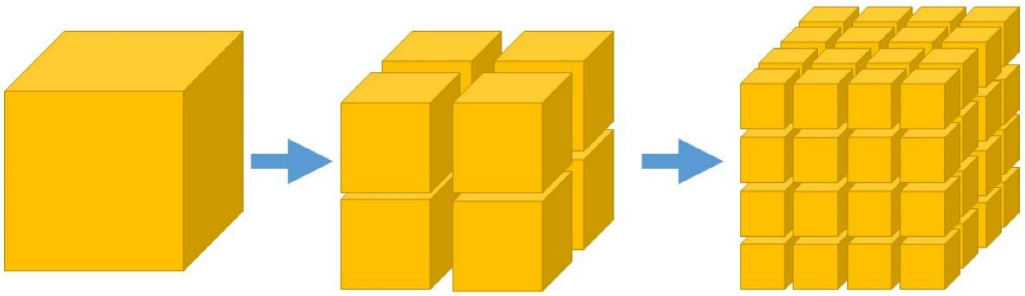

Figure 1.1.4. Schematic representation of the increase of surface area caused by subdividing a cube of a solid material.

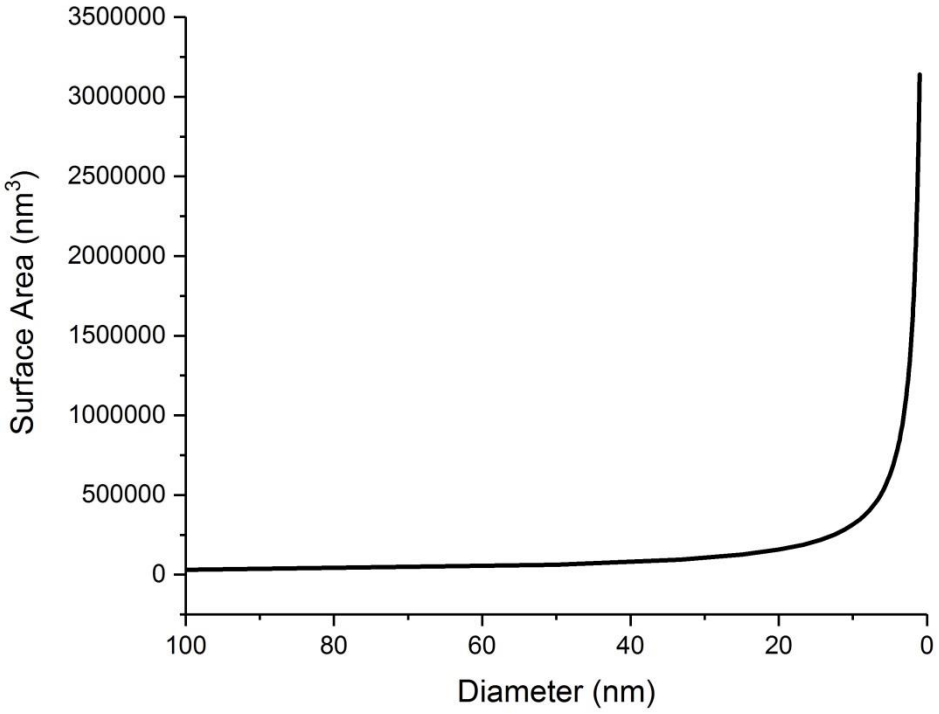

Figure 1.1.5. Increase of surface area as function of particle size

1.2 Properties of nanoparticles

While many catalysts were discovered largely by trial and error via the mixing of different reagents (i.e. different metals and ceramic supports), molecular insights into the catalytic processes are mainly derived from the study of model catalysts (well defined single-crystal metal surfaces or metal particles supported on oxide surfaces) [19]. Moreover, research is headed towards the creation of functional materials, devices, and systems through the control of matter on a scale of nanometres [20]. ”Nanoparticle” is a term employed to describe a class of materials with structural features and behaviours which are intermediate between that of atoms and bulk materials, with at least one dimension in the nanometre range [21]. Materials science and technology is a field that is evolving and is providing the most significant contributions to nanoscale research.

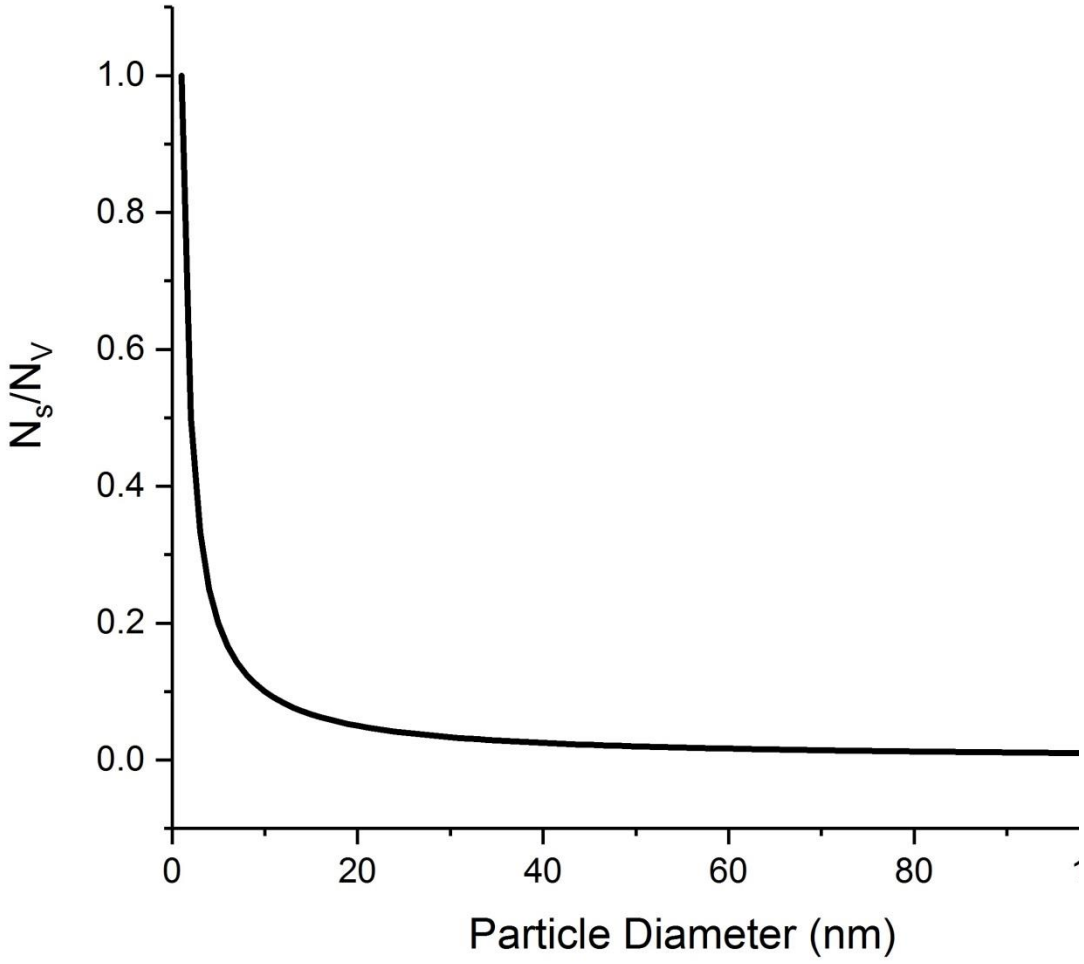

Figure 1.2.1. Proportion of surface atoms for spherical particles comprising N_v atoms with N_s at the surface.

Nanoparticles frequently show behaviours which are intermediate between that of a macroscopic (also known as bulk) solid and that of a molecular system [22]. For example, in the case of a nanoparticle it can be seen that its properties differ from that of a single atom, but it cannot be said that they will be the same of a bulk solid. The number of atoms on the surface of the particle is a significant fraction of the total number of atoms and therefore will have a huge influence on the properties of the nanoparticles, such as chemical reactivity or melting point [23]. It can be seen from figure 1.2.1 that these considerations are especially true when the size of an object is less than 10 nm. Around 5 nm diameter (approximately 8000 atoms) the proportion between surface and bulk atoms is about 20 %, while at 2 nm (around 500 atoms) it's 50 %. This proportion can be estimated for the transition metals by the relation shown in equation 1:

$$\frac{N_S}{N_V} \approx \frac{1}{2R} \qquad \text{Eq. 1.}$$

where R is the radius in nm [22]. This empirical law is true only up to 1 nm, where the proportion of surface atoms approaches 100 %. Size effects can also include atom magic numbers (such as 1, 13, 55, 147 atoms depending on the number of shell, which represent the lowest energy atom configuration in a nanoparticle [24]) following of atoms in metallic clusters, quantum mechanical effects [25] etc. In figure 1.2.2. it is shown how the electronic structure of a nanocrystal differs from those of bulk materials or molecules.

In atoms the atomic orbitals are discrete and defined, but as the atoms interact to form molecules they combine in molecular orbitals. As the number of atoms increases the difference in energy between the molecular orbitals decreases until, instead of discrete energy levels, they can be described as broad energy bands. This assumption is only valid however in the case of a periodic combination of atomic orbitals, where the contribution from the surface of the material are neglected by assuming an infinite solid [26], [27]

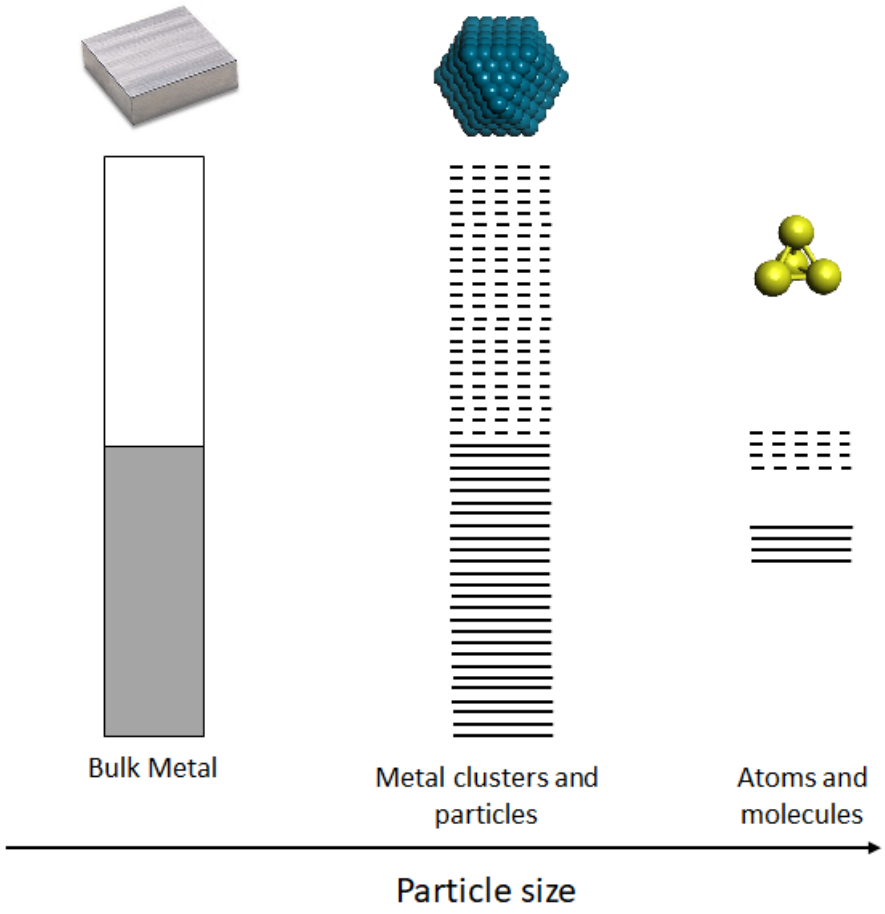

Figure 1.2.2. Formation of discrete electronic orbital energy levels moving from bulk structure (band structure) towards a single molecule (molecular orbitals).

In very small nanoparticles, the assumption of infinite size is no longer applicable and thus, these system cannot be described with the same model used for bulk solid. It is possible to imagine the electronic structure of a nanoparticle somewhere in between the behaviour of atomic system (discrete energy levels) and a bulk solid (band structure)[26]. The mixing between the electronic characteristics of atomic and bulk systems gives nanoparticles a huge range of applications, for example in electronics and electromagnetism [23].

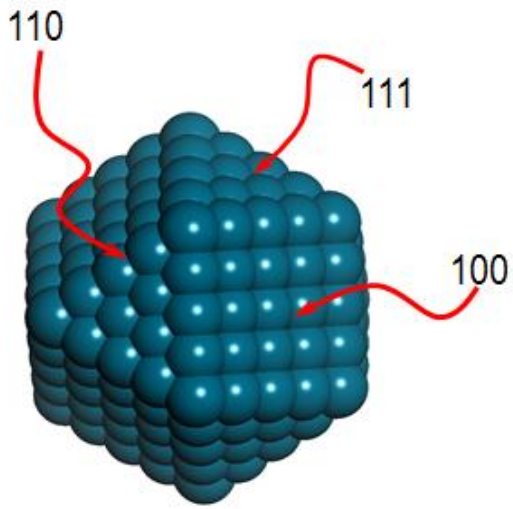

Figure 1.2.3. Truncated cube or cubo-octahedron, the equilibrium shape of an Face-centered cubic (fcc) crystal comprising 586 atoms. Indicated by the arrows are respectively the [110], [111] and [100] faces of the crystal.

A nanoparticle, in principles, could be considered no more than a fraction of the corresponding bulk crystal. However, the structure of a nanoparticle is dependent on the most favourable energy state, thus assuming even amorphous structures [22]. It should be noted that the modification happens differently depending on the metal, for example for silver, the icosahedral form (with a C_5 symmetry axis) is the most stable packing arrangement up to several hundred atoms, whereas the cubo-octahedron (the structure of the bulk crystal) is already the most stable for a few tens of atoms in the case of noble metals (Pd, Pt or Au) [22]. The equilibrium shape expected for a metal particle with the fcc structure is generally a cube truncated to form a cubo-octahedron as shown in figure 1.2.3. In particular, for a cubo-octahedron five types of surface atoms can be identified: corners (C_6^6), atoms within (100) faces ($C_8^{4,5}$), atoms within (111) faces (C_9^3), edges between two (111) faces (C_7^9) and edges between (100) and (111) faces (C_7^5) [28]. Of course, as the size of the nanoparticle gets bigger there is a rapid diminishing importance of corner and edge atoms and a dominance of terrace atoms. At the surface the interatomic distances are generally known to contract. This is a consequence of the fact that the surface atoms are undercoordinated. The higher reactivity of atoms with lower coordination (situated on edges or corners) in the case of nanoparticles or on steps in the case of a monocrystal with regard to the breaking of chemical bonds has been demonstrated on many occasions [29]. The contraction

between surface atoms and the immediate underlying plane depends on the coordination number Z of the surface atoms, increasing as the coordination number of the atoms decreases [22].

1.2.1 Nanoparticles in catalysis

One of the first applications of nanoparticles (NPs) in catalysis can be dated back to 1899 with the work from Bredig involving the catalytic decomposition of hydrogen peroxide over platinum nanoparticles [30]. Further pioneering catalytic applications of NPs were reported in 1940 on nitrobenzene hydrogenation by Rampino et al. [31] but research interest in nanoparticles became popular in the second half of the 20th century, when they became relevant for an important group of reactions, such as hydrogenation, hydrosilylation or reduction, with works such as that of Parravano on hydrogen atom transfer between benzene and cyclohexane in 1970 [30]. Later Bond and Sermon reported AuNP-catalysed olefin hydrogenation, and the work from Haruta on CO oxidation by O_2, emphasised the importance of nm-size in catalysis [32]–[34]. Nanoparticle-based catalysts are used nowadays in many different areas such as industrial catalysis such as in the Fischer-Tropsch process [35]–[37] or methanol synthesis [38], [13], [39], [40] or fuel cells [41] as well as water purification [42]. However the question regarding the nature of the active sites and the structure dependence of heterogeneous catalysts has been debated for almost a century [43]. Whereas some reactions are defined as structure insensitive, reaction which exhibit nearly identical turn-over frequencies (TOF) independent of the structure of the catalysts, such as ethylene hydrogenation on Pt [28], [44], a large number of reactions are affected by the particles size and shape. One example of the effect of particle size on catalysis is the Fischer-Tropsch reaction using Co nanoparticles [35]. Whereas it has been shown that the turn-over frequency, if the activity is calculated taking in account the surface specific activity, is not a function of the particle size when the Co nanoparticles are in the size range 6 to 27 nm, when nanoparticles becomes smaller than 6 nm the TOF becomes dependent on the particle size [45], [46]. The reason for this behaviour could be attributed to the surface residence time of reversibly bonded CH_x and OH_x intermediates, paired with a decrease of the CO residence time; moreover the surface coverages of the CH_x, OH_x and CO intermediates decreased for small particles and the combination of these two effects causes a decrease in the TOF that does not appears on larger particle (> 6 nm), presenting constant values for these

parameters. Another important reaction regarding the particle size effect can be seen in the work by Haruta et al on the CO oxidation on Au nanoparticles [32], [47] where it was shown that only particles in a particular size range (3 – 4 nm) were active. As for the particle size effect in hydrogenation reaction, Bertolini et al [48] have shown that the activity of surface atoms with regard to hydrogenation of unsaturated carbon on Pd atoms can be independent of the particle size (as in the case of 1-butene), but it can be strongly dependent on the dispersion (as happens with alkynes and conjugated dienes). Once again strong variations can be seen over a size range spanning 1.5 to 4 nm, as shown in figure 1.2.4, and in particular that very small particles are selective to over hydrogenation.

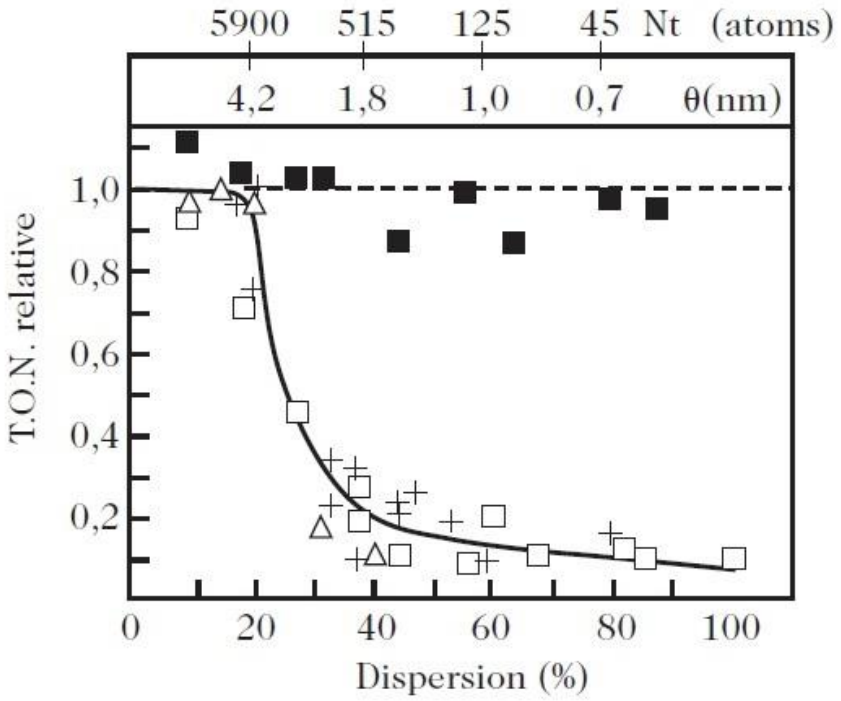

Figure 1.2.4. Variation of the turn-over number (TON) as a function of Pd nanoparticle dispersion/particle size/number of atoms for hydrogenation of butene-1 (black squares), butyne-1 (□), butadiene-1,3 (+), and isoprene (Δ). Reproduced with permission from Springer, Bertolini et al., *Nanomaterials and Nanochemistry*, 2007, chapter 10, pg. 293 [49].

A problem arises however when comparing catalysts prepared using different methods; the use of different precursors, catalyst support or preparation conditions may lead to catalysts whose property could be completely different disregarding their particle size [50]. Moreover, a particular attention must be placed on the

characterisation of particle size; often the reported particle size is the mean particle size; an average over a large number of particles. Methods of preparation such as impregnation may cause a large particle size distribution, as seen in a typical paper by Okumura et al. where a standard deviation ~50 % of the total gold nanoparticles were present [51]. This might cause problems in the identification of the real active part of the particle size due to possible interference of larger and smaller nanoparticle, or even atomically dispersed species such as in the case of a study from Rogers et al where the presence of ultra-small Au clusters (1-5 atoms) produced an increase in the catalytic capability for the reaction of glycerol oxidation [52]. Colloidal preparation methods, in particular reverse micelle techniques, might provide a suitable catalyst for a structure sensitivity study [53]. In this respect the reverse micelle method using polystyrene-b-poly(2)vinylpyridine co-block polymer method, developed by Spatz et al., has shown remarkable success in producing metal nanoparticles with a narrow particle size distribution, with a size distribution << 1 nm [54]. This method has been used by Croy et al for the decomposition of methanol on Pt catalysts, with particle sizes of 4, 6 and 8 nm, all with a standard deviation < 17 % [55]. The results obtained show a strong particle size dependency, with the smaller sized particles being the most active, in term of conversion, towards the reaction. In another study from Mistry et al., Au nanoparticles prepared using reverse micelle encapsulation were used to test the electrocatalytic reduction of CO_2 to CO, and, in the same reaction pot, CO reaction with hydrogen, to produce useful hydrocarbons, using nanoparticles in the size range of ~ 1 – 8 nm. The results showed again a remarkable size effect with a drastic increase in activity observed for nanoparticles below 2 nm, explained by the increase in the presence of low-coordinated sites. Furthermore, the results show an interesting selectivity dependence on particle size, with the lower part of the distribution (up to 5 nm), results in catalysts that are more active toward the production of CH_4, the intermediate sizes (between 5 and 7 nm) where methanol and Fischer-Tropsch is the predominant reaction, and above 7 nm where the selectivity shifts towards hydroformylation of alkenes to aldehydes [56].

An important role is also played by the support due the fact that while a support offers a facile way to immobilise nanoparticle catalysts, they also interact with the nanoparticle itself changing the morphology or the electronic properties [57], [58]. The interaction with the support depends on two primary effects; the first and foremost

is the electron transfer to or from the support; the particle has an excess or a deficit of electrons depending on the nature of the support. For example in the case of electron transfer between Pt nanoparticles and CeO_2, which causes a partial oxidation of the Pt paired with a reduction of the ceria nanoparticles [59]. The electron transfer may also depend on the reaction conditions, such as in the case of Au/ZnO nanorods. According to Liu et al. if this system is reduced thermally under an O_2 atmosphere the electron would be transferred from the gold to the support, causing the appearance of $Au^{\delta+}$ species [60]. If H_2 is used for reduction instead, the opposite behaviour occurs where the electrons are more attracted to the gold forming $Au^{\delta-}$ species. The second effect is thought to be related to a metal-support interaction and epitaxial stress that can modify the particle structure, the lattice parameter and/or the particle morphology, such as in the case of a Pd cluster on MgO(100), where, depending on the cluster size, different atomic arrangements appear either at the interface between Pd and MgO or on the facets of Pd nanoparticles [61]. These effects will be more marked the smaller the particle is, and will also change its chemical reactivity [22]. The support could also be part of the catalytic process as a whole, acting as an O_2 reservoir such in the case of CO oxidation on Au nanoparticles, where it is believed that the presence of a reducible support, such as TiO_2 or ZrO_2, leads to an increase of the catalytic activity due the role of support as an oxygen source, leaving Au nanoparticles the role of CO activation for the reaction [11], [62]. However, it is important to note that the advantage of having highly active sites may be offset by their blocking (deactivation) by strongly adsorbed residues [29] such as carbon and CHx species on Pd nanoparticles, for example, during methanol decomposition [63].

1.3 Gold nanoparticle in catalysis

1.3.1 A brief history of gold nanoparticles and their use in catalysis

Gold is one of the oldest metals with an important significance in human culture. It has been excavated since 5000 B.C. and has always played a pivotal role in the development of humanity [64]. Art has grown with the use of gold and wars have been fought for the ownership of the ore mines. It has been used in the past for a variety of purposes: as a currency and as a base for jewels and artefacts, due its rarity, colour and the ability to reflect the light and as a medicinal ingredient, due the association of gold with immortality [65].

Gold possesses a unique combination of physical and chemical properties in both macroscopic and microscopic states. Its properties do not follow the trends observed in other groups and bear few resemblance to the other members of its group (copper and silver) [65]. For a wide range of metallic properties gold behaves as one of the extremes, having excellent resistance to corrosion, high ductility and malleability as well as possessing high chemical stability and redox potential ($E_{0\ Au^0\text{-}Au^{3+}}$ = 1.5 eV, $E_{0\ Au^0\text{-}Au^{1+}}$ = 1.6981 eV) [65]. The high chemical stability makes gold lack reactivity, demonstrated by its inability to dissolve in most acids (with exception of *aqua regia*) or else an interaction with atmospheric gases to form oxides or sulphides like copper and silver [66]. These properties lead to a low, or in some cases no, catalytic activity of gold towards most chemical species. However, if gold is brought down to the nanoscale many of its properties change. One of the first things to notice is the change in colour, from yellow to deep red when particles reduced below 100 nm in size [67]. This change in colour has been used in the past such as the famous example of the Lycurgus Cup, manufactured between the 5th and 4th century B.C., as well as multiple other cases throughout history such as the Kunckel glass in the 17th century or the Perrot works from the early 18th century. [65]. It was Michael Faraday who first proposed that, after producing a deep red solution via reduction of the chloroaurate anion ($[AuCl_4]^-$), the presence of a "finely divided metallic state" gold was present [68]. Other effects that arise from the reducing of the size of gold particles down to the nanometre regime include: a sharp decrease in melting temperature (~ 500 K for a 2 nm nanoparticle compared to 1337 K for bulk gold) as well a decrease of interatomic separation (from 1.4 % of the normal Au-Au bond distance for 30 Å particle to 5.5 % for 8 Å particles) [69], [70]. These effects are caused by the increased presence of

surface atoms; the surface atoms energies produces behaviours akin to the surface tension of liquids [65]. At the same time the surface atoms, possessing a lower coordination number, possess increased chemical reactivity [65]. Whereas this type of effect is known in other types of metal catalyst e.g. palladium [71], [72], platinum [73], [74], in the case of gold, it makes a non-active element active and therefore an important subject of research with over 9,900 publications on gold + catalysis in 2017 alone according to Web of Science.

The reason for the 'enhanced' catalytic activity has not been fully explained, as it is thought to be a consequence of a series of effects occurring at the same time. It is however known that as the nanoparticle gets smaller, the gold becomes more active, with ~10 nm being the limit above which the catalytic activity drops dramatically [75]. This particle size effect could be correlated with an increase in the number of under-coordinated atoms (corners and edges) and the reduction in size and importance of larger [111] planes, previously showed to be catalytically negligible [65], [66]. Moreover, the support appears to plays an important role in the activity of Au cluster. In general for Au nanoparticles support can be distinguished in two categories: reducible (e.g. TiO_2. CeO_2) and non-reducible (e.g. Al_2O_3, SiO_2) [76], with the former usually more active. This distinction is mostly inferred from CO oxidation studies [32], [77], but it appears relevant for other reactions such as water gas shift reaction [78], [79]. The cause for this support dependency are not fully clear; whereas a general agreement is that the reducible support acts as an oxygen reserve during the reaction [76], [80], it has been suggested that the support may also interact with the Au causing a charge transfer [81], such as in the case of Au/CeO_2 [82], [83], where cationic $Au^{\delta+}$ species appear to be stabilised, or in Au/MgO_x where instead $Au^{\delta-}$ is present [84]. Therefore, whereas for most of the metals the activity can be estimated as the turnover frequency (mole of surface metal per s), for gold it is not recommended as is difficult to define which of the surface atoms are active [65].

1.3.2 Gold nanoparticles and catalysis

Gold holds an important place in catalysis industry, as a possible substitute for platinum group metal catalysts because of its ability to selectively reduce or oxidise molecules [81], [85]–[88]. Whereas real-world application of gold catalysis is not widespread, due to the high cost of the material compared to other commonly used PGM catalysts (~1200 $/oz for gold and ~700 $/oz for palladium as this thesis is being

written), it has been used industrially in three major reactions, two of which (synthesis of vinyl acetate, and oxidative esterification of methacrolein to methyl methactrylate) where gold is used in combination with other metals (Pd [89], [90] or Ni [91]) and the reaction of hydrochlorination of acetylene for the manufacture of vinyl chloride monomer, then used for the production of polyvinyl chloride [92], [93]. However, it is plausible that in the future gold will replace other catalyst due its higher selectivity and abundance compared to the other metals [94]. In particular regarding the selectivity it has been shown that gold has the ability to stop the reaction when the useful intermediate product is formed [95], [96].

It has also been shown in the past that Au nanoparticles show a high chemoselectivity even in the presence of more than one reactive group [97], [98]. An example of this behaviour is the oxidation of allylic alcohols, where Au/CeO_2 is able to chemoselectively oxidize, in a solvent free environment, the hydroxyl group while avoiding oxidation, isomerization or polymerization of the olefinic group. Another example of the chemoselectivity of Au nanoparticle includes their ability to chemoselectively reduce nitro groups when other reducible functionalities (e.g. C=C, C=O) are present, in particular when supported on TiO_2, Fe_2O_3 or γ-Al_2O_3 [99], [100].

Since the initial observation of the catalytic activity of gold nanoparticles, the research has moved toward understanding the possible application in various reaction. For example, the discovery from Haruta et al. of the ability of small gold nanoparticles (< 3 nm), supported on reducible transition metal oxide (TiO_2, Fe_2O_3 etc), to catalyse the oxidation of CO to CO_2; a reaction having vast environmental applications [34]. The reaction is not catalysed by single crystal surfaces (e.g. Au[111]) and only marginally catalysed by atomically dispersed species deposited on bulk metal or large particles (> 40 nm). Thus there is a clear importance of corners and edges with low coordination atoms, capable of chemisorb CO sufficiently but not too strongly [65], [101], [102]. The importance of undercoordinated atoms is particularly evident in the case of sub-nm Au cluster, which appears to be more active than larger species (1-3 nm) [103]. Moreover the capability of gold to oxidize CO extends even to the conditions when the CO is present in a high concentration of H_2, whilst at the same time it does not catalyse the reverse water gas shift reaction ($H_2 + CO_2 \leftrightarrow CO + H_2O$), making gold catalysts potentially viable in fuel cells [65].

Another oxidation reaction concerns that of alcohols and polyols. This set of reactions is usually performed using platinum and palladium nanoparticles which, albeit showing high activity, show a poor selectivity when the substrate is more complex in structure, e.g. long-chain alcohols/presence of multiple functional groups (such as NO or C-C double and triple bonds). The Rossi and Prati group have shown the ability of gold nanoparticles to oxidize alcohols very effectively [104] even at mild reaction condition (T = 343-363 K, pO_2 = 300 kPa) , and in a particular study from Carretin et al. it was shown that gold can even oxidize glycerol to glycerate with 100 % selectivity still under mild conditions (T = 333 K, using water as solvent) [105].

However one of the earliest and definitive pieces of work on supported gold nanoparticles, concerns the study performed by Bond et al in 1973 demonstrating the capacity of supported gold nanoparticles on ceramic oxides (e.g. SiO_2 and Al_2O_3) to hydrogenate double bonds, in particular 1-pentene, at temperatures lower than 473 K [106]. In particular the ability of gold to either selectively hydrogenate the C-C double bond [107]–[109], such as in the α,β-unsaturated aldehydes[110]–[112], or the important selective reduction of nitro groups [99], [100], [113], in the presence of other reducible functional groups. Furthermore, gold has shown the remarkable ability to not over-hydrogenate conjugated dienes, improving the purification of C_4 olefin industrial cuts [32], [114], [115].

1.3.2.1 Particle size effects in catalysis

Whereas many parameters influence the catalytic activity of gold nanoparticles, such as facet expression (whether Au [111] or Au [100]) and the metal-support interaction, particle size is one of the most important in the regards of the reactivity of gold [75], [116]. One of the first to discover the importance of particle size was Haruta [32]. He demonstrated that only particles of gold in a certain size range (<3 nm) were active towards CO oxidation [32]. Since then the literature has explored the effect of particle size towards a variety of reactions. The catalysis being performed using gold nanoparticles can be delineated into two major branches: reduction (using H_2) and oxidation (using O_2 or sacrificial oxidant such as H_2O_2). Dealing with the former first, the interaction between molecular hydrogen and gold has been reported to be affected by the particle size through H_2-D_2 exchange (HD formation), in a study from Kartusch [112] et al. and Fujitani et al. [117]; the smaller the particles, the more hydrogen atoms adsorb onto the gold nanoparticles. This is reflected in an early study from Bond et al.,

where ethane hydrogenation was investigated on Au nanoparticles supported on silica [118]. They calculated that the rate of hydrogenation per unit weight of gold increased as the gold loading on the support decreased (thus decreasing the particle size), with a similar rate as the one shown from H_2-D_2 exchange, thus implying that the rate of hydrogenation of ethene to ethane is dependent on the hydrogen dissociation on Au NP. A similar behaviour appears for the hydrogenation of acetylene to ethylene in a study from Gluhoi et al. where they showed that the more the particles grow the less active they become [119]. For example, CO oxidation, as shown in figure 1.3.1, when Au nanoparticles are supported on TiO_2 a sharp increase in the turnover frequency (TOF) when the particle size is below 4 nm is observed; this is in contrast to Pt/SiO_2 which shows a degree of particle size insensitivity with the TOF that is steady/decreasing with size.

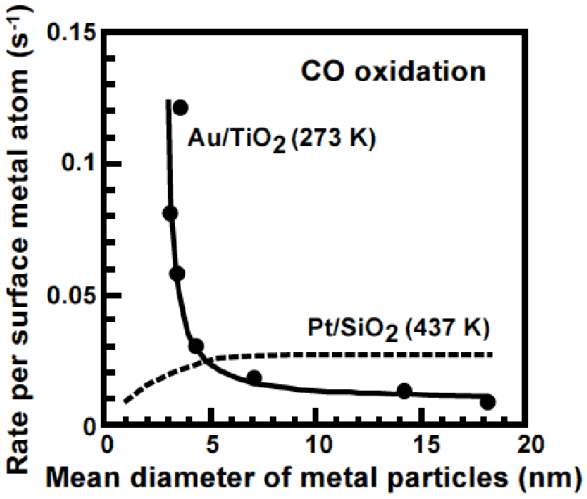

Figure 1.3.1. Turnover frequency (TOF) for CO oxidation over Au/TiO_2 as a function of the mean diameter of Au particles. Reproduced with permission from Wiley, Haruta, *Chem. Rec.*, 2002, vol 3, pg 75-87 [33]

Another reaction showing a particle size dependency is propylene epoxidation to produce propylene oxide [33]. In this reaction it has been shown by Hayashi. et al. that a particle size of 2 nm is critical toward the successful reaction; nanoparticles smaller than 2 nm sees the product of the reaction switch from propylene oxide to propane [120]. This phenomenon implies that a change in surface property of Au clusters might be induced by electron donation from Au towards O_2 to form negatively charged oxygen species [33]. This effect could also explain the catalytic activity of ethanol

dehydrogenation to acetaldehyde [58]. This reaction, studied for nanoparticles in a range of 2-15 nm, behaves differently depending on reaction conditions; when the reaction is performed without an O_2 co-feed it appears that nanoparticles < 2 nm are less active than 5 nm nanoparticles, which appear to peak in activity, only to decrease again and being more or less constant for particles bigger than 7 nm as shown in figure 1.3.2. [58]. This behaviour drastically changes when O_2 is introduced in the reaction mixture. The overall activity increases, even for the smaller particles, but, interestingly, the activity stays constant until a particle size of 7 nm is reached when activity starts to increase; after the increase in activity it can observed again to reach a constant rate independent from the particle size when reaching 10 nm or larger.

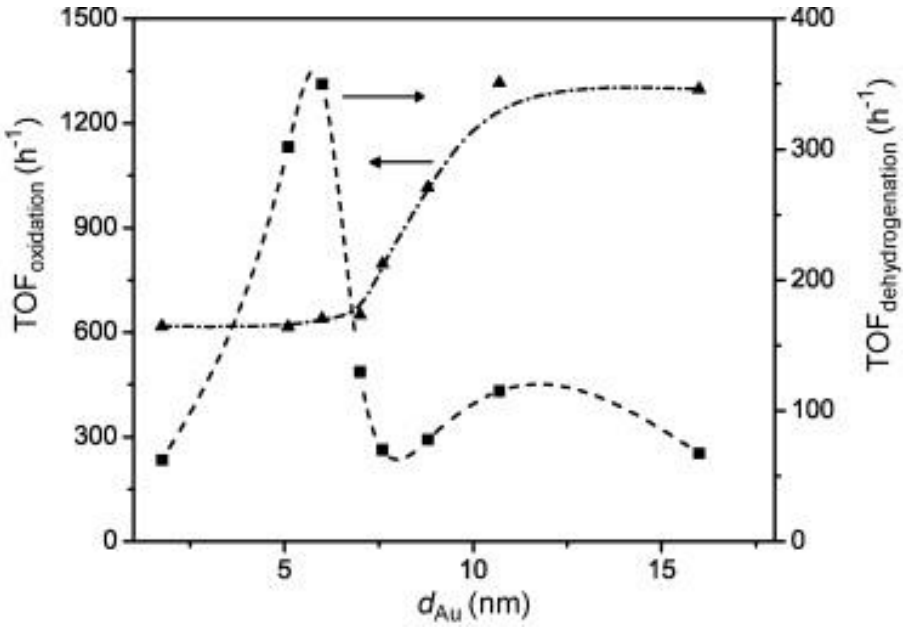

Figure 1.3.2. Turn-over frequency (TOF) for ethanol dehydrogenation in the absence (■, 250 °C) and presence (▲, 200 °C) of oxygen as a function of the gold particle size. Reproduced with permission from Elsevier, Guan et al, *Appl. Catal. A*, 2009, vol 361, pg 49-56 [58]

Although in the first case the behaviour could be explained from the rate limiting β-H elimination of the adsorbed alcohol, the second has been attributed again to strongly adsorbed O_2 atoms on the surface of Au nanoparticles. Overall there is still a lot of debate on the effect of particle size mostly due to underlying questions regarding the true active site of the reaction [65]. Whereas the number of edges and corners, the sites considered to be active, increase in number as the particles get smaller, it is not clear if the activity of those sites remains the same as the particle size increases [64], [121].

This leads to the supposition that changing the particle size only changes the total number of active sites rather than the behaviour of the active sites itself, and therefore that research effort should lead towards increasing the total number of particles supported rather than changing the size [122]. However as shown from the dehydrogenation of ethanol this is not as simple as it appears and information about the interaction of reactant with the Au nanoparticle is paramount in order to define the true effect of particle size [58].

1.4 Palladium nanoparticles in catalysis

1.4.1 A brief history of Pd nanoparticles and their use in catalysis

Compared to other metals, such as Au or Cu, Pd was unknown until the early 18th century AD, when William Wollaston managed to separate it from Pt when dissolved in aqua regia. Pd, as part of the residue, was then identified as a new metal [123]. While Pd belongs to the Pt-group of metals (composed of Ru, Rh, Os, Ir and Pt) it possess atypical characteristics. The configuration of its outermost electron shells (Pd $4d^{10}\ 5s^{0}$) is different from that of Ni ($3d^{8}\ 4s^{2}$) and Pt ($3d^{9}\ 4s^{1}$). It is also the least dense, with the lowest melting point in the group [124]. Pd is used in many different fields: jewellery (especially in combination with Au to form white gold), dentistry, electrical contacts (for active components such as diodes, transistors, semiconductors etc. etc.)[125]–[127]. However in industry, arguably the most important property of Pd is its capability to catalyse a various number of reactions [128]–[130]. Economically the most important reaction, in terms of Pd usage (more than half of the world supply), is the catalytic conversion of harmful automobile exhaust. The use of Pd in catalytic converters dates back to 1974 [127], [131], when Pd was mixed with Rh and Pt to form a three-way catalyst (TWC), capable of 'neutralising' unburned hydrocarbons, nitrogen oxides and CO. However, the high cost of Pt and Rh, in particular for Rh due to the scarce availability, lead the research toward the usage of Pd only TWC, due to the lower cost of Pd, and since then numerous studies has been performed in order to improve catalytic performance[130], [132]. In 1994 the Ford Motor Company successfully applied a Pd-only three-way catalyst, which allowed a significant cost saving in precious metal usage [131]. The advantages of Pd-based TWC, apart from the obvious economic one, includes a faster light-off, which lead to an improvement in hydrocarbon (HC) conversion [133], [134], their ability to adsorb more oxygen over

a wide temperature range, influencing the oxidation capacity [135], as well as their high resistance to temperature-induced sintering when compared to Pd and Rh, which lead to a higher overall stability [136]. Of course there are also drawbacks: it is susceptible to poisoning from sulfur and lead, although this has been mitigated somewhat by the improvement of fuel quality. Furthermore Pd catalysts show a lower activity compared to Pd/Rh catalysts towards NOx reduction and HC oxidation [131]. Research has then been focused on improving the catalytic performance of Pd-based TWC [137], [138].

Pd, in various forms, has been used to catalyse a vast series of reactions in the laboratory, i.e. alkane oxidation, hydrogenation of alkynes to alkanes and carbon-carbon bond forming reactions (Heck reaction and Suzuki coupling)[128], [139]–[141]. In particular, the Suzuki coupling reaction using Pd has been widely studied, even leading to the Nobel Prize being awarded to Akira Suzuki in 2010. In the Suzuki coupling reaction, coupling between arylboronic acid and aryl halide is traditionally performed using Pd (II) complexes, the majority of which contain phosphine ligands. These compounds, whereas very active, present problems regarding toxicity and cost [142], moreover there is the more general issue regarding the recoverability of complexes from the reaction mixture [129]. Phosphine-free compounds such as Pd-carbene complexes or phospa-palladacycles, as well as simple Pd salts such as $PdCl_2$ or $Pd(OAc)_2$ are being used in Heck and Suzuki reactions [143], as a substitute for phosphine-based compound. In particular for the reaction of aryl bromides with olefins to produce substituted olefins with an aryl group, $Pd(OAc)_2$ with or without N,N-dimethylglycine, has been shown to be one of the cheapest and most active catalysts [144]. However, it has been found by Reetz et al. [143] that the actual active component in the catalyst is the reduced Pd^0 forming Pd colloids, with an average particle size of 1.6 nm. This led to the idea that other phosphine-free Heck reactions and other C-C bond-forming processes (such as aryl-aryl bond formation [145] in the presence of Pd salts without special ligands) were actually catalysed by nanosized Pd colloids [143]. Since then PdNPs have attracted great interest, as a promising alternative in the search for a catalyst with milder reaction conditions and a more environmentally friendly approach [146]. However, a strong debate has developed whether the catalysis arises from leached metal atoms from the nanoparticles or the nanoparticles themselves [146]. According to a Pérez-Lorenzo study [146], due to

variations in reaction conditions from author to author, a direct comparison is difficult. It could be thought that Suzuki cross-coupling reactions may operate under homogeneous or heterogeneous catalytic conditions depending on a variety of factors, such as the nature of PdNPs and their stabilizers as well as the properties of the reactants involved. Both mechanisms could be considered as complementary and dependent on immobilization degree of PdNPs. The application of unsupported nanoparticles has been used for other coupling reactions such as Heck and Sonogashira, usually protected by some form of capping agent in order to prevent aggregation [139]. Simple filtering allows the recovery of the metal in order to start a new cycle.

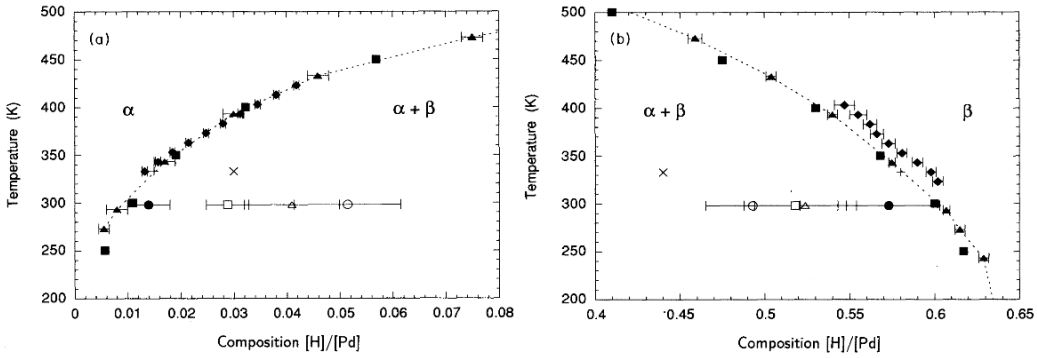

Figure 1.4.1. (a) Low- and (b) high-hydrogen-concentration portions of the miscibility gap in the Pd-H phase diagram. The phase-boundary positions derived from [147] for samples CCx (●), N1 (○), N2 (□), and N3 (△) are compared with the results of Miitschele and Kirchheim ([148]) for coarse-grained (+) and nanocrystalline (X) Pd at 333 K and with literature results for the phase boundaries in coarse-grained Pd given by Kuji et al. ([149]) (■), Wicke, Brodowsky, and Ziichner ([150]) (▲), and Lasser ([151]) (◆). Reproduced with permission from American Physical Society, Kestel B. J., *Physical Review B*, 1993, vol 48, pg 84-92 [147]

Pd has also shown an unique ability to selectively hydrogenate alkynes even in a large excess of alkenes. The reason for this high activity towards the hydrogenation reaction could be attributed to the high extent of interaction between Pd and hydrogen; Pd has shown the ability to dissolve hydrogen in the bulk as well as high activity for molecular hydrogen splitting [152]. The hydrogen dissolved in the Pd bulk forms a new phase, Pd hydride. This phase is an intermetallic species where hydrogen atoms occupy interstitial octahedral vacancies in the Pd lattice. Depending on the hydrogen

concentration two Pd hydride phases can be formed; alpha and beta phases as shown in figure 1.4.1. The two phases coexist over a broad range of H/Pd concentration, with pure alpha phase present a low concentration (H/Pd <0.017) and beta phase at higher concentration (H/Pd >0.55) [152], [153].

The reaction mechanism for the hydrogenation of C-C double and triple bonds was proposed by Horiuti and Polany [154]. They identified the following steps involved in the reaction: hydrogen dissociation on the metal surface, alkene adsorption, subsequent hydrogen addition to the alkene and desorption of the product. Debate arises regarding the role of different species of hydrogen on Pd, surfaces and bulk. Bulk hydrogen atoms are proposed to be key for the hydrogenation process of olefins[19]. Nowadays most of the research regarding hydrogenation reactions is focused on examining the role of particle size in the catalytic hydrogenation of carbon-carbon double bonds [155]–[158].

1.4.2 Particle size effect

As with most nanoparticulate systems, the size of the Pd particle is an important factor in catalytic performance. For example in the Suzuki reaction, a study performed on nanoparticles in the range of 3.0 to 6.6 nm shows a particular trend: as the nanoparticle decreases in size the activity (normalised per surface atoms) increases until 3.9 nm, to then decrease when the particle size is 3 nm [159] as shown in figure 1.4.2.

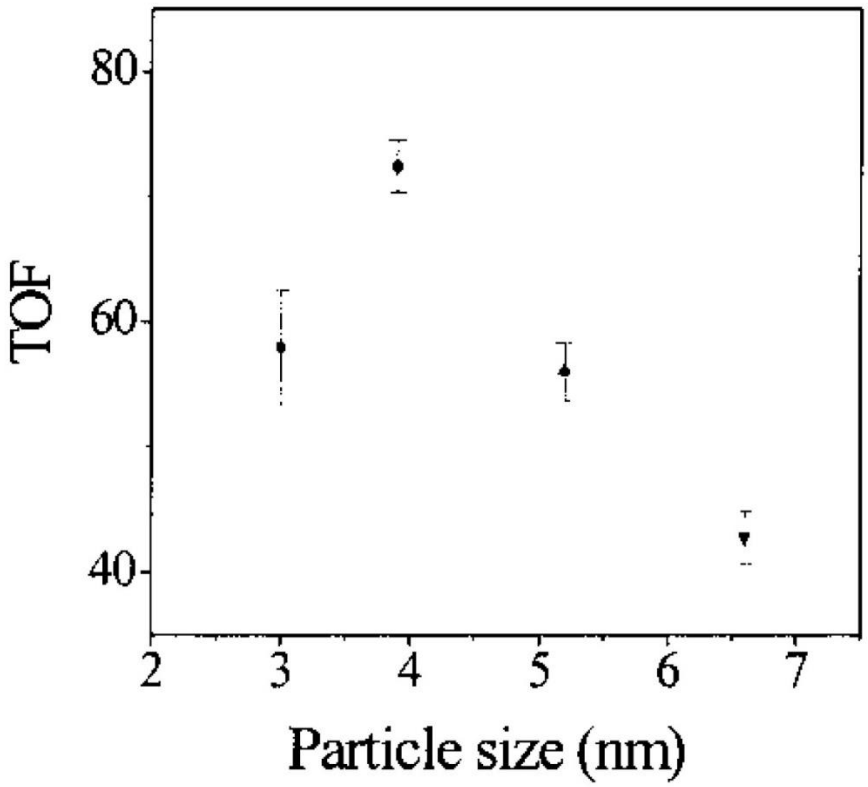

Figure 1.4.2. Turnover frequency (TOF) as a function of particle size for Pd catalysts supported on SiO_2 in the Suzuki coupling reaction. The TOF is calculated on the basis of the total number of surface atoms. Reproduced with permission from American Chemical Society, Li et al., *Langmuir*, 2002, vol. 18, pg. 4921-4925 [159]

This suggests that the reaction does not take place on all the surface atoms, otherwise there would be no difference in activity. The Suzuki reaction is suggested to be "structure-sensitive"; the active sites thought to be the low coordination number atoms situated at the vertex and edges of the nanoparticles and that their number increases as the particles get smaller. However, if the particle gets too small the strength of adsorption of some intermediates increases to the point of blocking the active sites, thus reducing the activity [159]. Similar behaviour was observed in the Heck reaction; according to a study performed by Le Bars et al. the active sites are low coordinated atoms. However, in the hydrogenation of allyl alcohol an interesting behaviour is observed; there is a particle size effect but not just because of changes in geometric configuration, but also due to a variation in electronic properties [160]. In this study Pd nanoparticles encapsulated in a dendrimer showed a monotonous decrease of the TOF as the particle size got smaller, if the TOF (mol H_2 consumed/ mol active sites*h) is calculated taking into consideration either surface or defect atoms as active sites.

However, if the TOF is calculated as a function of the number of face atoms for nanoparticles smaller than 1.5 nm the plot of TOF vs particle size presents a slope different than 0. The authors attribute this effect to a change in the electronic properties when the particle size reduces from 1.5 to 1.3 nm. In particular they define two "zones": when the particles are smaller than 1.5 nm the effects are predominantly electronic, while for bigger nanoparticles the effects are due to geometry [161]. For 1-hexyne hydrogenation however, the relationship between size and activity is negatively correlated, i.e. activity decreases as the particle size increases. In particular, a study from Semagina et al, showed that 11 nm is a critical particle size, above which the activity increases by an order of magnitude relative to Pd black (large Pd particulate of Pd metal) activity.

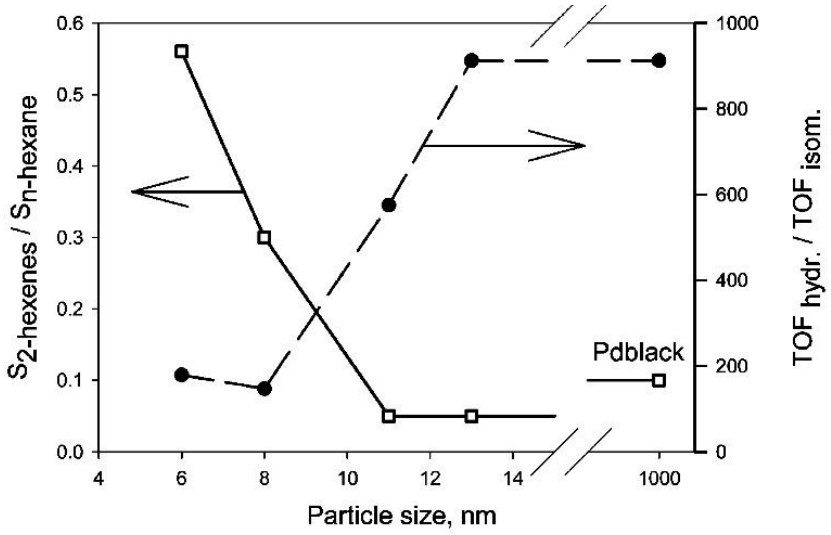

Figure 1.4.3. $S_{2\text{-hexenes}}/S_{n\text{-hexane}}$ ($S_{2\text{-hexenes}}$ = selectivity towards 2-hexenes; $S_{n\text{-hexane}}$ = selectivity towards n-hexane) at 25% conversion and a ratio of initial TOFs of a 1-hexyne hydrogenation to 2-hexenes formation (isomerization) vs Pd particle size. Reproduced with permission from American Chemical Society, Semagina et al, *Journal of Physical Chemistry C*, 2007, vol. 111, pg. 13933-13937 [72]

However, the selectivity towards the two by-products of the reaction (2-hexenes and n-hexane) varies only if the particle size gets smaller, with the unsaturated by-product increasing as the particle gets smaller as shown in figure 1.4.3 [72]. These results are explained by the need of 1-hexyne for a large ensemble of Pd atoms in order to adsorb and react. This could be explained by low coordinated atoms being responsible for isomerization, thus increasing the 2-hexene concentration. A different approach from Ruta et al [162] suggests the reason for a Pd particle size effect lies in the presence of

carbonaceous deposits on the nanoparticles. In their work they prepared highly monodisperse Pd nanoparticles (Pd nanoparticles size distribution < 20 %) with three different particle sizes (8, 11, 13 nm) on supported carbon nanofibers, and tested them for acetylene hydrogenation. It was shown that the 11 nm NPs represent somehow a critical diameter, above which the specific activity of the nanoparticles are not size-dependent. Interestingly, the sample possessing 8 nm sized particles shows a lower TOF than the 11 nm, an effect which cannot be explained by simply an electronic effect, since Pd particles > 5 nm exhibit bulk metallic (electronic) properties [38]. The difference might lie in the formation of Pd-C_x surface phases, a structure sensitive reaction, thus modifying the Pd surface [163]. On smaller particles C/Pd ratio is higher, leading to a smaller available Pd surface for reaction, thus reducing the TOF.

Regarding the ability of Pd to adsorb hydrogen this capability appears to be dependent on the particle size as well. A study from Tew et al showed that the formation of hydride is strongly particle size dependent, large particles form a higher amount of hydride, due to the existence of more interstitial spaces, whereas smaller particles offer a higher amount of surface adsorbed hydrogen.[164] Another study from Sachs et al shows that particle size presents a role in the behaviour towards the solubility of H_2 in the α-phase of PdH. The nanoparticles studied, in the range 2-5 nm, present a higher solubility compared to the bulk phase, up to 10-fold, as well a narrower miscibility gap. Interestingly a slope in the plateau region of the concentration-pressure plot for the two-phase system, albeit small, can be found, differently from bulk Pd which present a flat plateau. The reason for this plateau is not related to a particle size effect (the samples present negligible difference in the slope) but it is connected to the two-phase system phase transition [165]. The presence of the slope is also confirmed by Nutzenadel [166], however in their work they show that the plateau is particle size dependent, decreasing as the particle size gets smaller. The authors explain this effect as caused by the lattice relaxation close to the surface.

1.5 Hydrogenation of 1,3-Butadiene

1.5.1 Hydrogenation of 1,3-butadiene over gold catalysts

Light alkanes produced by catalytic cracking of petroleum contain significant amounts of dienes and alkynes. Typically, the ethylene cuts contain 0.5 to 3 % of acetylene and the propene cuts 2 to 8 % of propyne and propadiene [167]. For further polymerisation processing, however, the level of impurity in alkadienes or alkynes must be as low as 10 ppm [87], [167]. The production of high-purity butene streams for polymerization or copolymerization processes requires the hydrogenation of the butadiene impurities contained in butene cuts. The hydrogenation of 1,3-butadiene can lead to different products: partial hydrogenation yields of butene, while total hydrogenation leads to butane. As the target product is the alkene, the catalyst must not hydrogenate any of the butene molecules and reduce the di-olefin to butene rather than butane. Moreover the selective hydrogenation of 1,3-butadiene (C_4H_6) produces three isomers of butene (C_4H_8); 1-butene, cis-2-butene and trans-2-butene. The control over the selectivity of this catalytic reaction is then an important aspect regarding the preparation of the appropriate catalyst. The active components of the catalysts are usually noble metals, such as palladium, gold and platinum. The butadiene hydrogenation reaction mechanism is shown in the figure 1.5.1.

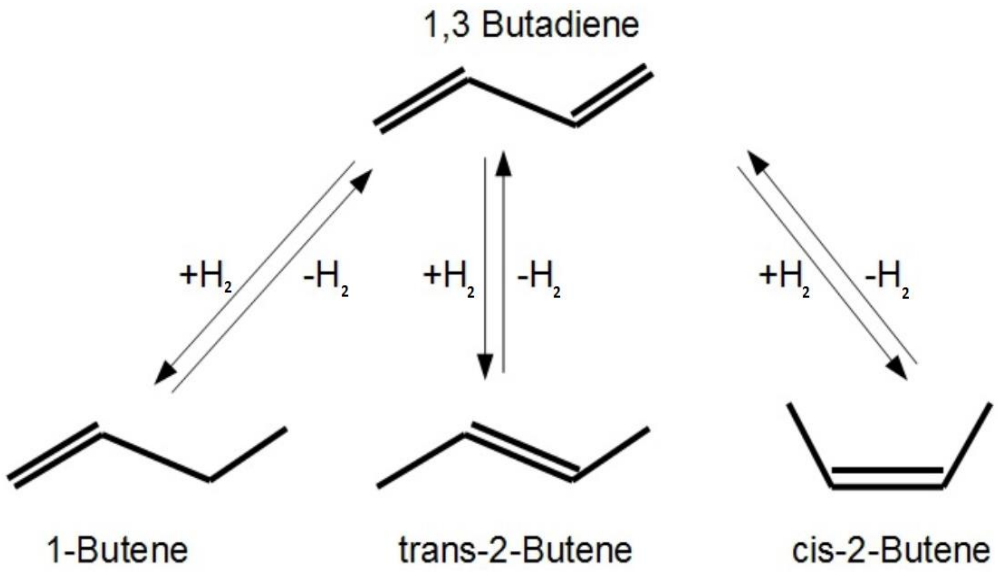

Figure 1.5.1 Reaction process for the hydrogenation of 1,3-butadiene leading to three possible (ideal) alkene products.

Palladium (supported) catalysts are so far regarded as the only commercially available catalyst to selectively hydrogenate alkadienes or alkynes in an excess of alkenes. However oligomers form during hydrogenation which increases the number of regeneration cycles for the catalyst and shortens its life time, due to long term catalyst poisoning [167]. Also, due to the high reactivity of palladium, at high conversion, alkenes start to be (over)hydrogenated, leading to decreasing selectivity in palladium catalysts [168].

Studies performed over supported gold catalysts showed that it was highly selective for hydrogenation of dienes or alkynes at low conversion, even though it was not as active as palladium. Bond and Wells reported that gold supported on γ-Al_2O_3 and boehmite (hydrated alumina) (AlO(OH)) was able to selectively hydrogenate, at 130 and 260 °C, 1,3-butadiene into butenes without butane formation[87], [167]. This lead to the idea of using supported gold catalysts in order to reduce or remove totally the amount of butane which the palladium usually forms. Gold nanoparticles also show high selectivity for a C_4 cut (1-3% presence of alkadienes), as proved by Hugon et al. They studied the reaction of hydrogenation of butadiene in the presence of an excess of propene and confirmed the high selectivity of gold even in the presence of a large amount of alkenes (1:100 ratio between 1,3-butadiene and propene) [167]. They proposed the high selectivity could be attributed to the stronger interaction between 1,3-butadiene and gold compared to propene-gold interaction. Moreover, opposite to palladium there is no competition between the hydrogenation of 1,3-butadiene and alkene hydrogenation (butenes and propene). Over gold catalysts, these two hydrogenation reactions operate over two different temperature ranges ($T < 433$ K 1,3-butadiene hydrogenation; $T > 433$ K propene hydrogenation), making the gold nanoparticles good catalysts for selective removal of butadiene [87]. Okumura et al studied the effect of particle size and support on Au nanoparticles prepared through different approaches [51]. The Au loadings of these catalyst were around 1 wt. % with different particle size and diameters. They made a comparison according to the turn over frequencies (TOF), based on the number of gold atoms exposed at the surfaces, of the catalyst with different preparation method [51]. Apart from the catalyst prepared via impregnation, the TOF were similar over the different catalysts, while the reaction rate increase with the decrease in the diameter of Au particles. Here it was proposed that H_2 is activated at the exposed surface of the Au particles; the total amount of the exposed surface area of Au particles was monotonically increased with a decrease of

the size of Au particle although the number low coordinated atoms (corners and edges) of Au particles increase with a decrease in size. Similar results were obtained with Au nanoparticles on different supports, although this showed minimal variation in the TOF across the three different support types (Al_2O_3, SiO_2 and TiO_2) studied. They concluded that for the 1,3-butadiene hydrogenation there is no structural effect in terms of particle size or support [51]. However, in a review by Nikolaev et al., a comparison of various types of hydrogenation reaction, acrolein, crotonaldehyde, acetylene and 1,3-butadiene was made and they observed that for most of these reactions, up to 3 nm, the activity would increase as the particle size decreased [109]. However, if the nanoparticle size decreases further, the activity starts to drop. Decreasing the size of gold nanoclusters from 10 to 3 nm lead to an increase in the number of sites and therefore activity. A problem which may arise when comparing catalysts with a large difference in particle size (e.g. 2 versus 20 nm) is the presence of a possible volcano plot in an activity/particle size correlation. The two systems, albeit being drastically different in term of properties, could show similar TOFs, as illustrated in figure 1.5.2, thus biasing the interpretation of the particle size dependency for the reaction [109].

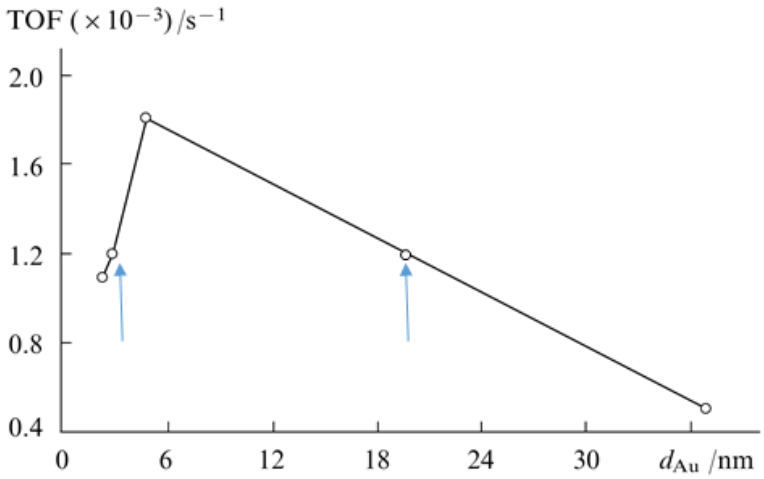

Figure 1.5.2. Turnover frequency of immobilized gold particles in hydrogenation of buta-1,3-diene at 423 K vs. Au particle size. Adapted with permission from Turpion, Nikolaev et al., *Russ. Chem. Rev.*, 2009, vol 78, pg 231-247 [109].

Further analysis from Yang et al found out that adsorption of cis-1,3-butadiene at the low-coordination sites of the edges or corners of gold nanoparticles is much more

favoured than for trans-1,3-butadiene, which is caused by the stronger orbital interactions between cis-1,3-butadiene and the low-coordination gold atoms. The adsorption of the cis isomer on gold nanoparticles is thus thermodynamically favoured. Transition state calculations indicate that the trans-to-cis transformation of butadiene is also kinetically facile. Therefore, gold catalysts exhibit a unique preference toward cis-2-butene as compared to the trans-2-butene, and the ratio of cis/trans isomers over gold nanoparticles is found to be highly size-dependent [169].

1.5.2 Hydrogenation of 1,3-butadiene over palladium catalysts

As aforementioned, Pd catalysts are the only commercially available system which allows the selective hydrogenation of 1,3-butadiene. While this is nowadays the standard process, it is limited by the tendency of Pd to hydrogenate the desired olefins and to isomerize those containing more than 3 carbon atoms[124]. However, a lot of debate has arisen regarding the effect of Pd particle size on the reaction. For Pd, a decrease in particle size apparently leads to a decrease in activity. For example, Tardy et al. showed a particle size dependence for the 1,3-butadiene hydrogenation; while particles with a diameter larger than 2.8 nm behave like bulk Pd, below this value a size-effect is observed, especially when the particle size is between 2.8 and 1.4 nm. This behaviour can be explained by deactivation due to strong butadiene adsorption; in addition some change may occur due to a geometric effect, and structural properties which can be induced by an epitaxial relation between the support and the metal [170]. However, this explanation cannot be extrapolated to particle sizes greater than 2.8 nm. Pd has shown structure sensitivity, with Pd(110) faces 5-fold more active than Pd(111) for single crystal catalysts. Pd nanoparticles usually exhibit facets of different crystallographic orientations. Variation in the relative abundance of the different facets with particle size will also affect the catalytic activity [171]. In a recent study from Silvestre-Albero et al, Pd nanoparticles are analysed with STM and reveal the Pd particles to be not always perfect cuboctahedra, presenting incomplete (111) and (100) terraces. The small (smaller than 3.5 nm) metal clusters were highly defective, and a slight increase in particle size led to an increase in the proportion of defects at the boundary of the incomplete facets. In contrast, particles > 3.5 nm started to develop large and well defined (111) and (100) facets [172], [173]. If the number of Pd atoms in incomplete (111) terraces is used for the rate normalisation, a plot of activity vs particle size

yields a constant TOF for particles larger than 4 nm. The authors therefore conclude that the selective hydrogenation of 1,3-butadiene was particle size independent for Pd particles ≥ 4 nm. For Pd particles < 4 nm, the normalisation was not straightforward due the highly defective nature of the small nanoparticles, which did not allow clear analysis. However, TOF values approached those of the Pd(110) single crystal when it was calculated considering the cuboctahedra model. Therefore the relative greater abundance of surface defects may allow for an enhanced hydrogen penetration, giving rise to greater-than-expected activity [172], [173]. This is further confirmed in a review Nikolaev et al concerning the hydrogenation reaction on different systems. The authors discerned that an increase in particle size from 1 to 5 nm results in a 25-fold increase in the catalyst activity for 3,7-dimethylocta-2,6-dienal hydrogenation, while a 5 to 30 nm increase barely affected the activity [109]. A recent study from Dal Santo et al [174] show that a combination of both particle size and morphology of PdNPs (the exposed plane) affect the catalytic behaviour for 1,3-butadiene hydrogenation. In the study they prepared two sets of supported nanoparticles on different oxides (TiO_2, CeO_2, ZnO) through chemical vapour deposition, with different pre-treatment of the support (namely calcination at 300 °C in air for one set and no pre-treatment for the other). The pre-treated supports give rise to highly dispersed nanoparticles (1.2 nm for TiO_2, 0.8 for ZnO) compared to the non-treated sample. The highly dispersed samples showed an overall higher selectivity to butenes compared to the non-treated larger particles. According to Lee et al. [175], a way to control Pd nanoparticles selectivity would be through a modification of the surface properties of Pd, such as decoration with TiO_x species formed by the addition of TiO_2 to SiO_2 supported Pd nanoparticle. Partially reduced TiO_x species migrates onto and decorates the Pd surface, significantly suppressing H_2 uptake; this lead to a lower hydrogenation rate for the butene species indicating that the amount of H_2 species on Pd nanoparticles affects the activity. Furthermore, the selectivity is affected by the suppression of π-allylic species, formed preferentially on a large ensemble surface of Pd. This has been shown by Goetz et al. [176], analysing Pd nanoparticles supported on Al_2O_3. Two type of nanoparticles structures are formed depending on the Pd concentration on the support; i.e. flat (111) surfaces (Pd = 0.1%) and particles with less interaction with the support (10) (Pd = 0.3%). Two reaction mechanisms for isomerization of 1-butene to 2-butenes species, and vice versa, are identified: a Horiuti-Polanyi

mechanism involving the addition of hydrogen atoms to form a half-hydrogenated radical and an intramolecular hydrogen shift mechanism which occurs without addition of hydrogen; the Horiuti-Polanyi occuring on corner and edge atoms, with the hydrogen shift thought to occur on face atoms. Therefore, decorating the Pd nanoparticles with TiO_x species reduces the Pd ensemble surfaces, thus reducing the rate of isomerization of 1-butene and facilitating its desorption [175].

1.6 Characterization of nanoparticles

Obtaining information regarding the properties of the nanoparticles has always been an important objective in order to understand structure activity relationships in heterogeneous catalysis. Whereas various techniques allows the determination of some of these properties, either through straight correlation between the physical interaction of the method and the nanoparticles, such as the use ultraviolet-visible spectroscopy in the qualitative determination of Au nanoparticles size through plasmon resonance [177], or through derivation from a different type of interaction, as in the case H_2 chemisorption for estimation of particles size of various metal element nanoparticles, Pd, Co, Pt [178]–[180], where the amount of H_2 chemisorbed can be directly linked to the nanoparticle size, as well as IR spectra of CO adsorbed on the nanoparticles to define the facets [52], [181] as depending on the facets of the nanoparticle different mode of adsorption are present. The development of techniques that allow for the visualization of the nanoparticles, such as transmission electron microscopy (TEM) [182], [183] and scanning tunnel microscopy (STM) [184], enables a particularly detailed interpretation of nanoparticle properties' in correlation with their function. Information regarding their electronic and structural properties can be obtained through the use of X-ray based techniques such as X-ray absorption fine spectroscopy (XAFS) or X-ray diffraction (XRD) [185].

The major difference between microscopy techniques and X-ray based techniques lies in their local versus averaging techniques. In particular, in the case of microscopy, the user is only able to observe a small fraction of the system, varying from few nanometres up to hundreds of nanometres, depending on the required resolution. This

severely limits the ability to observe changes to the nature of the catalysts, also introducing bias in the selection of the observable area. X-ray based techniques instead, thanks to their more averaging nature, are able to observe the catalyst as a whole, rather than a small part, and help to have a better understanding of the catalyst behaviour under reaction conditions.

However, one of the challenges with nanoparticle-catalysed reactions concerns knowledge of their behaviour under reaction conditions. Most of the studies regarding the structure of catalysts are performed ex situ or "post mortem" [1], thus it is not possible to exclude a structural plasticity and the ability or even a requirement to respond to the reactant 'environment' in a reversible way. Structural changes during CO oxidation of Au nanoparticles at room temperature have been observed through aberration-corrected environmental TEM by Yoshida et al [186] where [100] facet restructure itself in a Au[100]-hex configuration, shown in figure 1.6.1, where the atoms at the topmost layer have an unusual bonding configuration with the Au atoms of the second surface layer, which allows the adsorption of CO molecules in high density. This lead to the idea of nanoparticles being not inert during catalytic reaction but as dynamic, able to change and reshape according to their reaction environment. Under catalytic reaction conditions, active centres are created, produce products and then disappear [1]. The assumption that the catalysts do not change under reaction conditions is only acceptable for limiting case, with small conversions and simple reactions which lead to thermodynamically stable products [187]. However, if the local chemical potential at the active site is increased it could lead to a change in the surface of the catalyst under reaction condition, which may cause the formation of new active phases. The new phases might only be stable under given chemical potential of the reaction, and could be metastable or turn back to the original phase once the potential is changed [187].

Unfortunately, electron microscopy techniques cannot always be applied when the catalyst is under "operando" reaction conditions due technical limitations, such as the attenuation of electron beam due the presence of reactant molecules affecting image quality and resolution.

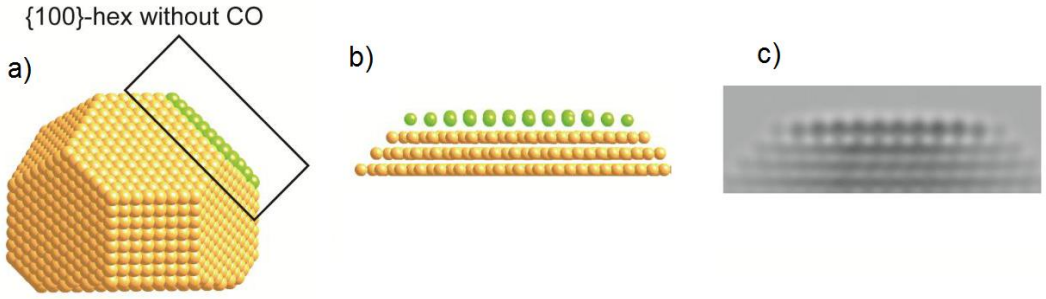

Figure 1.6.1. a) Au nanoparticles with a Au{100}-hex reconstructed without CO adsorption; b) enlargement of the selected rectangular area; c) simulated TEM image of Au{100}-hex. Reproduced with permission from American association for the advancement of science, Yoshida et al, *Science*, 2012, vol 335, pg 317-319 [186]

1.6.1 In situ techniques

The necessity to identify the physico-chemical characteristics of catalysts under reaction conditions has become paramount in industry in order to optimize the process of building a better catalyst [14]. In order to obtain information regarding the nature of the active sites a wide variety of analytical techniques have been applied. Whereas most of these techniques can be applied both ex situ, where the sample is kept in atmospheric conditions with no external interaction, be it gases, electricity, temperature, as well as in situ, where the sample is subject to reaction condition or conditions relevant to the reaction [188], only few of these can be used in operando condition, which, as defined by Schögl, involves identify the geometric or electronic structure of a catalysts under simultaneous documented production of the desired products. Whereas XRD is an example of a commonly used technique for in situ characterization, it presents a serious limitation in sensitivity on highly dispersed nanostructures, where the common size of the nanocrystal is less than 2 nm [189]. On the other hand X-ray absorption spectroscopy (XAS) does not have any lower limitation in the regards of crystallite size (although providing less and less information as the number of surface atoms becomes smaller [190]) and can be used even on sub nanometre species, such as in the case of the atomically dispersed Pd on γ-Al_2O_3 in the study from Peterson et al [191]. In this study the Pd was deposited on both pure γ-Al_2O_3 and a La_2O_3 doped γ-Al_2O_3 (La-Al_2O_3) and tested for CO oxidation using XAS to investigate the behaviour under reaction conditions. In both cases (pure and doped γ-Al_2O_3) the extended X-ray absorption fine structure spectroscopy (EXAFS) data showed the presence of oxidised Pd, under reaction conditions the Pd

state changes. The reaction examined was the oxidation of CO, with data taken over a range of temperature, from 60 to 125 °C and using a mixture of O_2/CO in a ratio 53.3/46.6 diluted in He. Whereas in both cases there is a decrease in the intensity of the Pd-O first shell, in the case of pure γ-Al_2O_3 there is the appearance and then a gradual increase of the Pd-metal first-shell peak height, implying the growth of Pd-metal at the expense of Pd-oxide. On the other hand, for the Pd/La-Al_2O_3 there is no appearance of Pd-metal first shell peak up to 363 K. This could be explained by the formation of a chemical state for Pd with an average Pd-O coordination << 4, which could be attributed to a Pd^+ species. This is further proved by the X-ray absorption near edge structure spectroscopy (XANES) where the edge energy observed for this state (24,3516 ± 0.3 eV) falls between that for Pd metal and PdO (24.350 and 24.353 keV respectively).

Since the development of QEXAFS (Quick-scanning EXAFS) by Frahm and the first experiment in 1987 [192] the time required for a scanning EXAFS experiment has being brought down dramatically, from ~ 15 min. to a few milliseconds [193]. This allows for the clarification of some processes where the higher length of time required for normal EXAFS would not allow for the details requires, such as in the formation of Cu nanoparticles due to the reduction of CuO on Cu/ZnO/Al_2O_3 methanol synthesis catalysts [194]. Copper reduction from CuO takes place within an extremely narrow temperature range and QEXAFS performed during the heating process hint to the formation of small cluster which then grow into nanoparticles. Moreover the smooth changes in the intensity of the QEXAFS curves indicated the lack of formation of other intermediate species, such as Cu_2O. The application of QEXAFS has then allowed time-resolved in situ measurement to be available such as in the case of the study performed by Paredis et al. [195] where it has been found that Pd nanoparticles supported on ZrO_2 undergo to drastic structural and chemical change under NO reduction with H_2. In particular the presence of the cationic Pd species are observed upon the introduction of the reactants and a redispersion of the Pd nanoparticles on the ZrO_2 surface, with the formation of small Pd clusters. These phenomena appear to stop when the temperature necessary for the onset for NO reduction is reached (393 K). This could be explained by the interaction with NO with surface atoms in the metallic Pd cluster; $Pd^{\delta+}$ species appear at the expense of Pd^0 from room temperature to 393 K which are thought to be stabilized by the OH defect on the ZrO_2 surface thus not

forming PdO_x species. Interestingly the selectivity depends on this redispersion since high selectivity toward N_2O is detected at the onset of the reaction ($T \geq 393$) but shifts towards N_2 as the temperature increases ($T > 423$ K) as the $Pd^{\delta+}$ species disappear to form larger metallic aggregates. Another example is a study from Föttinger et al. on Pd/ZnO where the formation of a PdZn alloy on the surface of the Pd nanoparticles is observed when the catalyst undergoes methanol steam reforming (MSR). This behaviour appears to be due to hydrogen spillover and reduction of ZnO as it is present as the catalyst undergoes a prolonged reduction under H_2 at 623 K as well as in the presence of methanol/water through the hydrogen formed during the reaction. As the time on stream increases the degree of alloying goes from 10 % after 1 h of reaction in methanol/H_2O atmosphere up to 20 – 25 %. This allowed the identification of the active phase for the MSR, PdZn, thanks to a change in selectivity from methanol decomposition (CO/H_2) to MSR (CO_2/H_2) as the amount of PdZn increased.

In situ techniques can be applied not only to observe the behaviour of nanoparticles under catalytic conditions but also to rationalize the formation of metal nanoparticles. A good example of this can be seen in the work of Polte et al. [196] where time-resolved small-angle X-ray scattering (SAXS) in combination with XANES has been used in order to identify the steps involved in the process of gold nanoparticle formation. In this study the XANES were used to investigate the degree of reduction of Au^{3+} (in the form of $[AuCl_4]^-$) to metallic Au^0. SAXS on the other hand allowed for observing the formation of the nanoparticles size and the degree of polydispersion. The authors were then able to deduce a mechanism for the formation of Au NP, following 4 distinct phases: nucleation, growth by aggregation, slow further growth and a fast, final growth step. The information obtained could then increase the degree of control on the nanoparticle synthesis toward nanoparticles tailored for the required catalytic system.

1.7 Synthesis of nanoparticles

To produce nanoparticles and nanostructures many methods are available. The methods could be classified depending on either the resulting structure, technique used or type of material processed. One of the most employed classifications in the synthesis of nanoparticles is the distinction between top-down and bottom-up methods [197] In top-down methods a macroscopic structure is subdivided until the desired

nanostructure is obtained. In a bottom-up approach, building blocks (atoms, molecules) are built up using chemical reactions or self-assembly processes.

1.7.1 Solid-phase synthesis

Top-down methods involve the breakdown of larger material until the required size is reached. Methods such as ball milling are commonly employed for the synthesis of catalysts [198]–[200], and sometimes in the synthesis of nanoparticulate catalysts [86],[87], the broad size produced by the catalysts makes it not ideal in particle selected reaction [203]. However, methods to produce top-down size selected nanoparticles are possible, using lithographic techniques. Lithography involves the interaction between a radiation and a resist material [204]. The radiation could come from electrons, ions or X-ray, with the first two radiation involving serial writing of a pattern with a small focused probe, whereas for X-ray a radiation resistant mask is used to produce a defined patted [204]. Whereas these methods are able to produce nanoparticles with regular physical attributes (e.g. size, shape, pattern) they are generally not viable on an industrial scale. It has been used however to produce model catalysts, such as in the case of the preparation of Pt nanoparticles array for ethylene hydrogenation through electron beam lithography [205] or formation of Au nanoparticles through chemical electron beam lithography [206] .

1.7.2 Gas-phase synthesis

Preparation through vapour phase is one of the old method to produce nanoparticles. Champion defines gas phase synthesis as divided in three stages [22]:

- Introduction of the compound in vapour form
- Condensation of the vapour in form of nanoparticles, with a chemical reaction in some cases.
- Control and preservation of the dispersed nanocrystalline state.

Depending on the process it can be either called physical vapour deposition (PVD) or chemical vapour deposition (CVD). In PVD the target material is vaporised using heat or an electron beam. The evaporated atoms are the deposited on the surface of the substrate with no chemical reaction involved [207]. In CVD the reactant species are introduced in the reaction chamber, where they react with each other and deposit one layer of product material. CVD offers a uniform, robust method of deposition of materials and can be used to deposit nanoparticle on a wide variety of materials,

including SiO_2, Al, W [207]. A subclass of chemical vapour deposition is called atomic layer deposition (ALD), where the precursor species are not introduced in the chamber simultaneously but in series of sequential, non-overlapping pulses. In this manner the reactant are kept separate and react on the surface in a self-limiting process, without the presence of a gas phase reaction step [208].

Whereas these methods have been applied successfully to produce well defined nanoparticles, the high length of time required and the small quantity of material produced, paired with the high cost of equipment, makes these methods only useful to produce model catalysts [209]–[211].

1.7.3 Liquid-phase synthesis

Liquid synthesis provides a versatile, low-cost method to produce nanoparticles, as it does not require the use of a complex mechanical system and can be performed in any laboratory. Moreover, the homogeneous nature of the starting block (dissolved metal ions) helps in the formation of homogeneous products. As such they are by far and away the most common methods used to prepare nanoparticles for use in heterogeneous catalytic reactions.

1.7.3.1 Impregnation method

Impregnation denotes a procedure whereby a certain volume of the solution containing the precursor of the desired element is contacted with a solid support. After a certain time, the sludge is separated from the solution and the excess solvent is dried. The amount of the active precursor mounted onto the support, its concentration profile and the chemical environment of the catalyst on the support surface depend on the condition during the mixing and the drying process steps. A post treatment in order to reduce the precursor (a positive charged metal ion) to a nanoparticle is then required. The reduction process could be chemical (e.g. reduction under H_2 atmosphere) paired with a thermal treatment. Depending on the volume of precursor solution used, the technique can be called wet-impregnation or incipient wetness impregnation. In wet impregnation the solution is in large excess compared to the support and the quantity deposited depends on the solid/liquid ratio [212]. In the incipient wetness impregnation the volume of solution is empirically determined to correspond to that beyond which the catalyst begins to look wet and is used for the deposition of species with very weak interaction with the support surface or for the deposition of quantities

which exceed the number of adsorption sites on the surface [212]. However, this synthesis method does not prevent the agglomeration of the nanoparticle thus causing a wide particle size distribution and inhomogeneous particle to be formed [213].

1.7.3.2 Deposition-Precipitation/Co-precipitation

Marcilly, in 1984, introduced a method of catalyst production through precipitation, which has become commonly used to produce supported metal nanoparticles [214]–[216]. The chemical process involves a reactant (commonly a reducing agent) which transforms the metal precursor into a solid phase and allows for its deposition onto a support which has been previously added to the solution. In co-precipitation both the catalyst and the support are produced at the same time, such as in the synthesis of Au/Fe_2O_3 [217] and Pd/Al_2O_3 [218], being able to produce relatively well dispersed nanoparticles. However a drawback which has to be taken in account, due the interference which the metallic precursor may cause with the polymerization chemistry of the material, often resulting in sample with undesired properties [213].

In the deposition precipitation, the metallic precursor instead precipitate to the metal hydroxide first (e.g. $Au(OH)_3$) and then are deposited on the support. A further calcination is required in order to produce the metal nanoparticles [213]. Deposition precipitation has shown better results in the synthesis of smaller nanoparticles, such as in the case of Au and Pt supported on TiO_2 [219], [220], however particle agglomeration is quite common [213].

Whereas impregnation, deposition-precipitation, co-precipitation methods present some advantages (ease of production and scale up, low cost) the lack of control in the nanoparticles properties, paired with the tendency of nanoparticles to agglomerate, does not allow in-depth studies on the correlation between catalytic activity and nanoparticles properties.

1.7.3.3 Colloidal methods

One of the problems that arise during the synthesis of metal nanoparticle is the agglomeration of the particles due to a combination of attractive Van der Waals forces and the tendency of the nanoparticles to minimize their surface energy. In order to prevent this, repulsive interparticle forces are required [221]. One way to produce these forces would be the dispersion by electrostatic repulsion using electric double layers surrounding the particles the repulsion force is produced [221]. This

stabilization method is mostly effective in dilute systems of aqueous or polar organic solvents. The method itself is very sensitive and a change in concentration of the electrolyte might cause sudden agglomeration due destruction of the electric double layer [222].

Another way would be to use steric forces to prevent agglomeration via a steric interaction [221]. This is obtained by the coordination of bulky organic molecules that act as protective shields on the metallic surface. Nanoparticles are thus separated and agglomeration is prevented. There are many protective group in the literature: polymers and block copolymers; phospane, amine, thioethers; solvents such as THF, THF/MeOH, surfactants (e.g. long-chain alcohol)[223] .

One of the most well-known approaches that uses the colloidal method is the Turkevich method, which uses citrate both as reductant and as capping agent and is one of the most common and simple methods for the preparation of gold nanoparticles [224]–[235]. In the Turkevich method a solution of $HAuCl_4$ in water is brought to boil in a beaker. Subsequently a small amount of a solution containing sodium tris-citrate is added and after 15 min the solution is cooled down to room temperature [224].

1.7.4 Surfactant based synthesis

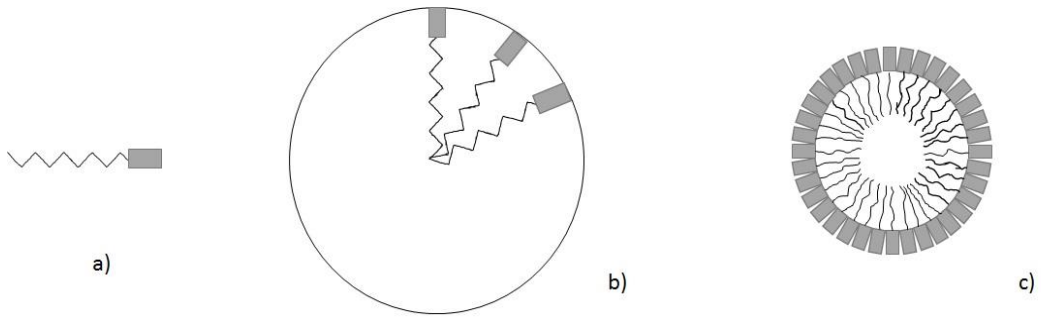

Figure 1.7.1. Formation of a micelle. (a) Surfactant with bulky polar head (grey block in the figure) and short non-polar chain (black in the figure). (b) Surfactants join together. (c) A micelle forms.

Surfactants (portmanteau; surface active agent) are molecules with a hydrophilic polar head and a hydrophobic hydrocarbon chain. These molecules usually position themselves at the interface between two phases, such as water and oil, lowering the surface tension [236]. If dissolved in water, above certain concentrations (termed the critical micelle concentration, CMC), the chains will associate together, as a result of

entropy/enthalpy balancing, to form aggregates called micelles (figure 1.7.1). While the micelles are usually spherical at low concentration of surfactant, they may change shape with increasing concentration, assuming cylindrical shapes or multi-layered spheres (with a hydrophilic core and hydrophilic shell, as in figure 1.7.2) [237]. The value of phase change concentration (from dispersed surfactant to micelles, to a more complex form) depends on the structure and the chain length of the hydrophobic group, the shape of the hydrophilic group and the presence of salts in the solution [238]–[240]. For example when the chain length of the polystyrene-b-poly(acrylic acid) changes from 170 units to 1400 the radius of the micelles changes from 23 to 90 nm [241], and a similar effect can be seen in the case of PS-P4VP, in a study from Förster, where the radius changes from 39.5 to 10.2 nm when the number of P4VP unit changes from 142 to 35 [242]. Moreover, it's also possible for the micelles to confine a second phase in their core, for example oil which has an affinity for the hydrophobic chain. This way an oil droplet can be dispersed in a water matrix, being stabilized by the surfactant.

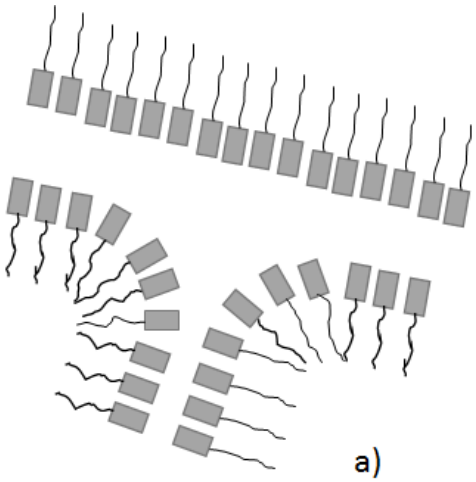

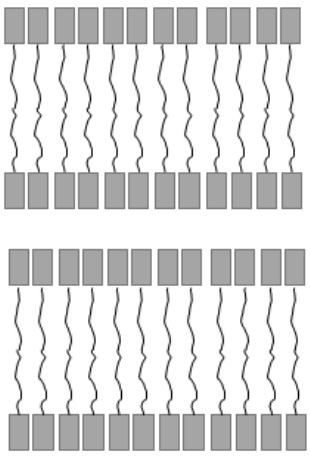

Figure 1.7.2. Different form that the micelles can assume at higher concentration level, a) interconnected cylinder; b) double layer. In gray the bulky polar hear, in black the non-polar chain.

Micellar systems are dynamic; each surfactant chain comprising the micelle can be easily replaced by free chains moving freely in the aqueous phase [243]. However, the shape of the micelle structure itself is always conserved. While the term “micelles” is commonly associated to a system where the surfactant, containing a polar head and the non-polar chains, is dispersed in water, micellar structures can be formed also in different solvents, including non-polar solvents. In this case the micelles are termed ”reverse micelles” possessing a hydrophobic head and a hydrophilic chain (figure 1.4.3-1). The reverse micelle can collapse and exchange their aqueous content, to form again two reverse micelles (figure 1.4.3-2) [237]. Moreover, another property of reverse micelles that is different from micelles: their size changes linearly with the amount of water added to the system, from 4 to 18 nm [238] . The water content of the system is defined as $w = [H_2O]/[SA]$, where [SA] is the surfactant concentration.

The concept of nanoparticle synthesis through the use of reverse micelles was proposed around 1988 by Petit et al. [229]. Since there is a size control on the reverse micelles and due to the capability of exchange their aqueous contents, the reverse micelles were thought to be a good variable-size nanoreactors [238]. Considering two reactants A and B, dissolved separately in two micelle solutions; upon mixing they would make contact through the exchange induced by Brownian motion, allowing them to react. This made it possible to fabricate many nanosized compounds [244]. Since the size of the reverse micelles is controlled by their water content, also the size of the resulting nanocrystal can be controlled. However, this method has some disadvantages. First of all, the more the reverse micelles become smaller (in order to synthesize smaller nanoparticles) the more unstable they become with the amount of metal salt added, limiting the yield of nanoparticles when compared to the amount of surfactant and solvents added [237]. Furthermore, many nanoparticles can be formed in a single reverse micelle, raising the polydispersity. To avoid this a stabilizing agent can be added, raising the total cost of the synthesis. Nevertheless, these problem can be circumvented by using polymer-based micelles [238].

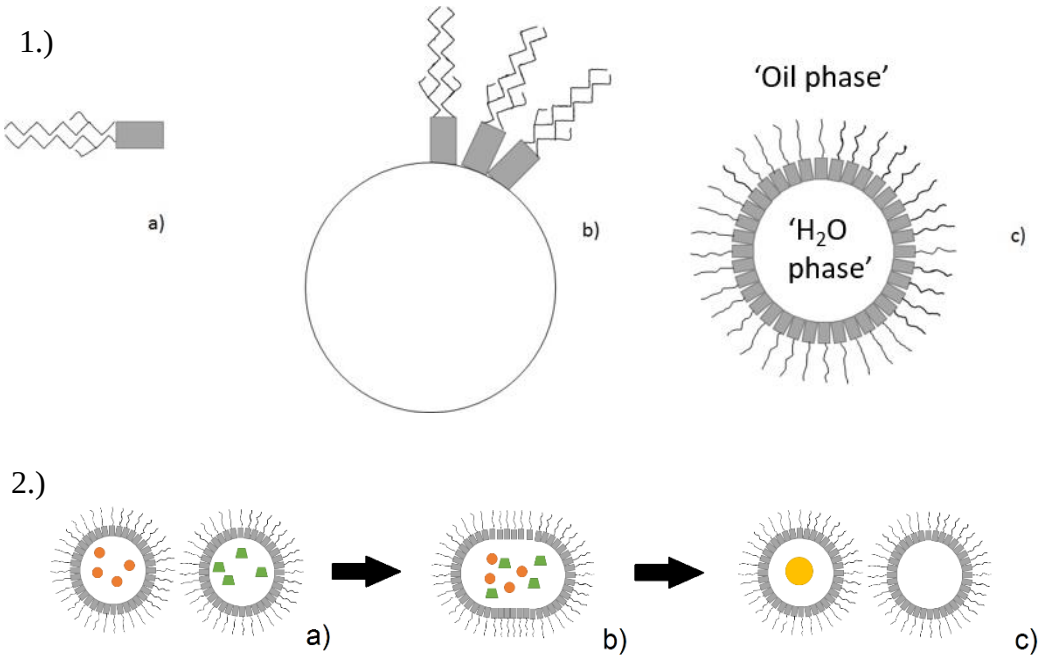

Figure 1.4.3. 1.) Formation of a reverse micelle. (a) Surfactant with small polar head (gray block in the image) and ramified chain (black line in the figure). (b) Surfactants join together. (c) A reverse micelle forms. 2.) Exchange of aqueous cores. (a) Reverse micelles subject to Brownian motion filled with two different compound (shown in orange and green). (b) Collapsed reverse micelles and mixing of aqueous contents. (c) Formation of two micelles, identical to the initial micelles with one containing the result of the mixing (in yellow in the figure). In gray the bulky polar , in black the non-polar chain.

1.7.4.1 Polymer-based reverse micelles encapsulation

In 1992 Saito et al. prepared silver colloids using poly-2-vinyl pyridine block of polystyrene-b-poly-2-vinyl pyridine (PS - P2VP) [245]. In the same year the synthesis of a narrowly distributed gold colloids was demonstrated using polystyrene-b-poly-4-vinyl pyridine (PS - P4VP) [246]. Spatz et al. [54] used the co-block polymer Polystyrene-b-Poly(2-vinyl) Pyridine in order to create reverse micelles in toluene, then used to produce nanoparticles as shown in figure 1.4.5.

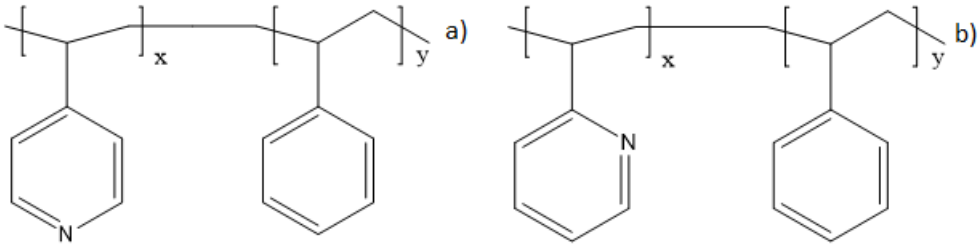

Figure 1.4.4. Structure of a) polystyrene-b-poly-2-vinyl pyridine; b) polystyrene-b-poly-4-vinyl pyridine

The presence of nitrogen in the structure of the pyridine decreases its affinity for the organic solvent compared to the polystyrene part. This led to the formation of micelles with a CMC between 0.01 and 0.1 mg/mL [247], consisting of P2VP cores and PS tails, estimated to consist of approximately 50 polymer strands. Moreover, Spatz discovered that the nitrogen atom can be protonated or form a complex with metal salts. Depending on the salt the pyridine group is either protonated to a pyridium ion, with the metal salt acting as counter ion, or using the free electron pair of the nitrogen the metal salt, can form a complex with the pyridine [54], [248]. Furthermore, the metal salts act as a stabilizer for the micelles when occluded into the core [238]. Comparing the polymer-based micelles with the normal surfactant micelles numerous advantages can be seen. The lower CMC (for comparison 0.1 mg/mL of PS-P2VP versus 7 mg/ml of AOT (sodium bis[2-ethylhexyl] sulfosuccinate) [249], a commonly used surfactant in reverse micelle encapsulation [243], [250]) means that less polymer is needed in order to form a stable structure. The structure is more kinetically stable compared to surfactant-based micelles, with less agglomeration and less spontaneous breakup; therefore no additional stabilizer is needed [238]. Due to this stability, polymer-based micelles can be adapted to many different substrates and many different metals [251]. In this particular system the interparticle distance is given by the length of the polystyrene chain while the nanoparticles size can be controlled by the P2VP core and the amount of salt added [54]. Moreover the results obtained by this method in term of particle size distribution, often with a standard deviation << 1 nm [55], [252]–[259], compared to other commonly used method such as [51], [220], [260], [261] makes it an ideal approach for studying effect of nanoparticles properties such as particle size. Moreover, the reproducibility and the wide applicability of this method allows the study of other properties, such as support effect, being able to exclude other effect related to intrinsic nanoparticles properties such as shape and size.

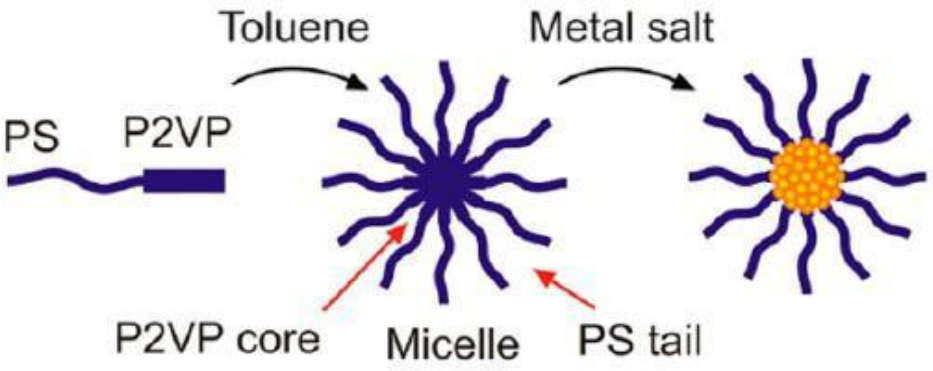

Figure 1.4.4. Formation of the micelle and loading of the metal salt inside the core. Reproduced with permission from ACS Publications, Cuenya et al., *Accounts of Chemical Research*, 2013, vol 46, pg 1682-1691 [262]

1.8 Aim of this thesis

The focus of this work is to prepare, characterise and test, Au and Pd nanoparticles, presenting an highly homogenous particle size ($\sigma << 1$ nm), over a range of non-reducible supports, Al_2O_3, SiO_2 and Si_3N_4. The nanoparticles will be prepared using a slightly modified reverse micelle method, firstly developed by Spatz et al. [54]. The modification lies in the use of p-toluene sulfonyl hydrazide instead of the commonly used hydrazine (N_2H_4), in order to avoid the use of toxic and explosive reagent as well as reduce the rate of reduction. In order to understand the mechanism of formation of the Au nanoparticles during the synthesis procedure, XAFS/SAXS measurement were performed, paired with *ex-situ* dynamic light scattering (DLS), UV-Vis and TEM measurements. Understanding the mechanism of formation allows for the identification of the key parameters which affect the resultants Au nanoparticles. The then formed nanoparticles were used in the hydrogenation of 1,3-butadiene, where the behaviour of the nanoparticle were examined using in situ XAFS measurements. This, paired *ex-situ* characterisation, TEM, and testing, allows to form structure-activity correlations for the 1,3-butadiene hydrogenation using Au and Pd nanoparticulated catalysts.

2 Methodology

2.1 Sample preparation

2.1.1 Micellar encapsulation

Following the paper of Spatz et al [54] a methodology was devised to synthesize gold and palladium nanoparticles. The method itself follows Spatz et al. recipe for most of the synthesis a part for a change in the usage of p-toluene sulfonyl hydrazide instead of hydrazine. First of all, the polymer was dissolved in Toulene (Fluka, puriss. p.a. ACS reagent 99.7 %) at a concentration of 0.5 wt % (5 mg/mL). The polymers used in the synthesis are:

- P4708-S2VP (Polystyrene(PS)=16000 MW, Poly-2 Vinyl pyridine(P2VP)=3500 MW), polydispersity = 1.05;
- P18226-S2VP (Polystyrene(PS)=30000 MW, Poly-2 Vinyl pyridine(P2VP)=8500 MW), polydispersity= 1.06,
- PS5073-S2VP(Polystyrene(PS)=175000 MW, Poly-2 Vinyl pyridine (P2VP)=70000 MW, polydispersity= 1.08),

After three days it is proposed the micelles are formed and the chloroauric acid ($HAuCl_4$) (Aldrich 99.99999% trace metal basis) or potassium tetrachloropalladate (K_2PdCl_4) (Aldrich 99.99999% trace metal basis), depending on the metal nanoparticles prepared, was added in order to load the micelles with metal salt. The amount of metal salt to be loaded is determined as follows: the mass of the polymer dissolved, the amount of polymer strands including the micelle and also the amount of nitrogen sites available for metal salt attachment as shown in Eq. 2.1. The number of sites actually occupied divided by the number of sites available is defined as the loading factor L. Previous studies have determined that only half of the available nitrogen ligands can be associated with the metal salt [238]. A combination of selected loading factor with the number of sites available gives the amount of metal salt needed which can be calculated as a mass. Finally, the formula in order calculate the metal salt needed is as follows:

$$m_{salt} = \frac{m_{poly} MM_{pvp} MM_{salt} L}{MM_{poly} MM_{vp}} \qquad \text{Eq. 2.1}$$

with m_{salt} and m_{poly} being the mass in grams of the metal salt and the polymer, MM_{pvp} the molecular mass of the P2VP part of the polymer in g/mol and MM_{vp} the molecular mass of a single 2-vinyl pyridine unit (105 g/mol). The resulting particle size can be estimated once the amount of metal salt per strand is known, keeping in mind a single micelle is composed approximately of 50 polymer strands according to previous studies [238]. Considering the low concentration the micelles are assumed to have perfect spherical shape which results in:

$$V_p = \frac{4}{3}\pi r^3 = \frac{m_p}{\rho_p} \qquad \text{Eq. 2.2}$$

$$m_p = n_p MM_{metal} \qquad \text{Eq. 2.3}$$

$$\frac{4}{3}\pi r^3 = n_{metal} \frac{MM_{metal}}{\rho_p} \qquad \text{Eq. 2.4}$$

$$\frac{\#atom}{particle} = n_{metal} N_A \quad \text{Eq. 2.5}$$

$$\frac{\#sites}{micelle} = 50 \frac{MM_{pvp}}{MM_{vp}} \quad \text{Eq. 2.6}$$

With V_p the particle volume, n_{metal} the amount of metal in the particle (moles), ρ_p the particle density, m_p the mass of the polymer, and N_A Avogadro's number. Assuming that every micelle forms exactly one particle consisting of all the attached metal atoms, the loading factor L becomes by definition:

$$L = \frac{\#atoms/particle}{\#sites/micelle} = \frac{n_{metal} N_A MM_{vp}}{50 MM_{vp}} \quad \text{Eq. 2.7}$$

$$\frac{n_{metal}=50\, L MM_{pvp}}{N_A MM_{vp}} \quad \text{Eq. 2.8}$$

Inserting Eq. 2.8 into Eq. 2.4:

$$\frac{4}{3}\pi r^3 = \frac{50 L MM_{pvp} MM_{metal}}{\rho_p N_A MM_{vp}} \quad \text{Eq. 2.9}$$

$$r = \sqrt[3]{\frac{150 L MM_{pvp} MM_{metal}}{4\pi \rho_p N_A MM_{vp}}} \quad \text{Eq. 2.10}$$

Finally the interparticle distance and thus, the deposition density, can be estimated according to Spatz et al [248]:

$$\frac{50 MM_{poly}}{N_A} = \frac{4}{3} \rho_{poly} \pi r_{micelle}^3 \quad \text{Eq. 2.11}$$

With ρ_{poly} the polymer density (1100 kg/m^3) and $r_{micelle}$ the radius of the micelle (including the poly(styrene) corona).

After four days of stirring the metal salt will have been incorporated into the micelle. A reducing agent (P-Tosyl hydrazide used with 4-fold the metal concentration) is then dissolved in toluene, in a 1:1 volume ratio, and added to the solution. After ~3 minutes, in some instances a small amount of 37 % HCl (0.5 ml for 50 ml) is added to the solution. After ~10 minutes the support, in powder form, is added to the solution in order to obtain a 1 % metal/support weight and left to stir-dry in air overnight or until toluene is completely evaporated. The samples were then calcined at 500 °C in a static air for 2.5 h in an alumina crucible using a ramp rate of 1 °C/min. The calcination was performed in order to remove all the ligand and obtain bare particles and the

temperature was necessary as evidenced by Thermogravimetric analysis (TGA) shown in figure S2.1

2.2 Sample characterisation

2.2.1 Transmission Electron Microscopy (TEM)

2.2.1.1 Introduction to TEM

Obtaining information about particle size and shape is paramount in order to understand the properties of nanoparticles. A classical technique such as light microscopy, however, does not allow the visualization of the particle in the sub-micrometre size due to the Rayleigh criterion [263] (Eq. 2.12)

$$\delta = \frac{0.61\lambda}{\mu \sin \beta} \qquad \text{Eq.2.12}$$

Where δ is the spatial resolution, λ is the wavelength of the radiation, μ the refractive index of the viewing medium, and β the semi-angle of collection of the magnifying lens. This problem has been solved when, in 1927, De Broglie enunciated the matter-wave relationship

$$\lambda = \frac{h}{\rho} \qquad \text{Eq. 2.13}$$

where λ is the wavelength of the matter, h is Plank's constant (6.626 x 10^{-34} J·s) and ρ is the momentum associated with the particle. In the particular case of the electron the relationship in Eq 2.13 can be written as

$$\lambda \approx \frac{h}{\sqrt{2m_0E\left(1+\frac{E}{2m_0c^2}\right)}} \qquad \text{Eq. 2.14}$$

where m_0 is the rest mass of the electron, c is the speed of light and E is the energy of the accelerated electron [263]. When the energy of the electron reaches between ~100 to 300 keV the wavelength becomes sufficient to obtain a spatial resolution in the nanometre regime. Using this principle, Ernst Ruska, in 1932, managed to develop what would be a prototype of the TEM, allowing direct imaging of a specimen, further developed 4 year later to create a commercially available TEM instrument [263].

A TEM consists principally of a column subject to a vacuum in the region of 10^{-8} bar, in order to reduce the absorption and scattering from any molecules contained in air. The filament (or electron gun), on the top of the column, emits an electron beam which

is then accelerated to an energy of 200 keV in most cases. The beam is focused through a series of electromagnetic lenses and then reaches the specimen, giving rise to the interaction phenomena of absorption and scattering. Depending on the electron density these phenomena will be more or less pronounced. Through the use of projector lenses the beam is then shone upon a fluorescent screen, forming a rough resolution contrast image based on the electron density (e.g. Au atoms appear darker than Si atoms). Underneath the fluorescent screen is positioned a charge couple device (CCD) camera, which is able to accurately map the variation in electron density. The information is then processed using software in order to obtain an image [264].

2.2.1.2 TEM sample preparation

A small amount of sample is dispersed in ethanol and then sonicated in order to improve the dispersion and reduce the catalyst particle volume. Following sonication, a drop of solution is dropped onto a holey carbon film supported by a 300 mesh copper TEM grid. The TEM used for catalyst analysis at Research complex at Harwell (RCaH) is a JEOL: JEM-2100 operating at 200 keV with a LaB_6 filament. Depending on the sample 5 to 20 micrographs were taken at different points in the sample in order to give a representative overview. Subsequently the micrographs were analysed through the use of the software ImageJ [265] in order to obtain information regarding average particle size of the sample, with at least 150 nanoparticles counted per sample.

2.2.2 Ultraviolet-Visible Spectroscopy (UV-Vis)

In the particular case of Au nanoparticles ultraviolet-visible spectroscopy (UV-Vis) is well established as a method of characterization [177], [266]–[268]. One of gold nanoparticles' properties is the appearance of a peak in the UV-Vis spectra, called a plasmon peak. The word plasmon corresponds to the quantum of energy associated with an eigenfrequency of plasma oscillation [66]. In the case of a metal, the conduction electrons play a role similar to the electric charges in a plasma gas, since they are detached from their ionic core and can be excited by an electromagnetic wave such as an optical beam. Therefore, when a small spherical metallic nanoparticle is irradiated by light, the oscillating electric field causes the conduction electrons to oscillate coherently. This phenomenon is clearly exemplified by the red-purple colour of a solution containing gold nanoparticles. This is called the localized surface plasmon resonance (LSPR) [65].

The position and intensity of the plasmon peak resulting when UV-Vis radiation interacts with the nanoparticles can be calculated according to Mie theory: given that the sum of the incident electric field and a second field produced by the nanoparticle is expressed by the following relationship

$$\vec{E}_{ext} = \vec{E}_0 - \alpha E_0 \left[-2\frac{cos\theta}{r^3}\vec{u}_r - \frac{sin\theta}{r^3}\vec{u}_\theta\right] \qquad \text{Eq. 2.15}$$

Where $\vec{E}$ is the electric field, and α is the sphere polarizability, given by:

$$\alpha = 4\pi\varepsilon_0 R^3 \frac{\varepsilon-\varepsilon_{diel}}{\varepsilon+2\varepsilon_{diel}} \qquad \text{Eq.2.16}$$

Where ε is the dielectric function (ε = ε(ω)). Therefore $|\alpha|$ (and therefore the intensity of the plasmon resonance) is maximized when the following relationship is fulfilled:

$$|\varepsilon + 2\,\varepsilon_{diel}| \text{ is a minimum.} \qquad \text{Eq.2.17}$$

This relationship identifies the position of the plasmon peak depending on the surrounding media (air, Al_2O_3 etc etc) [65].

Amongst the factors that influence the position of the plasmon peak one of the most important is the medium surrounding the nanoparticles, through its optical index *n* [269], [270] along with the shift of the plasmon resonance to higher wavelengths, the increase of the index of the surrounding medium is accompanied by a sharp increase of the absorption cross section. Another factor determining the shift and the intensity of the plasmon peaks is the size and the shape of the nanoparticles [177], [268]. According to Mie theory nanoparticle size does not affect the LSPR. However, this approximation does not stand anymore when the particle is larger than 60 nm, as multipolar effects come into play, as well as when the particle size becomes smaller than the mean free path of the free electrons [66]. Under these conditions collisions of electrons with the particle surface becomes important. This results in a slight broadening of the plasmon band for AuNPs smaller than 10 nm, culminating in a blue-shift for gold nanoparticles smaller than 2.5 and a decrease of intensity to total disappearance as shown in figure 2.1 [65].

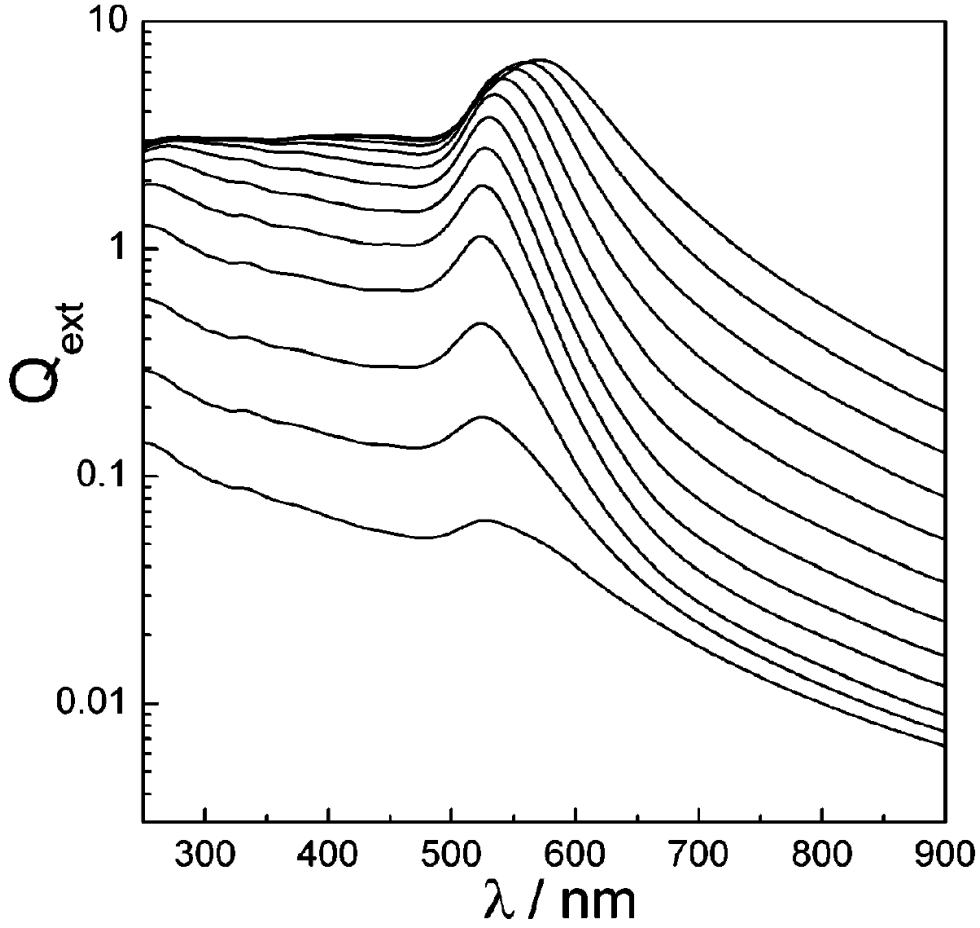

Figure 2.1. Calculated extinction efficiency (Qext) in dependence of λ for particle diameters of 2.5, 5, 10, 20, 30, 40, 50, 60, 70, 80, 90, 100 nm (from bottom to top). Reproduced with permission from the American chemical society, Haiss et al., *Analytical chemistry*, 2007, vol. 79, pg. 4215-4221 [177].

2.2.2.1 UV-Vis measurements

UV-Vis spectroscopy measurements were performed using a Shimadzu UV-1800 spectrometer, with the samples loaded into a cuvette with 5 mm pathlength to determine the nature of the Au species present and to determine the presence and position of an Au plasmon peak. For solid samples the UV-Vis measurements were taken using a Shimadzu UV-2600 spectrometer in reflective mode, using a light spot of 2 mm. A small amount of sample is pressed into a sample holder (5 mm in diameter and 1mm deep) and the surface was smoothed. The reflectance versus wavelength data obtained is the converted to intensity vs wavelength data through the use of the Kubelka-Munk theorem [271].

2.2.3 Dynamic Light Scattering (DLS)

Dynamic light scattering (DLS) is a technique that is used to obtain information regarding the size distribution of small particles in suspension.

Dynamic light scattering has numerous advantages such as:

- Short measurement duration (in the order of seconds)
- Ease of use due to high automatization of the process of data acquisition

to cite the most relevant. But some disadvantages are to be noted: the possible non trivial analysis for non-rigid macromolecules, the low sensitivity to small oligomers and the fact that above 0 K the molecules deviate from their average position since particles suspended in liquid undergo Brownian Motion [272]. The smaller the particle, the greater the Brownian motion. The technique works by the shining of monochromatic light, a laser for example, leading to a Doppler shift when the light hits the moving particle, changing the wavelength of the incoming light [273]. The change of the wavelength is related to the size of the particle and it is possible to calculate the size distribution, assuming a spherical shape, and its motion through the medium by measuring the diffusion coefficient of the particle and using the autocorrelation function of the intensity trace recorded during the experiment [274].

2.2.3.1 DLS measurement

DLS measurements were performed using Zetasizer nano ZS from Malvern. The refractive index used in the setup was derived from polystyrene (η=1.5). Micelles containing solutions were loaded into a cuvette with 5 mm pathlength.

2.2.4 X-ray Absorption Fine Structure Spectroscopy (XAFS)

2.2.4.1 A brief history of XAFS

X-ray absorption fine structure (XAFS) spectroscopy is a powerful characterization technique for determining the local structural and electronic properties of a material under investigation. The development in 1916 in Lund (Sweden) of the first vacuum X-Ray spectrometry by Siegbahn and Stenström and successive improvements can be considered as the birth of X-Ray spectroscopy [275]. In 1931 Hanawalt observed the effect that the chemical and physical state of the sample have on the fine structure of the XAS (X-ray Absorption spectroscopy) spectra. He proved that substances sublimating in the molecular form As ($4As_{solid} \rightarrow (As_4)_{gas}$) or $AsCl_3$ are characterized

by XAFS spectra exhibiting different fine structure above the edge when measured in the solid or in the vapour phases, and he observed that the monatomic vapours of Zn, Hg, Xe, and Kr elements exhibit no such structure. These experiments were some of the first to contain basic XAFS spectroscopy methods but decades were needed in order to fully explain and exploit XAFS [276].

The first theoretical attempt to explain fine structure in the XAFS spectra was proposed in the years 1931-32 by Kronig who developed a model based on the presence of known long-range order in the system [275]. Several other authors attempted to establish the basis of the modern concept of XAFS but at that point it was merely a spectroscopic curiosity. No quantitative information was extracted and only qualitative conclusions could be reached. For example, the decrease of the amplitude of XAFS oscillations when increasing the sample temperature and that metals with the same crystal structure had similar fine structure. During the sixties, commercial diffractometers were modified so that absorption spectra of much better quality could be obtained using conventional X-ray tubes as sources [275]. The first example of the application of EXAFS in catalysis was reported by Van Nordstrand et al, who performed a systematic study on many transition metal compounds and classified their XANES spectra according to the atomic structure and valence of the metal element in the compound, subsequently noting the electronic shift with valence [277]. However in 1971 Sayers, Stern and Lytle applied a Fourier transformation on the background-subtracted oscillations giving, in reciprocal-space (”R-space”), a pattern close to the function of radial distribution of atomic density. The work represented a milestone for EXAFS spectroscopy and thanks to the progressive availability of several and more brilliant synchrotron radiation sources determined the establishment of EXAFS and XANES spectroscopies as reliable tools to understand the structural and electronic configuration of unknown systems [276].

2.2.4.2 EXAFS Theory

The aim of XAFS is the measure of the absorption coefficient of a given sample, μ(E), as a function of the photon energy E. For any sample μ(E) is a monotonically decreasing function of the photon energy, given in a first approximation by

$$\frac{\mu(E)}{\rho} \approx \frac{Z^4}{AE^3} \qquad \text{Eq. 2.18}$$

where ρ is the sample density, Z the atomic number and A the atomic mass. When a beam of X-ray photons passes through a material, the incident intensity *I* will be decreased by an amount that is determined by the absorption characteristics of the material being irradiated. For a path length *dx* of the radiation through the material the decrease *dI* is given by

$$dI = -\mu(E) I \, dx \qquad \text{Eq. 2.19}$$

with the linear absorption coefficient μ(E) a function of the photon energy, when eq. 2.19 is integrated over the total thickness *x* gives Lambert's law

$$I_t = I_0 e^{-\mu(E)x} \qquad \text{Eq. 2.20}$$

When the energy of the incoming photons is large enough to excite an electron from a core level to a vacant excited state or to the continuum, a sharp rise in the absorption intensity appears, called an absorption edge. At the absorption edge, E_{edge}, the kinetic energy of the electron (E_k) is defined to be equal to E_0, often referred to as the zero-point energy.

For any energy above this, the photoelectron kinetic energy is given by

$$E_k = h\nu - E_{binding} \qquad \text{Eq. 2.21}$$

The photoelectron can be represented as a spherical wave with a wavelength defined as

$$\lambda = \frac{2\pi}{k} \qquad \text{Eq. 2.22}$$

where

$$k = \sqrt{\left(\frac{8\pi^2 m}{h^2}\right)(E_k)} \qquad \text{Eq. 2.23}$$

where *k* is the wave-vector, *m* the electron mass and *h* Plank's constant [278]. The linear absorption coefficient μ(E) is proportional to the transition probability of the photoelectric event according to Fermi's Golden Rule:

$$\mu(E) = C\left|\langle \phi_f | \hat{e} r | \phi_i \rangle\right|^2 \sigma\left(E_f - E_i - h\nu\right) \qquad \text{Eq. 2.24}$$

Here $\hat{e}$ is the electric field polarisation vector of the photon, and *r* the coordinate vector of the electron. The interaction of an atom with a photoelectron will produce a

backscattered wave with a kinetic energy given by Eq. 2.21 The outgoing electron can be viewed as a spherical wave that scatters off neighbouring atoms, producing a backscattered wave as shown in Figure 2.2.The outgoing and backscattered waves interfere, causing an interference pattern. Since the path length of both waves define their final phase, it can be seen that the distance to the neighbouring atoms determines the interference pattern [278].

$$\chi(k) = \frac{[\mu(k) - \mu_0(k)]}{\mu_0(k)} \qquad \text{Eq. 2.25}$$

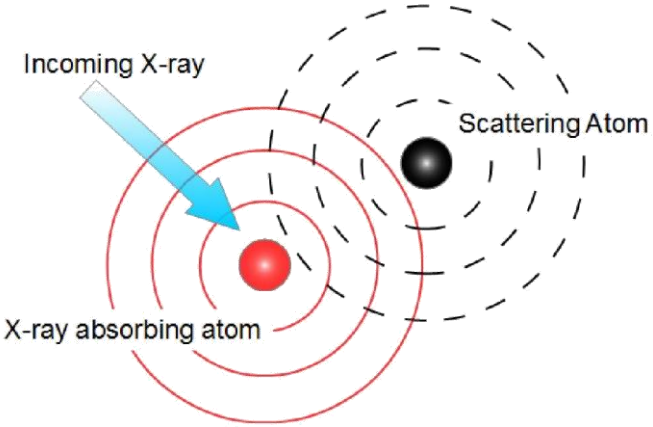

Figure 2.2. Scattering of a spherical wave from the absorbing atom to a neighbouring atom. The incoming X-ray beam causes the transition of an electron from the core to the continuum forming a spherical wave (depicted in red in the figure). After interacting with a scattering atoms, a backscattered wave is formed (in black in the figure) and the interaction between the two waves causes the formation of an interference pattern.

To separate the structural information from the energy dependence of the absorption cross sections, the normal EXAFS spectrum is usually defined as the normalized oscillatory part of μ(E). The obtained EXAFS function, or χ function, is conventionally expressed versus k, the wavenumber of the photoelectron out-going from the absorber atom, according to the k-E relationship reported in Eq. 2.23 [278].

In the Single-Scattering (SS) approach, the k-weighted χ (k) function can be modelled using the equation known as the "standard EXAFS equation"

$$\chi(k) = S_0^2 \sum_j \frac{N_j A_j}{r_i^2} e^{\left(-\frac{2r_j}{\lambda}\right)} e^{\left(-2\sigma_j^2 k^2\right)} \sin[2kr_j + 2\Phi_j(k)] \qquad \text{Eq. 2.26}$$

where S_0^2 is the so-called amplitude reduction factor, λ is the photoelectron mean-free path, the sum over *i* runs over the different coordination shells around the absorbing

atom, $A_i(k)$ is the backscattering amplitude function of the scattering atom [279] (measured in Å), e $\Phi_i(k)$ is the phase function of the couple absorber/scatterer, defined as

$$\phi_j(k) = 2\phi_{adsober}(k) + \phi_{scatterer}(k) \qquad \text{Eq. 2.27}$$

N_i is the coordination number, r_i is the interatomic distance and σ_i is the Debye-Waller factor that quantifies the disorder of the *i*th shell. For each shell, σ_i consist of a dynamic term due to the thermal motion of the atoms ($\sigma_{i;T}$) and a static term due to structural disorder ($\sigma_{i;D}$)

$$\sigma_i^2 = \sigma_{i,T}^2 + \sigma_{i,D}^2 \qquad \text{Eq. 2.28}$$

The equation plays a relevant role in the interpretation of the EXAFS spectra collected on catalysts, because disorder is often an important parameter in such materials [278]. The standard EXAFS formula provides a convenient parametrization for fitting the local atomic structure around the absorbing atom to the experimental EXAFS data. The short-range structure probed by an EXAFS experiment is easily explained by considering the finite lifetime of the core-hole and the limited mean free path (λ) of the photoelectron as expressed by the exponential term $e^{-2rj/\lambda}$ [278]. The strength of the interfering waves depends on the type and number of neighbouring atoms through the backscattering amplitude $A_j(k)$ and the coordination number N_j and, is primarily responsible of the magnitude of the EXAFS signal [276].

2.2.4.3 EXAFS Data analysis

By performing a Fourier transform of the $\chi(k)$, weighted by k^n (n=1, 2 or 3) to empirically balance the loss of EXAFS signal in the high k region, it is possible to single out the contributions of the different coordination shells in the R-space. Once the $A_j(k)$ and $\phi_j(k)$ functions have been independently measured on model compounds or determined using ab initio methods, the structural parameters N_j, r_j and σ_j^2, can be determined in a least-squares approach where the difference between the experimental and the modelled $k^n\chi(k_j)$ function is minimized using least squares regression along the sampled experimental points k_j [275]. The minimization routine can be done either in k-space, directly on the measured $k^n\chi(k_j)$ function, or in R-space, working on the Fourier transformed functions. The maximum number (n_{ind}) of analysable parameters

is defined, according to the Nyquist theorem, by the product of the examined k-space (δk) and the interval in R-space (δR) containing the optimized shells

$$n_{ind} = \frac{2\delta k \delta R}{\pi} \qquad \text{Eq. 2.29}$$

The distance resolution (λr) of an EXAFS spectrum is defined from k_{max} as

$$\delta r = \frac{\pi}{(2k_{max})} \qquad \text{Eq. 2.30}$$

The standard EXAFS formula considers only single scattering contributions. Actually, all possible scattering paths where the photoelectron is diffused by N different neighbours can contribute to the interference phenomenon. All the paths where the number of different scattering atoms involved in the scattering process is higher than two are called multiple scattering (MS), as for example a triangular path A-S1-S2-A where A is the atom of origin and S1 and S2 two different scattering atom. Very often MS paths have a low or very low contribution to the EXAFS signal with respect to single scattering ones, since the low free mean path of the photoelectron penalizes longer paths [276].

2.2.4.3.1 XAFS Measurement

Measurements were performed on the B18 beamline at Diamond Light Source at the palladium *K* edge (24.35 keV) and gold L_{III} edge (11.91 keV) in transmission mode for the solid-state samples, and on the DUBBLE beamline (BM26A) of the European Synchrotron Radiation Facility (ESRF) using gold L_{III} edge (11.91 keV) in fluorescence mode using a 9-element monolithic Ge detector (Ortec). For each sample a series of spectra were collected and summed in order to improve the signal to noise ratio.The parameter used for data acquisition are shown in table 2.1.

Table 2.1. Acquisition parameter for XAFS data

Sample	Energy range (keV)	Acquisition time (min)	Current (mA)	Number of spectra
Au Pellets	11.714 – 13.116	2	300	3
In situ Au	11.714 – 13.017	1.33	300	10
Pd Pellets	24.150 – 25.600	2	300	3
In situ Pd	24.150 – 25.600	1.5	300	10
Au Solution	11.819 – 12.500	11.1	200	3

Data processing and analysis were performed using the Athena and Artemis software from the Demeter IFEFFIT package [280][281]. The FEFF6 code was used to construct theoretical EXAFS signals that included single-scattering contributions from atomic shells through the nearest neighbours in the face-centered cubic (FCC) structure of Au and Pd. The *k*-range used for the fitting 2.5 to 10.3 $Å^{-1}$ and the *r*-range from 1 to 3.7 Å respectively. The path degeneracy was allowed to vary in order to account the size effects that cause surface atoms to be less coordinated than those in the particle interior. The amplitude reduction factor (S_0^2) was fixed at 0.860, as obtained from the fitting of the bulk Au foil and bulk Pd foil.

2.2.5 Small Angle X-ray Scattering (SAXS)

Small-angle X-ray scattering (SAXS) is a small-angle scattering technique which uses X-rays as a mean to investigate the shape of "large-scale" nanostructures (from 10 Å to micrometre). The scattering intensity distribution contains information regarding particle size distribution, particle shape and orientation [282]. In particular, it is used for interrogating dilute systems under dynamic conditions i.e. chemical aggregation, surfactants, colloids etc. [196], [283]. SAXS measurements require an X-Ray beam to pass through the sample, which can be either generated by a sealed tube, a rotating generator anode or from synchrotron radiation. In the set up an X-ray beam hits a sample and an elastic scattering phenomena occur due to the interaction between X-rays and the sample. The scattered X-rays are recorded at low angle (usually between 0.1 – 10 °), forming a scattering pattern recorded usually by a 2-dimensional flat X-Ray detector, as shown in figure 2.3.

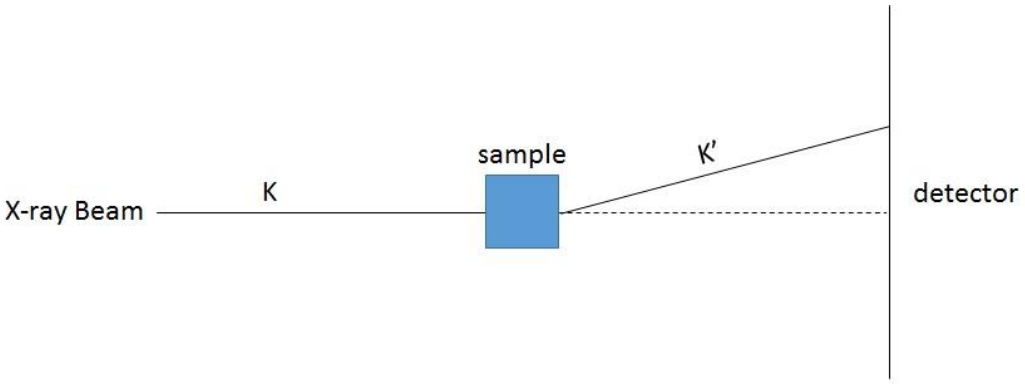

Figure 2.3. Schematic of SAXS experiment, with K being the incident beam and K' the scattered beam. The detector is positioned perpendicular to the incoming beam.

The 2D SAXS frames are then converted through integration into a plot of scattering intensity versus scattering angle $q = \frac{4\pi \sin(\theta)}{\lambda}$ where θ is the scattering angle and λ the wavelength of the incident X-ray.

2.2.5.1 SAXS measurement

SAXS measurements were conducted on the DUBBLE beamline (BM26A) of the European Synchrotron Radiation Facility (ESRF) using X-ray photons of 11.850 keV. The 2D SAXS images were recorded in transmission using the Mar CCD 165 detector with the pixel size of 80 µm. The modulus of the scattering vector **q** was calibrated using silver behenate ($AgC_{22}H_{43}O_2$). The sample to detector distance was approximately 2 m, resulting in a q range between 0.016 and 0.4.

The data were corrected for the detector dark field and background scattering from the capillary with polymer and solvent only. The data reduction was performed using Fit2D and 1D curves were fitted using SANS Analysis package for the Igor Pro software [284].

2.2.5.2 Scattering Intensity Calculation

Scattering intensity of the Au NPs solution reads as follows

$$I(q) = A \cdot \int_0^\infty F(q) f(R) dR \qquad \text{Eq. 2.31}$$

where A-scaling parameter, F(q) - NP form factor, f(R) – NPs distribution function.

The Schultz-Zimm distribution function was chosen, that can account for the assymetrical NPs size distribution based on the microscopy data. Also this model was successfully used in the past to reveal the mechanism of the Au NPs formation in the classical citrate method [196]. The Schultz-Zimm distribution can be written as [285]

$$f(R) = \left(\frac{z+1}{R_a}\right)^{z+1} R^z exp\left[-\left(\frac{z+1}{R_a}R\right)\right] \frac{1}{\Gamma(z+1)} \qquad \text{Eq. 2.32}$$

where R_a - is the mean radius, z – is a parameter related to the polydispersity ($\rho=\sigma/R_a$) by $\rho = 1/(z+1)^{0.5}$ where σ is the root-mean-square deviation from the mean size.

NP is considered to be a hard (uniform density) sphere with the radius R and volume V and its form factor is given by the Rayleigh formula[286]

$$F(q) = (\Delta\rho)^2 \cdot V^2 \left[3\frac{\sin(qR) - qR\cos(qR)}{(qR)^3}\right]^2 \qquad \text{Eq. 2.33}$$

where Δρ-density difference between the particle and the medium, q – modulus of the scattering vector.

The SAXS data analysis were performed by a collaborator within the group.

2.3 Catalyst testing

2.3.1 Fixed bed reactor

Figure 2.4 shows a schematic set up of the fixed bed reactor which was set up in RCaH. A catalyst bed is located in the middle of a quartz tube (ø = 7 mm), using quartz wool in order to hold the catalyst in place. The tube is then put inside a tubular furnace and connected to the gas inlet and outlet. In order to monitor the temperature of the catalyst, a thermocouple is inserted inside the tube, in contact with the catalyst. The reaction is carried in gas phase by flowing the reaction mixture through the catalyst bed (top-to-bottom). The course of the reaction was followed by mass spectroscopy, as well as gas chromatography, which were connect directly to the tube exit. The gas outlet was not heated as no resultant product would incur in phenomena of condensation.

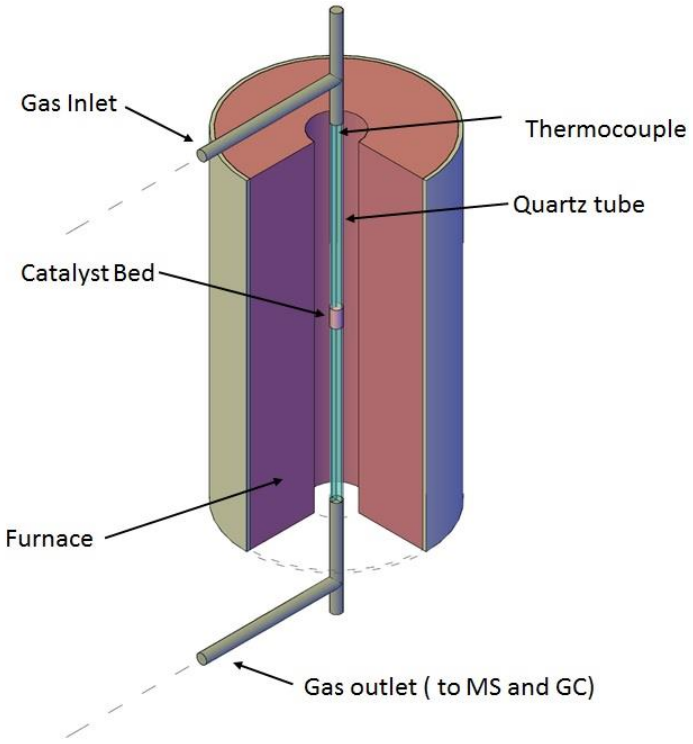

Figure 2.4. Schematic set up of a fixed bed reactor.

2.3.1.1 Reaction procedure and conditions

A typical reaction procedure for 1,3-butadiene hydrogenation is as follows; the catalyst is pressed into a pellet and then sieved down to a sieve fraction of 250/425 μm. The amount of catalyst needed in each experiment was determined by the space velocity, defined the volumetric flow rate (ml/h) per mass of catalyst, desired (7500

and 22500 h^{-1} ml/g catalyst for gold and palladium catalysts respectively) and in order to keep a bed length of 1 cm. Depending on the metal species (Au or Pd) the reaction conditions were slightly different due to the different catalytic behaviour. Au catalysts were heated to 433 K ramping at 10 °C/min from room temperature under a H_2 atmosphere (4% H_2/Helium BOC) and cooled down to 383 K. Pd catalysts were treated for 30 min. under H_2 at 323 K. This was done in order to avoid any possible presence of oxides, either Au_xO_y or PdO. After this reduction treatment the catalysts were brought room temperature (~298 K) and the reaction mixture introduced into the reactor. The pre-treatment in H_2 was necessary in order to remove any possible AuO or PdO which could have been formed in the catalysts.

2.3.2 Gas Chromatography (GC)

Gas chromatography (GC) is a type of chromatography used for separating and analysing different gaseous compounds present in a reaction mixture. Through calibration it is possible to obtain quantitative information about the composition of the mixture, making this technique an important tool for quantitative catalytic studies. Samples can to be either gas or liquid (which are then vaporised without decomposition in order to be analysed). In particular, in this project GC has been used to obtain information about the product distribution and yield for the reactions. Usually, a sample is injected into a column using an inert gas (i.e. He or Ar). The compounds flow inside a separation column at different speeds, dependent on their affinity to the stationary phase packed inside the column. The column is placed inside an oven in order to enable temperature control. The temperature plays a role in the mobility of the compound thus by changing the temperature profile it is possible to vary the speed of the compounds inside the column. After separation and elution from the column the constituents of the sample are passed through a detector. The signal obtained from the detector is proportional to the concentration of the individual constituents of the sample allowing for quantification. The GC used in this project were a SRI 8610C for gas phase 1,3-butadiene hydrogenation.

2.3.2.1 SRI GC

In figure 2.5 a schematic of the setup of the SRI GC used (SRI 8610C Chromatograph Multiple Gas #3). In the image are indicated in black the valve connection during the "load" phase and in red the valve connection during the "inject" phase. The machine

is directly connected to the outlet of the catalyst reactor; when the load phase is activated, 10 ml of sample is injected into a sample loop. The sample would then flow through column 1 (Agilent J&W, 2 meter, Hayesep D packing), which only retains lighter gases (i.e. H_2,O_2), and then flows to column 2 (Restek MXT-1, 15 meter, packed with cross-bonded dimethyl silane) which enables for the separation of the heavier compound (i.e. C_xH_y, $C_xO_yH_z$). The columns were selected in order to archive the highest product separation possible. The compound then is separated by the column before reaching the detector.

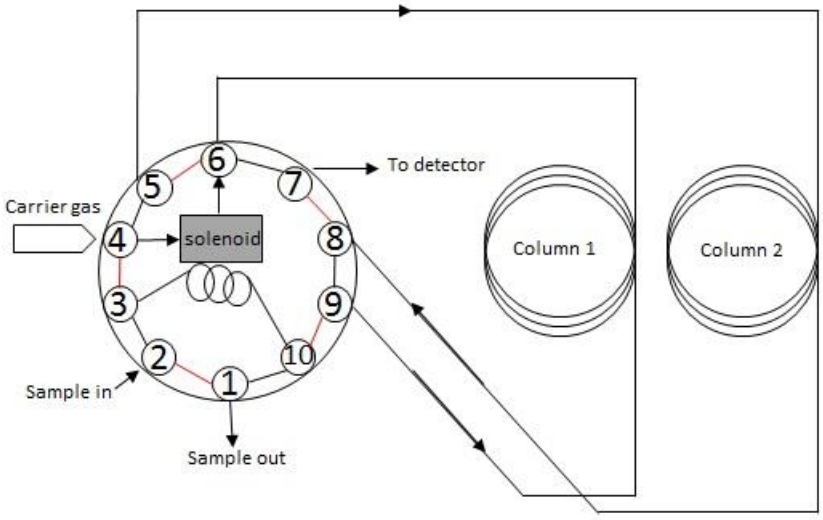

Figure 2.5 Schematic of SRI GC machine. The number represent the valves, with the carrier gas entering through valve 4, and the sample in and out phase managed by valve 2 and 1 (for in and out respectively). Depending on the phase, different valve connection are used. In black valve connection during the "load" phase and in red the valve connection during the "inject" phase

2.3.2.1.1 Flame Ionization Detector (FID)

A flame ionization detector (FID) was used to analyse the products of the reaction after being separated by the column. This detector works via the detection of ions formed during the combustion of organic compounds in a hydrogen flame. The concentration of the ions generated is directly proportional to the concentration of the organic species in the gas stream. The molar response for a hydrocarbon is typically equal to the number of carbon atoms in the structure, whereas, in compound containing heteroatoms, the response factor is lower. Moreover, CO and CO_2 are not detected at all.

2.3.2.2 Calibration of 1,3-butadiene hydrogenation reaction product for SRI GC

The required calibration for quantitative measurement of the product of 1,3-butadiene hydrogenation (1-butene, trans/cis-2-butene, n-butane) was performed using a calibration mixture (0.05 % cis-2-butene, 0.15 % trans-2-butene, 0.1 % N-butane, 0.3 % 1-butene all balanced in He, BOC). 1,3-butadiene calibration was performed as well in order to monitor the total conversion, using a 1 % 1,3-butadiene in He gas mixture. The calibration has been performed using a similar total gas flow as the one used in the reaction, using He to dilute the pure mixture. The amount of 1,3-butadiene is varied to simulate a products to reactant ratio between 0 and 1. A similar approach was used for the calibration mixture, with the calibration mixture volume based on a hypothetical conversion rate between 20 and 100 %. Table 2.2 shows the concentration of calibration mixture and 1,3-butadiene. The concentration is calculated as ml/min of the compound. Each concentration was measured 3 times, with the average taken for the calibration curve. In table 2.3 the area associated with each peak at different products to reactant ratio.

Table 2.2. Concentration of each compound used for calibration as a function product to reactant ratio.

Products/Reactant ratio	1,3-Butadiene (ml/min)	n-Butane (ml/min)	Cis-2-butene (ml/min)	Trans-2-butene (ml/min)	1-butene (ml/min)
0	0.16	0	0	0	0
0.2	0.128	0.00533	0.00267	0.008	0.016
0.4	0.096	0.01067	0.00533	0.016	0.032
0.6	0.064	0.016	0.008	0.024	0.048
0.8	0.032	0.02133	0.01067	0.032	0.064
1	0	0.02667	0.01333	0.04	0.08

Table 2.3 Peak area associated of each compound used for calibration as a function of the conversion rate

Conversion Rate	Area 1,3-Butadiene	Area n-Butane	Area Cis-2-butene	Area Trans-2-butene	Area 1-butene
0	736.4	0	0	0	0
20	585.9	23.4	11.9	34.7	70.7
40	438.	48.2	24.7	71.4	145.2
60	293.9	72.4	37.1	107.2	218.1
80	147	104.9	55	157	313.7
100	0	125.1	64.4	184	374.6

A linear fit, following the formula y = *a*x, where y area of the peak, x is the flow rate of the gas and *a* is the slope of the straight line, was performed, and the results are shown in table 2.4 and in figure 2.6, with R^2 being the error from the fit and slope being the value obtained from the fit.

Calculation of the concentration of the compounds were done using eq. 2.24

$$Flow\ rate\ of\ compound\ \left(\frac{ml}{\min}\right) = \frac{Peak\ Area}{Slope} \qquad \text{Eq. 2.24}$$

Once the flow rates are calculated, assuming that the flow rate correspond to the concentration of 1,3-butadiene, the conversion for the hydrogenation is therefore expressed by eq. 2.25.

$$100 - \left(100 * \frac{Final\ flow\ rate}{Initial\ flow\ rate}\right) = Conversion \qquad \text{Eq. 2.25}$$

and the selectivity of each product as described in eq. 2.26

$$Selectivity = 100 * \frac{Compound\ flow\ rate}{Sum\ of\ all\ the\ product\ flow\ rate} \qquad \text{Eq. 2.26}$$

Table 2.4. Result of the fits

Compound	R^2	Slope
1,3-Butadiene	1	17892.295
n-Butane	0.9973	19161.589
Cis-2-butene	0.9978	18906.581
Trans-2-butene	0.9975	19108.023
1-butene	0.9981	19873.136

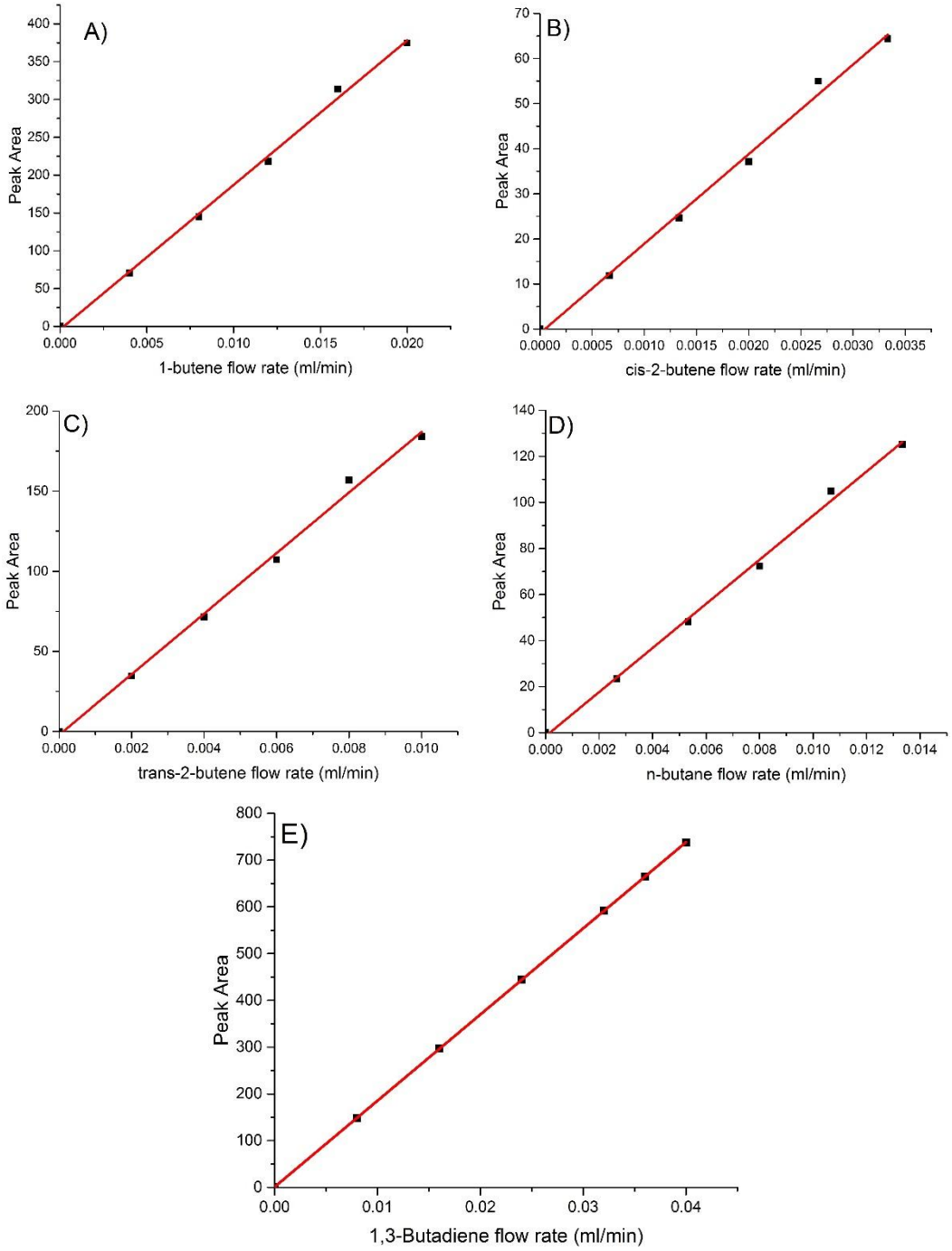

Figure 2.6. a) 1-butene; b) cis-2-butene; c) trans-2-butene; d) n-butane; e) 1,3-butadiene calibration plot

3 Investigation of Au NP self-assembly process in reverse micelle

3.1 Introduction

Metal nanoparticles (NPs) can be used in a variety of applications ranging from catalysis to sensors, antibacterials and drug delivery [28], [287]–[289]. In order to prepare a nanoparticle, various methods have been developed [290], [291]. Methods can be divided into top-down methods (NPs are removed from 'bulk' material) and bottom-up (atoms are built-up in order to form NPs) [290], [291]. Whereas top-down approaches, such as e-beam lithography [292], allow NP production with regular physical attributes (e.g. size and shape), it is generally not viable on the industrial scale due to expensive instrumentation and the fact that it only allows for the formation of 1D and 2D supported NP arrays [293] and therefore is only suitable for the model systems. The bottom-up approach is the most commonly used method to prepare NPs, where ions are reduced in a solution before they agglomerate [196], [290], [294], [295]. Bottom-up methods include chemical [196], electrochemical [294], templating [290] and sonochemical [295] reduction, with the common occurrence in these types of synthesis of a capping agent, often a surfactant, in order to reduce the NPs growth to the desired size and shape. The main disadvantage of these bottom-up approaches is that they do not produce homogeneous NPs, often resulting in a broad particle size distribution and the average particle size varies from batch to batch. This uncertainty in the NP size makes it difficult to truly understand the impact of NP size on its properties e.g. catalytic activity [296], [297] or colorimetric sensing [288]; the synthesis of NPs with a particle size distribution as narrow as possible is therefore critical in this regards.

The fabrication of monodisperse NPs is not trivial and is hampered by our lack of detailed knowledge of the self-assembly process [290]. Various studies have been performed in order to understand the evolution of colloidal solution from the ions to NPs in different systems, such as Au [196], Fe_2O_3 [298], Ag [299], and several NPs' growth modes including Ostwald ripening, fusion, coalescence, condensation and coagulation, and combinations of these modes, thoroughly described in a review article from Thanh *et al* [300] Despite similarities in the fabrication mechanisms, the NP growth appears to depend on the synthesis method [196],[301]. Polte *et al*. studied

the mechanism of Au NPs formation in the commonly used citrate method and showed that the combination of small-angle X-ray scattering (SAXS) and X-ray absorption near edge structure (XANES) is able to reveal insight into the growth of metal nanoparticles during synthesis [196]. In that study the authors affirmed that NP growth goes through four different phases:

- fast initial formation of small gold nuclei comprising a few atoms;

- coalescence of these nuclei into a nanoparticle;

- slow growth of the nanoparticle sustained by an ongoing reduction of the precursor;

- fast reduction ending with the complete consumption of the precursor species.

The second step (coalescence of the nuclei) has been identified as a key step in order to form monodisperse nanoparticles.[196] On the other hand, a study from Sakai *et al* shows that in the case of a block copolymer (poly(ethylene oxide)-poly(propylene oxide)- poly(ethylene oxide), also known as PEO-PPO-PEO) the NPs can be grown in a single step, due to the presence of the polymer acting both as a stabilizer as well as a reductant [301]. Here the presumed mechanism of gold NPs formation is proposed as below:

- reduction of the metal ions facilitated by the polymer to form clusters (i.e. structures containing a small number of atoms);

- simultaneous adsorption of the polymer on these clusters and a reduction of $[AuCl_4]^-$ ions adsorbed on the surface of the clusters;

- growth of the NP through a repeat of step 2 until stabilisation.

In this process the polymer plays an important role in determining the particle size resulting from the synthesis. This is due to the dual attribute of the polymer as reductant and stabilizer, which varies the reaction activity of $[AuCl_4]^-$ based on the polymer molecular weight [301].

By comparing the citrate[196] and copolymer-assisted [301] methods one can conclude that the reduction of metal ions into a cluster and the coalescence of the clusters are two common steps during metal NP synthesis. However, there are also key differences in the mechanism for gold NP growth. This could be, for example, due to the different stabilizer (citrate in one case and block copolymer in the other) that changes the pathway of the reduction process.

Polymer-encapsulated reverse micelle synthesis, introduced by Spatz *et al*, can be used to prepare uniform, monodisperse metal NPs [54]. This advanced fabrication method mimics water-in-oil system by employing precursor filled micelles formed by PS-*b*-P2VP diblock-copolymer in organic solvent, that allows to fully encapsulate all metal ions and inhibits the formation of sub-species [302]. Another advantage of this approach includes self-assembly into regular arrays with considerably larger inter-particle distances when deposited on a flat substrate that plays an important role for many applications e.g. minimises the magnetostatic interaction of NPs and prevents sintering during heat treatment [302], [303]. The size of the deposited NPs and their density (e.g. inter-particle distance) can be conveniently controlled by altering the length of shell- (PS) or core-forming (P2VP) copolymer blocks [303]. In particular by increasing the length of the PS it is possible to increase the separation between the micelles, whereas the P2VP length determines the size of the Au containing core. Despite multiple reports where this synthesis method has been shown to produce well-defined metal NPs with suitably small particle size distributions [54], [302], [303], to the best of our knowledge no detailed studies have been performed to understand the mechanism of gold-containing micelles formation. Questions remain regarding the time required to complete the reduction process, and the step-by-step pathway to self-assemble metal ions into Au NPs.

In situ X-ray absorption fine structure (XAFS) is a powerful method to follow the changes in the electronic structure of metals during the reduction process [304]. In particular, XANES is used to observe changes in oxidation state of the Au species, whereas extended X-ray absorption fine structure (EXAFS) can monitor the formation of Au clusters through detection of the Au-Au scattering pair evolution [196], [304]. Whereas XAFS reveals information on the local environment of the gold atoms (i.e. the short-range order) in the micelles, SAXS is sensitive (in a size range of 1 to 100 nm) to the changes in the electron density fluctuations and is more suitable to probe the micelles' core where gold clusters formation occurs [196], [299]. Thus, a combination of these two X-ray techniques with the use of other more commonly available experimental methods such as dynamic light scattering (DLS), ultraviolet-visible spectroscopy (UV-Vis) and transmission electron microscopy (TEM), allows to understand the chemical and physical processes happening during the formation of the metal NPs.

This work is focused on the investigation of gold NP formation during polymer-encapsulated reverse micelle synthesis using *in situ* X-ray spectroscopy and scattering. The reverse micelle method, by offering tight control over the NPs' size, allows a more detailed mechanistic insight into the process of homogeneous NP formation. Key to this study is the avoidance of 'fast' reducing agents such as $NaBH_4$ [305] or citrate [196], that can often result in uncontrolled particle growth and a large particle size distribution, hindering our attempts at a detailed understanding of the self-assembly process [306]. The insight obtained using these advanced characterization methods in combination with the reverse micelle method allow us to identify key stages in the self-assembly process that are useful when trying to optimize NPs for a wide range of practical applications.

3.2 Materials and Methods

3.2.1 Nanoparticles preparation

Gold nanoparticles solutions were prepared by the polymer-encapsulated reverse micelles method [54]. Two block-copolymers P18226-S2VP and P5073-S2VP were purchased from the Polymer Source Inc (electronic grade purity). The metal salt used was chlorauric acid ($HAuCl_4$) (Aldrich 99.99999% trace metal basis). P-Toluene sulfonyl hydrazide (P-Tosyl hydrazide) (Aldrich 97%) was used as the reducing agent, as an alternative to the more commonly used toxic and explosive hydrazine [307]. All reagents were used as received. 0.5 wt % polymer (c= 5 mg/ml) solution was prepared in 25 ml of toluene (Aldrich 99.9%) and left to stir for 3 days in order to allow the polymer to dissolve and homogenize. After 3 days, the metal precursor was added to the solution depending on the polymer used (0.021 g for P18226-S2VP and 0.0335 g for P5073-S2VP) in order to obtain an Au/pyridine atomic ratio of 0.3 and the solutions were left to allow the metal salt to incorporate inside the micelles. The polymers were selected in order to obtain different particle size. Before the measurements 10 ml of each solution was put in a glass vial with a 10 ml of a solution of P-tosyl hydrazide. To compare the effect of the HCl, used in literature to remove the excess of hydrazide[54], on the metal reduction inside the polymer micelle, 50 μl of HCl (ACS reagent 37%, Fluka) was added to the solutions after ~30 seconds and left to stir. Table 3.2.1 summarises a list of the samples used in this work.

Table 3.2.1. Samples list.

Sample name	Polymer	M_n x 10^3 PS-b-P2VP	PDI[1]	HCl
A	P18226-S2VP	30.0-8.5	1.06	no
A-HCl	P18226-S2VP	30.0-8.5	1.06	yes
B	P5073-S2VP	175.0-70.0	1.08	no
B-HCl	P5073-S2VP	175.0-70.0	1.08	yes

1. Polydispersion Index

In order to verify the stability of the system after toluene evaporation we filled one capillary with an aliquot of sample A solution and let the toluene evaporate in an oven set at 70 °C.

3.2.2 In situ SAXS

In situ Small-angle X-ray Scattering SAXS measurements were conducted on the DUBBLE beamline (BM26A) of the European Synchrotron Radiation Facility (ESRF) using X-ray photons of 11.850 keV. The 2D SAXS images were recorded in transmission mode using the Mar CCD 165 detector with a pixel size of 80 μm. The modulus of the scattering vector $\mathbf{q} = 4\pi\sin\theta/\lambda$, where θ is the Bragg angle and λ is the wavelength, was calibrated using silver behenate. The sample to detector distance was approximately 2 m, resulting in a q range comprised between 0.016 and 0.4 nm^{-1}.

For the sample measurement, an aliquot of each solution, taken at different reduction time (0, 20, 75, 135, 410 min), was loaded in 1 ml quartz capillary of 1 mm diameter.

The data were corrected for the detector dark field and background scattering from the capillary with polymer and solvent only. The data reduction was performed using Fit2D and 1D curves were fitted using SANS Analysis package for the Igor Pro software [284]. The scattering intensity calculation were performed using the method described in chapter 2.

3.2.3 In situ XAFS

In situ Extended X-ray Absorption Fine Structure (EXAFS) and X-ray Absorption Near Edge Structure (XANES) were measured on the DUBBLE beamline (BM26A)

of the European Synchrotron Radiation Facility (ESRF) using gold L_{III} edge (11.91 keV) in fluorescence mode using a 9-element monolithic Ge detector (Ortec).

An aliquot of each solution, taken at different times during the reduction process (5 and 150 min), was loaded in 1 ml quartz capillary and mounted on the sample holder. In order to verify the stability of the system after toluene has been evaporated, a 1 ml capillary was filled with the sample B-HCl and left to dry at 120 °C for 2 h. In order to observe the stability of the micelles a solution loaded capillary has been put into an oven and set at 70 °C in order to allow toluene to evaporate. The micelles deposited on the surface of the capillary were analysed using XAFS. The sample holder was mounted at 45 ° with respect to the incident beam in order to maximize the fluorescence yield.

EXAFS analysis was performed on samples listed in Table 3.3.1. The FEFF6 code was used to construct theoretical EXAFS signals that included single-scattering contributions from atomic shells through the nearest neighbours in the chlorine-bridged dimer, as well as the face-centered cubic (FCC) structure of Au. The *k*-range used for the fitting 2.5 to 10.3 $Å^{-1}$ and the *r*-range from 1 to 3.7 Å. The path degeneracy was allowed to vary in order to account the size effects that cause surface atoms to be less coordinated than those in the particle interior. The amplitude reduction factor (S_0^2) was fixed at 0.860, as obtained from the fitting of the bulk Au foil.

3.2.4 TEM

Transmission Electron Microscopy (TEM) was measured using JEOL: JEM-2100 operating at 200 KeV using a LaB_6 filament, after deposition through drop-casting on a film supported by a 300 mesh copper TEM grid. Sample A and B solutions before and after the addition of $HAuCl_4$ and after the reduction treatment were analysed. In the case of Sample A the small scattering contrast compared to the carbon paired with the smaller size of the polymer made impossible to obtain information regarding the state of the micelles before the addition of the Au precursor.

3.2.5 UV-Vis spectroscopy

UV-Vis spectroscopy measurements were obtained using the methods described in 2.2.2.1.

3.2.6 DLS

Dynamic light scattering (DLS) measurements were performed on samples reduced over different times using Zetasizer nano ZS from Malvern. The incident laser wavelength used in the setup was 532 nm and the refractive index was derived from polystyrene (η=1.5). Micelles containing solutions were loaded into a cuvette with 5 mm pathlength. Three scan per point, each with the duration of 3 min, was taken in order to average the results.

3.3 Result and Discussion

3.3.1 DLS

With the help of DLS one can observe how the micellar system in its entirety responds during the reduction of metal ions through the impact this has on the micelles' hydrodynamic radius.

DLS plots for the sample A during reduction are exemplarily shown in Figure 3.3.1. The average radius of micelles is 32 ± 6 nm (Figure 3.3.1a) and it increases to 36 ± 4 nm after addition of the reducing agent (Figure 3.3.1b). As can be seen on Figure 3.3.1c-d the swelling of the metal-containing polymer particles continues and results in doubling of the average micelle size, to 55 ± 3. A similar effect is observed in sample A-HCL when HCl is added during the reduction process (Figure 3.3.2), where the micelles radius increases, from 32 to 55 nm, with the reduction time.

DLS plots for sample B and B-HCl, shown in figure 3.3.3-4, show a proportional increase during the reduction process, as the average radius of the micelles increases from 90 ± 15 nm (figure 3.3.3 a) to 146 ± 9 nm (figure 3.3.3d) and 150 ± 12 nm (figure 3.3.4d) for sample B and sample B-HCl respectively.

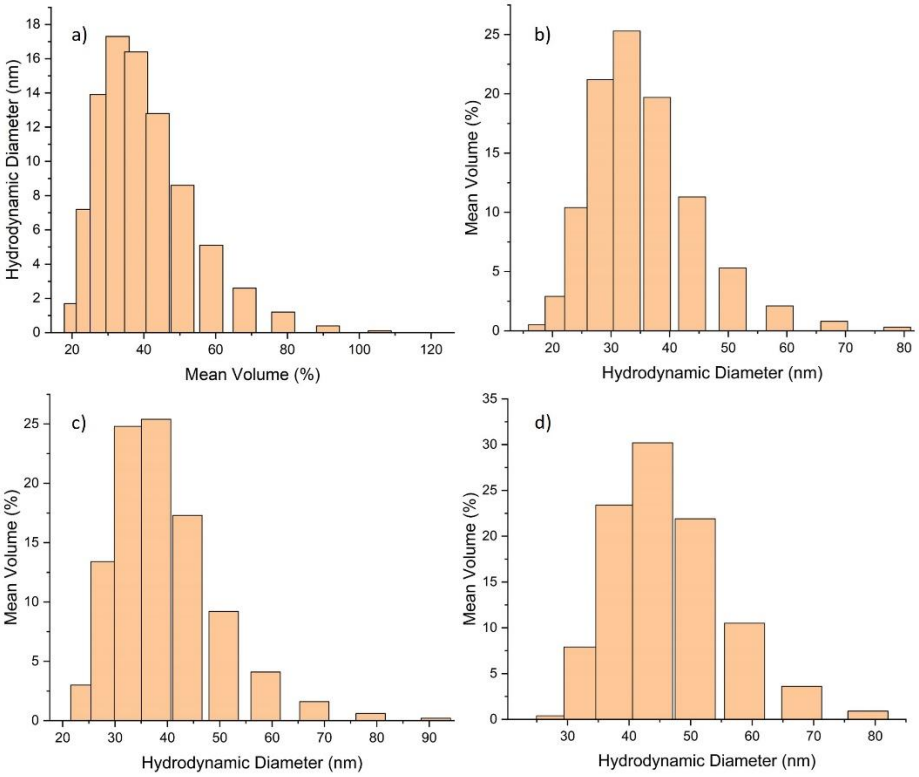

Figure 3.3.1. DLS plots of sample A before reduction (a) and after 10 min (b), 1h (c) and 1 day (d) of the reduction process. The average size of the polymer micelle increases from ~30 to ~55 nm after the reduction.

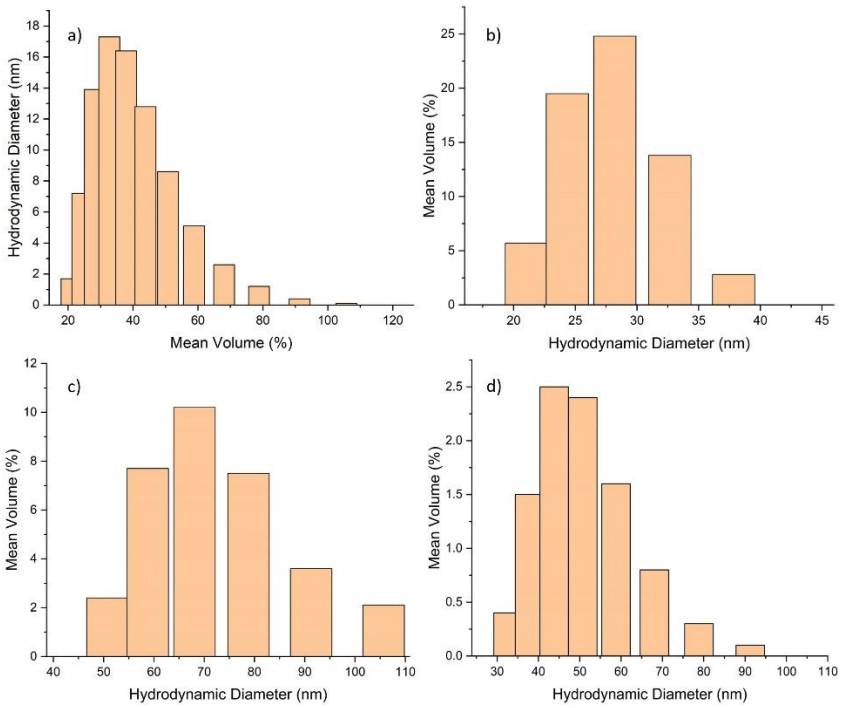

Figure 3.3.2. DLS plots of sample A-HCl before reduction (a) after 10 min (b), 1h (c) and 1 day (d) of the reduction process. The average size of the polymer micelle increases from ~30 to ~55 nm after the reduction. After 1h the presence of very large particles, ~1µm, was observed and they were cut off from the graph due to the lack of relevance.

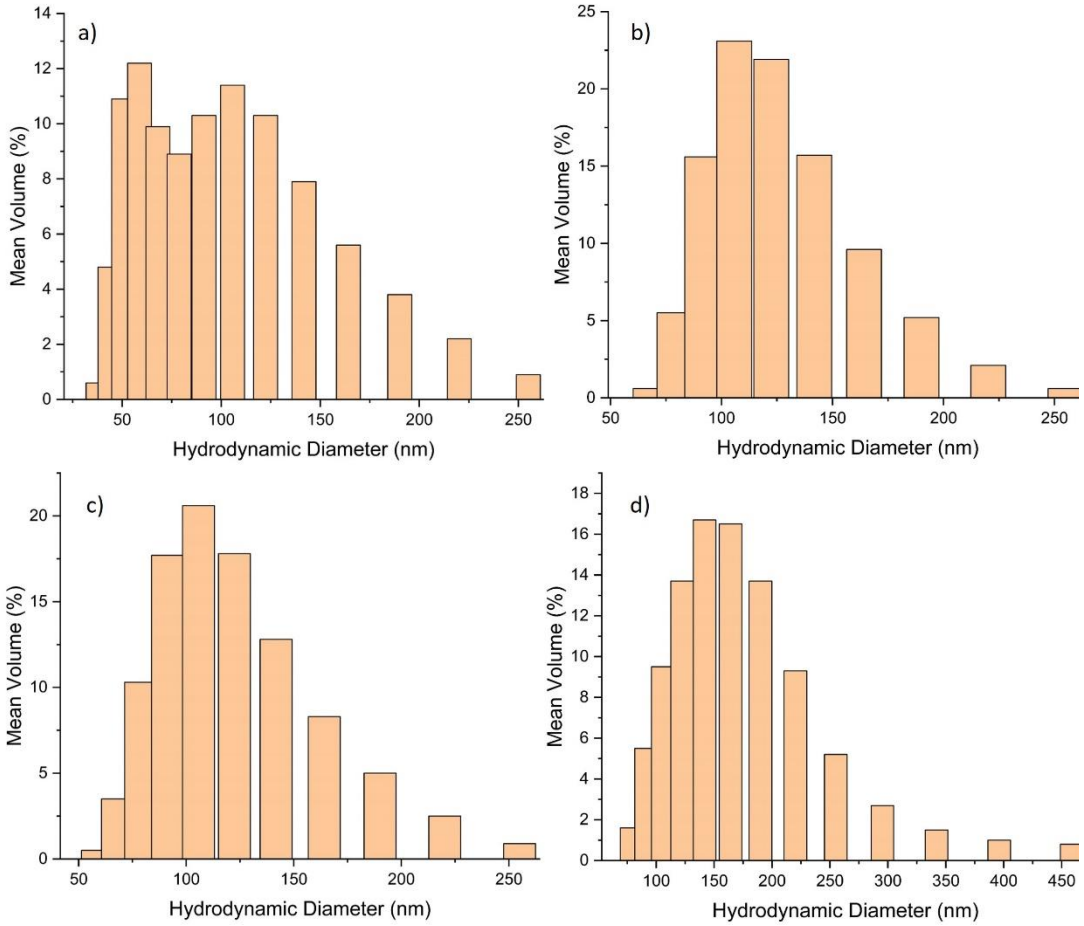

Figure 3.3.3. DLS plots of sample B before reduction (a) and after 10 min (b), 1h (c) and 1 day (d) of the reduction process. The average size of the polymer micelle increases from ~100 to ~150 nm after the reduction.

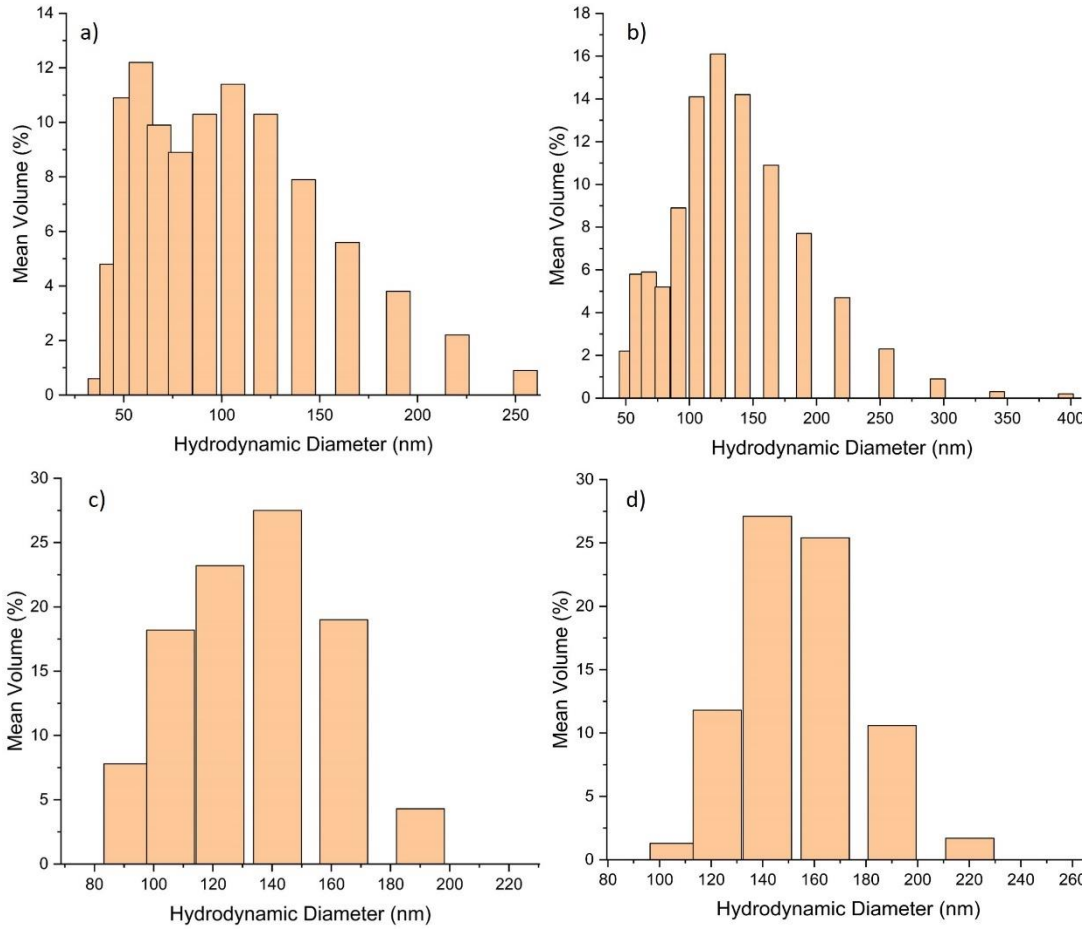

Figure 3.3.4. DLS plots of sample B-HCl before reduction (a) and after 10 min (b), 1h (c) and 1 day (d) of the reduction process. The average size of the polymer micelle increases from ~100 to ~150 nm after the reduction

We suggest that the observed increase of the micelle size is due to the distortion of the P2VP backbone chain during the reduction of the metal salt. Considering the reduction reaction of $[AuCl_4]^-$ with H_2, produced by the P-tosyl hydrazide decomposition, to Au(I) that reads as follows

$$H[AuCl_4] + H_2 \rightarrow AuCl + 3HCl \qquad \text{Eq. 3.4}$$

and the reduction of Au(I) to form metallic Au

$$2\,AuCl + H_2 \rightarrow 2Au + 2\,HCl \qquad \text{Eq. 3.5}$$

which can be recap as follows

$$2H[AuCl_4] + 3\,H_2 \rightarrow 2\,Au^0 + 8\,HCl \qquad \text{Eq. 3.6}$$

With HCl staying in the core of micelles due to its hydrophilic nature. There is a large increase in moles (from 5 of the reagents to 8 of the products) which can contribute to the increase volume from within micelles size. Furthermore, this may provide a strong entropic driving force for the formation of Au^0 species and its further agglomeration in nanoparticles.

The technique was employed in the past to probe similar systems including copolymer- and surfactant-based reverse micelles [308]–[310], colloidal gold and polystyrene nanoparticles [311], [312], and even reverse micelles filled with Au nanoparticles [247], [313]. The most relevant study is a piece of work from Mössmer *et al* [313] where, using a PS-P2VP of similar blocks length to the one here employed, a radius of 28 nm for the micelles filled with $H[AuCl_4]$ was observed, similar to the one here reported, and 30 nm for the Au nanoparticles filled one, compared to the 55 nm radius obtained for sample A at the end of the reduction process. This discrepancy could be due to the different reductant used, hydrazine for reported result and the much bulkier P-tosyl hydrazide for sample A, which should cause a larger steric strain of the micelles. However, no information was given for the intermediate phase of the reduction process whereas here it appears that the swelling of the micelles is not an instantaneous process but evolves gradually as the reduction process is taking place. This swelling process, which as aforementioned can be related to the growth of the nanoparticles inside the micelles, has, to the best of our knowledge, never been reported.

Note that DLS is only capable of measuring the total diameter of the core-shell polymer micelle, consisting of PS core and P2VP shell based on the miscibility of copolymer blocks, and does not allow for probing the local structural changes concerning the atoms of interest [313]. Therefore, the combination of microscopic and spectroscopic methods have also been employed to obtain information regarding the local environment of the gold loaded P2VP core and the role of HCl in the reduction process.

3.3.2 TEM

TEM has been used to characterize the morphology (e.g. shape and size) of the polymer micelles during Au NP synthesis and to identify the location of Au species inside the micelles. Figure 3.3.5a shows the micelles formed by dissolving the PS-*b*-P2VP polymer in toluene above the critical micelle concentration (CMC) [247].

Spherical polymer micelles form a close-packed hexagonal array where P2VP cores are embedded in the PS matrix. As a result of the low Z-contrast it was not possible to obtain an accurate measure of the micelles' core size. Due to the smaller P2VP chain, and therefore smaller P2VP core, it was not possible to obtain any information on sample A. However, for sample B, with a much denser P2VP core, it was possible to determine the core size distribution plot of the micelles without metal, which, as shown in the TEM image corresponds to the size of ~15 nm (Figure 3.3.5a).

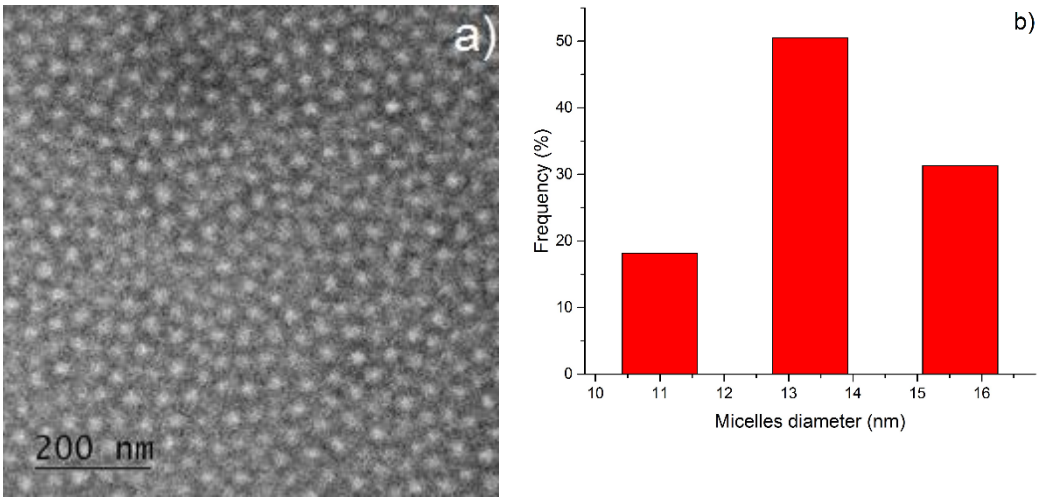

Figure 3.3.5. a) TEM micrograph of sample B without $HAuCl_4$ precursor. The core of the micelles appears as white due the lower contrast compared to the outer shell. b) particle size distribution Average core size 15 ± 2 nm.

Figure 3.3.6-7 show the PS-*b*-P2VP micelles loaded initially only with $HAuCl_4$. It can be seen that the metal ions are preferentially located in the micelle cores, in particular, in the case of sample B with larger amount of the gold precursor providing a clear Z-contrast (figure 3.3.6). For sample A, the gold appears as sub-nanometre clusters

inside the core of the micelle (figure 3.3.6b). Similar clusters have been reported previously and could be accounted for the reduction of $HAuCl_4$ in the electron beam [313]. This does not appear to be present in the case of sample B due to both dense packing of Au clusters and more protection from the larger polystyrene shell in comparison to sample A. TEM data shows that the cores become more separated as the PS block length increases and the micelles' core size depends also on the P2VP block length, with sample A and B possessing a core size of ~11 nm (Figure 3.3.6) and ~22 nm (Figure 3.3.7), respectively. An effect of gold precursor on the micelle's core size can be clearly seen for sample B, where spherical P2VP core increases from ~15 to ~22 nm, possibly due the steric strain caused by the formation of a complex between the protonated pyridine moieties of the P2VP core and $[AuCl_4]^-$ ions.

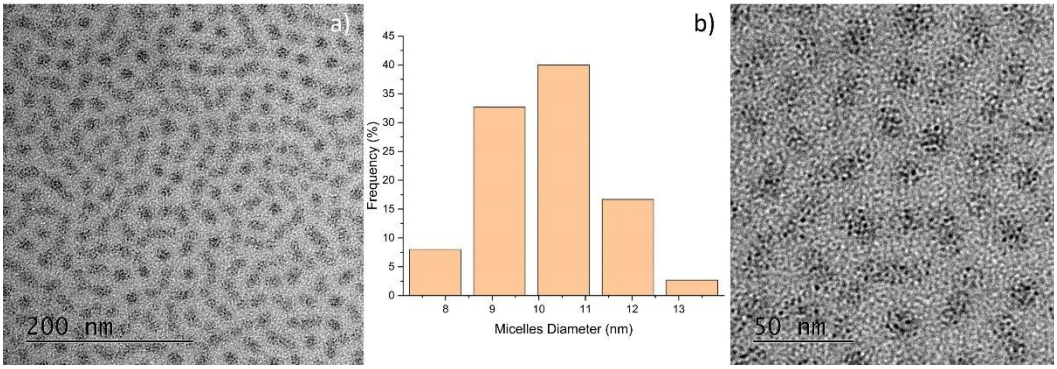

Figure 3.3.6. a) TEM micrograph of sample A loaded with $HAuCl_4$; b) an enlargement. Average micelle core size is 11 ± 1 nm.

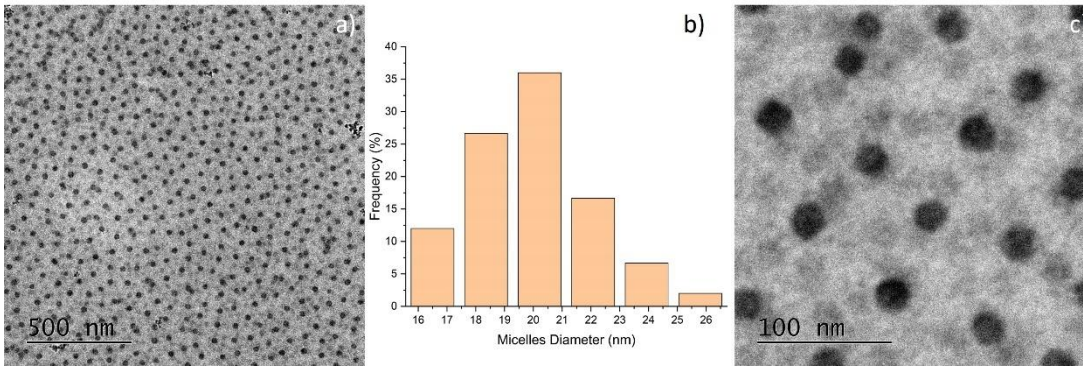

Figure 3.3.7. a) TEM micrographs of sample B loaded with $HAuCl_4$; b) an enlargement. Average micelle core size is 21 ± 2 nm

After P-tosyl hydrazide is added to the micelles-containing solution, reduction of Au ions occurs and leads to the formation of nanoparticles, as shown in Figure 3.3.8 for the reduced sample A-HCl after 24 h. The particle size calculated from the TEM data is 4.5 ± 0.8 nm. Considering that during TEM analysis the micelles are removed from the solution containing reducing agent, it does not allow to determine the exact time to complete the reduction process that is one of the purposes of this study. Furthermore, the possible Au species which have yet to be reduced could suffer from beam damage, thus causing the enlargement of the particle size obtained by TEM. However, it is not possible to correlate DLS measurements, which take in account the whole micelle, with the TEM data, which only show the Au containing P2VP core. The use of spectroscopic techniques is then required in order to really ascertain the behaviour of Au species in solutions.

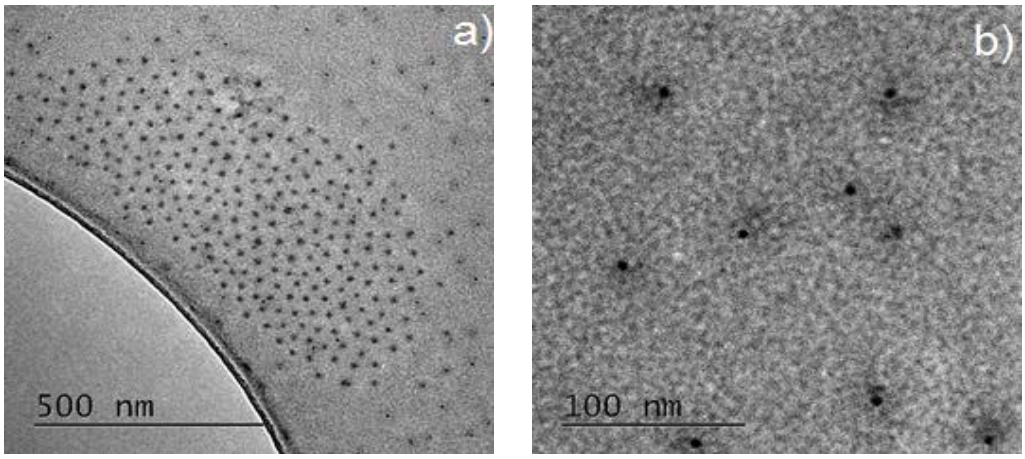

Figure 3.3.8. a) TEM micrographs of sample A-HCl after reduction process; b) an enlargement.

3.3.3 UV-Vis

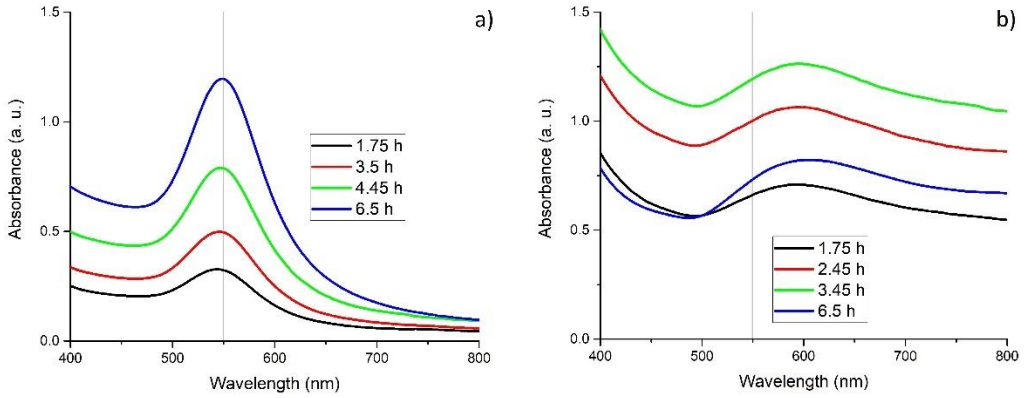

Figure 3.3.9. UV-Vis spectra of: a) samples A and b) A-HCl during reduction. The grey line, used an eye guide, represents the common position for the plasmon peak.

UV-vis spectroscopy was employed to follow Au species evolution in solution during the reduction process. The UV-vis spectra shown in Figure 3.3.9 contains a plasmon peak at 550 nm characteristic of Au^0 clusters of around 2 nm, formed by the reduction of $HAuCl_4$ [268]. The increase in intensity with time suggests continuous reduction and formation of Au NPs; interestingly the band does not change position suggesting a continue increase in the amount of Au nanoparticles present in solution without any dramatic change in size. In the case of sample A-HCl the red shift of the plasmon peak from 550 to 600 nm could be explained by nanoparticle aggregation which could also be observed in the DLS where the presence of large aggregate (> 1μ) was observed, possibly caused by the presence of "water pockets" caused by the addition of HCl, or by he unlike possibility of particles larger than the micelles themselves (>> 100 nm) or else anisotropic particles [177]. This makes difficult to obtain size from the λ max due to the interference of the nanoparticles aggregation. It was not possible to record the UV-Vis spectra after 1 day of reduction since the micelles containing reduced Au NPs were observed to precipitate as can be seen in Figure S3.3.5.

3.3.4 XAFS

XAFS was used to determine further mechanism of the Au reduction and aggregation in the gold clusters. In figure 3.3.10 are shown XANES, EXAFS and the EXAFS Fourier transform. The results of the EXAFS fit for all four samples after 5 and 150 min of the reduction process are summarised in Table 3.3.1. Figure 3.3.11-12 contains the XANES spectra and EXAFS Fourier Transforms (FTs) for sample A and B. A reference $AuCl_3$ solution which contains a strong white line at 11.920 keV is also shown, related to the electronic transition from 2p to unoccupied 5d orbitals [314]. After the reductant is added there is a drop in the intensity in the white line (reduced transition probability) as a consequence of increased filling of the Au 5d orbitals. This change is observed in conjunction with a slight shift of the edge position towards higher energies (from 11.197 to 11.199 keV). Both changes are consistent with reduction of Au (III) to Au (I) [315]. However, no further changes were observed with increasing reduction time suggesting the Au(I) species formed are stable (Figure 3.3.9a-b). The EXAFS data for samples A and B in Figure 3.3.11b and Figure 3.3.12b are clearly different to that of the reference compounds but do possess a peak at ~ 2.24 Å which can be assigned to a Au-Cl scattering contribution, although the reduced amplitude (when compared with $AuCl_4$ in solution) suggests the presence of Au(I)Cl

species (see Eq (3.4)). These values (and FTs) are similar to those observed previously by Salama et al [316] in Na-Y zeolites and are consistent with the formation of a linear $AuCl_2$ species. Au(I) species in the form of a Au_2Cl_2 closed square dimer configuration previously reported by Hargittai et al. [317] can be ruled out on the basis that the Au-Cl distance reported there (2.567 Å) is too long. Interestingly, the Debye-Waller factors obtained for both samples are comparatively low suggesting low static/thermal disorder in the AuCl species. No sign of any metallic Au NPs were observed after 150 min of reaction (see Figure 3.3.11b and Figure 3.3.12b).

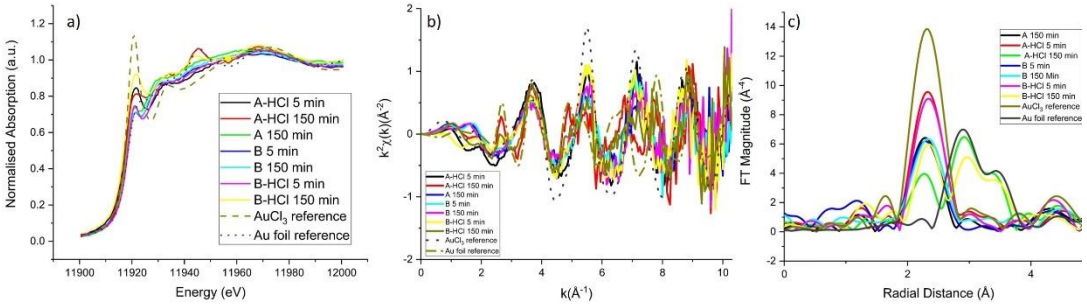

Figure 3.3.10. XAFS spectra of all samples including $AuCl_3$ and Au^0 reference; a) XANES spectra; b) EXAFS k-range data; c) EXAFS Fourier transform

Table 3.3.1. EXAFS fit results for Au species. CN is the coordination number, R the radial distance and σ^2 the Debye-Waller factor

Sample	Reduction time	CN_{Au-Cl}	R_{Au-Cl} (Å)	σ^2_{Au-Cl} ($Å^{-2}$)	CN_{Au-Au}	R_{Au-Au} (Å)	σ^2_{Au-Cl} ($Å^{-2}$)	ΔE	R_{factor}	Particle size
Au foil	-	-	-	-	12 ± 0.5	2.86 ± 0.002	0.008 ± 0.0002	4.3 ± 0.3	0.014	Bulk
$AuCl_4$ in solution	-	4.3 ± 0.2	2.28 ± 0.003	0.002 ± 0.0003				4.3 ± 0.3	0.007	-
A	150 min	2.0 ± 0.2	2.248 ± 0.008	0.003 ± 0.0012	-	-	-	7 ± 1	0.02	-
A-HCl	5 min	2.9 ± 0.4	2.266 ± 0.009	0.0025 ± 0.0013	-	-	-	8 ± 1	0.03	-
A-HCl	150 min	0.7 ± 0.4	2.25 ± 0.02	0.0027 ± 0.0018	8 ± 2	2.86 ± 0.01	0.007 ± 0.002	7 ± 1	0.05	1.5
B	5 min	1.9 ± 0.3	2.24 ± 0.02	0.002 ± 0.0033	-	-	-	6 ± 2	0.02	-
B	150 min	2.05 ± 0.5	2.24 ± 0.01	0.0012 ± 0.0022	-	-	-	4 ± 3	0.06	-
B-HCl	5 min	2.5 ± 0.3	2.28 ± 0.09	0.0015 ± 0.0013	-	-	-	8 ± 1	0.02	-
B-HCl	150 min	1.8 ± 0.6	2.21 ± 0.06	0.0034 ± 0.0003	1.7 ± 0.7	2.866 ± 0.02	0.0016 ± 0.004	4 ± 4	0.06	0.4

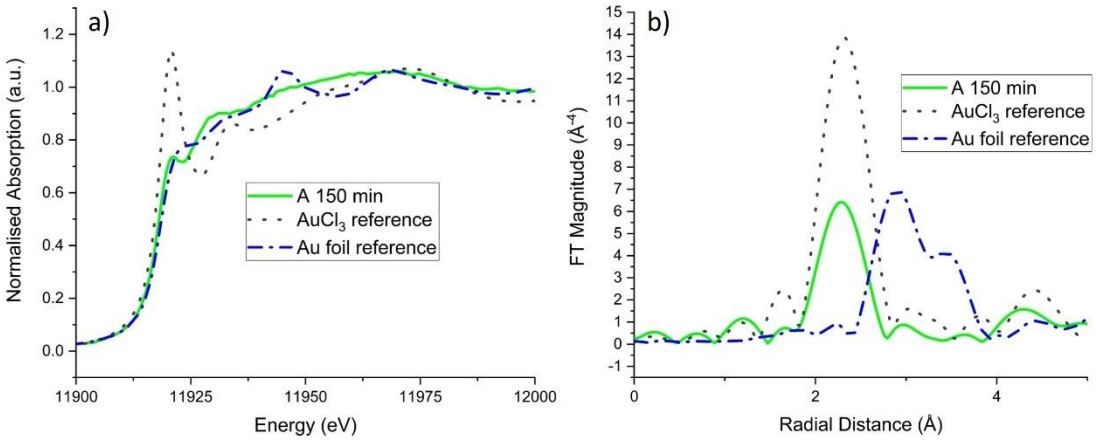

Figure 3.3.11. XAFS spectra of sample A after 150 min of the reduction process; a) XANES spectra including $AuCl_3$ and Au^0 reference ; b) EXAFS Fourier Transform.

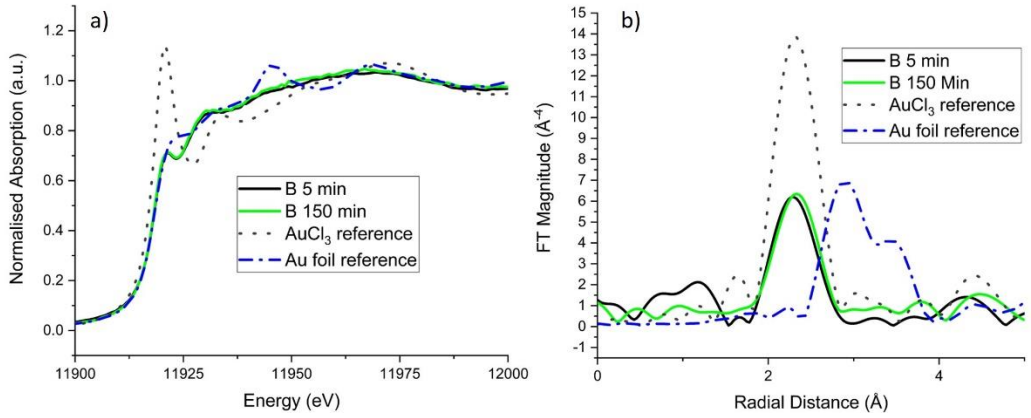

Figure 3.3.12. XAFS spectra of sample B after 5 and 150 min of the reduction process; a) XANES spectra including $AuCl_3$ reference; b) EXAFS Fourier Transform.

For sample A-HCl, the higher Au-Cl coordination number (> 2) after 5 min suggests that initially the reduction process is slightly less advanced in comparison to the non-HCl samples. However, after 150 min the formation Au NPs can be seen by the presence of the Au-Au scattering contribution at 2.86 Å in the second shell of the FT (Figure 3.3.13b). Assuming an isotropic shape, one can estimate the size of the Au NPs from the $CN_{Au\text{-}Au}$ value to be of the order of ~ 1.5nm, similar to the information obtained from UV-Vis [190]. However, reduction is not complete at this stage as a clearly discernible, if low, CN value is obtained for the Au-Cl first shell. XANES spectra also confirm the presence of metallic Au by the increase intensity of the feature located at 11.945 keV which can be attributed to a multiple scattering path of metallic Au [318] (Figure 3.3.13a). However, the higher edge energy and the intense white line

of sample A-HCl compared to Au^0 also suggest that AuCl species are still present after 150 min.

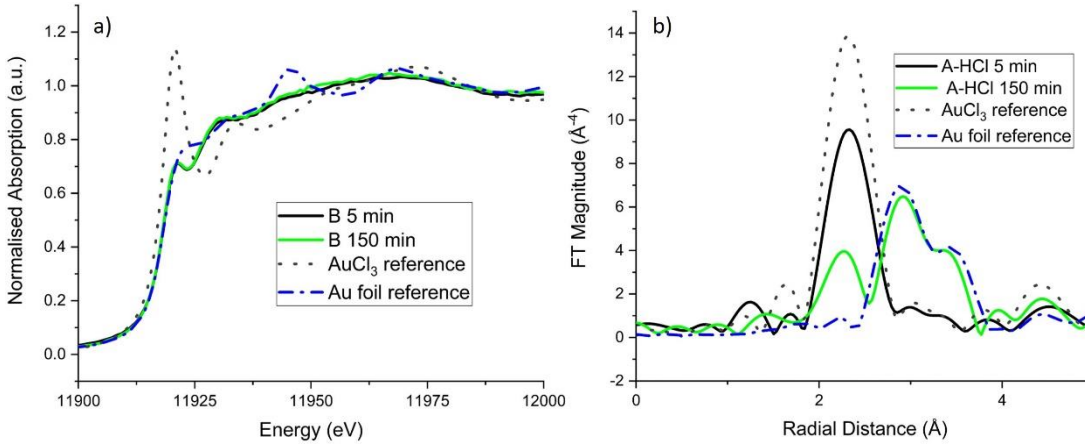

Figure 3.3.13 XAFS spectra of sample A-HCl at 5 and 150 min reduction time; a) XANES spectra including $AuCl_3$ reference; b) EXAFS Fourier Transform.

XAFS data shown in Figure 3.3.14 and Table 3.3.1 for sample B-HCl also appears to contain more unreduced $AuCl_4$ after 5 min similar to A-HCl and in comparison to the non-HCl samples. After 150 min. reduction has occurred although to a lesser extent than in sample A-HCl; this we conclude based on the Au-Cl CN of 1.8 for sample B-HCl and an Au-Au CN contribution of < 2, the latter value of which suggests very small Au clusters have begun to form. Further confirmation of Au reduction can be observed in the XANES (Figure 3.3.14a) however, in contrast to samples without HCl, it appears that, with time, as the reduction process continues the intensity of the white line, at 11.920 keV, increases and the edge position shifts from 11.918 to 11.917 keV. A similar spectra was reported by Salama et al [316] in Na-Y zeolites treated at 353 K and indeed seems consistent with the continued presence of Cl in the coordination shell of the Au species. However, it seems likely that in the B-HCl sample, part of the Au has oxidized back to form $Au(III)Cl_3$ most likely due to water-promoted disproportionation of the AuCl [316].

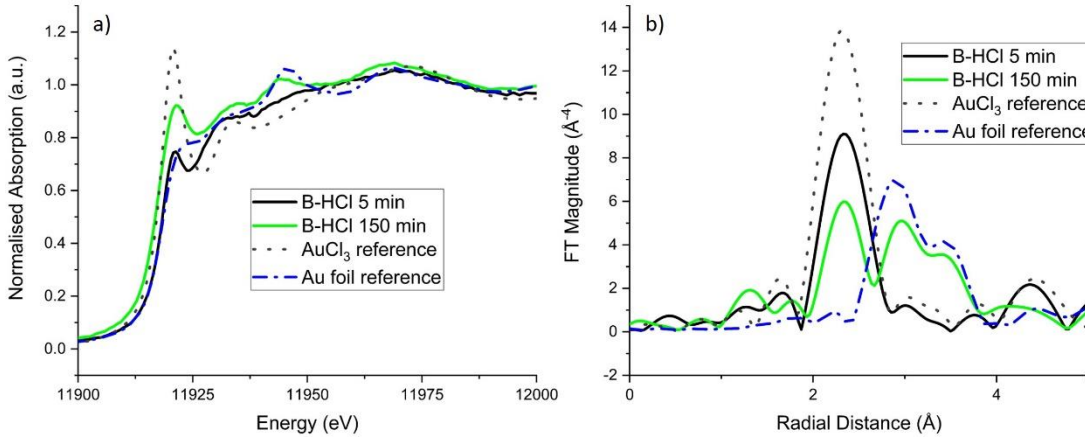

Figure 3.3.14. XAFS spectra of the sample B-HCl at 5 and 150 min reduction time; a) XANES spectra including $AuCl_3$ reference; b) EXAFS Fourier Transform.

3.3.5 SAXS

In order to investigate the structural transformation, in particular in terms of size and polydispersity, of the nanoparticles formed in the micelle's core during the reduction process *in situ* SAXS studies were conducted. 1D SAXS profiles for all the samples during the reduction process is shown in Figure 3.3.15. 1D SAXS profiles for sample A during the reduction process are shown in Figure 3.3.15a. According to the fit (for the details see Experimental section and Figure 3.3.16) there is a slight increase in the scattering component size from 6.8 to 6.9 nm (Figure 3.3.17a and Table 3.3.2) after 400 min of reduction. For sample A-HCl a shift of the scattering component towards smaller q-values can be seen (Figure 3.3.15b) which corresponds to sizes from 7.9 to 8.9 nm depending on reduction time, with 75 min being the time when the size stabilizes (Figure 3.3.17a and Table 3.3.2). The changes observe for sample B during reduction, whereas following same trend as sample A, are more pronounced, as can be seen from Figure 3.3.15c, apart from an abrupt increase in size from 14.3 to 20.5 nm at 400 min of reduction (Figure 3.3.17b and Table 3.3.3). Sample B-HCl shows a similar behaviour to A-HCl, however P2VP cores containing gold species achieve the same size of 20.5 nm after 400 min of reduction with or without the presence of HCl (Figure 3.3.15d; Table 3.3.2).

The *in situ* SAXS fit results summarised in figure 3.3.17 indicate a growth of the NPs of both sizes during the reduction process that is in a good agreement with the DLS data (Figure 3.3.1-4) whereas the difference in size obtained (~ 7 nm SAXS, ~ 30 nm DLS) is due to the PS shell which is not detected by the SAXS due the low electron

density contrast between toluene and polystyrene (see appendix figure S3.3.5). The increase of the P2VP core size, as shown in Figure 3.3.17a-b, from 7 to 9 nm for sample A and from 14 to 21 nm for sample B, when HCl is included into the solution can be attributed to an increment in the speed of NPs' growth. This was also suggested from the XAFS analysis, indicating that HCl acts as a catalyst for the reduction of the Au species.

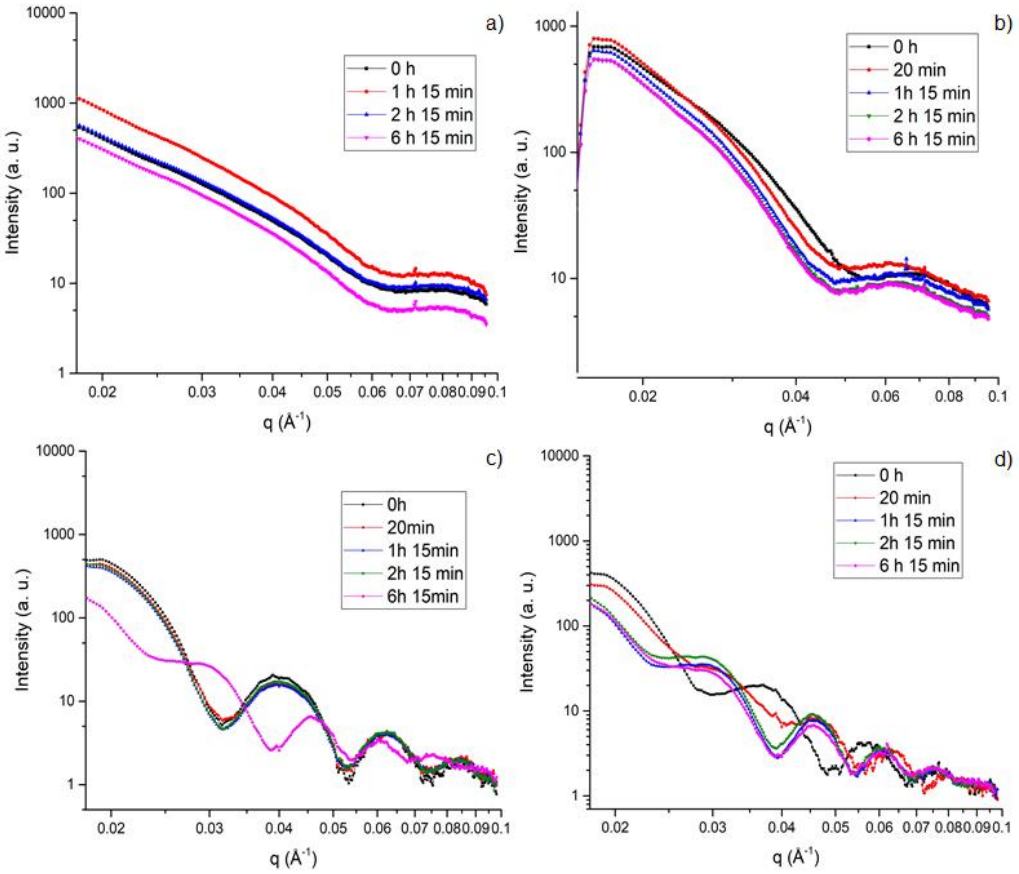

Figure 3.3.15. Structural changes during reduction as followed by *in situ* SAXS. 1D SAXS profiles for the sample A (a), A-HCl (b), B (c) and B-HCl (d).

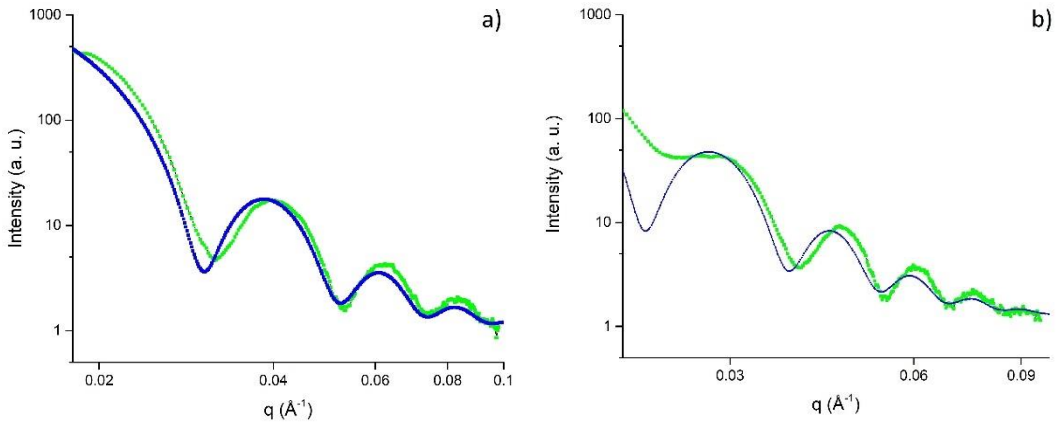

Figure 3.3.16. Examples of the SAXS data fit. 1D SAXS curves and corresponding fitted curves for samples B (a) and B-HCl (b) at 2h15 min.

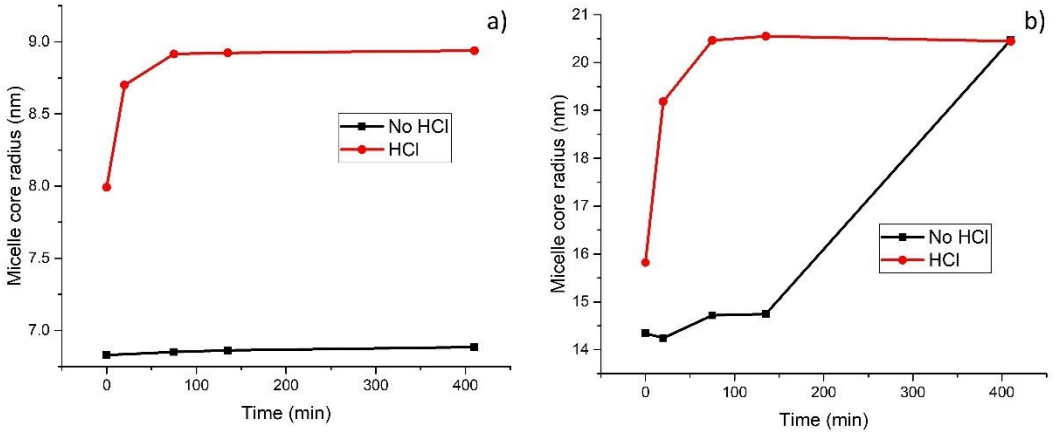

Figure 3.3.17. Evolution of the micelles core radius with time for the samples A and A-HCl (a), B and B-HCl (b).

Table 3.3.2 Summary of the NP size and polydispersity resulting from the SAXS fitting for sample A and A-HCl.

Reduction Time (min)	Micelle core radius sample A (nm)	Micelle core radius sample A-HCl (nm)
0	6.8 ± 0.1	7.9 ± 0.1
20	-	8.7 ± 0.1
75	6.8 ± 0.1	8.9 ± 0.1
135	6.9 ± 0.1	8.9 ± 0.1
400	6.9 ± 0.1	8.9 ± 0.1

Table 3.3.3. Summary of the NP size and polydispersity resulting from the SAXS fitting for sample B and B-HCl.

Reduction Time (min)	Micelle core radius sample B (nm)	Micelle core radius sample B-HCl (nm)
0	14.34 ± 0.05	15.82 ± 0.05
20	14.24 ± 0.06	19.18 ± 0.07
75	14.72 ± 0.05	20.46 ± 0.05
135	14.75 ± 0.05	20.55 ± 0.05
400	20.47 ± 0.04	20.44 ± 0.06

3.4 Discussion

From the results obtained by the combination of time-resolved DLS, UV-Vis, XAFS, SAXS and TEM it was possible to propose a model for the self-assembly of the metal nanoparticles in the reverse micelles system shown in Figure 3.4.1, that can be divided in the three steps:

- an initial fast reduction of $[AuCl_4]^-$ to Au (I) species;

- further slow reduction of the Au (I) and formation of Au clusters;

- agglomeration of the small clusters to form nanoparticle confined inside the core of the micelle.

According to TEM data (Figure 3.3.6-7), the micelle core is loaded with the gold precursor at the beginning of synthesis (stage 1 in Figure 3.4.1). We propose that Au is initially homogeneously dispersed all over the micelle cores by forming a complex between the nitrogen from pyridine and $[AuCl_4]^-$, in a similar way to that seen for iron and molybdenum precursors [238]. After the reductant is added (stage 2 in Figure 3.4.1) the $[AuCl4]^-$ ions reduce almost immediately to Au(I) species, namely AuCl, as shown by XAFS results (Table 3.3.1). The NP radius obtained by the SAXS fit, ~7 nm for sample A and ~15 nm for sample B (Figure 3.3.15c-d), in addition to the TEM data suggest the size obtained by the SAXS measurement appears to correspond to the size of the micelle core when filled with Au (I) species (Figure 3.4.1). After 150 min (stage 3 in figure 3.4.1) the formation of Au^0 species can be seen for sample A-HCl and B-HCl (Figure 3.3.12b and 3.3.13b), that represent a combination of atoms and small clusters (2-4 atoms) based on CN_{Au-Au} shown in Table 3.3.1. The large increase of the NP radius during the reduction process measured using SAXS, for the samples containing HCl, further confirms the self-assembly of gold clusters into the NPs (Figure 3.3.17). The swelling of the micelle core continues (~75 min) until an equilibrium state is reached.

Due to the time constrains during *in situ* XAFS/SAXS studies, the further agglomeration of the gold cluster to form nanoparticles (stage 4 in figure 3.4.1) was confirmed only with the help of TEM analysis (Figure 3.3.8), showing, that once the reduction process is complete, the formed NPs are positioned at the centre of the micelles. Moreover, time-resolved DLS data allowed us to conclude that the whole

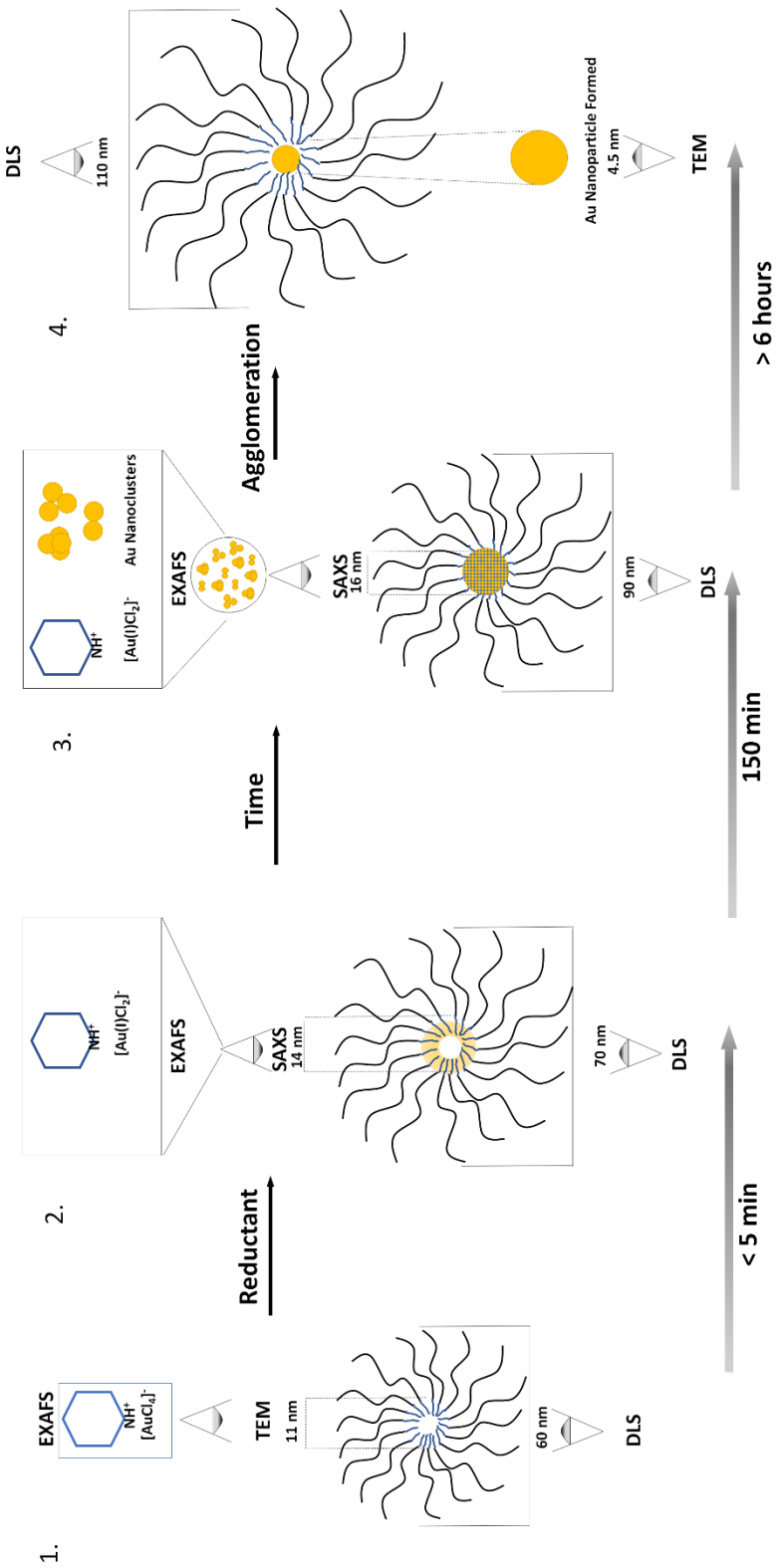

Figure 3.4.1. Proposed schematic for the formation of Au nanoparticles in the reverse micelles for sample A, stating the techniques used to identify the step properties: 1. The $[AuCl_4]^-$ ions attach to the pyridine group; 2. The $[AuCl_4]^-$ species get reduced to Au (I) species; 3. Au (I) start to agglomerate to form Au nanoclusters 4. The Au nanoparticles are formed inside the micelles. The addition of HCl increase the rate of formation of Au clusters

micelle, and not just its core, is affected during the reduction of the gold precursor to the metal NP (Fig. 3.3.1-2).

The XAFS, UV-Vis and SAXS data suggested that the presence of HCl speed the reduction process of Au (I) to Au^0 and its agglomeration. We rationalise that HCl helps with the *in situ* formation of hydrazine through the following reaction sequence:

$$NH_2 - NH - p - \text{toluensulfonyl} + HCl \leftrightarrow NH_2NH_2 + Cl - p - \text{toluensulfonyl} \quad \text{Eq. 3.7}$$

which will then act as a reducing agent according to the following equations

$$H[AuCl_4] + N_2H_4 \rightarrow N_2 + 6HCl + 2AuCl \quad \text{Eq. 3.8}$$

$$4AuCl + N_2H_4 \rightarrow N_2 + 4HCl + 4\,Au \quad \text{Eq. 3.9}$$

that can be summarised as:

$$4H[AuCl_4] + 3N_2H_4 \rightarrow 4Au + 3N_2 + 16HCl \quad \text{Eq. 3.10}$$

We rationalize that the rate and extent of N_2H_4 production (Eq. 3.7) increases becoming autocatalytic due to the formation of HCl as a by-product of Au reduction (Eq. 3.8-9). Therefore, it is plausible to assume that HCl added at the start accelerates the formation of N_2H_4 and therefore the extent of reduction earlier. This increased N_2H_4 productions seems to lead, in addition to fast Au(I) reduction, to nucleation of Au clusters (see UV-Vis data in Figure 3.3.7 b) although the final Au NPs possess similar characteristics to those obtained from the samples in which no HCl is added. This suggests that the final step, agglomeration, was given sufficient time to occur in both cases (with and without HCl) and that this step is important for realizing uniformity in the particle size. However, this understanding of the self-assembly mechanism and the impact of HCl allows to realise when it is possible to utilize different reaction times/conditions to change the properties of the final nanoparticles i.e. stopping the reaction earlier may allow for realizing 'raspberry type' Au NPs or else to control the incorporation of different species, for example metal ions, to produce either bimetallic nanoclusters/alloys (a second metal precursor is added during nucleation process) or core shell NPs (a second metal is added to the already formed nanoparticle) [190], [319]. This would help to design better and more efficient catalyst for a wider range of reactions.

The low polydispersity values calculated from the SAXS data are consistent with the presence of micelles containing evenly loaded and highly dispersed Au ions attached

as molecular species to the pyridine groups of the P2VP chain. We propose that this interaction is important as it slows the Au reduction and agglomeration process, compared to more commonly used Au NP synthesis procedures such as the Turkevich method [196], [224]. This retardation then seems to realise a more controlled Au NP nucleation and growth process resulting in a much more narrow particle size distribution in comparison (often << 1 nm). This also demonstrates the protective effect of the polymer micelles, preventing undesired coalescence of metal NPs. Our results can be interpreted as being more widely reflective of how Au NP assembly occurs in the presence of species that can coordinate and/or complex with Au species (i.e. block co-polymers, capping agents such as PVP [52], PVA [320] etc.) For example Sakai et al. using block PEO-PPO-PEO co-polymers observed the reduction of $[AuCl_4]^-$ precursor to Au^0, simultaneous formation of Au clusters and finally formation and growth of the nanoparticles [301]. However, since their study did not obtain time-resolved X-ray data, they could not have seen the presence of Au(I) species as intermediates in the formation process. Indeed such Au(I) species are often suspected but rarely seen in Au NP self-assembly.

3.5 Conclusion and future work

The self-assembly of gold nanoparticles prepared using polymer-encapsulated reverse micelles was studied using XAFS and Small Angle X-ray Scattering (SAXS) supported by DLS, UV-Vis spectroscopy and transmission electron microscopy (TEM). The combination of spectroscopic and scattering techniques with the reverse micelle approach allows for detailed insight into the self-assembly process leading to the formation of uniform monodisperse Au NPs. The mechanism comprises three key steps: fast reduction of gold precursor to Au (I) species, slow reduction of Au (I) to Au atoms and their agglomeration in sub nanometric clusters, final coalescence of Au clusters into the nanoparticles. The presence of HCl appears to considerably accelerate the formation of the Au clusters during the second step due to the higher production of in situ hydrazine. Moreover, whereas this mechanism has been explored for the reverse micelle method, it is reasonable to assume that other reaction procedures, which employ polymers as capping agent, follow a similar, if not identical, reaction process. The detailed mechanistic insight will enable to modulate the synthesis process by changing the variables involved in the metal nanoparticles formation, such as time or presence of HCl, thus allowing a better control over NP size and particle

size distribution. Moreover, the high control over the synthesis process allows for modification in the preparation method, such as addition of other species to form bimetallic nanoparticles. Challenges for future studies are an improved resolution for the time-resolved techniques (SAXS, XAFS) paired with an exploration of the various synthesis parameter, such as metal/pyridine ratio or concentration of HCl, to derive kinetic parameters for this important metal NP’s synthesis method.

4 Particle size and support effect on the catalytic properties of Au nanoparticles for 1,3-butadiene hydrogenation

4.1 Aim of the chapter

The main aim of this chapter lies in understanding particle size and support effects for gold nanoparticles when used to catalyse 1,3-butadiene hydrogenation. The nanoparticles were prepared using reverse micelle encapsulation, which provides a method to produce highly homogenous nanoparticles. *In situ* XAFS spectroscopy will be used to characterize the nanoparticles (previously characterized through TEM, UV-vis and ex situ XAFS) in order to identify any modification caused by adsorption and interaction of the reaction gases (H_2, 1,3-butadiene and the mixture of the two during the hydrogenation of 1,3-butadiene to produce butenes).

4.2 Methods

4.2.1 Synthesis

Gold nanoparticles were synthesized by the reverse micelle methods, as previously explained in chapter 2. The polymer used were:

- P4708-S2VP (Polystyrene(PS) = 16000 MW, Poly-2 Vinyl pyridine(P2VP)=3500 MW), polydispersity = 1.05;
- P18226-S2VP (Polystyrene(PS) = 30000 MW, Poly-2 Vinyl pyridine(P2VP) = 8500 MW), polydispersity = 1.06,
- PS5073-S2VP(Polystyrene(PS) = 175000 MW, Poly-2 Vinyl pyridine (P2VP) = 70000 MW, polydispersity = 1.08),

all from Polymer Source Inc, the polymer purity is 100 % for all of them.

The metal salt used was chlorauric acid ($HAuCl_4$) (Aldrich 99.99999 % trace metal basis). The metal atoms to pyridine ratio MS/Pyr (metal loading) was fixed at 0.3 MS/Pyr for all the samples while the reducing agent used was P-toluene sulfonyl hydrazide (P-tosyl hydrazide) (97 % Aldrich). A 0.5 wt % (c = 5 mg/ml) solution (50 ml) was prepared and left it to stir for 3 days in order to let the polymer dissolve and homogenize. After 3 days, metal precursor was added to the solution depending on the polymer used in order to obtain an Au/pyridine ratio 0.3 of (0.052 g for P4708-S2VP, 0.043 g for P18226-S2VP and 0.067 g for PS5073-S2VP) and left it to incorporate

inside the micelles After a further 3 days an aliquot of P-tosyl hydrazide (4-fold the concentration of metal) was dissolved in 50 ml of toluene and added to the solution. After ~3 minutes 500 µl of HCl (ACS reagent 37 %, Fluka) was added and after a further ~ 10 min. the support, in powder form, was also added to the solution. The supports used are listed in table 4.2.1.

Table 4.2.1 List of supports and their properties

Support	**Molecular Formula**	**Surface area**	**Purity**	**Source**
Aluminium oxide	Al_2O_3	100 m^2/g	99.9 % (0.1 % SiO_2)	Alfa Aesar
Silicon (IV) oxide amorphous	SiO_2	85-113 m^2/g	n.a.	Alfa Aesar
Silicon (IV) nitride amorphous	Si_3N_4	103-123 m^2/g	98.5 + %	Alfa Aesar

The solids were mixed with the solution in order to obtain a 1 % metal/support weight and left to stir-dry in air overnight, until all toluene had evaporated. The samples were then calcined at 500 °C, in a static air for 2.5 h in an alumina crucible and subsequently characterized. Shown in table 4.2.2 is a summary of the samples prepared.

Table 4.2.2. List of samples. The samples name is expressed as Au/X Y-Z where X is the support used, Y and Z are the molecular weights of the polymer used in the synthesis (Y = PS, Z = P2VP) divided by 10^3

Sample Name	**Polymer**	**Support**
Au/SiO_2 30-8.5	P18226-S2VP	Silicon oxide (SiO_2)
Au/SiO_2 175-70	PS5073-S2VP	Silicon oxide (SiO_2)
Au/SiO_2 16-3.5	P4708-S2VP	Silicon oxide (SiO_2)
Au/Al_2O_3 175-70	PS5073-S2VP	Aluminium Oxide (Al_2O_3)
Au/Si_3N_4 175-70	PS5073-S2VP	Silicon Nitride (Si_3N_4)

4.2.2 TEM

The various samples have been characterized with transmission electron microscopy (TEM), using a JEOL: JEM-2100 operating at 200 keV with a LaB_6 filament, in order to define the particle size and the particle size distribution. A small amount of sample is dissolved in ethanol and subject to sonication to allow dispersion. Subsequently a few drops of the resulting solution is deposited onto a holey carbon film supported by a 300 mesh copper TEM grid.

4.2.3 XAFS

Ex situ XAFS measurement at B18 beamline at Diamond Light Source using gold L_{III} edge (11.91 keV) using the detector in transmission mode. The samples (300 mg for SiO_2 and Si_3N_4 supported samples, 250 mg for Al_2O_3 supported samples) were pressed in pellet form, in a 1.3 mm pellet press, and then mounted on a sample holder. XAFS spectra were then collected and data processing and analysis was performed using the Athena and Artemis software from the Demeter IFEFIT package.[280], [281]

The 1,3-Butadiene hydrogenation reaction has been followed using X-ray absorption spectroscopy in order to identify any modification happening during the reaction conditions. The measurements were performed on the B18 beamline at Diamond Light Source at the Au L_{III} edge (11.91 keV) using the detector in transmission mode. The catalysts, after being pressed in a form of a pellet, were sieved in fraction of 125/250 μm, loaded into a capillary (ø = 3mm), and mounted on a catalysis testing station, with the capillary connected to gas lines on one side and a residual gas analyser (Mass Spectrometer) on the other [321]. While under helium flow the catalysts were brought to 413 K and subsequently different gas composition (hydrogen (10% in He, BOC), 1,3-butadiene (1% in He, BOC) and a mixture of butadiene and hydrogen (2/98 ratio)) were passed through the catalysts and XAFS spectra were recorded at steady state for 30 min for each gas composition.

The resultant EXAFS data have been used to determine changes in particle structure and metal-support interaction as explained in chapter 2. Due to the high correlation between Deybe-Waller factor (DWF) and First shell coordination number (1CN) (>0.95) fitting where both parameters are allowed to freely refine leads to unphysical values. Therefore, the standard procedure for fitting was slightly modified in order to

obtain significant information from the samples. The spectra were fitted keeping one of the parameter, either DWF or 1CN as a constant determined from a fit of the Au foil at room temperature.

4.2.4 Catalytic testing

The samples in table 4.2.2 were tested for 1,3-Butadiene hydrogenation. The reaction was performed in a flow reactor as shown in chapter 2. The catalysts, in different amount dependent on the density of the material, (550 mg for Au/Al_2O_3 175-70 and Si_3N_4 175-70, 330 mg for Au/SiO_2 175-70 and 30-8.5, 200 mg for Au/SiO_2 16-3.5), in the sieve fraction 250/425 µm, were loaded inside the reactor tube (7 mm diameter quartz tube), and then placed inside a tubular furnace and connected with the gas lines through a Swagelok fitting. The reactions were performed using a space velocity of 7500 h^{-1} ml/g catalyst using a reaction mixture composed of hydrogen (4% in Helium, BOC) and 1,3-butadiene (1% in Helium, BOC) in a percentage ratio of 98/2, with a total flow of 135 ml/min, of which 125 ml/min of H_2 and 10 ml/min of 1,3-Butadiene. The samples were brought to 160 °C from room temperature under hydrogen atmosphere and cooled down to 120 °C. After flowing 1,3-butadiene over the catalyst for 15 minutes, H_2 was injected together with the 1,3-butadiene in the reactor tube. For Au/SiO_2 175-70, Au/SiO_2 30-8.5 and Au/Al_2O_3 175-70 further data were taken as the samples cooled down to room temperature in order to obtain the evolution of activity/selectivity as function of temperature. The activity and selectivity were obtained using mass spectroscopy and gas chromatography and compared after the presence of a steady state (~15 min after injection of H_2). The gas chromatograph response has been calibrated using a mixture of products (0.05 % cis-2-butene, 0.15 % trans-2-butene, 0.1 % n-butane, 0.3 % 1-butene all balanced in He, BOC). The error on the catalytic results is estimated 10% of the value.

4.3 Results

4.3.1 Ex situ characterisation

4.3.1.1 TEM

In Figure 4.3.1-5 are shown the TEM micrographs obtained, paired with the particle size analysis, derived through ImageJ software package [265]. The average particle size was obtained by analysing different figures taken at different position (10 images on average) on the catalyst in order to obtain a more representative view of the catalyst

system. As seen from the figures the particles, identified as darker spots due to the higher atomic weight of Au, appear to be densely packed. This could be due the electrostatic attraction between the nanoparticles which usually causes nanoparticles to agglomerate. This is prevented in the deposition phase on the support by the steric interaction caused by the polymers. Moreover, the particles appear to possess a regular circular shape, which suggests the formation of spherical nanoparticles. Unfortunately, due to high support agglomeration, gold nanoparticle presence could only be determined with confidence on the flatter surfaces. In table 4.3.3 are shown the results of TEM analysis of the samples described in table 4.2.2. The standard deviation obtained by analysis show a particle size distribution lower than << 1 nm, depending on the particle size. Moreover, the three samples prepared using the same polymer type (175-70) appears to possess very similar particle size.

Table 4.3.3. Summary of the size and size distribution of sample obtained by TEM

Sample	Particle Size (nm)
Au on SiO_2 (30-8.5)	1.9 ± 0.3
Au on SiO_2 (16-3.5)	2.1 ± 0.6
Au on SiO_2 (175-70)	2.7 ± 0.5
Au on Si_3N_4 (175-70)	2.7 ± 0.53
Au on Al_2O_3 (175-70)	2.7 ± 0.6

Au/SiO_2 175-70

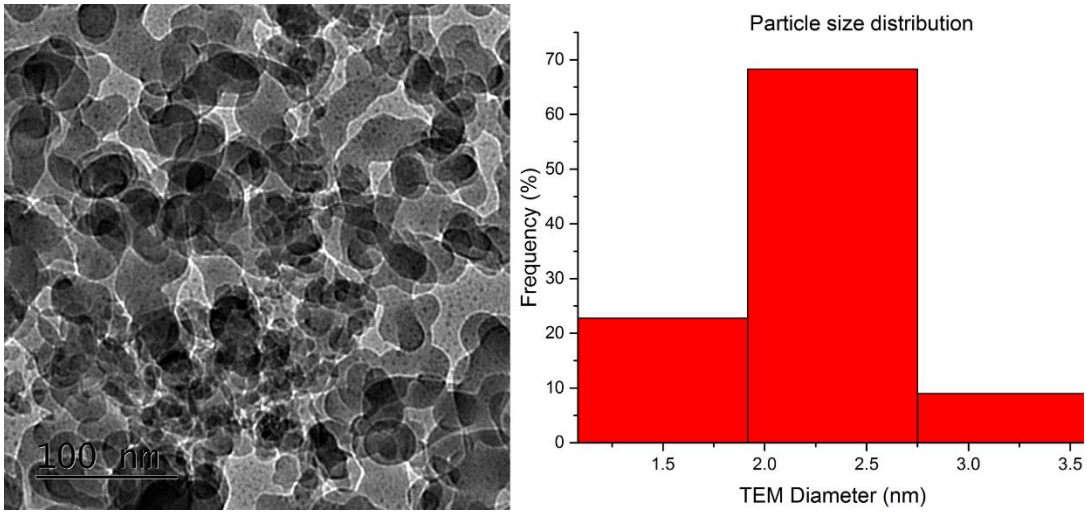

Figure 4.3.1. On the left: TEM micrograph of Au/SiO_2 175-70 samples; on the right: particle size distribution (200 particles counted toward particle size distribution). Average particle size 2.7 ± 0.5 nm

Au/SiO_2 30-8.5

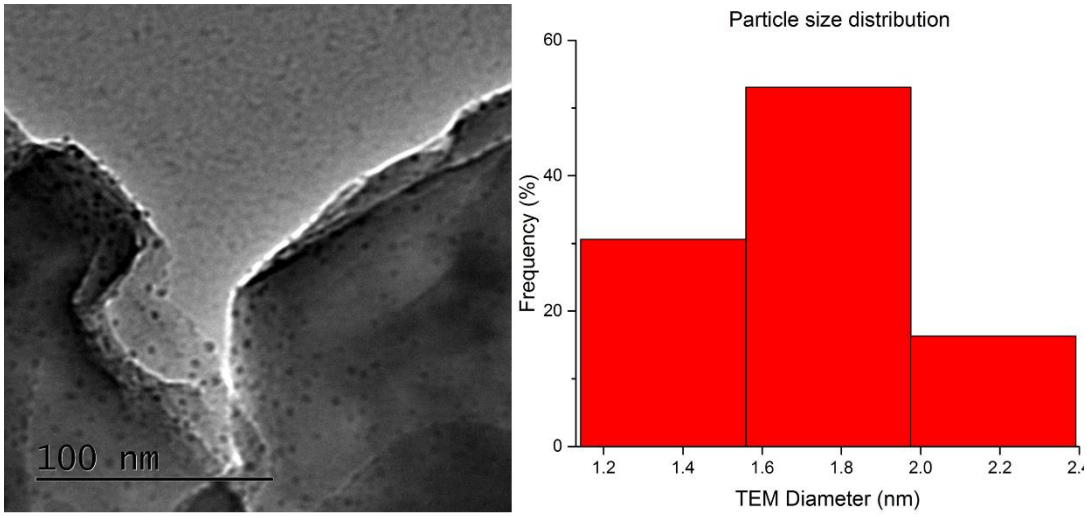

Figure 4.3.2. On the left: TEM micrograph of Au/SiO_2 30-8.5 samples; on the right: particle size distribution (200 particles counted toward particle size distribution). Average particle size 1.9 ± 0.3 nm

Au/SiO_2 16-3.5

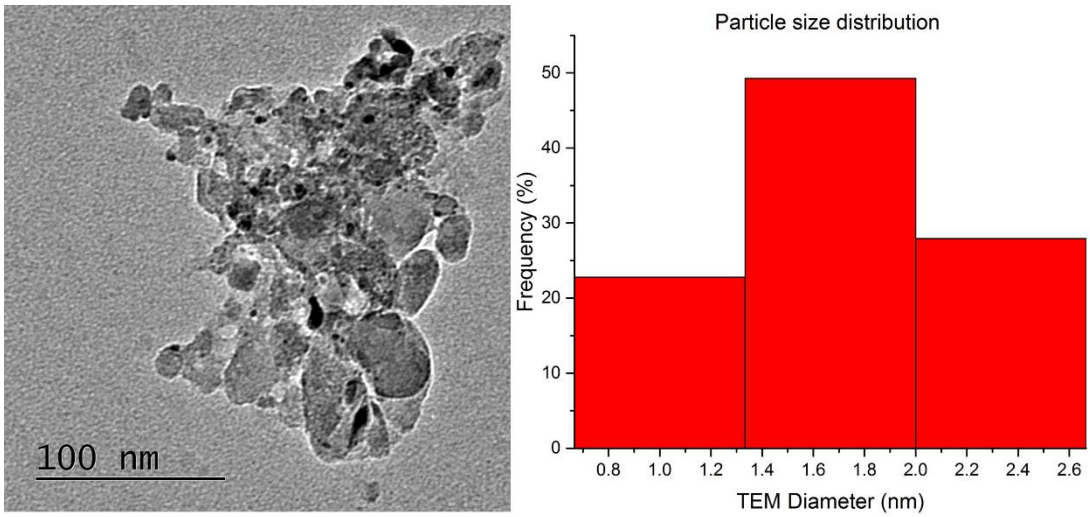

Figure 4.3.3. On the left: TEM micrograph of Au/SiO_2 16-3.5 samples; on the right: particle size distribution (200 particles counted toward particle size distribution). Average particle size 2.1 ± 0.6 nm

Au/Al_2O_3 175-70

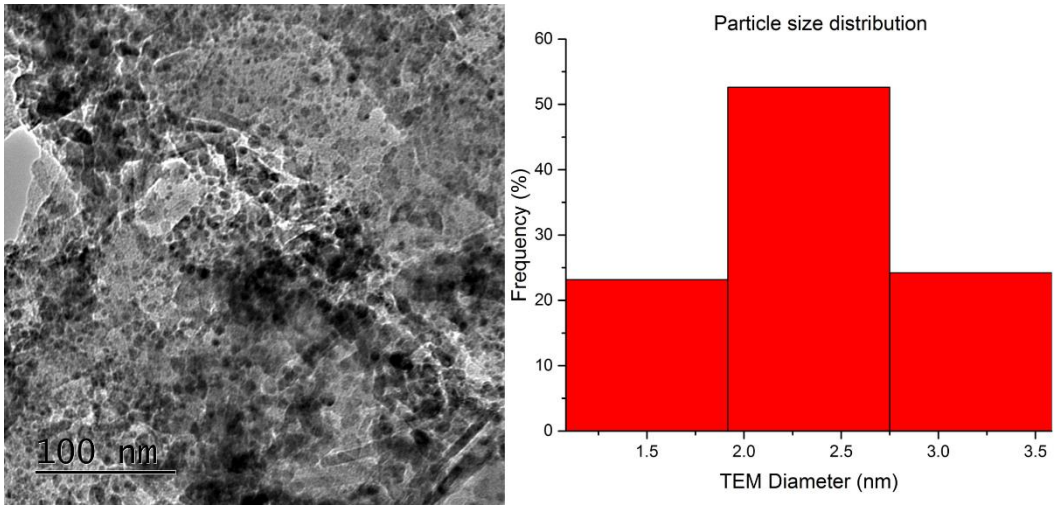

Figure 4.3.4. On the left: TEM micrograph of Au/Al_2O_3 175-70 samples; on the right: particle size distribution (200 particles counted toward particle size distribution). Average particle size 2.7 ± 0.6 nm

Au/Si_3N_4 175-70

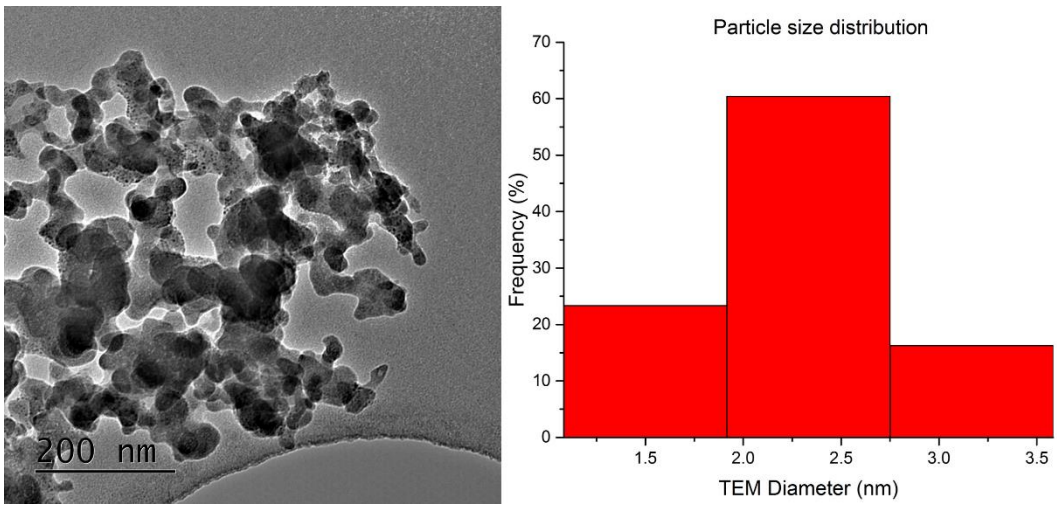

Figure 4.3.5. On the right: TEM micrograph of Au/SiO_2 16-3.5 samples; on the left: particle size distribution (200 particle counted toward particle size distribution). Average particle size 2.7 ± 0.5 nm

4.3.1.2 UV-Vis

One of the properties of gold nanoparticles (AuNPs) is the behaviour of their conduction electrons that gives rise to a plasmon resonance [322]. Shown in figure 4.3.6, are the UV-Vis spectra for the samples listed in table 4.2.2. As can be seen, the centroid position of the plasmon peak appears for all the samples close to 520 nm, indicating the presence of nanoparticles below 5 nm [268]. The position and the intensity of the peak does not only depend on the particle size but also in the media surrounding the nanoparticles, in this case the supports [65]. As it can be seen from figure 4.3.7 the intensity of the plasmon peak drops as the particle size gets smaller due to limited interaction of the photons with the Au nanoparticles electronic clouds [323].

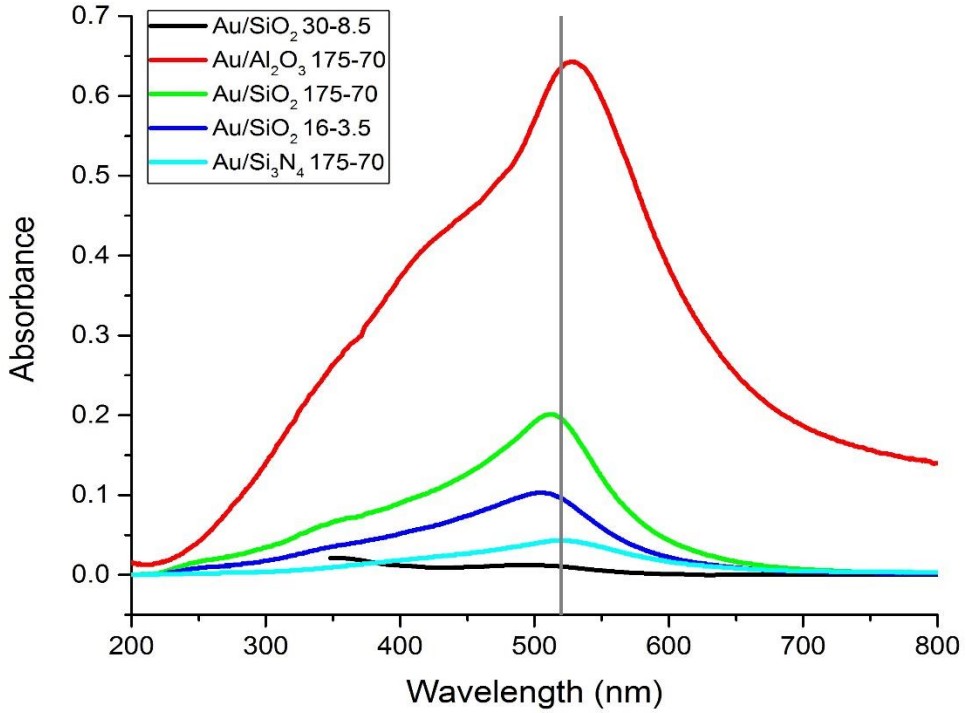

Figure 4.3.6. UV-Vis spectra of Au nanoparticles on various supports. The intensity and the position varies depending on the particle size and the surrounding media. The position of this plasmon peak around 520 nm (grey line), suggests the particle size of the AuNP to be smaller than 5 nm

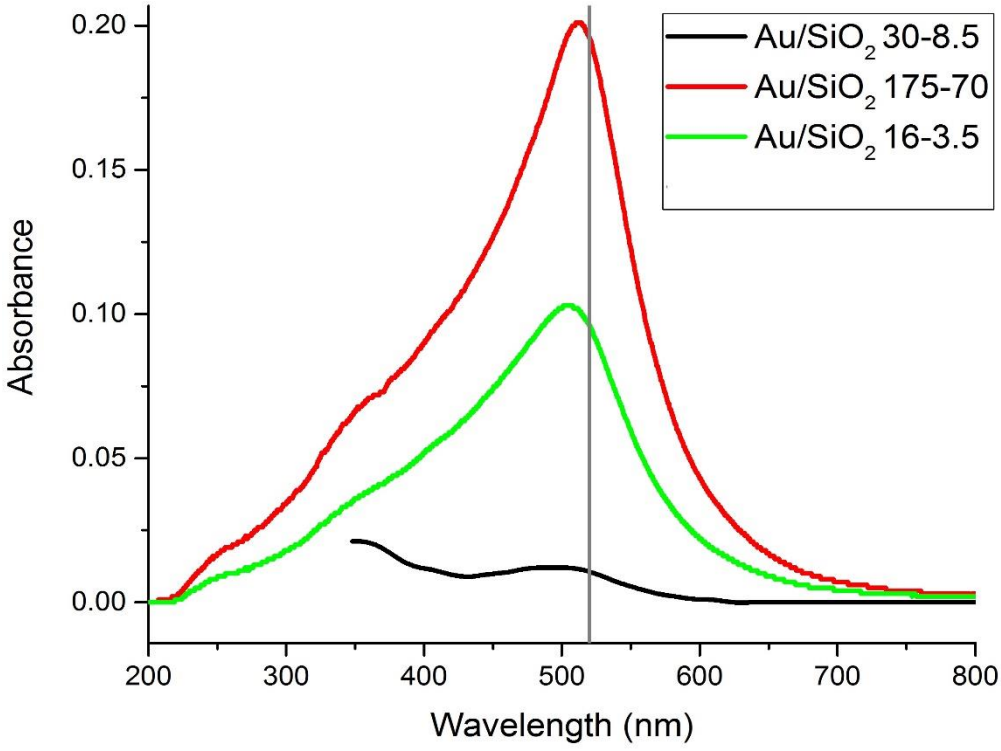

Figure 4.3.7. UV-Vis spectra of SiO_2 supported nanoparticles

4.3.1.3 EXAFS

In table 4.3.4 are shown the results obtained by analysis of the EXAFS data via least squares analysis. In figure 4.3.6 are shown XANES, EXAFS and the EXAFS Fourier transform for all the samples in table 4.3.4. The FT plots of the EXAFS show the presence of a peak at ~2.9 Å which can be ascribed to a metallic Au-Au scattering pair. According to Beale et al. [190] the intensity of the 1CN can be used to estimate particle size assuming a sphere. Moreover, it can be seen that for all the samples the radial distance for the 1st shell is smaller than the one present in bulk Au (2.884), which is consistent with the previously reported results indicating the contraction of Au-Au as the nanoparticles become smaller [69]. In addition, we include a comparative particle size determination previously obtained by TEM. It appears that there is good correspondence between the particle size determined from EXAFS and the TEM measurement (within the experimental error), although as the nanoparticles become larger the mismatch becomes greater. We note however that we did not observe any larger Au species in any of the samples and as such we ascribe any mismatch to error in the accurate determination of particle size which would be particularly exacerbated by any deviation from the assumed isotropic shape. Other fits to the data can be seen in figure SI 4.3.1-4.

Table 4.3.4. EXAFS fit results for supported gold nanoparticles and comparison with TEM results

Sample	1st shell CN	1st shell radius (Å)	σ^2 (Å^{-2})	R_{factor}	ΔE	Particle Size EXAFS (nm)	Particle Size TEM (nm)
Au on SiO_2 (30-8.5)	9.97± 0.9	2.847 ± 0.007	0.0079 ± 0.0005	0.06446	3 ± 2	1.9 ± 0.2	1.9 ± 0.3
Au on SiO_2 (16-3.5)	10.22 ± 0.93	2.852 ± 0.007	0.0081 ± 0.0006	0.108564	4 ± 2	2.6 ± 0.2	2.2 ± 0.6
Au on SiO_2 (175-70)	10.59 ± 1.88	2.84 ± 0.01	0.0082 ± 0.0005	0.3037	2. ± 3	2.9 ± 0.5	2.7 ± 0.5
Au on Si_3N_4 (175-70)	11.032 ± 2.39	2.859 ± 0.008	0.008 ± 0.0009	0.1218	4 ± 2	3.3 ± 0.1	2.7 ± 0.5
Au on Al_2O_3 (175-70)	10.71 ± 2.13	2.861 ± 0.007	0.0078 ± 0.0008	0.09702	5 ± 2	3 ± 0.1	2.7 ± 0.6

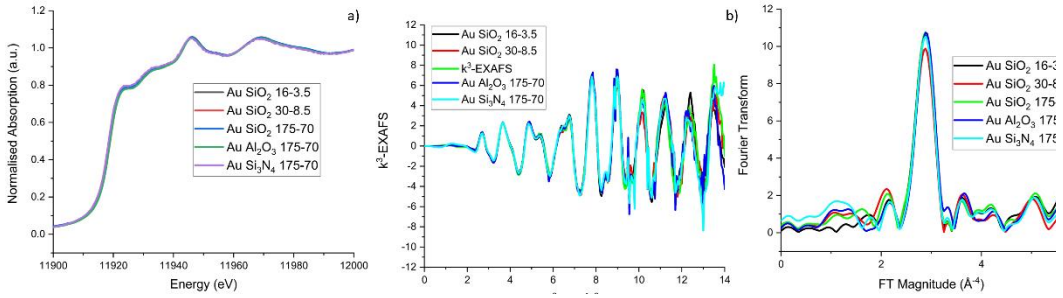

Figure 4.3.6. XAFS spectra of all samples ; a) XANES spectra; b) EXAFS k-range data; c) EXAFS Fourier transform

4.3.2 Catalytic test results

4.3.2.1 Particle size and support effect

As seen in figure 4.3.7, the support plays an important role in the activity and the selectivity of the catalysts. The most active catalyst after 15 min of reaction at 120 °C in this comparison, summarized in table 4.3.5, is the SiO_2 supported one, with a conversion of 94.9 %; however, the presence of a significant amount of n-butane (~15 %) lowers the yield of butenes to 76.4 %. The Al_2O_3 supported sample is the second most active catalyst, but it possesses a lower activity, at 42.43 % conversion, with no presence of n-butane as a product. The least catalytically active sample is Au/Si_3N_4 175-70, with a total conversion of 15.5 % and a yield (due presence of n-butane produced) of 13.1 %.

Table 4.3.5. Catalytic activity/selectivity comparison at 120 °C between samples with similar Au particle size, 2.7 nm, but different support, SiO_2, Si_3N_4 and Al_2O_3 after 15 min of time. The error for each measurement is 10% of the measurement.

Sample	Conversion (%)	N-Butane selectivity (%)	Trans-2-Butene selectivity (%)	1-Butene selectivity (%)	Cis-2-Butene selectivity (%)	Yield (%)
Au/Si_3N_4 175-70	15.4	15.4	2.1	47	36.4	84.7
Au/Al_2O_3 175-70	42.4	0	39.6	51.6	8.7	100
Au/SiO_2 175-70	94.9	23.5	44.9	15.3	16.2	76.4

A major difference which appears comparing the results obtained is the butene product distribution. For the Si_3N_4 sample the primary products are 1-butene and cis-2-butene (46.7 and 36.3 % selectivity respectively) with only a minor presence of trans-2-butene (2.1 % selectivity). On the other hand, for the Al_2O_3 sample, an opposite behaviour, with trans-2-butene and 1-butene being the major products (39.6 and 51.6 % selectivity respectively) and cis-2-butene being lower in presence (8.7 % selectivity) is observed. When the results for the Au/SiO_2 175-70 are considered, there is a further difference in performance; in this sample the major product is trans-2-butene (44.9 % selectivity), with the other two products, cis-2-butene and 1-butene, being produced to about at the same extent (16.2 and 15.3 % selectivity respectively).

Figure 4.3.8 shows the effect of particle size on the reaction, summarized in table 4.3.6; note that we exclude the Au/SiO_2 16-3.5 results from too close scrutiny since the lower conversion observed could be caused by the different amount of catalyst used in the reaction. Comparing then the two remaining catalysts it can be seen that when the particle size increases the activity drops by ~ 10 % in the same conditions while keeping the same selectivity. In addition, the production of n-butene decreases as the particle size gets smaller, from ~20 % to ~6 %. This difference in selectivity could be due to a different adsorption energy of hydrogen and the butenes on the distinct particle size [169]. Although the results for the Au/SiO_2 16-3.5 are most likely compromised for the aforementioned reasons, it should be noted that the particular selectivity of Au/SiO_2 samples appears comparable to the other two samples.

Table 4.3.6. Catalytic activity/selectivity comparison at 120 °C between samples supported on SiO_2 with different particle size (Au/SiO_2 30-8.5 particle size (PS) = 1.9 nm, Au/SiO_2 16-3.5 PS= 2.6 nm, Au/SiO_2 175-70 PS= 2.9 nm). The error for each measurement is 10% of the measurement.

Sample	Conversion (%)	N-Butane selectivity (%)	Trans-2-Butene selectivity (%)	1-Butene selectivity (%)	Cis-2-Butene selectivity (%)	Yield (%)
Au/SiO_2 30-8.5	100	6.3	53.4	19.5	20.8	93.7
Au/SiO_2 16-3.5	51.2	0	46.4	43.1	10.4	100
Au/SiO_2 175-70	96.4	24.2	44.3	13.1	18.4	76.4

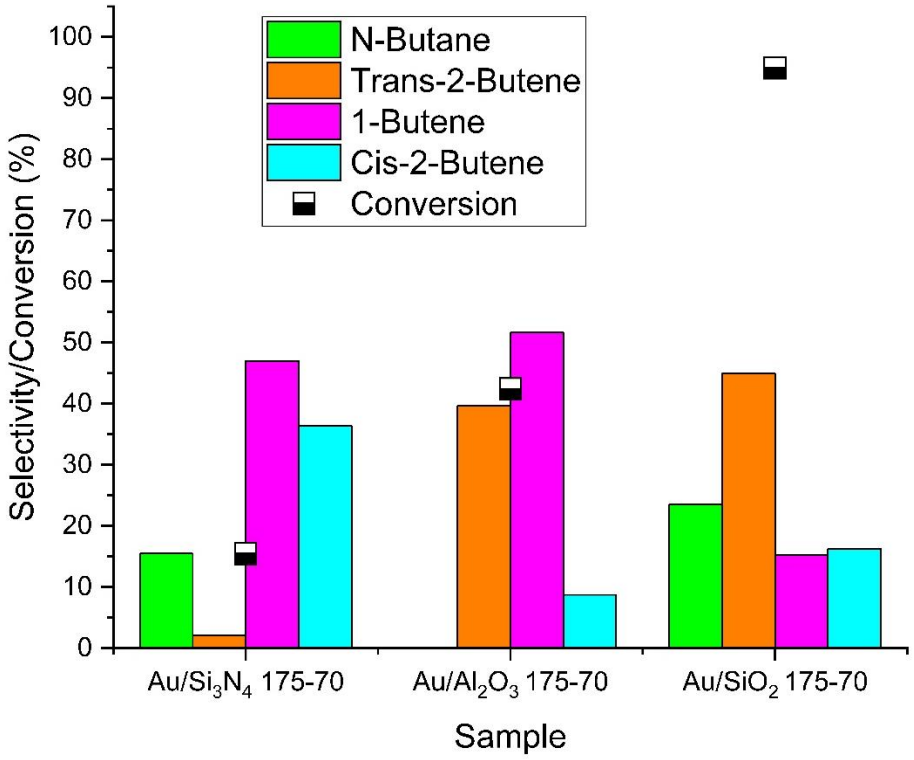

Figure 4.3.7. Catalytic activity/selectivity comparison between samples with similar particle size but different support at 120 °C using 1,3-butadiene/H_2 mixture in a 98/2 ratio.

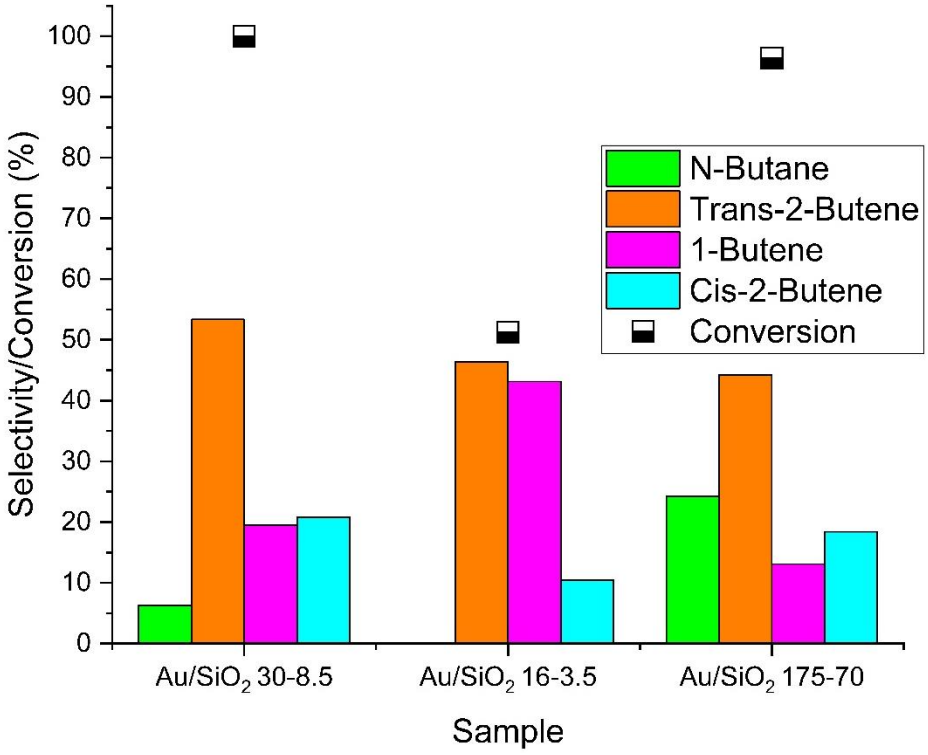

Figure 4.3.8 Catalytic activity/selectivity comparison between samples with different particle size but same support. (Au/SiO_2 30-8.5 particle size (PS) = 1.9 nm, Au/SiO_2 16-3.5 PS= 2.6 nm, Au/SiO_2 175-70 PS= 2.9 nm) at 120 °C using a 1,3-butadiene/H_2 mixture in a 98/2 ratio.

4.3.2.2 Temperature effect

In figure 4.3.9 and 4.3.10 are shown the evolution of butadiene, butenes and butane as a function of reaction temperature for Au/SiO_2 30-8.5 and Au/SiO_2 175-70 respectively. As it can be seen the conversion profile varies depending on the particle size; Au/SiO_2 30-8.5 reaches 100 % conversion at just 90 °C while it requires a temperature higher than 120 °C for Au/SiO_2 175-70. Furthermore, the selectivity varies depending on the temperature: for Au/SiO_2 30-8.5 as the conversion changes from 70 % at 70 °C to 100 % at 90 °C the selectivity switches from a higher production of 1-butene to trans-2-butene. This increase of trans-2-butene as the temperature increases has been previously reported by Hugon et al. but the change here observed appears at a much lower temperature (90 °C) than the one reported (> 300 °C) [167]. The reason for a higher presence of 2-butenes species as the temperature increase could be attributed to an increase in the isomerization rate of 1-butene as the temperature increases, in particular toward the production of trans-2-butene, which is the most thermodynamically stable butene [167]. The lower production of 1-butene

can be further seen when the temperature increases from 90 °C to 150 °C, and, while the conversion is 100 %, the amount of 1-butene decreases while the cis-2-butene increases as well as, interestingly enough, the amount of n-butane. Regarding Au/SiO_2 175-70, the selectivity toward trans-2-butene remains constant for the whole catalytic test. However, the ratio between 1-butene and cis-2-butene changes as the temperature rises, with 1-butene decreasing and cis-2-butene increasing. For Au/Al_2O_3 175-70, as shown in figure 4.3.11, in contrast with the SiO_2 samples, the product selectivity does not change as the temperature changes but the conversion increases.

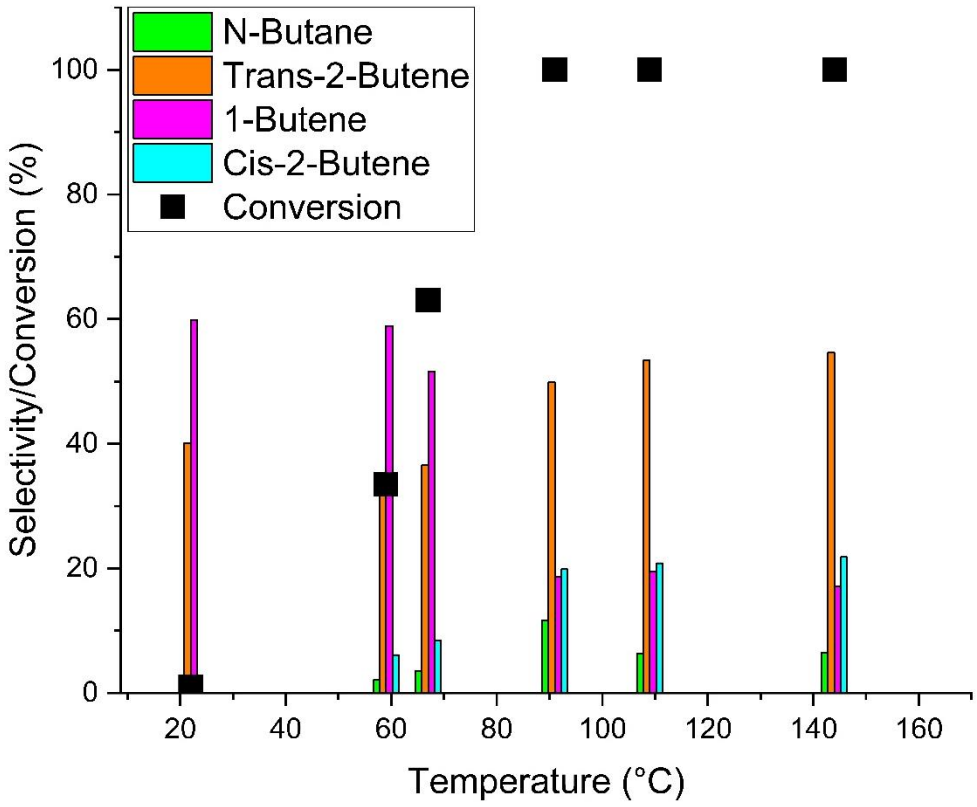

Figure 4.3.9. Evolution of the conversion and products as function of reaction temperature in selective hydrogenation of butadiene for Au/SiO_2 30-8.5 using 1,3-butadiene/H_2 mixture in a 98/2 ratio

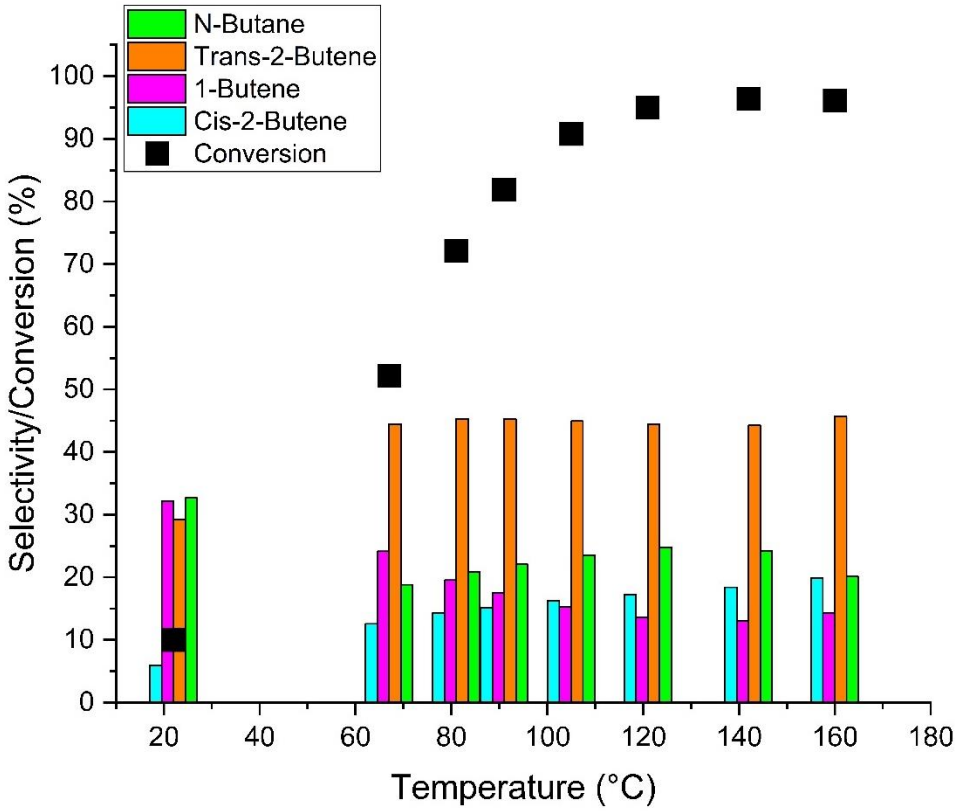

Figure 4.3.10. Evolution of the conversion and products as function of reaction temperature in selective hydrogenation of butadiene for Au/SiO_2 175-70 using 1,3-butadiene/H_2 mixture in a 98/2 ratio

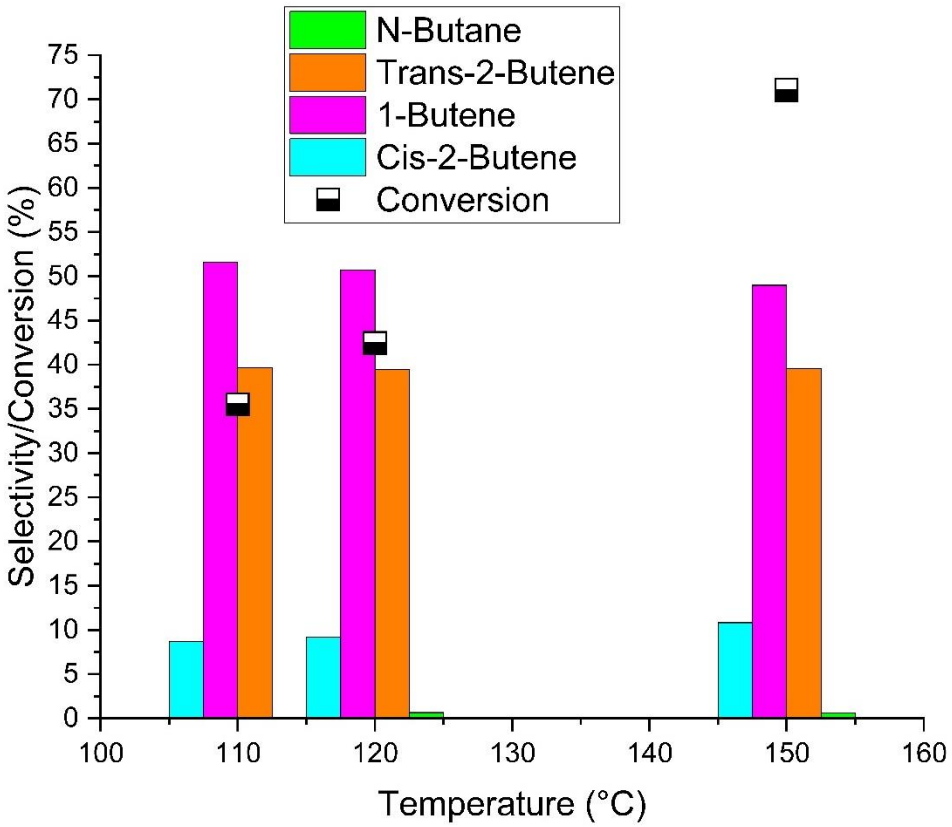

Figure 4.3.11. Evolution of the conversion and products as function of reaction temperature in selective hydrogenation of butadiene for Au/Al_2O_3 175-70 using 1,3-butadiene/H_2 mixture in a 98/2 ratio

4.3.3 In situ XAFS

4.3.3.1 X-ray Absorption Near Edge Structure (XANES)

It has been shown in the past that the adsorption of reactive gases, such as H_2 [324] or ethene [325], may cause a change in the XANES spectra. This change has been explained by Weiher et al [326], in the case of the absorption of CO, as a back-bonding of the gold d-band to the $2\pi^*$ of the molecular orbitals of CO, reducing the density of d-states, making the $2p_{3/2}$-5d dipole transition allowed [327]. The effect of this absorption is not readily noticeable when observing the XANES data due to the low intensity but by subtracting a reference spectrum the changes are made more pronounced (with the resulting spectra called delta-mu or Δμ spectra) [327]. In figure 4.3.12 are shown the XANES (a) as well as the delta-mu (Au^0 foil taken as reference) (b) spectra of Au/SiO_2 30-8.5. Whereas no discernible change can be observed from the XANES spectra, the delta-mu is able to provide some additional information here. As it can be seen from 4.3.12b the delta-mu spectra show a peak for the sample at

11.919 keV under the various atmospheres. This positive delta-mu spectra is consistent with the previously reported data for Au nanoparticle subject to H_2 [324] and C=C double bond [327]. This suggests a depletion of the density of d-states under 1,3-butadiene atmosphere and that this appears to be more pronounced than under other atmospheres, a result which can be rationalize by the larger back-bonding effect of the C=C double bond. Interestingly the mixture of H_2/1,3-butadiene appears to possess an intensity in between the H_2 and 1,3-butadiene atmospheres respectively. This could be interpreted by an almost equal coverage of the two species on the surface of Au nanoparticles under reaction condition. A similar behaviour can be seen in figures 4.4.7a and 4.4.7c for the Au/SiO_2 175-70 and Au/SiO_2 16-3.5 samples, albeit in a much lower intensity scale whereas for Al_2O_3 supported sample, no peak can be seen at the 11919 eV position and in the case of Si_3N_4 supported sample (figure 4.4.7d) no changes can be seen as the atmosphere changes.

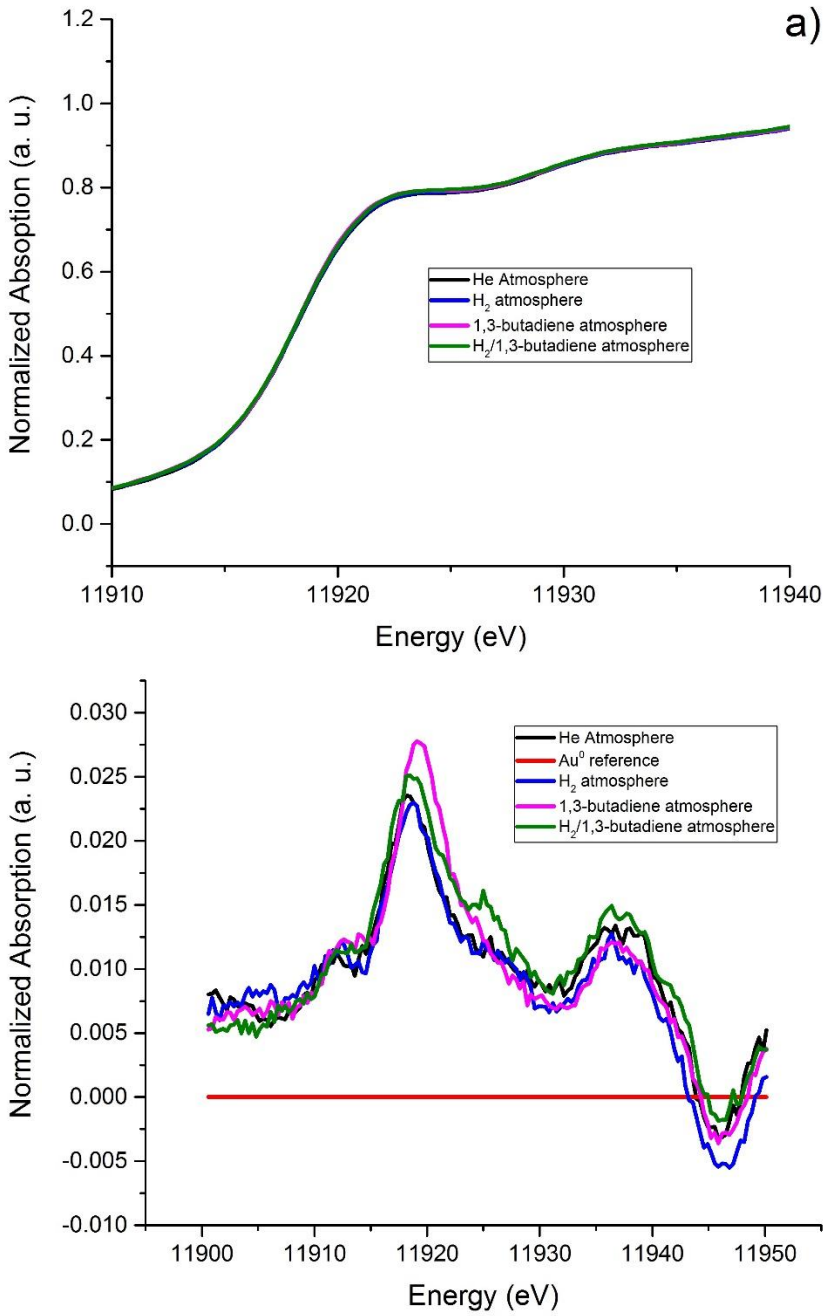

Figure 4.3.12. a) XANES spectra of Au/SiO_2 30-8.5 catalyst under different atmospheres; b) Delta-mu XANES spectra of Au/SiO_2 30-8.5 under different atmospheres. The spectra obtained from Au^0 foil was used as starting position. The atmospheres involved are: He, H_2, 1,3-butadiene and H_2/1,3-butadiene

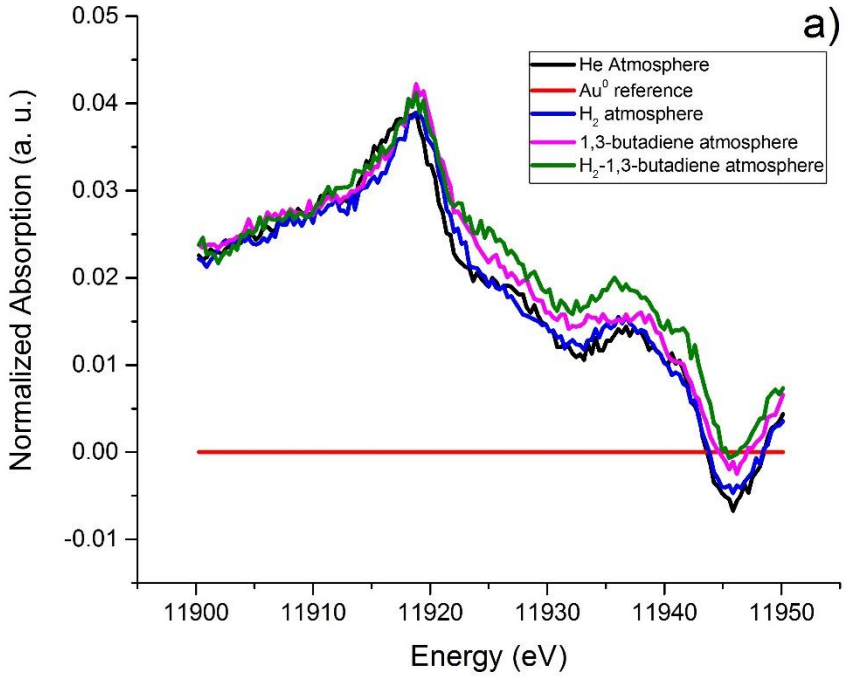
a)
He Atmosphere
Au0 reference
H2 atmosphere
1,3-butadiene atmosphere
H2-1,3-butadiene atmosphere
Normalized Absorption (a. u.)
0.05
0.04
0.03
0.02
0.01
0.00
-0.01
11900
11910
11920
11930
11940
11950
Energy (eV)

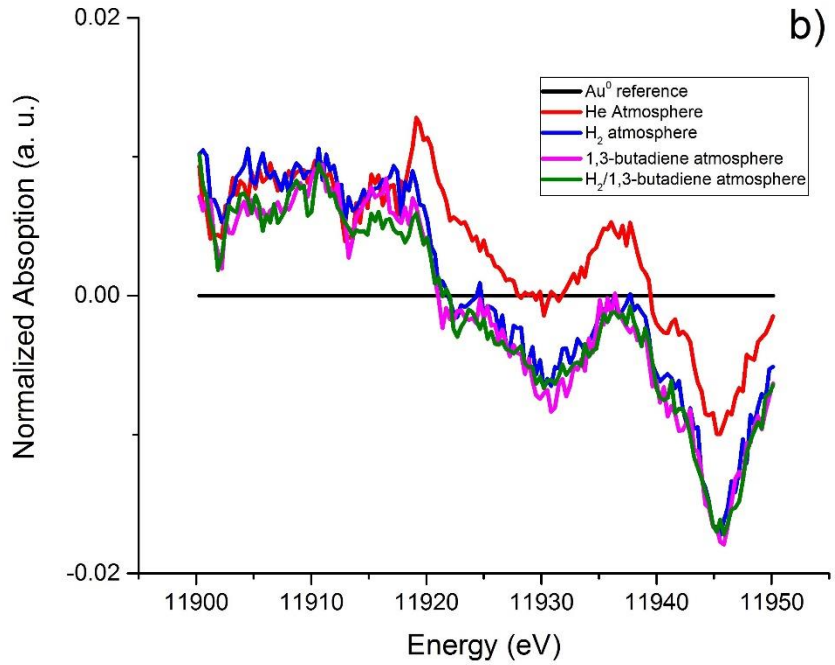
b)
Au0 reference
He Atmosphere
H2 atmosphere
1,3-butadiene atmosphere
H2/1,3-butadiene atmosphere
Normalized Absoption (a. u.)
0.02
0.00
-0.02
11900
11910
11920
11930
11940
11950
Energy (eV)

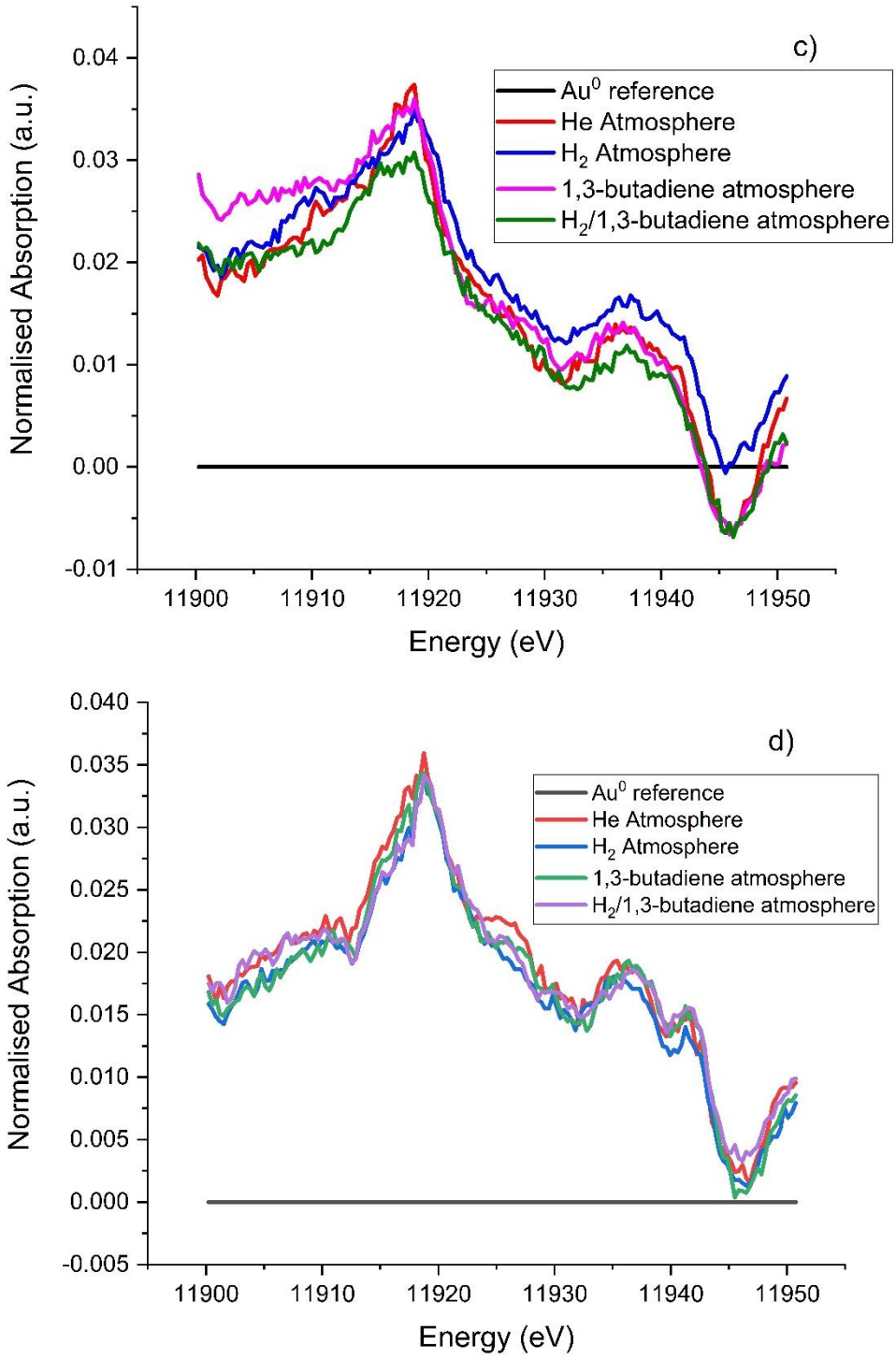

Figure 4.3.13. Delta-mu XANES spectra of a) Au/SiO_2 175-70; b) Au/Al_2O_3 175-70; c) Au/SiO_2 16-3.5 and d) Au/Si_3N_4 175-70 under different atmospheres. The spectra obtained from Au^0 foil was used as starting position. The atmospheres involved are: He, H_2, 1,3-butadiene and H_2/1,3-butadiene

4.3.3.2 EXAFS

Tables 4.3.7-11 show the fit results obtained for each sample obtained keeping the DWF constant for the 1st shell of Au-Au; the fit was performed up to the 4th shell and the values obtained for these are given in the appendix in table S4.1-5. Figures 4.3.14-15 show the results of the fit for k^3-weighted spectra for Au/SiO_2 30-8. under H_2 and 1,3-butadiene atmosphere. The fit results for the other samples can be found in the appendix at figure S4.5-12. The decision to focus only on changes concerning the first shell is based on there being already enough information present here to understand how the sample responds to its atmosphere; especially since the particles are small i.e. high surface to volume ratio. It is due to be noted that, since the DWF used in the fit is fixed, the 1CN obtained may not reflect the true value of coordination number; however, the variation of the 1CN as function of the gas composition, as the only variable, can give an indication of the catalyst response. The most intense peak in all sample appears at ~2.9 Å, which is attributed to the Au-Au scattering pair of bulk gold. Moreover, the values obtained for the 1st shell radii are also consistent with that obtained from the fit at room temperature shown in table 4.3.4. It can be seen however that the 1st shell radius decreases as the atmosphere changes from He to H_2 in the case of SiO_2 supported samples. The presence of AuH species, assuming a similar behaviour to PdH [328], would have caused an increase in the 1st shell radius under a H_2 atmosphere due to presence of H interstitials within the Au cubic lattice. The contraction in the lattice allows us to exclude the presence of the formation of a significant amount of AuH species under a H_2 atmosphere.

It appears, (see figure 4.3.16), that for all the samples supported on SiO_2 the 1CN grows as the atmosphere switches from H_2 to 1,3-butadiene, compared to the behaviour of Al_2O_3 and Si_3N_4 supported samples, figure 4.3.17, where it decreases or does not change respectively. Moreover, it seems that this behaviour is affected by the particle size, with the smallest particles (Au/SiO_2 30-8.5, PS = 1.9 nm) being subject to changes in a greater extent (~24 % variation versus ~6 % of the Au/SiO_2 175-70). Furthermore, when subject to the reaction mixture (H_2/1,3-butadiene) the 1CN appears to assume value which is intermediate between the H_2 and 1,3-butadiene atmospheres, as shown in figure 4.3.18-19 for Au/SiO_2 30-8.5, here taken as example for the Au/SiO_2 samples, and Au/Al_2O_3 175-70.

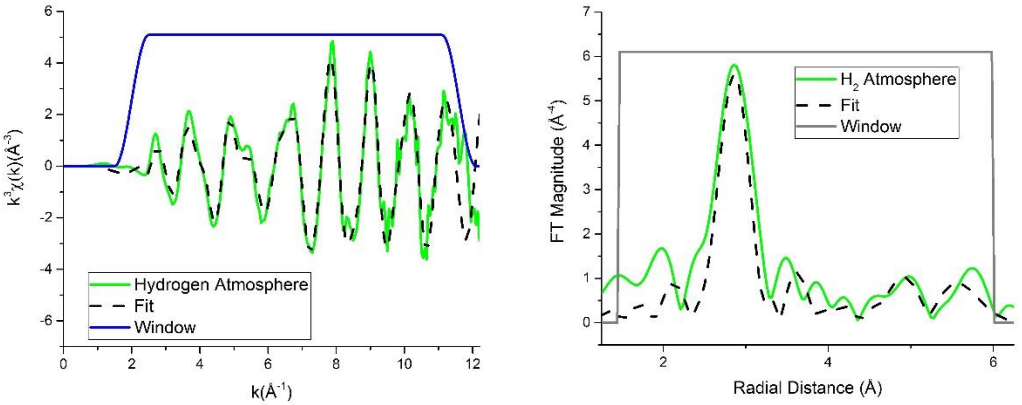

Figure 4.3.14. k^3-weighted EXAFS fit in k (on the left) and R (on the right) space of Au/SiO_2 30-8.5 under H_2 atmosphere. The blue and grey box represent the fit range.

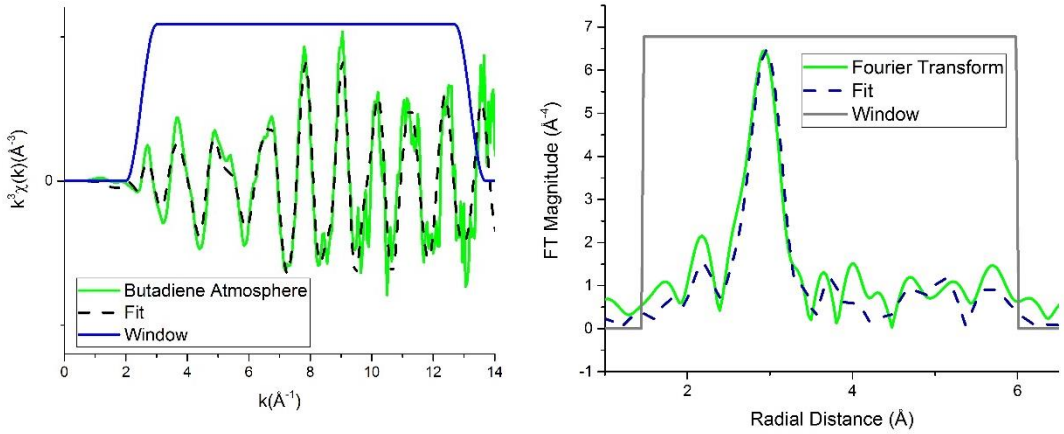

Figure 4.3.15. k^3-weighted EXAFS fit in k (on the left) and R (on the right) space of Au/SiO_2 30-8.5 under 1,3-butadiene atmosphere

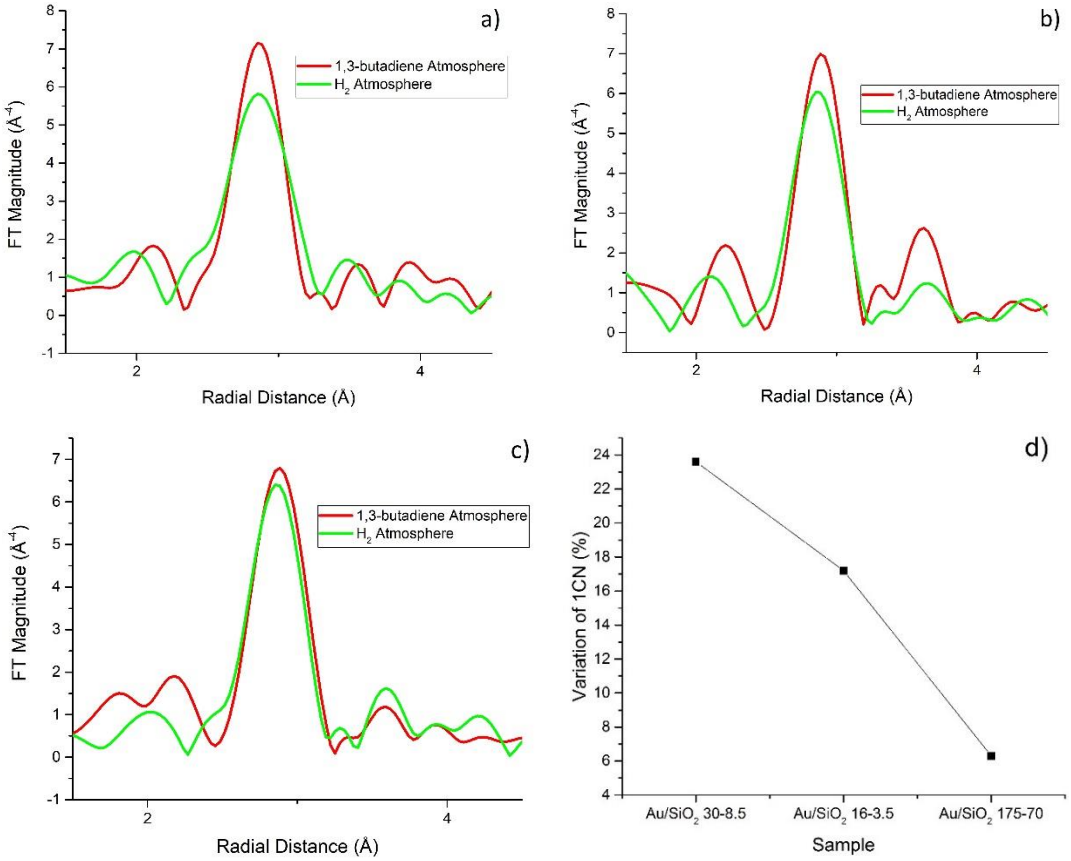

Figure 4.3.16. k^3-weighted Fourier Transform, under two different atmosphere, hydrogen and 1,3-butadiene, of a) Au/SiO_2 30-8.5; b) Au/SiO_2 16-3.5; c) Au/SiO_2 175-70; d) ratio between the coordination number obtained by the fit when the samples are subject to H_2 atmosphere to 1,3-Butadiene atmosphere as function of PS.

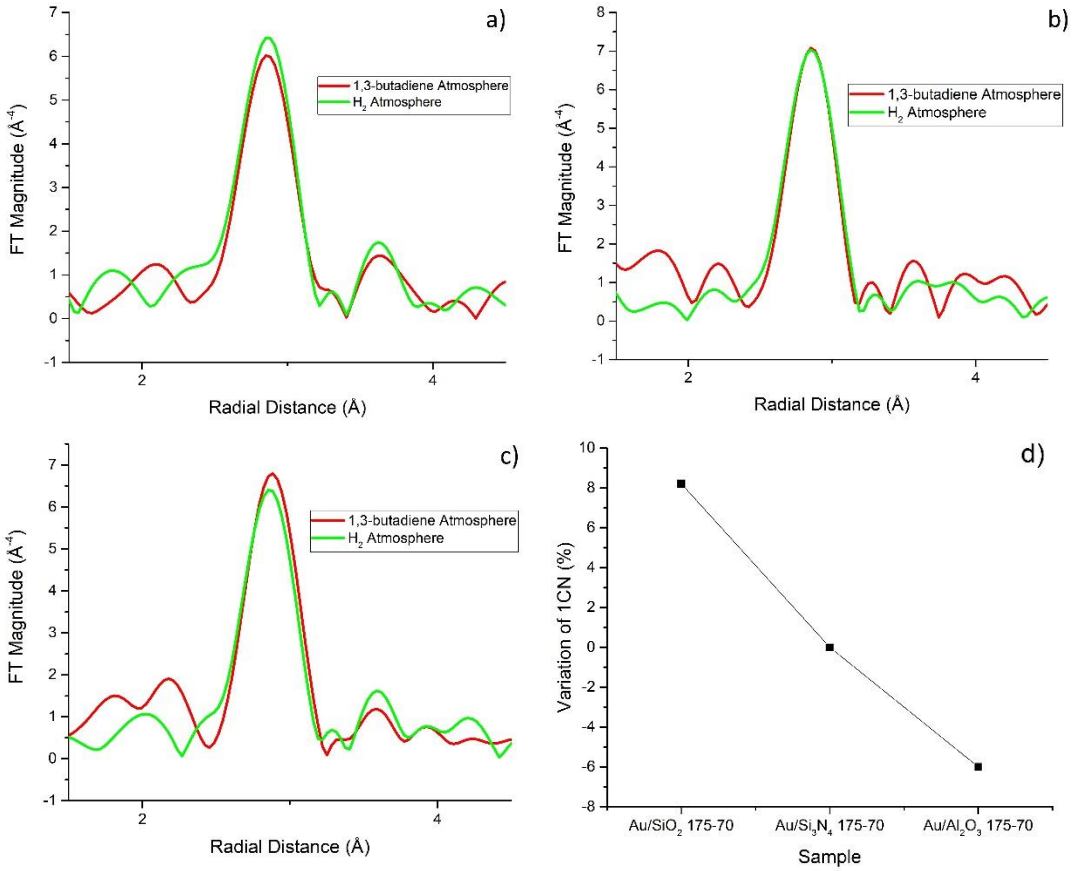

Figure 4.3.17. k^3-weighted Fourier Transform, under two different atmosphere, hydrogen and 1,3-butadiene, of a) Au/Al_2O_3 175-70; b) Au/Si_3N_4 175-70; c) Au/SiO_2 175-70; d) ratio between the coordination number obtained by the fit when the samples are subject to H_2 atmosphere to 1,3-Butadiene atmosphere.

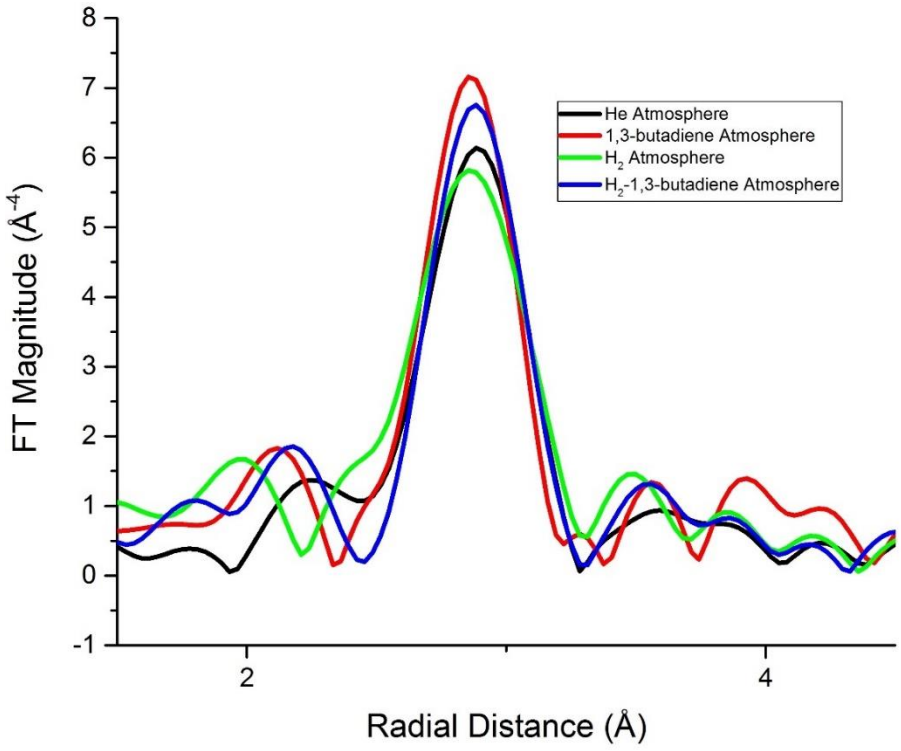

Figure 4.3.18 k^3-weighted Fourier Transform of Au/SiO_2 30-8.5, under different atmospheres: helium, hydrogen, 1,3-butadiene and the mixture of the two gas. The intensity of the Au-Au scattering peak at ~2.8 Å varies as the composition changes.

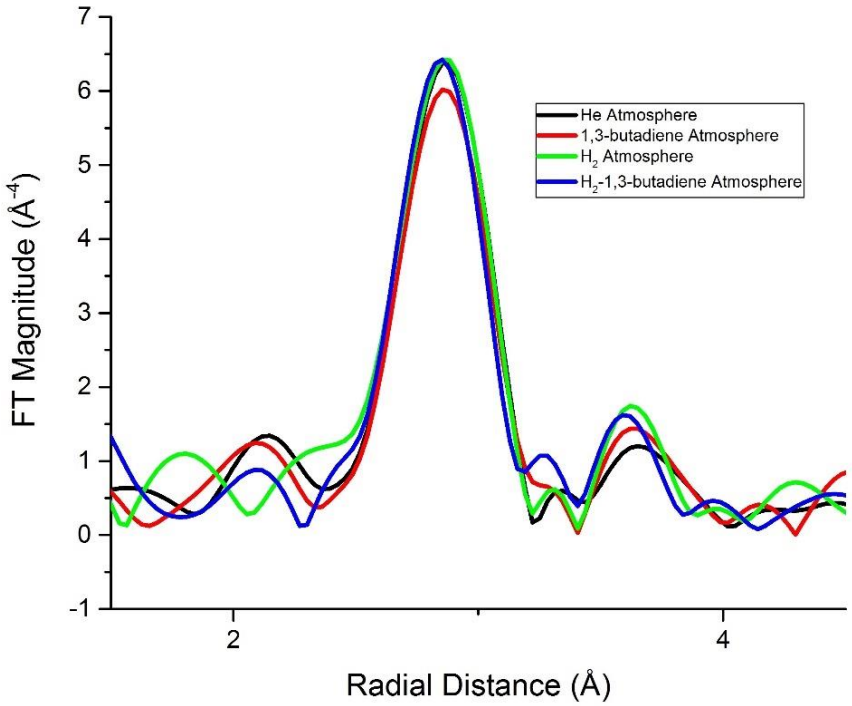

Figure 4.3.19. k^3-weighted Fourier Transform of Au/Al_2O_3 175-70, under two different atmosphere, hydrogen and 1,3-butadiene. The intensity of the Au-Au scattering peak at ~2.8 Å varies as the composition changes.

Table 4.3.7. EXAFS fit results obtained from Au/SiO_2 30-8.5, using a constant Debye-Waller factor, as a function of the gas composition

Gas composition	1st shell radius (Å)	1CN	R_{factor}	ΔE
Helium	2.86 ± 0.01	6.1 ± 0.6	0.191	5 ± 2
Hydrogen	2.84 ± 0.01	5.7 ± 0.9	0.2	4 ± 3
1,3-Butadiene	2.845± 0.009	7.1 ± 0.7	0.147	4 ± 2
Hydrogen/ 1,3-Butadiene	2.856 ± 0.01	6.6 ± 0.6	0.122	5 ± 2
Hydrogen (After reaction)	2.851 ± 0.009	6.8 ± 0.6	0.0147	5 ± 2

Table 4.3.8. EXAFS fit results obtained from Au/SiO_2 16-3.5, using a constant Debye-Waller factor, as a function of the gas composition

Gas composition	1st shell radius (Å)	1CN	R_{factor}	ΔE
Helium	2.82 ± 0.02	7 ± 1	0.191	2 ±1
Hydrogen	2.85 ± 0.02	6 ± 1	0.2556	4 ±3
1,3-Butadiene	2.86 ± 0.01	7 ± 1	0.147	5 ± 3
Hydrogen/ 1,3-Butadiene	2.84 ± 0.01	6.7 ± 0.7	0.122	3 ± 2
Hydrogen (After reaction)	2.83 ± 0.01	7.3 ± 0.8	0.0147	2 ± 2

Table 4.3.9. EXAFS fit results obtained from Au/SiO_2 175-70, using a constant Debye-Waller factor, as a function of the gas composition

Gas composition	1st shell radius (Å)	1CN	R_{factor}	ΔE
Helium	2.850 ± 0.01	6 ± 1	0.156	5 ± 2
Hydrogen	2.841 ± 0.009	6 ± 1	0.157	3 ± 2
1,3-Butadiene	2.856± 0.009	7 ± 1	0.161	5 ± 2
Hydrogen/ 1,3-Butadiene	2.857 ± 0.009	6.7 ± 0.7	0.169	5 ± 2

Table 4.3.10. EXAFS fit results obtained from Au/Al_2O_3 175-70, using a constant Debye-Waller factor, as a function of the gas composition

Gas composition	**1st shell radius (Å)**	**1CN**	**R_{factor}**	**ΔE**
Helium	2.84 ± 0.01	6.3 ± 0.8	0.23	4 ± 3
Hydrogen	2.84 ± 0.01	6.4 ± 0.9	0.25	4 ± 2
1,3-Butadiene	2.84 ± 0.01	6.0 ± 0.89	0.27	3 ± 3
Hydrogen/ 1,3-Butadiene	2.84 ± 0.01	6.3 ± 0.98	0.29	3 ± 3
Hydrogen (After reaction)	2.85 ± 0.02	7 ± 1	0.32	4 ± 4

Table 4.3.11. EXAFS fit results obtained from Au/Si_3N_4 175-70, using a constant Debye-Waller factor, as a function of the gas composition

Gas composition	**1st shell radius (Å)**	**1CN**	**R_{factor}**	**ΔE**
Helium	2.85 ± 0.01	7.1 ± 0.8	0.175	4 ± 2
Hydrogen	2.84 ± 0.01	6.9 ± 0.8	0.183	4 ± 2
1,3-Butadiene	2.85 ± 0.02	7 ± 1	0.268	4 ± 3
Hydrogen/ 1,3-Butadiene	2.85 ± 0.02	7.1 ± 0.8	0.185	4 ± 2
Hydrogen (After reaction)	2.85 ± 0.01	7 ± 1	0.343	4 ± 4

4.4 Discussion

4.4.1 In situ XAFS

The results show that as the atmosphere surrounding the samples change, (switching from H_2 to 1,3-butadiene) so a change in the 1CN value is observed. In the case of the Au/SiO_2 30-8.5 there is an increase of intensity of the 1st shell peak, of ~ 20% whereas for the Al_2O_3 supported sample there is a decrease of ~ 6 %. This change could be attributed to a change in nanoparticles' structure as a result of adsorption of reactant gas at the nanoparticle surface [259]. Whereas the delta-mu XANES obtained for Au/SiO_2 30-8.5 suggest that the adsorption of the various gases influences the 5d electron density of Au nanoparticles, it is not possible to affirm with certainty that a similar effect could be seen in the other samples. It can be however seen that for Au/SiO_2 30-8.5 the gas dependency of delta-mu XANES intensity mirrors the one appearing in 1CN under similar reaction condition. It is therefore possible to assume that the delta-mu XANES is actually observing the restructuring process which Au nanoparticles undergo under the various gas atmospheres. Considering that the restructuring process is both particle size and support dependent, it is possible to rationalize the results obtained for the other samples, showing almost no discernible changes in the delta-mu XANES, comparing to the smaller amount of restructuring shown in the EXAFS. It has to be noted that, while it is not possible to exclude an electronic effect caused by the adsorption of the gas, it is hard to extricate the effect of reshaping and adsorption on delta-mu XANES separately. When flowing the reaction mixture (1,3-butadiene/H_2 ratio: 1/49) the results obtained show a behaviour intermediate between the gas compositions. This is further confirmed by the analysis of the FT intensity of 2CN:1CN ratio as a function of gas atmosphere, shown in figure 4.4.1 for the Au/SiO_2 30-8.5 and Au/Al_2O_3 175-70, which, according to Beale et al. [190], could be used to identify the shape of nanoparticles. Whereas it is not possible to directly compare the absolute values obtained here with those reported in that study, it is possible to rationalize trends in the changes occurring as the atmosphere around the nanoparticles changes.

On the basis that the shape of Au nanoparticles under He atmosphere can most likely be approximated to a supported hemisphere, the increase in the 2CN:1CN ratio when H_2 is introduced to the system, paired with the slight decrease in the 1CN for Au/SiO_2 30-8.5, suggest that the nanoparticles become more cylindrical. Whereas the successive decrease in the 2CN:1CN ratio, when the nanoparticles are subject to a 1,3-butadiene and H_2/1,3-butadiene atmospheres, paired with the aforementioned increase of 1CN in the H_2 atmosphere, suggests that under these gas atmospheres a change towards a more isotropic shape occurs. This effect is however, less apparent with larger particle sizes. This lack of a response could be explained by two factors: first of all, the increase in size of the nanoparticle leads to an increase in the number of Au-Au interactions; therefore, the changes happening due to reshaping have a lower impact on the intensity of the first shell peak (Au-Au scattering pair contribution). Secondly the interaction of 1,3-butadiene with the Au surfaces is weaker as the particle gets bigger. These effects reflect as well on the catalytic activity: larger particles appear to perform slightly worse, both in terms of conversion and selectivity, than the smaller particles over a wide range of temperatures in hydrogenating 1,3-Butadiene. A similar behaviour could be seen in figure 4.4.2a-b with the Au/SiO_2 16-3.5 and 175-70 which suggest that the restructuring process happen on all SiO_2 supported samples. In the case of the Al_2O_3 supported sample, the reshaping appears to proceed in the opposite direction to that of Au/SiO_2 30-8.5 where a decrease in 1CN is observed when the nanoparticles are subject to 1,3-butadiene atmosphere and which can be rationalised in terms of a flattening of the hemisphere; a flattening of the Au nanoparticles over the support increases, albeit slightly, the contact surface between the Au and the support thus decreasing the Au-Au scattering pair contribution. For the Si_3N_4 supported sample, no discernible nanoparticle restructuring is observed in the 1CN as the atmosphere changes from H_2 to 1,3-butadiene. However, the 2CN:1CN ratio (Figure 4.4.2) shows, under 1,3-butadiene, a change which we interpret to indicate reverting back towards a more hemispherical shape, i.e. a shape similar to the one observed under a H_2 atmosphere. Another way to rationalise the process would be to take in account the different surface energy of the supports. Unfortunately, in the literature, no information is available regarding the surface energy interaction between Au and the support. However, from the surface energy obtained from the support interaction with H_2O some information could be inferred. In particular Al_2O_3 possess the highest surface energy, ~1.6 J/m^2 [329], followed by Si_3N_4 at 1 J/m^2 [330] and last

SiO_2 at 0.34 J/m^2 [331]. The flattening of the nanoparticle on the case of Al_2O_3 could then be attributed to a stronger interaction of Au with the support surface compared to SiO_2. In fact, in the case of SiO_2, the low surface energy could favour a reshaping toward a more spherical, and therefore more thermodynamically favoured, shape.

The three different behaviours could be summarized in the model depicted in figure 4.4.3

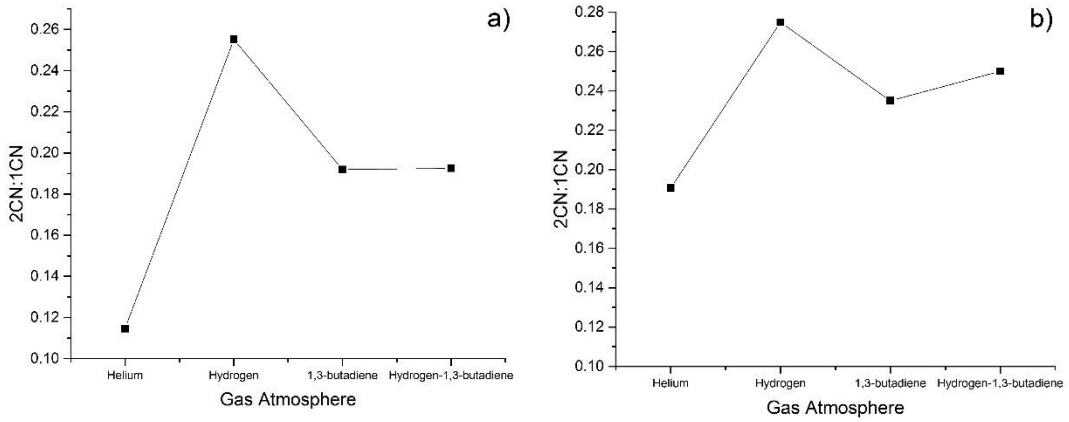

Figure 4.4.1. Variation of 2CN:1CN ratio as function of the gas atmosphere for a) Au/SiO_2 30-8.5; b) Au/Al_2O_3 175-70

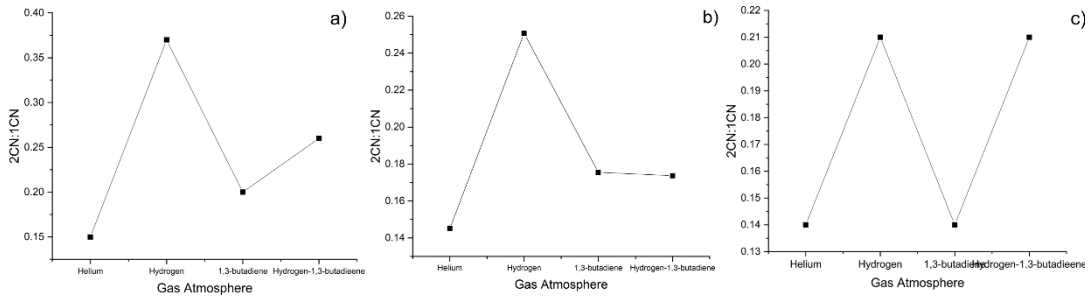

Figure 4.4.2. Variation of 2CN:1CN ratio as function of the gas atmosphere for a) Au/SiO_2 30-8.5; b) Au/Al_2O_3 175-70

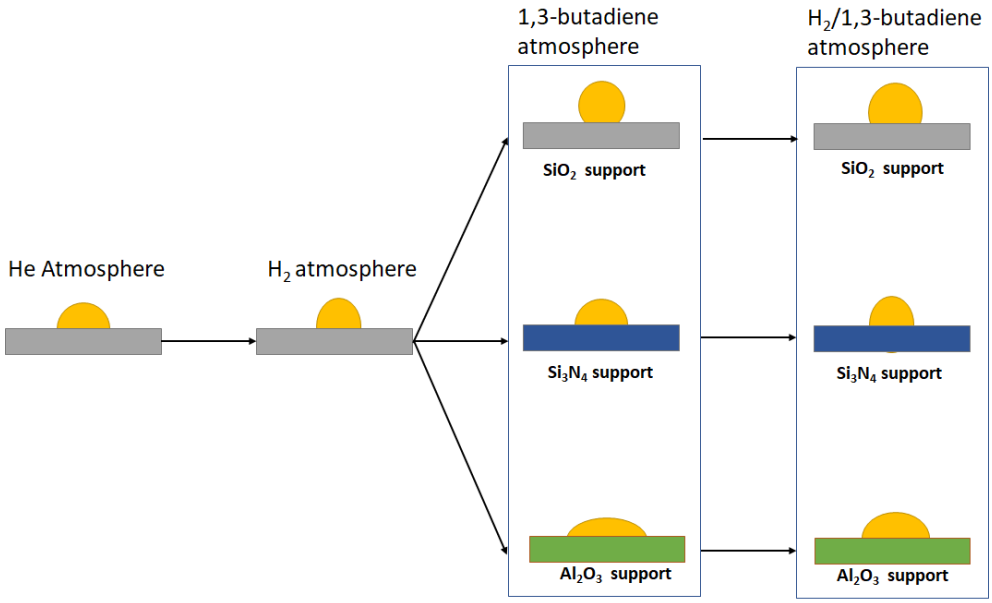

Figure 4.4.3. Model representation of the reshaping process the Au nanoparticles undergo during 1,3-butadiene hydrogenation. For all the samples an exposure to H_2 atmosphere causes a slight reshaping toward a more "cylindrical" shape. Under 1,3-butadiene, SiO2 supported samples see the height/diameter (H:D) ratio of the Au nanoparticles increasing, whereas on Si_3N_4 the H:D ratio does not change and on Al_2O_3 it decreases. The mixture of H_2 and 1,3-butadiene causes the nanoparticles to assume a shape intermediate between the H_2 and the 1,3-butadiene configuration.

4.4.2 Catalytic activity

According to Okumura et al. for nanoparticles of similar size, SiO_2 supported samples should show lower activity compared to Al_2O_3, but in the work here presented the relationship is reversed [51]. This could be due to the different synthesis methods used for preparing the nanoparticles. In the Okumura et al. study the synthesis method applied (gas-phase grafting method) produces a wider particle size distribution (standard deviation > 3 nm) that might lead to formation of nanoparticles with lower if not null catalytic activity, lowering the TOF for the SiO_2 samples analysed. The higher control offered by reverse micelle methods allows for a more direct comparison of the support effect thus resulting in a different catalytic profile.

Regarding selectivity, it can be seen that the support plays an important role in the product distribution. Bond et al divides the selectivity of gold nanoparticles in two main categories: those which behave as Pt does in which the butene yields follow: 1-Butene > Cis-2-Butene > Trans-2-Butene, and Iridium, where the amount of 1-Butene is reduced and trans-2-butene replaces cis-2-butene in the product distribution [66].

Most of the reported literature regarding butadiene hydrogenation with Au catalysts falls into the platinum group [66] . In particular the product profile from the Au/Si_3N_4 catalyst falls into this category eventually going on to form n-butane. Regarding Al_2O_3 the selectivity appears to follow the Iridium group, having lower amounts of cis-2-butene produced and no formation of n-butane. The SiO_2 samples tested show a completely different selectivity than the previously reported result: trans-2-butene is the principal product, and 1-butene and cis-2-butene appear in similar quantities. However, it produces a higher quantity of n-butane. Moreover, contrary to the previous claim from Okumura et al [51], it appears that particle size does affect the catalytic performance of Au. The smaller particle size sample (Au/SiO_2 30-8.5, 1.9 nm) appears to convert more 1,3-butadiene than the larger particle containing Au/SiO_2 175-70 sample, not only at 120 ° (figure 4.3.8) but also at all the temperatures (figures 4.3.9-10). More interestingly, it appears that the selectivity towards n-butane is particle size dependent, with the smaller particle size being more selective toward the butenes than the larger one. The reason for the presence of an indicative particle size dependency, compared to previous studies, can, as mentioned previously, be attributed to the lack of control in the particle size distribution present in the previous work, not being able to fully explore the characteristic of supported Au catalysts.

4.4.3 Correlation between catalytic performance and particle properties

In light of the results obtained is it possible to rationalize the correlation between the particle properties and their catalytic performance. It is clear that the nanoparticles behaviour is highly dependent on their support, both in terms of catalytic results (figure 4.3.7) as well as the nanoparticle (re-)shape (figure 4.4.2). Focusing only on the behaviour of the Au nanoparticles and their response to the various gas atmospheres we can rationalise the importance of these changes in terms of butadiene hydrogenation as follows. On the basis that the Au/SiO_2 30-8.5 sample responds the most and is the most active we propose that the reaction-gas-induced restructuring, leads to an increase in the presence of Au sites such as edges and corners, suitable for the adsorption, and subsequently hydrogenation, of 1,3-butadiene and hence the increased activity. We propose that the number of these species are most numerous in

Au/SiO_2 30-8.5 and least prevalent in Au/Si_3N_4 175-70. This may also influence the selectivity between the cis- and the trans-2-butene species formed. On the basis that 1,3-butadiene can exist in both trans- and cis-1,3-butadiene configuration due to the free rotation of the C=C double bond around the central C-C bond, as illustrated in figure 4.4.3, the modality of adsorption may be dependent on the arrangement of atoms at the nanoparticle surface. A lower number of undercoordinated sites, as in the case of Au/Si_3N_4 175-70, could be rationalised as allowing for the stabilization of the cis-1,3-butadiene configuration adsorbed on the surface due to the interaction between the Au atoms and the free rotating C=C double bond. Yang et al. has shown that the adsorption of 1,3-butadiene in a cis- configuration leads to a higher formation of cis-2-butene instead of the more thermodynamically stable trans-2-butene [169]. On the other hand, the presence of undercoordinated atoms such as those found at edges and corners of nanoparticles, as in the case of SiO_2 and Al_2O_3 supported samples, may induce an adsorption in a trans configuration, thus resulting in a higher presence of trans-2-butene in the product distribution.

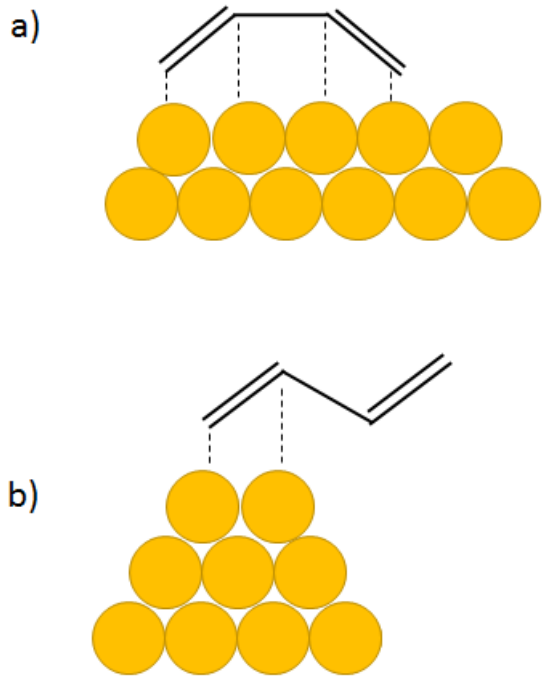

Figure 4.4.3. Proposed mechanism of absorption of 1,3-butadiene on a) low defective Au surfaces; b) high defective Au surfaces.

Regarding the selectivity toward n-butane it appears again that this is affected by both the support and the particle size. The support effect could again be explained by the

different shapes assumed by the nanoparticles on different support types. Taking the two opposite situation, Au/SiO_2 175-70 and Au/Al_2O_3 175-70, and considering the shapes the nanoparticles assumes (a truncated sphere for Au/SiO_2 175-70 and a flattened hemisphere for Au/Al_2O_3), one can assume that the interfacial site formed between the nanoparticles and the supports (highlighted by figure 4.4.4 for Au/SiO_2 175-70) may be the source of the site for hydrogenation of butenes. A reason for this behaviour may be caused by a longer retention time of butenes species in these interstitial sites, ready to be hydrogenated. This effect is reflected also in the particle size dependency of n-butane selectivity, since is reasonable to assume that a larger particle size (2.7 versus 1.9 nm) possess a larger number of these Au-support interfacial atoms, thus causing a higher production n-butane.

It is important to note that as the nanoparticle get smaller the melting temperature decreases exponentially, in particular in the region between 3-2 nm, where the melting temperature (T_m) goes from ~800-900 K for a 3 nm particle to ~600K for a 2 nm one [332]. However, atoms start to become mobile at temperatures much lower than the melting temperatures, with surface and bulk atoms becoming mobile at different temperature, Hütting temperature ($T_H = 0.3\ T_m$) for surface atoms and Tammann temperature ($T_t = 0.5\ T_m$) for bulk atoms [333]. This could explain the higher activity of smaller nanoparticles, for which the reaction temperature is always above the Tammann temperature (T_t = ~300 K for a 1.9 nm Au nanoparticle), whereas only approach at higher temperature for the larger particles (T_t = ~400-450 K). The higher fluxionality of smaller-sized Au nanoparticles is much higher than for the larger sample and this could be correlated with the higher activity. However, as the temperature increases to ~400K and the larger nanoparticles approach Tammann temperature the difference become less significant.

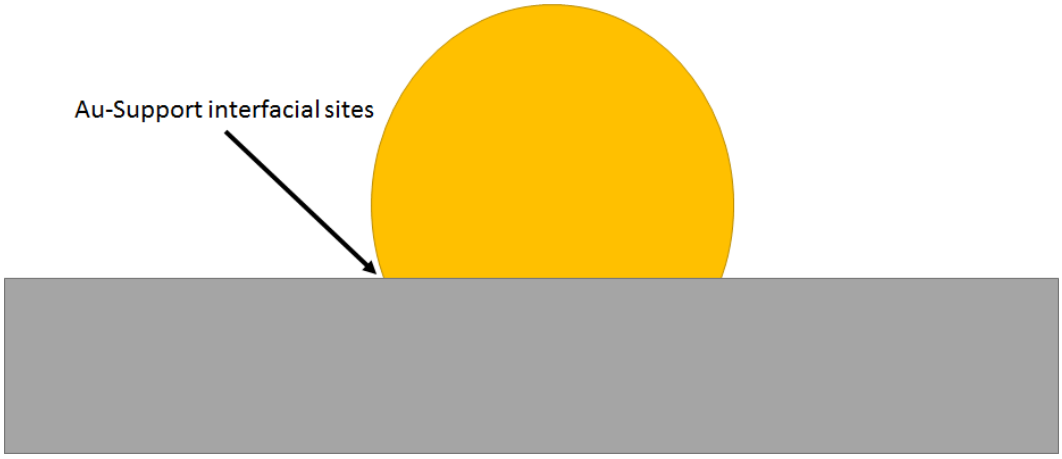

Figure 4.4.4. Highlight of the Au-Support interfacial sites

4.5 Summary and Conclusion

From the data obtained a clearer understanding of the effect of particle size and support for Au nanoparticles in the hydrogenation of 1,3-butadiene has been reached an in particular we observe:

1. The hydrogenation of 1,3-butadiene present both a particle size and support dependency; in particular it appear that smaller particle size cause higher conversion at the same temperature. Furthermore SiO_2 appear to be the most active support, followed by Al_2O_3 lastly SiC
2. Au nanoparticles appears to be undergoes a restructuring process as the gas atmosphere surrounding the catalysts changes and the extent of restructuring is dependent on particle size while the shape assumed under reaction condition is dependent on the support

It is reasonable to assume that the restructuring process which the nanoparticles undergo when subject to the reaction mixture might lead to an effect on the catalytic

performances of supported Au nanoparticles due to a change in the presence of suitable active sites for the hydrogenation, as well as increasing the number of defective sites on the Au nanoparticles surfaces. However, the high degree of nanoparticles modification in sample containing small nanoparticles (Au/SiO_2 30-8.5, PS= 1.9 nm) could be the result of combination of factor. One is the interaction of the nanoparticles with the gas, while the other could be due to the enhanced mobility of surface atoms at the reaction temperature, which allows a higher degree of fluxionality of Au nanoparticles. Thus, considering the structure-performance relationship which has been described, future approaches should focus in designing catalysts which present the required structural characteristic for the required reaction.

5 Particle size and support effect on the catalytic properties of Pd nanoparticles in 1,3-butadiene hydrogenation

5.1 Aim of the chapter

The main aim of this chapter lies in understanding particle size and support effects for Pd nanoparticles when used to catalyse 1,3-butadiene hydrogenation. The nanoparticles were prepared using reverse micelle encapsulation, which provides a method to produce highly homogenously sized nanoparticles. *In situ* XAFS

spectroscopy will be used to characterize the nanoparticles (previously characterized through TEM and ex situ XAFS) in order to identify any modification caused by adsorption and interaction of the reaction gases (H_2, 1,3-butadiene and the mixture of the two during the hydrogenation of 1,3-butadiene to produce butenes).

5.2 Methods

5.2.1 Synthesis

Pd nanoparticles were synthesized by reverse micelle methods. The polymers used were:

- P4708-S2VP (Polystyrene (PS) = 16000 MW, Poly-2 Vinylpyridine (P2VP) = 3500 MW), polydispersity = 1.05;
- P18226-S2VP (Polystyrene (PS) = 30000 MW, Poly-2 Vinylpyridine (P2VP) = 8500 MW), polydispersity = 1.06,
- PS5073-S2VP (Polystyrene (PS) = 175000 MW, Poly-2 Vinylpyridine (P2VP) = 70000 MW, polydispersity = 1.08),

all from Polymer Source Inc.; the purity 100% in all cases.

The metal salt used was potassium tetrachloropalladate (Aldrich 99.99999 % trace metal basis). The metal atom-to-pyridine ratio MS:Pyr (metal loading) was fixed at 0.3 MS:Pyr for all the samples while the reducing agent is p-Toluene Sulfonyl hydrazide (p-Tosyl hydrazide) (97 % Aldrich). A 50 ml, 0.5 wt % (c = 5 mg/ml) solution was prepared and mixed for 3 days in order to let the polymer dissolve and homogenize. Subsequently, the metal precursor was added to the solution, the amount depending on the polymer used (0.053 g for P4708-S2VP, 0.042 g for P18226-S2VP and 0.069 g for PS5073-S2VP) and left to incorporate inside the micelles. After a further 3 days stirring, an aliquot of P-Tosyl hydrazide (4-fold the concentration of metal) is dissolved in 50 ml of toluene and added to the solution and, ~3 minutes later, 0.5 ml of HCl (ACS reagent 37 %, Fluka) is added to the the solution and after ~ 10 min. the support, in powder form, is added to the solution. The supports used are:

Table 5.2.1 List of supports and their specification

Molecular Formula	Surface area	Purity	Source
Al_2O_3	100 m^2/g	99.9% (0.1% SiO_2)	Alfa Aesar
SiO_2	85-113 m^2/g	n.a.	Alfa Aesar
Si_3N_4	103-123 m^2/g	98.5+%	Alfa Aesar

and they were mixed to the solution in order to obtain a 1 % concentration on the support and left to stir-dry in air overnight (i.e. until all toluene evaporated). The samples were then calcined at 500 °C, in a static air for 2.5 h in an alumina crucible and subsequently characterized. Shown in table 5.2.2 is a summary of the samples prepared.

Table 5.2.2 List of samples

Sample Name	Polymer	Support
Pd/SiO_2 30-8.5	P18226-S2VP	Silicon oxide (SiO_2)
Pd/SiO_2 175-70	PS5073-S2VP	Silicon oxide (SiO_2)
Pd/SiO_2 16-3.5	P4708-S2VP	Silicon oxide (SiO_2)
Pd/Al_2O_3 30-8.5	PS5073-S2VP	Aluminium Oxide (Al_2O_3)
Pd/Si_3N_4 30-8.5	PS5073-S2VP	Silicon Nitride (Si_3N_4)

5.2.2 Catalyst testing

The samples prepared were tested for 1,3-Butadiene hydrogenation. The catalysts (~ 275 mg for Al_2O_3, and Si_3N_4 supported samples, ~ 165 mg for SiO_2 supported samples), with a sieve fraction 250 – 425 μm, were then loaded inside a reactor tube (7 mm diameter), and then placed inside a tubular furnace and connected with gas lines through Swagelok fittings. The samples were initially treated in H_2 in order to reduce PdO to Pd^0 (30 min under H_2 atmosphere at 323 K). After treatment the catalysts were brought to room temperature (~298 K) in order to compare the results obtained with previously published results and butadiene hydrogenation was performed using a space velocity of 22500 h^{-1} using a reaction mixture composed of hydrogen (4 % in Helium, BOC Ltd.) and 1,3-butadiene (1 % in Helium, BOC Ltd.) in a percentage ratio of 95.2/4.8, using helium to balance; the flow, in ml/min, was 150 H_2, 30 butadiene, 225 He respectively. In order to obtain a direct correlation between the catalytic

activity results and the in situ XAFS measurement the catalysts were regenerated in H_2 (30 min at 323K) and then the catalytic test was performed at 353K. The activity and selectivity was monitored using a mass spectrometer (MS) and gas chromatograph (GC). The Gas chromatograph was calibrated using a calibration mixture comprising (0.05% cis-2-butene, 0.15% trans-2-butene, 0.1 % N-butane, 0.3 % 1-butene all balanced in He, BOC). For all catalysts tested a first GC measurement was performed 10-15 seconds after the online MS was able to detect the first reaction products.

5.2.3 In situ XAFS

The measurements were performed on the B18 beamline at Diamond Light Source at the palladium *K* edge (24.35 keV) and were performed in transmission mode for 75.7 second per scan. The catalysts, using the sieve fraction of 125 – 250 μm, were loaded into a capillary and mounted on a catalyst test rig with the capillary connected to gas lines on one side and a residual gas analyser (MS) on the other. While under He flow, the catalysts were brought to 80 °C and subsequently different gases, 10 % H_2 in He, 1 % 1,3-butadiene in He and a mixture of the two (2:98 in relative %) were passed over the catalysts and XAFS spectra were recorded after the samples were kept under steady state for 20 min at each gas composition. In order to verify the reversibility of the system hydrogen (10 % in He) was passed over the catalyst after the reaction has been performed. Data processing and analysis were done using the Athena and Artemis software from the Demeter IFEFFIT package [280][281]. The FEFF6 code was used to construct theoretical EXAFS signals that included single-scattering contributions from atomic shells through the nearest neighbours in the face-centered cubic (FCC) structure of Pd, up to the fourth coordination shell The *k*-range used for the fitting 3 to 12 $Å^{-1}$ and the *r*-range from 1.15 to 3 Å. The path degeneracy was allowed to vary in the fit in order to account for the size effects that cause surface atoms to be less coordinated than those in the particle interior. The amplitude reduction factor (S_0^2) was fixed at 0.860, as obtained from the fitting of the bulk Pd foil. Due to the high correlation between Debye-Waller factor (DWF) and first shell coordination number (1CN) (>0.95) the fitting leads to a high error: the results obtained do not match with the variation that can be seen from the Fourier transform of the EXAFS data taken at different gat composition. Therefore, the DWF has been fixed to the results obtained by fitting the sample under 1,3-butadiene atmosphere. The XANES

data for PdH and PdC were obtain from previous experiment performed within the experimental group.

5.3 Results

5.3.1 Catalyst characterization

The TEM results are shown in Figures 5.3.1-5. The average particle size was obtained by analysing 150 nanoparticles (on average 5-10 images) taken from different parts of the catalyst in order to obtain a representative overview of the particle size distribution. In general, it appears the nanoparticles present themselves as spherical. It appears that the nanoparticles show a low dispersion in particle size, with the standard deviation being << 1 nm; moreover nanoparticles which were produced using the same polymer appear to present a similar particle size, evidence that the method can be applied when using different supports.

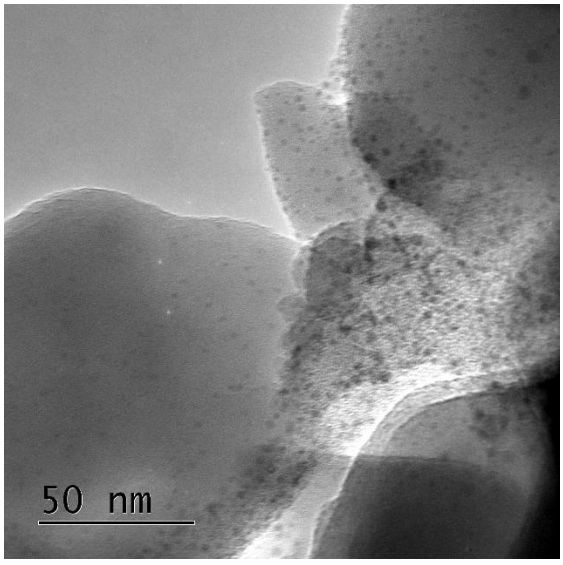

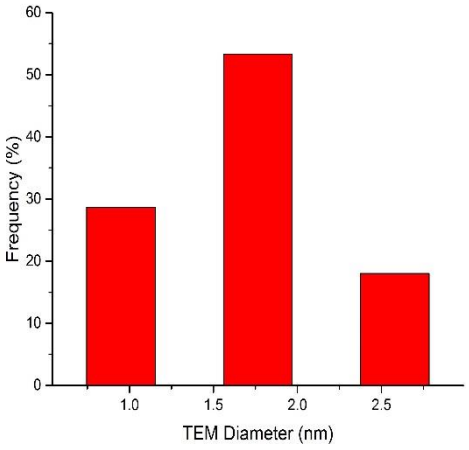

Average Particle size (nm)	1.9
Standard Deviation	0.3

Figure 5.3.1. On the left: TEM micrograph of Pd/SiO_2 30-8.5 samples; on the right: particle size distribution (150 particle counted towards particle size distribution)

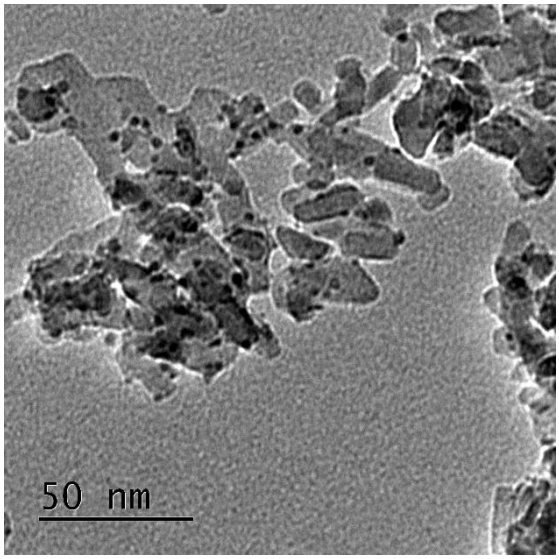

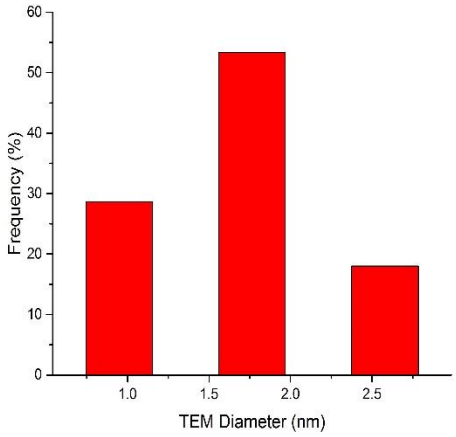

Average Particlesize (nm)	2.09
Standard Deviation	0.52

Figure 5.4.2. On the left: TEM micrograph of Pd/Al_2O_3 30-8.5 samples; on the right: particle size distribution (150 particle counted towards particle size distribution)

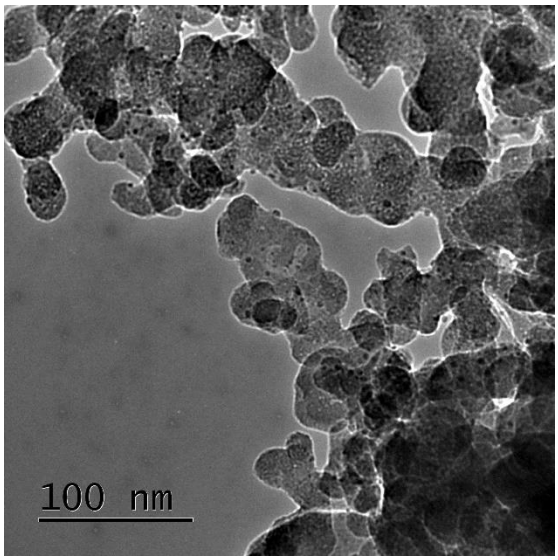

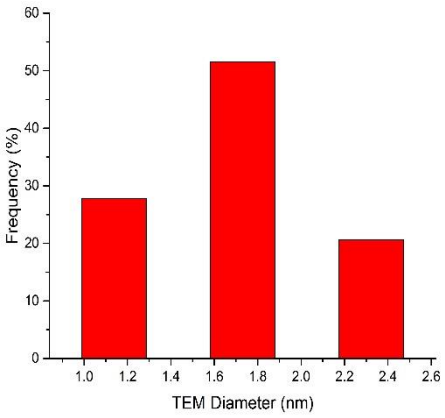

Average Particle size (nm)	2.07
Standard Deviation	0.51

Figure 5.4.3. On the left: TEM micrograph of Au/Si_3N_4 30-8.5 samples; on the right: particle size distribution (150 particle counted towards particle size distribution)

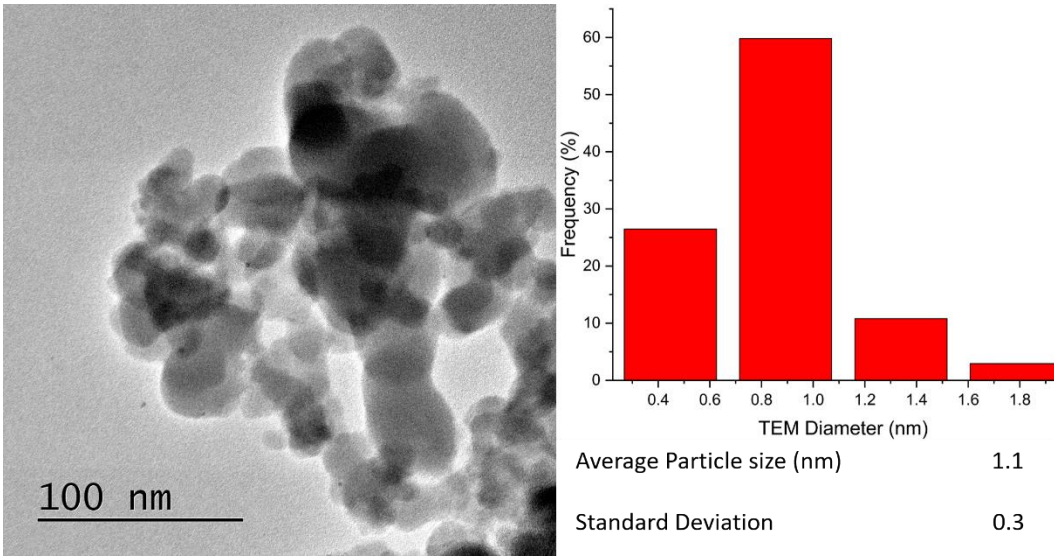

Figure 5.4.4. On the left: TEM micrograph of Au/SiO_2 16-3.5 samples; on the right: particle size distribution (150 particle counted towards particle size distribution)

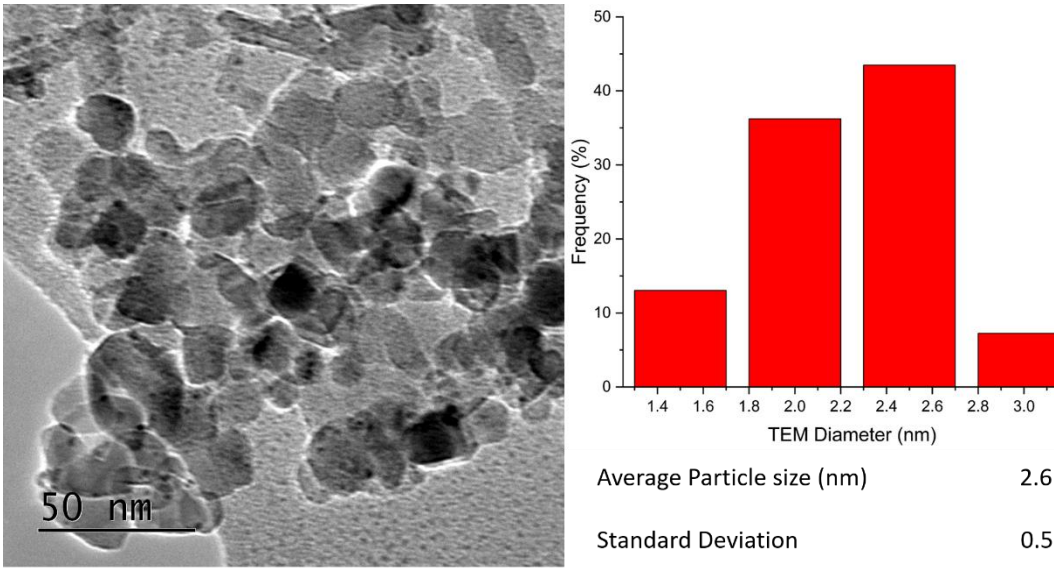

Figure 5.4.5. On the left: TEM micrograph of Au/SiO_2 175-70 samples; on the right: particle size distribution (150 particle counted towards particle size distribution)

In Table 5.3.1 are shown the TEM results obtained for all samples which provides an illustration of the 'number averaged' particle size, together with the particle size diameter obtained from EXAFS analysis which provides a particle size based on a bulk average [190]. Since the as prepared nanoparticle only present PdO it is not possible to extract particle size information from it. Thus, for the particle size calculation, the data used were from the nanoparticle after being subject to activation under H_2 and subsequent removal of PdH phase after reaction with 1,3-butadiene as

shown in chapter 5.4.2. In general, there is a good correlation between the two measurements with mostly < 1 nm difference. However, the particle size observed by EXAFS was always greater than that reported for TEM. This difference between the TEM and EXAFS results could be explained by the presence of larger Pd nanoparticles, not seen in the TEM area examined, thus increasing the Pd-Pd contribution in the EXAFS. We propose that since we did not observe any particles larger than the mean value, those which were present were few and large and therefore not likely to influence catalytic activity particularly

Table 5.3.1. List of samples and their mean particle size obtained from TEM and EXAFS respectively

Sample	Polymer used	Particle Size TEM (nm)	Particle Size EXAFS (nm)
Pd on SiO_2 (16-3.5)	P4708-S2VP	1.1 ± 0.3	2.4 ± 0.24
Pd on SiO_2 (30-8.5)	P18226-S2VP	1.9 ± 0.3	2.7 ± 0.27
Pd on SiO_2 (175-70)	PS5073-S2VP	2.6 ± 0.5	3.2 ± 0.32
Pd on Al_2O_3 (30-8.5)	PS5073-S2VP	2.1 ± 0.5	1.1 ± 0.1[1]
Pd on Si_3N_4 (30-8.5)	PS5073-S2VP	2.1 ± 0.5	3 ± 0.3
1. The value obtained from the fit could be influenced by the presence of PdH which lowers the amplitude of the EXAFS and therefore of the 1CN.			

5.4 Catalytic results

5.4.1.1 Test at 298 K

5.4.1.1.1 Effect of the support

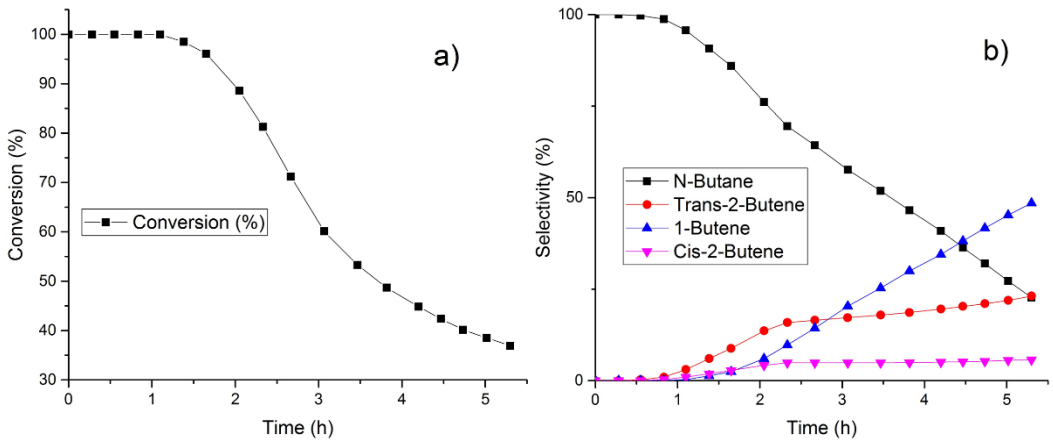

Figure 5.4.1. Evolution of conversion (a) and selectivity (b) for 1,3-butadiene hydrogenation over Pd/Al_2O_3 30-8.5 a function of time on stream.

The catalyst performance of the samples was investigated in the hydrogenation of 1,3-butadiene in order to get further insight into the role of the support and the effect of the particle size of Pd NPs. As seen in Figure 5.4.1 the Pd/Al_2O_3 30-8.5 sample converted completely the 1,3-butadiene to butane for the first hour of reaction. With time on stream (TOS) a decrease in conversion was observed (Figure 5.4.1a). As the activity decreased, it appeared that the product composition changed; a continuous drop in butane formation was accompanied by an increase in butene selectivity. The cause for this was likely to be due to a depletion of volume-adsorbed hydrogen which was supposed to be the responsible for over-hydrogenation [63]. After 4 hours of reaction the main product detected was 1-butene, with minor amounts of trans- and cis-2-butene also seen. This product distribution was commonly seen in literature but there was no explanation regarding its cause [172], [334]. The production of 1-butene was attributed to a 1,2-hydrogenation whereas the 1,4-hydrogenation produces the cis/trans-butenes. However the way these isomers were produced depends on the structure of the absorption layer and the availability of hydrogen [335]. In order, to compare the catalytic performance of the different samples studied, all catalytic reactions were allowed to continue until no further drop in conversion occurred. For Pd/Al_2O_3 30-8.5 the reaction was stopped after 5.3 h due its high activity which did not allow the sample to completely deactivate.

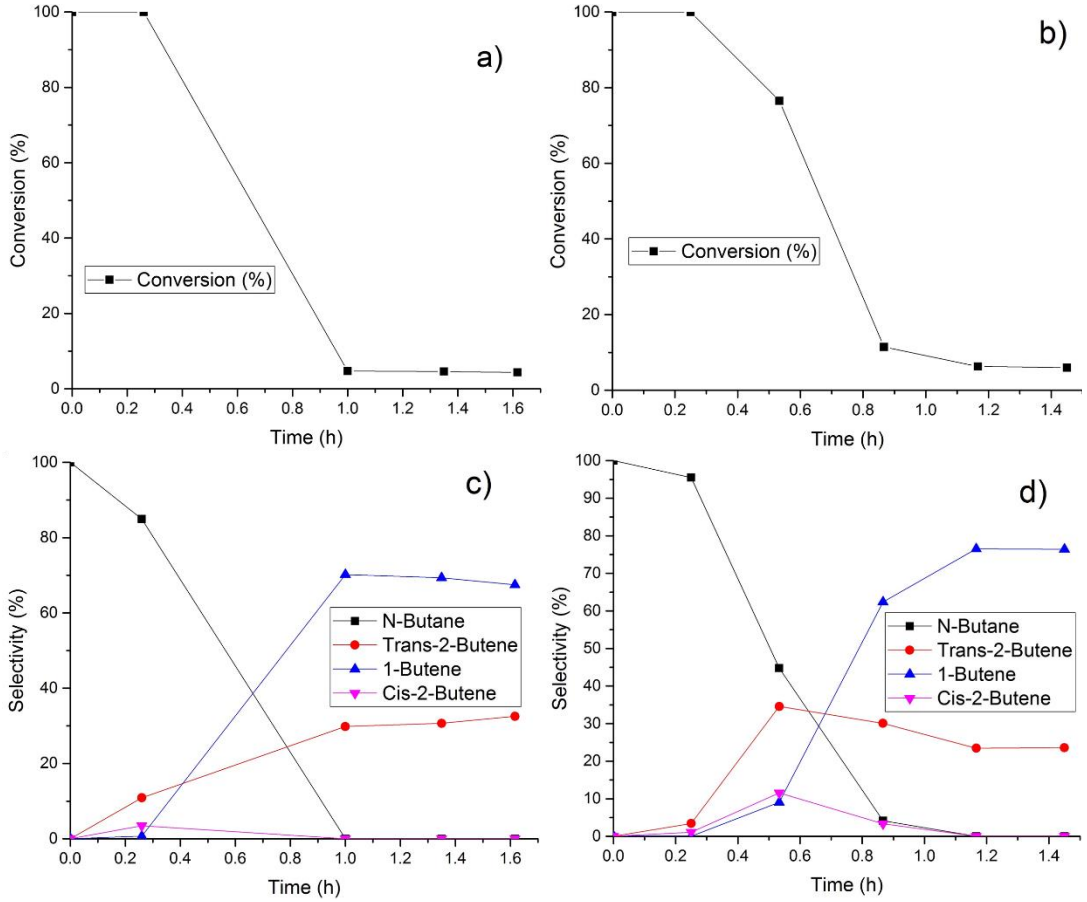

Figure 5.4.2. Evolution of conversion (a-b) and selectivity (c-d) for 1,3-butadiene hydrogenation over Pd/Si_3N_4 30-8.5 (a-c) and Pd/SiO_2 30-8.5 (b-d) as a function of time on stream.

The Pd/Si_3N_4 30-8.5 sample (Figure 5.4.2a-c) deactivates much more quickly than Pd/Al_2O_3 30-8.5 reaching a consistently low level of conversion after 1 h; a consequence of this was an increase in selectivity to *1*-butene. In Figure 5.4.2b-d is shown the catalytic performance of Pd/SiO_2 30-8.5. The deactivation of the catalyst and the selectivity profile for this catalyst appears to proceed similarly to the one reported for the Si_3N_4 supported sample shown in Figure 5.4.2. As can be seen from Table 5.4.1 the type of support appears to affect the activity considerably. After 1.4 h Pd/Al_2O_3 30-8.5 shows the highest conversion amongst the samples examined (98 % total conversion) but a low selectivity towards butenes (9.25 %). The samples supported on SiO_2 and Si_3N_4 performed worse in terms of conversion, (12.65 and 4.5 % respectively) but the selectivity to butenes was higher than for the Al_2O_3 supported sample, with no formation of *n*-butane; moreover, no formation of *cis*-2-butene was observed. This could be explained either by the absence of facets where the absorption of the 1,3-butadiene in a cis-configuration allows the 1,4-hydrogenation to happen, as well as a fast isomerization process skewed towards the production of trans-2-butene.

After 5.3 h of reaction the Al_2O_3 supported sample conversion drops to 37 %, drastically improving its selectivity towards butenes (from 9.25 to 77.3 %).

Table 5.4.1. Catalytic activity/selectivity comparison between samples with similar Pd particle size but different support, SiO_2, Si_3N_4 and Al_2O_3 at 1.4 h time on stream. The error for each measurement is 10% of the measurement.

Sample	Conversion (%)	N-Butane selectivity (%)	Trans-2-Butene selectivity (%)	1-Butene selectivity (%)	Cis-2-Butene selectivity (%)
Pd/Al_2O_3 30-8.5	98.4	90.8	6	1.3	1.9
Pd/Si_3N_4 30-8.5	4.3	0	32.6	67.1	0
Pd/SiO_2 30-8.5	5.9	0	23.6	76.4	0

5.4.1.1.2 Effect of particle size

SiO_2 supported samples were used to investigate the particle size effect of Pd on 1,3-butadiene hydrogenation. The three samples appeared to show that a particle size effect was indeed present. In Figure 5.4.3 are shown the catalytic profiles for the SiO_2 supported sample, summarized in Table 5.4.2 for clarity. It appeared that the Pd/SiO_2 30-8.5 sample presented the lowest activity amongst the SiO_2 supported catalysts tested (12.65 % conversion) with Pd/SiO_2 16-3.5 presenting the highest activity overall (31.57 % conversion). These results showed an unexpected reverse volcano plot. The selectivity for all the samples were similar: Pd/SiO_2 16-3.5 and 175-70 (1.1 and 2.6 nm respectively) showed the production of *cis*-2-butene after 1.5 h, possibly due to isomerization from *trans*-2-butene, since the amount of 1-butene obtained from all the reaction was consistently ~75 % of the total product.

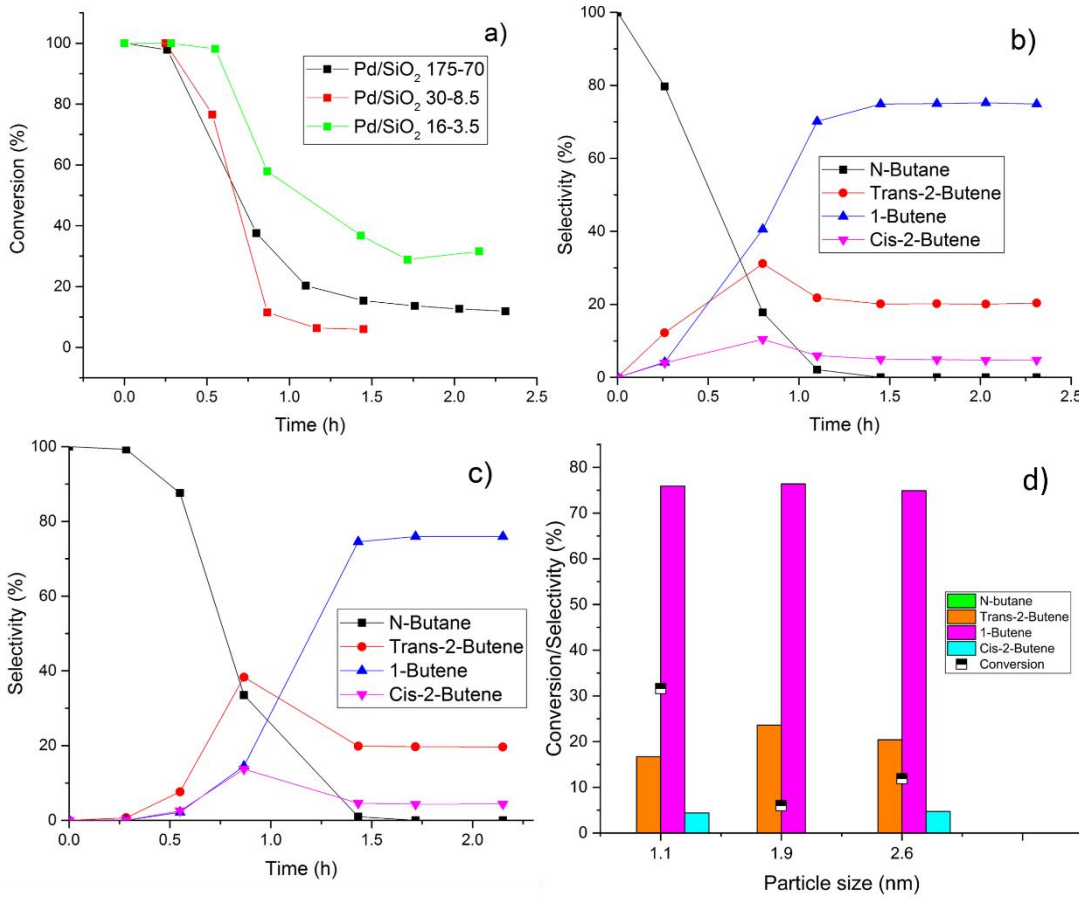

Figure 5.4.3. Evolution of conversion (a) and selectivity (b(Pd/SiO_2 175-70)-c(Pd-SiO_2 16-3.5) for 1,3-butadiene hydrogenation over Pd/SiO_2 catalysts as a function of time on stream. In d) comparison of conversion and selectivity as dependent on particle size.

Table 5.4.2. Catalytic activity/selectivity comparison between samples supported on SiO_2 but different particle size (1.1, 1.9, 2.7 nm respectively) after 1.5h. The error for each measurement is 10% of the measurement.

Sample	Conversion (%)	N-Butane selectivity (%)	Trans-2-Butene selectivity (%)	1-Butene selectivity (%)	Cis-2-Butene selectivity (%)
Pd/SiO_2 16-3.5	31.6	0	19.7	75.9	4.4
Pd/SiO_2 30-8.5	6	0	23.6	76.4	0
Pd/SiO_2 175-70	11.9	0	20.4	74.9	4.7

5.4.1.2 Test at 353K

5.4.1.2.1 Effect of support

The catalysts were tested following the same procedure at 353 K in order to replicate the condition present during XAFS data acquisition. Pd/Al_2O_3 30-8.5 was tested for 6 hours but no decrease in conversion was observed compared to the room temperature. The only product was n-butane even after 6 hours of time on stream. Pd/SiO_2 30-8.5 (figure 5.4.4a) on the other hand produces no n-butane throughout the reduction process. Compared to room temperature, the catalytic conversion increased, from ~ 6 to ~ 20 % as shown in table 5.4.3. Interestingly the Pd/Si_3N_4 30-8.5 (figure 5.4.4b) behaviour is drastically different compared to room temperature, from 4 % to 100 %, paired with a loss in selectivity towards the formation of n-butane (table 5.4.3). Due the scarce literature regarding Si_3N_4 as support it is hard to gauge the reason for this drastic difference. However, it could be supposed that Si_3N_4 supported sample require higher temperature to activate under hydrogen (353K vs 323K for the room temperature test) compared to SiO_2 and Al_2O_3 supported sample.

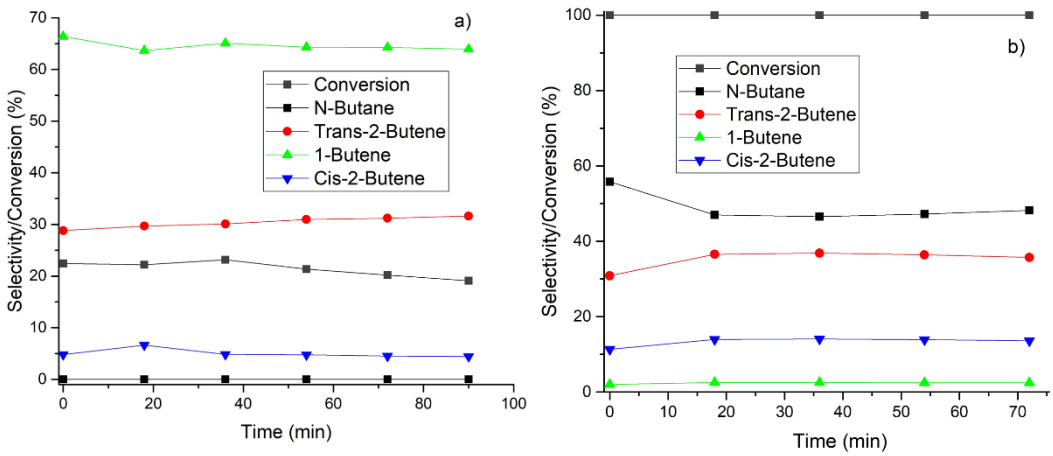

Figure 5.4.4. Evolution of conversion and selectivity for 1,3-butadiene hydrogenation over a) Pd/SiO_2 30-8.5; b) Pd/Si_3N_4 30-8.5 as a function of time on stream

Table 5.4.3. Catalytic activity/selectivity comparison between samples with similar Pd particle size but different support, SiO_2, Si_3N_4 and Al_2O_3 at 1.3. h time on stream. The error for each measurement is 10% of the measurement.

Sample	Conversion (%)	N-Butane selectivity (%)	Trans-2-Butene selectivity (%)	1-Butene selectivity (%)	Cis-2-Butene selectivity (%)
Pd/Al_2O_3 30-8.5	100	100	0	0	0
Pd/Si_3N_4 30-8.5	100	48.2	35.7	2.4	13.6
Pd/SiO_2 30-8.5	20.2	0	31.2	64.3	4.5

5.4.1.2.2 Effect of particle size

Regarding the particle size effect, it appears that the activity profile (Pd/SiO_2 1.1 nm > 2.6 nm > 1.9 nm) shown in figure 5.4.3 is still present at higher temperature, albeit the difference in catalytic performance, as shown in table 5.4.4 and figure 5.4.5-6 (from ~31% to 100% for Pd/SiO_2 16-3.5 and from ~12% to ~90% for Pd/SiO_2 175-70). However, the selectivity changes quite dramatically for Pd/SiO_2 175-70 and 16-3.5 compared to the results obtained at lower temperature (figure 5.4.3 b-c and table 5.4.2). The major product appears to be the over-hydrogenated n-butane, possibly due the higher reaction rate caused by the higher temperature. Moreover, trans-2-butene becomes the predominant product among the butenes, suppressing the production of cis-2-butene and 1-butene. Interestingly this behaviour does not appear in the case of Pd/SiO_2 30-8.5. This could be related to the lower catalytic activity, which, other than preventing the formation of n-butane, causes the selective formation of 1-butene.

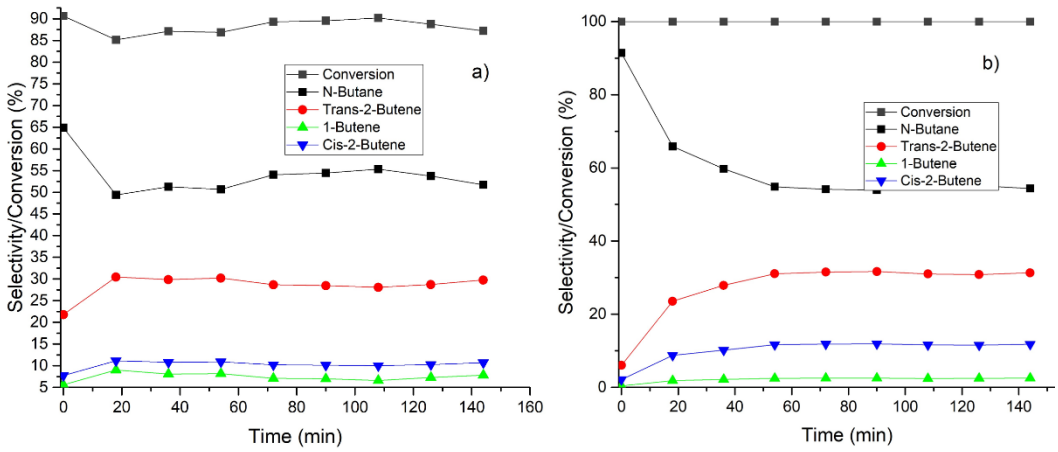

Figure 5.4.5. Evolution of conversion and selectivity for 1,3-butadiene hydrogenation over a) Pd/SiO_2 175-70; b) Pd/SiO_2 16-3.5 as a function of time on stream

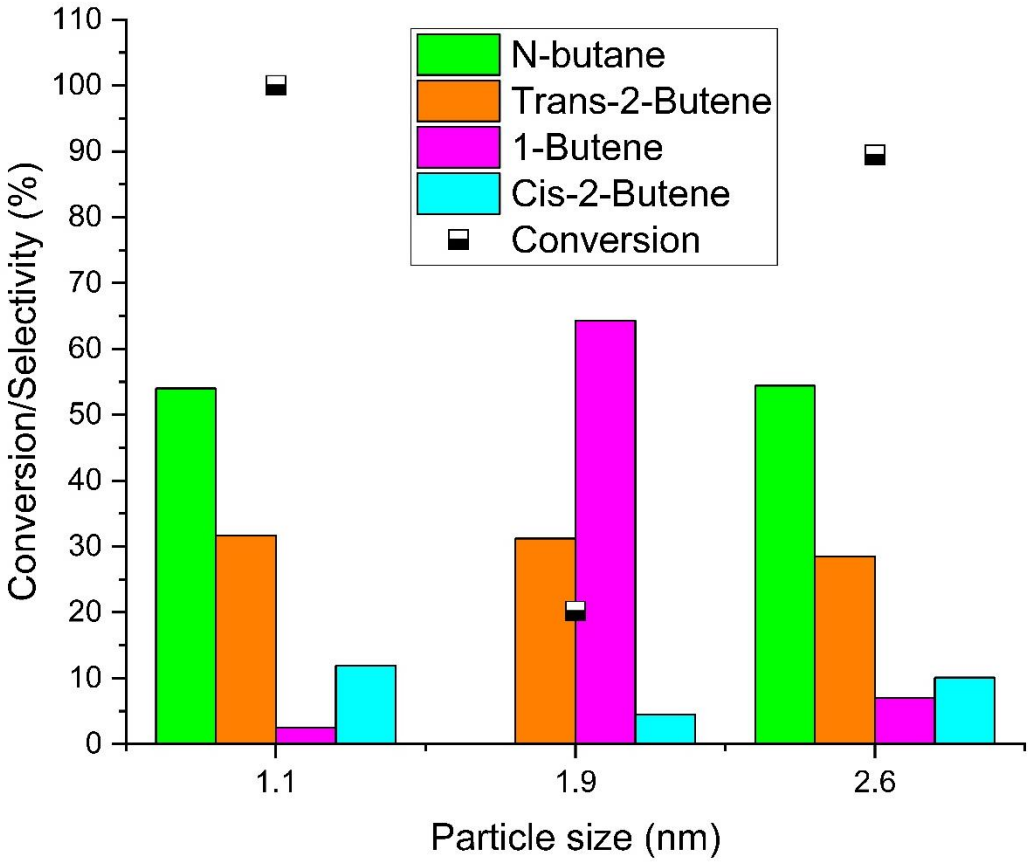

Figure 5.4.5. Conversion and Selectivity as dependent on particle size for SiO_2 supported nanoparticles

Table 5.4.4. Catalytic activity/selectivity comparison between samples supported on SiO_2 but different particle size (1.1, 1.9, 2.7 nm respectively) after 1.5h. The error for each measurement is 10% of the measurement.

Sample	Conversion (%)	N-Butane selectivity (%)	Trans-2-Butene selectivity (%)	1-Butene selectivity (%)	Cis-2-Butene selectivity (%)
Pd/SiO_2 16-3.5	100	53.9	31.7	2.5	11.9
Pd/SiO_2 30-8.5	20.2	0	31.2	64.3	4.5
Pd/SiO_2 175-70	89.5	54.4	28.5	7	10.1

5.4.2 In situ XAFS

The 1,3-butadiene hydrogenation has been followed using X-ray absorption spectroscopy in order to identify any evolution of the Pd nanoparticle under reaction conditions. In figure S5.1-5 are shown the XANES and k-range data EXAFS for all the samples.

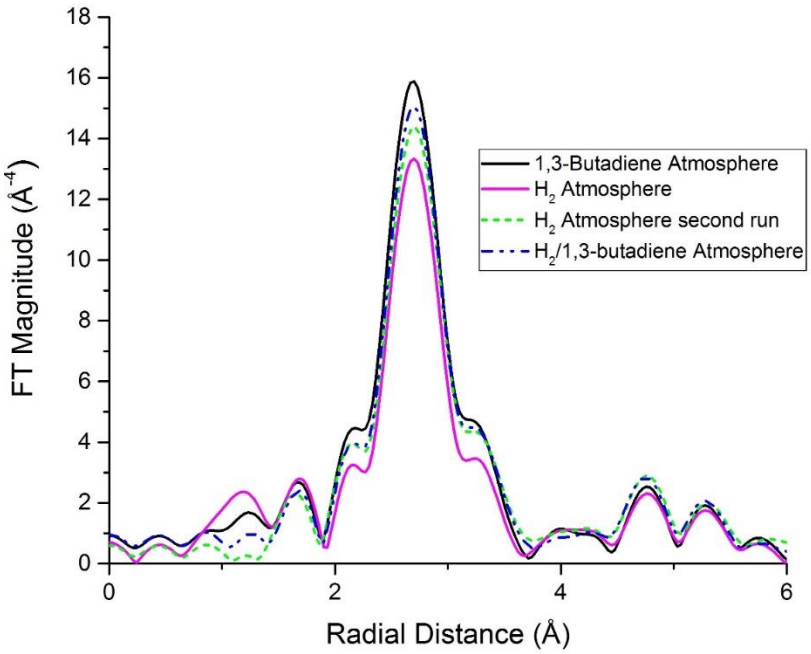

Figure 5.4.7. k^3-weighted Fourier transform of Pd/SiO_2 30-8.5, under hydrogen and 1,3-butadiene and the mixture of the two (H_2/1,3-butadiene ratio 49/1 during reaction). As the gas composition changes a change in intensity of the first Pd-Pd scattering shell (~ 2.7 Å), as a result of the 'gas interaction' with the Pd nanoparticles.

The gas sequence, as stated in section 5.2.3 is the following: H_2 atmosphere, 1,3-butadiene atmosphere, the mix of the two gases, H_2/1,3-butadiene atmosphere and subsequently H_2 atmosphere again. A clear change in the EXAFS can be seen with the changes in the FT as the gas composition varies, as shown in Figure 5.4.7 for Pd/SiO_2 175-70. As the composition changed from H_2 (pink solid line in the figure) to 1,3-butadiene (solid black line), a sizeable increase (14 %) in the first shell FT intensity appeared. Subsequently after the introduction of the reaction mixture, a minor decrease by 3 % of FT intensity occurred, followed by a further 3 % decrease as the gas atmosphere changed back to H_2. The same behaviour was observed for all the other samples examined, as shown in Figure 5.4.8, where the most significant FT intensity changes are shown, and that this change occurred from switching of the H_2 atmosphere to 1,3-butadiene.

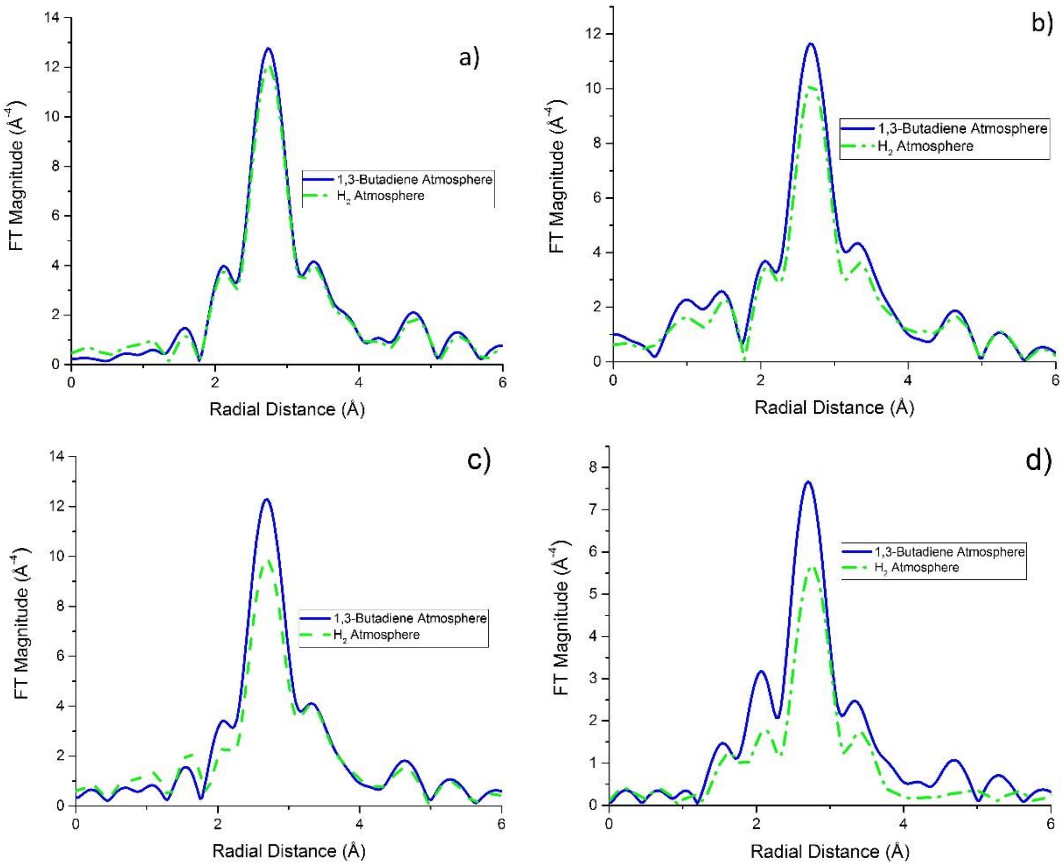

Figure 5.4.8. k^3-weighted Fourier transform of: a) Pd/SiO_2 30-8.5; b) Pd/SiO_2 16-3.5; c) Pd/Si_3N_4 30-8.5; d) Pd/Al_2O_3 30-8.5; under two different atmospheres, hydrogen and 1,3-butadiene. As the gas composition changed an increase in the intensity of the Pd-Pd scattering first shell contribution was observed.

Table 5.4.5. EXAFS fit results obtained from Pd/SiO_2 30-8.5, using a constant Debye-Waller factor, as a function of the gas composition

Gas composition	**1CN**	**1st shell radius (Å)**	**ΔE**	**R_{factor}**
Hydrogen	9.76 ± 0.42	2.745 ± 0.004	-4.0 ± 0.6	0.021
1,3-Butadiene	10.32 ± 0.44	2.737 ± 0.002	-3.8 ± 0.3	0.004
Hydrogen/ 1,3-Butadiene	10.16 ± 0.36	2.742 ± 0.004	-3.8 ± 0.5	0.013
Hydrogen (After reaction)	10.06 ± 0.45	2.744 ± 0.005	-5 ± 0.5	0.023

In order to understand the changes, a fit of the data was needed. In Figure 5.4.9 is shown one example of the results of an EXAFS fit for Pd/SiO_2 175-70, to show the good agreement between the experimental and simulated data. The other fit results are shown in Figure S5.6-11. In Tables 5.4.5-9 are summarized the results obtained from the fit and it can be seen that for all catalysts, in the presence of 1,3-butadiene an increase in the 1st shell coordination (1CN) number and a slight decrease in the Pd-Pd bond distance was observed. This, we propose, could be explained by a removal of palladium hydride (PdH) from the Pd nanoparticles. The reason for this increase can be attributed to the removal of the interference between Pd and PdH EXAFS signals, as illustrated in Figure S5.12. The EXAFS signal for the PdH phase has a lower amplitude and is heavily out of phase with Pd^0 scattering phase, leading to a reduction in the total EXAFS amplitude. Hence the presence of PdH is strongly inferred by the changing FT intensities with/without hydrogen flowing. As can be seen from table 4, under reaction conditions (H_2/1,3-butadiene) the 1st coordination number (1CN) clearly decreases. A reduction in FT intensity for the Pd-Pd contribution is seen under reaction conditions suggestive of the (re)appearance of the hydride phase, the extent of its formation seemingly mitigated by the presence of 1,3-butadiene during the reaction process.

Table 5.4.7. EXAFS fit results obtained from Pd/SiO_2 175-70, using a constant Debye-Waller factor, as a function of the gas composition

Gas composition	**1CN**	**1st shell radius (Å)**	**ΔE**	**R_{factor}**
Hydrogen	9.59 ± 0.53	2.746 ± 0.006	-5.11 ± 0.85	0.009
1,3-Butadiene	10.94 ± 0.81	2.740 ± 0.004	-5.04 ± 0.52	0.002
Hydrogen/ 1,3-Butadiene	10.63 ± 0.31	2.744 ± 0.003	-5.12 ± 0.44	0.002
Hydrogen (After reaction)	10.33 ± 0.43	2.743 ± 0.0045	-4.87 ± 0.63	0.005

Table 5.4.8. EXAFS fit results obtained from Pd/SiO_2 16-3.5, using a constant Debye-Waller factor, as a function of the gas composition

Gas composition	1CN	1st shell radius (Å)	ΔE	R_{factor}
Hydrogen	8.56 ± 0.58	2.746 ± 0.007	-4.64 ± 0.97	0.015
1,3-Butadiene	10.14 ± 0.88	2.738 ± 0.004	-4.28 ± 0.62	0.003
Hydrogen/ 1,3-Butadiene	10.06 ± 0.48	2.736 ± 0.005	-4.54 ± 0.7	0.007
Hydrogen (After reaction)	9.73 ± 0.35	2.743 ± 0.004	-4.51 ± 0.51	0.004

Table 5.4.9. EXAFS fit results obtained from Pd/Si_3N_4 30-8.5, using a constant Debye-Waller factor, as a function of the gas composition

Gas composition	1CN	1st shell radius (Å)	ΔE	R_{factor}
Hydrogen	8.86 ± 0.42	2.747 ± 0.005	-6.41 ± 0.68	0.007
1,3-Butadiene	10.89 ± 0.61	2.739 ± 0.003	-5.895 ± 0.402	0.001
Hydrogen/ 1,3-Butadiene	10.84 ± 0.45	2.745 ± 0.004	-5.8 ± 0.61	0.006

Table 5.4.10. EXAFS fit results obtained from Pd/Al_2O_3 30-8.5, using a constant Debye-Waller factor, as a function of the gas composition

Gas composition	1CN	1st shell radius (Å)	ΔE	R_{factor}
Hydrogen	5.35 ± 0.69	2.752 ± 0.007	-7.49 ± 1.11	0.018
1,3-Butadiene	7.27 ± 2.79	2.737 ± 0.004	-7.75 ± 0.62	0.004
Hydrogen/ 1,3-Butadiene	7.65 ± 0.69	2.752 ± 0.007	-6.07 ± 1.2	0.016
Hydrogen (After reaction)	6.72 ± 0.53	2.77 ± 0.01	-8.09 ± 1.8	0.038

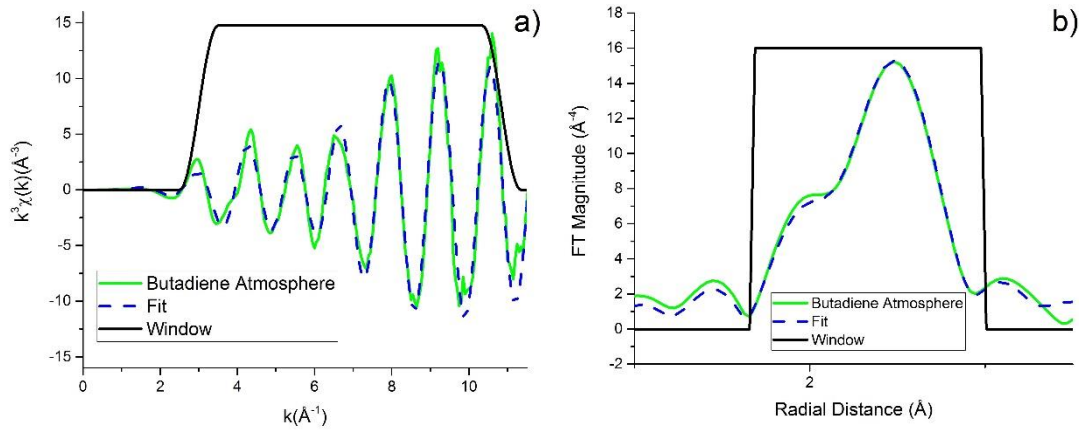

Figure 5.4.9. k^3-weighted EXAFS fit in k (on the left) and R (on the right) space of Pd/SiO_2 175-70 under 1,3-butadiene atmosphere

The accompanying XANES spectra of Pd/Al_2O_3 30-8.5, shown in Figure 5.4.10, appeared to confirm the presence of PdH in the sample when it was under H_2, due to the characteristic edge shift towards lower energy compared to metallic palladium indicated in the figure by arrow 1, as shown by Bugaev et al [328]. This was further evidenced by the shift of the first multiscattering component of the XANES (indicated by arrow 2 in the figure) due to the different scattering contribution of PdH. However, when the Al_2O_3 supported sample was kept under 1,3-butadiene atmosphere a further shift towards higher energy appeared which suggested the formation of palladium carbide. This was further indicated by a strong shift of the multiple scattering component (arrow 2) towards higher energy which suggested a noticeable formation of PdC and the subsequent change in the scattering contribution.

The high amount of PdC caused a reduction in the intensity of the EXAFS signal (particularly Pd-Pd contribution in the FT) for the same reason as formation of PdH does [328].

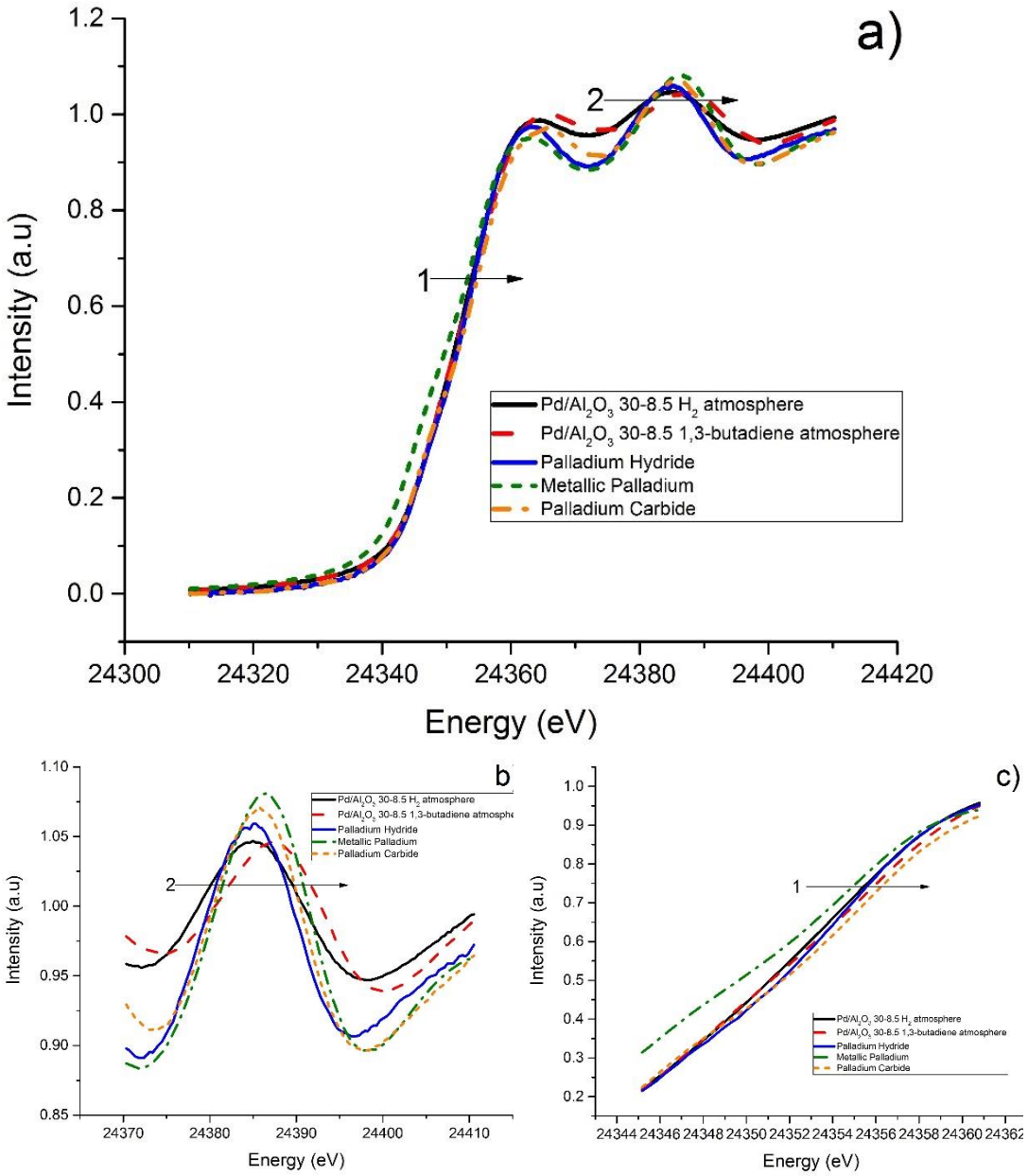

Figure 5.4.10. a) XANES spectra of Pd/Al_2O_3 30-8.5 under H_2 and 1,3-butadiene, compared to Pd^0 and PdH reference. Arrows 1 and 2 indicate the shift towards higher energy of the Pd K-edge signal due to hydride and carbide formation; b) close-up of the edge shift indicated by arrow 1; c) close-up of the feature indicated by arrow 2.

5.5 Discussion

The catalytic results obtained here match well with previous reported literature; a study similar to the one here reported by Cerventes et al. showed the same support influence using the supports examined here [336]. This was inclusive of a similar deactivation effect with TOS although the time required for deactivation for the samples used in this work was much shorter, roughly a third of what was reported using similar reaction conditions albeit the Cerventes study used a slightly lower H_2/1,3-butadiene ratio (87/13) compared to the ones used here (98/2). The authors speculated that the deactivation was due to the formation of carbonaceous species on the surface of the nanoparticles. The role of these carbonaceous species on the selectivity of the Pd nanoparticles is still under discussion; according to some studies, a pre-treatment of 1,3-butadiene leads to a sharp decrease in activity and to a higher quantity of *n*-butene produced due to formation of PdC on the surface, identified through the expansion of the Pd lattice by XRD [337], [338]. However. another study showed that in a fixed bed reactor at 298 K and using a molar ratio of the reaction mixture 1:1.2 1,3-butadiene/H_2, a greater amount of 1-butene was observed with time and which was thought to be due to butadiene oligomers forming a carbonaceous overlayer and increasing this selectivity, albeit with a reduction of activity [339]. The reason for this variation in results using similar catalysts might lie in the different reaction conditions applied in both cases: batch [337], [338] and fixed bed reactor [339] studies. The presence of palladium carbide was shown to apply a dramatic effect in increasing the amount of sub-surface palladium hydride, which has shown to be a key factor in the hydrogenation of butenes [63]. It reasonable to assume that in a batch reaction the longer retention time of hydrocarbon on the surface causes the formation of a carbonaceous layer, thus causing an over-hydrogenation of the butenes.

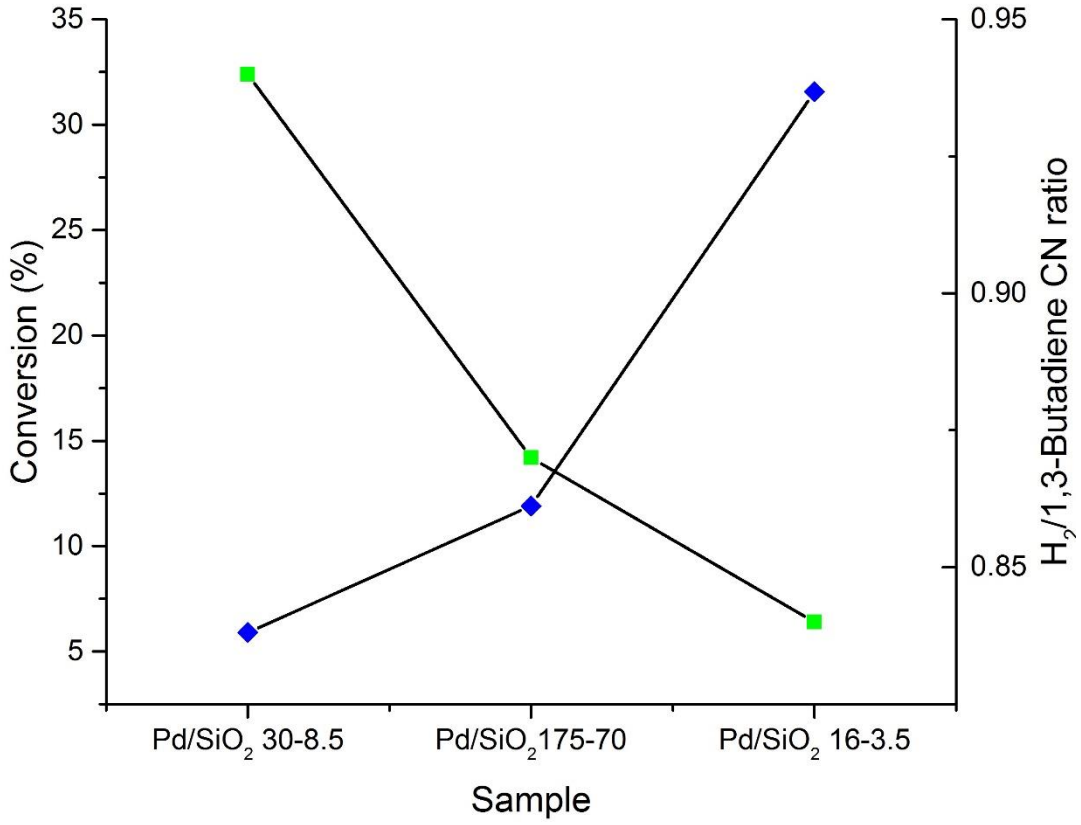

Figure 5.5.1. Variation of conversion as function of the PdH concentration, calculated as the ration between the coordination number of the sample under H_2 atmosphere and 1,3-butadiene atmosphere, for Pd/SiO_2 supported samples. The conversion results shown are for the sample at room temperature after 1.5h.

The importance of PdH in the formation of n-butene can be seen through the EXAFS results obtained. The phase diagram shown in figure 5.5.2 shows that at the pressure and temperature used in the experiment it is possible to have an H/Pd ratio of 0.6 at 0.1 atm of H_2 further confirming the results obtained by the XAFS.

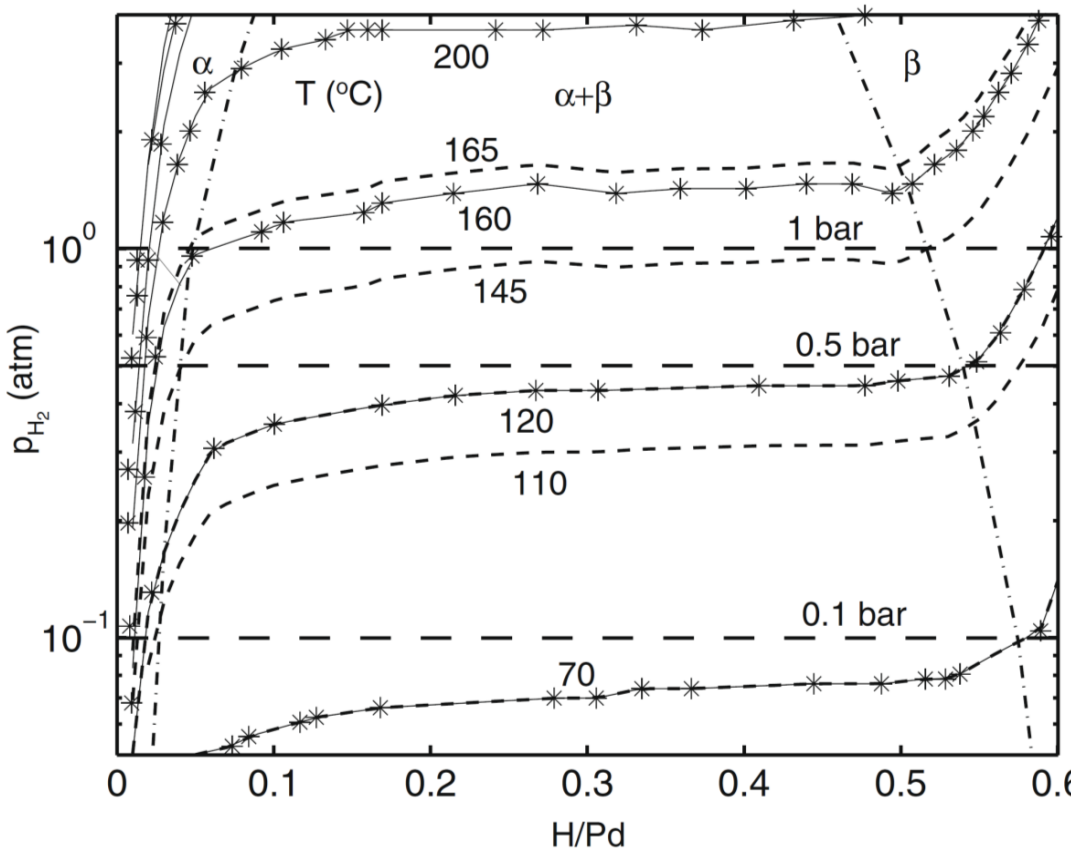

Figure 5.5.2. The equilibrium pressure of hydrogen as a function of the bulk H/Pd ratio. Reproduced with permission from Elsevier, Johansson et al, Surface science, vol 604, 2010, pp. 718-729 [152].

The amount of PdH present in the samples, calculated as the ratio of the CN of the samples under H_2 atmosphere over the CN of the samples under 1,3-butadiene, in particular in the case of Pd/SiO_2, can be directly correlated to the catalytic activity as shown by figure 5.5.1. A greater presence of hydride corresponds to a greater butadiene conversion to butane. In a previously reported study on the isomerization and hydrogenation of *cis*-2-butene, it was shown that while the hydrogenation activity decreased, the isomerization rate remained constant [63]. The authors attributed this behaviour to a lack of hydrogen capable of reacting with the carbon-carbon double bond. As time on stream increased the hydrogenation became selectively suppressed because bulk H species are consumed and cannot be replenished under steady-state conditions. Is therefore plausible that in this previous study that the presence of interstitial hydrogen was directly correlated to the catalytic conversion and its removal preventing the formation of n-butane. This phenomenon was clearly visible in the

Pd/Al_2O_3 30-8.5 sample, where the large amount of PdH, even after being under a 1,3-butadiene atmosphere for ~ 30 min. It appears that Al_2O_3 is able to promote significant formation of PdH which leads to an extensive formation of *n*-butane. However, amongst the other samples, the behaviour of Pd/Si_3N_4 30-8.5 appeared to be an outlier; whereas the amount of hydride found was higher than for the SiO_2 samples, the activity was actually the lowest. This could be explained by suggesting that the support plays more of a role in the catalytic process than just to facilitate PdH formation. The results obtained from the Pd/SiO_2 30-8.5 shows catalytic performances more akin to the Si_3N_4 support sample rather than the Al_2O_3 one, albeit with a slightly higher catalytic activity. The different behaviour observed for SiO_2 and Si_3N_4 supported samples, compared to Al_2O_3, could be caused by the lack of replenishment of interstitial hydrogen and paired with a lack in the formation of PdC, possibly due a different metal-support interaction. In general, it appears that the presence of PdH (possibly in conjunction with PdC) is detrimental to the selectivity towards butenes, causing a higher production of *n*-butane; working on the basis that excessive PdC formation is detrimental to catalyst performance in general, it can be assumed that the active phase toward the production of butenes is metallic Pd as shown by the higher selectivity of SiO_2 and Si_3N_4 supported samples. This is further highlighted in the catalytic results obtained at 353 K, where Pd/Al_2O_3 appears to produce only n-butane due to the high amount of PdH still present in the system. Interestingly the activity/selectivity for Si_3N_4 30-8.5 changes quite dramatically between room temperature and 353 K, with a drastic improvement in the activity (from 4% to 100%) but a drop in selectivity (the amount of n-butane formed went from 0% to ~48%). However, it has to be noted that this results correlate well with the EXAFS results here obtained, which see Pd/Si_3N_4 presenting a larger increase, compared to the SiO_2 supported samples, to its coordination number when the atmosphere is switched from H_2 to 1,3-butadiene. A possible explanation for the different behaviour of Pd/Si_3N_4 30-8.5 between 298 and 353 K could be attributed to a higher activation barrier required for bulk PdH formation on the nanoparticles. This explain the low deactivation time at low temperature as only surface PdH is formed and is quickly depleted.

It appears also that particle size affect quite dramatically the behaviour of Pd supported catalyst on 1,3-butadiene hydrogenation. Small nanoparticle (Pd/SiO_2 16-3.5 ~1 nm), which possess a higher amount of undercoordinated atoms, appear the most active

overall. The undercoordinated atoms are often tied to an increase of activity when the particles are below 4 nm, due their behaviour being similar to Pd (110) facets in activity [172], [173]. This leads to an overall increase in the activity compared to larger particles (Pd/SiO_2 30-8.5 ~1.7 nm). The increase of activity for the bigger particle (Pd/SiO_2 175-70 ~2.6 nm) compared to 1.7 nm supported samples could be due the formation of Pd(100) or Pd (111) terraces which has been previously proved to increase the activity [173].

5.6 Conclusion

Due to the synthesis method, which allowed a high control over the particle size of the nanoparticle, a clearer understanding of the effect of particle size and support effects for Pd nanoparticle in the hydrogenation of 1,3-butadiene has been reached and in particular we observe:

1. a clear the correlation between the hydride phase and the catalytic behaviour of the system; the presence of a large amount of PdH leads to the formation of over-hydrogenated species (*n*-butane), particularly in the case of the Al_2O_3 supported sample;
2. the active phase toward the selective production of butenes is metallic palladium, being the only phase present in the more selective SiO_2 and Si_3N_4 supported samples;
3. the support plays an important role in the activity of the catalyst as it can be seen by the low activity, but higher selectivity, of the Si_3N_4 supported sample (~ 4 % conversion at later stage of deactivation) at room temperature and the SiO_2 sample becoming more selective due the lower formation of PdH.
4. particle size plays also an important role in determining the catalytic activity of Pd NPs. The observation of a reverse volcano plot can be understood in terms of either the very high surface area of very small nanoparticles (1.1 nm) or else to the presence of highly-active, low-index facets, (i.e. (100) and (111)), for nanoparticles 2.6 nm in size. The catalyst (Pd/SiO_2 30-8.5) which possesses an intermediate particle size (i.e. with a lower surface area than the smallest particle but with smaller low-index facets than the largest particle size) shows the least activity.

6 Conclusion

Chapter 3 was dedicated to understanding mechanism of formation of nanoparticles and the identify of variables which influence the possible synthetic outcomes. The results obtained through both ex-situ and in-situ characterisation allows for the identification of a possible reaction scheme, shown in figure 3.4.1. It was also possible to observe that HCl is able to catalyse the reaction and the addition of it is necessary to faster obtain nanoparticles. These results would allow a better planning of the synthesis process as well as to allow for modifying the synthesis procedure for the possible preparation of bimetallic species of different nature (random alloy or core-shell) depending on the synthesis variables. The ability of reverse micelle to complex metal precursor has been here shown so it is reasonable to assume that by varying the required synthesis procedures (time, amount of precursors) it is possible to produce the required structure with relative ease. This would also allow to produce structure which are less commonly explored such as an Au shell/Pd core structure, as well as vary the thickness of both the core and the shell.

Using this method, it was possible to prepare nanoparticles with all the required properties necessaries to study the effect of particle size and support on the catalytic hydrogenation of 1,3-butadiene. In particular the most important aim was to produce the nanoparticle with a particle size as narrow as possible (<<1 nm) which would allow for a clear identification of structure-activity relationship. For Au nanoparticles this result was obtained as shown by the high correlation between XAFS and TEM data, reported in table 4.3.4. Thanks to the high homogeneity in particle size, it was possible, for supported Au nanoparticles, to obtain the information that during the reaction of hydrogenation of 1,3-butadiene, Au nanoparticles are not just static in their structures but they modify their shape according to the gas composition, a behaviour which appears to have an effect in the resulting activity/selectivity profile. However, the driving force behind the restructuring it has to be fully defined yet. A reasonable explanation would be the interaction of mobile atoms with the interacting gases, paired with electronic interaction with the support. The presence of mobile atoms could be explained by looking at the Hütting (T_h) and Tammann (T_t) temperatures, temperatures at with atoms at the surface (Hütting) or in the bulk (Tammann) become mobile. For

small particles these temperatures become so low (T_t ~300 K for a 2 nm particle) that restructuring become easily available. However, as the particles gets larger their melting temperatures, as well as their Hütting and Tammann temperature, increases exponentially. This could allow for some possible shape selective annealing for lager particle which operates at temperature well below their Hütting temperatures, by a simple modification of the annealing environment (e.g. H_2 instead of O_2). Possible theoretical calculation, paired with further experimental studies on size-selected nanoparticles catalysts, would allow to shine light on the driving force behind nanoparticle reshaping as well as indicate what would be the ideal structure to obtain the required activity/selectivity profile.

Similarly to Au nanoparticles, Pd nanoparticle were produced in an homogenous size, as shown by table 5.3.1, and it was possible to obtain information on the structure-activity relationship. In the case of Pd supported nanoparticles the results obtained demonstrate the effect of the PdH species on the activity and selectivity, which has been previously speculated but never shown through the use accurate techniques such as XAFS. In particular, a higher presence of PdH appears to be strongly correlated to an increase in the formation of over-hydrogenated species (e.g. *n*-butane in the case of the hydrogenation of 1,3-butadiene), which are often the least desirable product of hydrogenation reactions. Moreover, it appears that the presence of PdH is related to both particle size and support, with Al_2O_3 supported particles able to retain a significant amount of Pd species even under reaction condition.

The information obtained for both Au and Pd nanoparticulate catalysts would allow for a more rational approach in preparing the most optimal catalyst for the hydrogenation of 1,3-butadiene, but also allow to shine light on the importance of studying highly uniform system, where the properties of the nanoparticles are not obscured by the averaging caused by a large distribution of particle size, but instead able to being correlate with their function.

7 Bibliography

[1] R. Schlögl, “Heterogeneous Catalysis,” *Angew. Chemie Int. Ed.*, vol. 54, no. 11, pp. 3465–3520, Mar. 2015.

[2] B. Lindström and L. J. Pettersson, “A Brief History of Catalysis,” *CATTECH*, vol. 7, no. 4, pp. 130–138, 2003.

[3] W. Weber and M. Tacke, “United States Patent 1191,” *United States Pat. 1191*, 1977.

[4] C. Bosch, A. Mittasch, H. Wolf, and G. Stern, “Catalytic agent for use in producing ammonia.” Google Patents, 03-Aug-1915.

[5] A. O. Process, “The Ammonia Oxidation Process for Nitric Acid Manufacture,” no. 4, pp. 129–134, 1958.

[6] Arends I., R. Sheldon, and U. Hanefeld, “Introduction: Green Chemistry and Catalysis,” *Green Chemistry and Catalysis*. 12-Apr-2007.

[7] P. C. Mijhring and N. J. Coville, “Homogeneous Group 4 metallocene Ziegler-Natta the influence of cyclopentadienyl-ring substituents catalysts :,” *J. Organomet. Chem.*, vol. 479, pp. 1–29, 1994.

[8] J.-M. Choi, S.-S. Han, and H.-S. Kim, “Industrial applications of enzyme biocatalysis: Current status and future aspects,” *Biotechnol. Adv.*, vol. 33, no. 7, pp. 1443–1454, Nov. 2015.

[9] A. Schmid, J. S. Dordick, B. Hauer, A. Kiener, M. Wubbolts, and B. Witholt, “Industrial biocatalysis today and tomorrow,” *Nature*, vol. 409, p. 258, Jan. 2001.

[10] J. Ross, “Chapter 1 - Introduction,” in *Heterogeneous Catalysis*, 1st ed., Amsterdam: Elsevier B.V, 2012, pp. 1–12.

[11] J. M. Thomas and W. J. Thomas, *Principles and Practice of Heterogeneous Catalysis, 2nd Edition*. John Wiley and Sons, 2014.

[12] P. Schwach, N. Hamilton, M. Eichelbaum, L. Thum, T. Lunkenbein, R.

Schlögl, and A. Trunschke, “Structure sensitivity of the oxidative activation of methane over MgO model catalysts: II. Nature of active sites and reaction mechanism,” *J. Catal.*, vol. 329, pp. 574–587, Sep. 2015.

[13] M. Behrens, F. Studt, I. Kasatkin, S. Kühl, M. Hävecker, F. Abild-Pedersen, S. Zander, F. Girgsdies, P. Kurr, B.-L. Kniep, M. Tovar, R. W. Fischer, J. K. Nørskov, and R. Schlögl, “The Active Site of Methanol Synthesis over Cu/ZnO/Al2O3 Industrial Catalysts,” *Science (80-.).*, vol. 336, no. 6083, p. 893 LP-897, May 2012.

[14] J. M. Thomas and W. J. Thomas, *Principles and pratices of Heterogeneous Catalysis*, 2nd ed. Weinheim: Wiley-VCH Verlag GmbH & Co. KGaA, 2014.

[15] J. R. H. Ross, “Chapter 3 - How Does a Catalyst Work?,” in *Heterogeneous Catalysis*, 1st ed., Amsterdam: Elsevier B.V, 2012, pp. 47–64.

[16] M. Eddaoudi, D. B. Moler, H. Li, B. Chen, T. M. Reineke, M. O’Keeffe, and O. M. Yaghi, “Modular Chemistry: Secondary Building Units as a Basis for the Design of Highly Porous and Robust Metal−Organic Carboxylate Frameworks,” *Acc. Chem. Res.*, vol. 34, no. 4, pp. 319–330, Apr. 2001.

[17] R. Banerjee, H. Furukawa, D. Britt, C. Knobler, M. O’Keeffe, and O. M. Yaghi, “Control of Pore Size and Functionality in Isoreticular Zeolitic Imidazolate Frameworks and their Carbon Dioxide Selective Capture Properties,” *J. Am. Chem. Soc.*, vol. 131, no. 11, pp. 3875–3877, Mar. 2009.

[18] H. Li, M. Eddaoudi, M. O’Keeffe, and O. M. Yaghi, “Design and synthesis of an exceptionally stable and highly porous metal-organic framework,” *Nature*, vol. 402, no. 6759, pp. 276–279, Nov. 1999.

[19] H.-J. Freund, “Model Studies in Heterogeneous Catalysis,” *Chem. – A Eur. J.*, vol. 16, no. 31, pp. 9384–9397, Aug. 2010.

[20] M. Köhler and W. Fritzsche, “Introduction,” in *Nanotechnology*, Wiley-VCH Verlag GmbH & Co. KGaA, 2007, pp. 1–11.

[21] G. Schmid, “CHAPTER 1 - General Features of Metal Nanoparticles Physics and Chemistry,” in *Metal Nanoclusters in Catalysis and Materials Science*, 1st ed., Amsterdam: Elsevier, 2008, pp. 3–20.

[22] M. Lahmani, C. Bréchignac, and P. Houdy, *Nanomaterials and Nanochemistry*. Springer-Verlag Berlin Heidelberg, 2007.

[23] G. Schmid, *Clusters and Colloids: From Theory to Applications*, 1st ed. Wiley-VCH Verlag GmbH, 1994.

[24] T. P. Martin, "Shells of atoms," *Phys. Rep.*, vol. 273, no. 4, pp. 199–241, 1996.

[25] *Nanotechnology An introduction to nanostructuring techniques*. 2004.

[26] W. J. Parak, L. Manna, F. C. Simmel, D. Gerion, and P. Alivisatos, "Quantum Dots," *Nanoparticles*. 28-Jan-2005.

[27] E. Roduner, "Size matters: why nanomaterials are different," *Chem. Soc. Rev.*, vol. 35, no. 7, pp. 583–592, 2006.

[28] F. Tao and J. Spivey, *Metal Nanoparticles for Catalysis*. Cambridge: The Royal Society of Chemistry, 2014.

[29] R. C. Egeberg, S. Dahl, A. Logadottir, J. H. Larsen, J. K. Nørskov, and I. Chorkendorff, "N2 dissociation on Fe(1 1 0) and Fe/Ru(0 0 0 1): what is the role of steps?," *Surf. Sci.*, vol. 491, no. 1–2, pp. 183–194, Sep. 2001.

[30] D. Astruc, "Transition-metal Nanoparticles in Catalysis: From Historical Background to the State-of-the Art," in *Nanoparticles and Catalysis*, Wiley-VCH Verlag GmbH & Co. KGaA, 2007, pp. 1–48.

[31] L. D. Rampino and F. F. Nord, "Preparation of palladium and platinum synthetic high polymer catalysts and the relationship between particle size and rate of hydrogenation," *J. Am. Chem. Soc.*, vol. 63, no. 10, pp. 2745–2749, 1941.

[32] M. Haruta, "Size- and support-dependency in the catalysis of gold," *Catal. Today*, vol. 36, no. 1, pp. 153–166, 1997.

[33] M. Haruta, "When Gold Is Not Noble : Catalysis by nanoparticles," *Chem. Rec.*, vol. 3, no. 2, pp. 75–87, 2002.

[34] M. Haruta, T. Kobayashi, H. Sano, and N. Yamada, "Novel Gold Catalysts for the Oxidation of Carbon Monoxide at a Temperature far Below 0 °C," *Chem.*

Lett., vol. 16, no. 2, pp. 405–408, Feb. 1987.

[35] J. P. den Breejen, P. B. Radstake, G. L. Bezemer, J. H. Bitter, V. Frøseth, A. Holmen, and K. P. de Jong, "On the Origin of the Cobalt Particle Size Effects in Fischer−Tropsch Catalysis," *J. Am. Chem. Soc.*, vol. 131, no. 20, pp. 7197–7203, May 2009.

[36] H. M. Torres Galvis, J. H. Bitter, C. B. Khare, M. Ruitenbeek, A. I. Dugulan, and K. P. de Jong, "Supported Iron Nanoparticles as Catalysts for Sustainable Production of Lower Olefins," *Science (80-.).*, vol. 335, no. 6070, p. 835 LP-838, Feb. 2012.

[37] A. Y. Khodakov, W. Chu, and P. Fongarland, "Advances in the Development of Novel Cobalt Fischer−Tropsch Catalysts for Synthesis of Long-Chain Hydrocarbons and Clean Fuels," *Chem. Rev.*, vol. 107, no. 5, pp. 1692–1744, May 2007.

[38] M. Che and C. O. Bennett, "The Influence of Particle-Size on the Catalytic Properties of Supported Metals," *Adv. Catal.*, vol. 36, pp. 55–172, 1989.

[39] T. Ressler, B. L. Kniep, I. Kasatkin, and R. Schlögl, "The Microstructure of Copper Zinc Oxide Catalysts: Bridging the Materials Gap," *Angew. Chemie Int. Ed.*, vol. 44, no. 30, pp. 4704–4707, Jul. 2005.

[40] J. Strunk, K. Kähler, X. Xia, and M. Muhler, "The surface chemistry of ZnO nanoparticles applied as heterogeneous catalysts in methanol synthesis," *Surf. Sci.*, vol. 603, no. 10–12, pp. 1776–1783, Jun. 2009.

[41] M. Sevilla, C. Sanchís, T. Valdés-Solís, E. Morallón, and A. B. Fuertes, "Highly dispersed platinum nanoparticles on carbon nanocoils and their electrocatalytic performance for fuel cell reactions," *Electrochim. Acta*, vol. 54, no. 8, pp. 2234–2238, Mar. 2009.

[42] N. Savage and M. S. Diallo, "Nanomaterials and Water Purification: Opportunities and Challenges," *J. Nanoparticle Res.*, vol. 7, no. 4, pp. 331–342, 2005.

[43] J. K. Nørskov, T. Bligaard, B. Hvolbæk, and F. Abild-pedersen, "The nature of the active site in heterogeneous metal catalysis w," *Chem. Soc. Rev.*, no. 10,

p. 2163, 2008.

[44] G. A. Somorjai and J. Y. Park, “Colloid Science of Metal Nanoparticle Catalysts in 2D and 3D Structures. Challenges of Nucleation, Growth, Composition, Particle Shape, Size Control and Their Influence on Activity and Selectivity,” *Top. Catal.*, vol. 49, no. 3, pp. 126–135, 2008.

[45] G. L. Bezemer, J. H. Bitter, H. P. C. E. Kuipers, H. Oosterbeek, J. E. Holewijn, X. Xu, F. Kapteijn, A. J. van Dillen, and K. P. de Jong, “Cobalt Particle Size Effects in the Fischer−Tropsch Reaction Studied with Carbon Nanofiber Supported Catalysts,” *J. Am. Chem. Soc.*, vol. 128, no. 12, pp. 3956–3964, Mar. 2006.

[46] A. Barbier, A. Tuel, I. Arcon, A. Kodre, and G. A. Martin, “Characterization and Catalytic Behavior of Co/SiO2 Catalysts: Influence of Dispersion in the Fischer–Tropsch Reaction,” *J. Catal.*, vol. 200, no. 1, pp. 106–116, 2001.

[47] M. Haruta, “Relevance of Metal Nanoclusters Size Control in Gold(0) Catalytic Chemistry,” in *Metal Nanoclusters in Catalysis and Materials Science*, Amsterdam: Elsevier, 2008, pp. 183–199.

[48] J. P. Boitiaux, J. Cosyns, and S. Vasudevan, “Hydrogenation of highly unsaturated hydrocarbons over highly dispersed palladium catalyst,” *Appl. Catal.*, vol. 6, no. 1, pp. 41–51, 1983.

[49] J.-C. Bertolini and J.-L. Rousset, “Reactivity of Metal Nanoparticles,” in *Nanomaterials and Nanochemistry*, C. Bréchignac, P. Houdy, and M. Lahmani, Eds. Berlin, Heidelberg: Springer Berlin Heidelberg, 2007, pp. 281–304.

[50] N. Semagina and L. Kiwi-Minsker, “Recent Advances in the Liquid-Phase Synthesis of Metal Nanostructures with Controlled Shape and Size for Catalysis,” *Catal. Rev.*, vol. 51, no. 2, pp. 147–217, 2009.

[51] M. Okumura, T. Akita, and M. Haruta, “Hydrogenation of 1,3-butadiene and of crotonaldehyde over highly dispersed Au catalysts,” *Catal. Today*, vol. 74, no. 3–4, pp. 265–269, 2002.

[52] S. M. Rogers, C. R. A. Catlow, C. E. Chan-Thaw, D. Gianolio, E. K. Gibson,

A. L. Gould, N. Jian, A. J. Logsdail, R. E. Palmer, L. Prati, N. Dimitratos, A. Villa, and P. P. Wells, “Tailoring Gold Nanoparticle Characteristics and the Impact on Aqueous-Phase Oxidation of Glycerol,” *ACS Catal.*, vol. 5, no. 7, pp. 4377–4384, 2015.

[53] N. Semagina, A. Renken, D. Laub, and L. Kiwi-Minsker, “Synthesis of monodispersed palladium nanoparticles to study structure sensitivity of solvent-free selective hydrogenation of 2-methyl-3-butyn-2-ol,” *J. Catal.*, vol. 246, no. 2, pp. 308–314, 2007.

[54] J. P. Spatz, S. Mössmer, C. Hartmann, M. Möller, T. Herzog, M. Krieger, H. G. Boyen, P. Ziemann, and B. Kabius, “Ordered deposition of inorganic clusters from micellar block copolymer films,” *Langmuir*, vol. 16, no. 2, pp. 407–415, 2000.

[55] J. R. Croy, S. Mostafa, J. Liu, Y. Sohn, and B. Roldan Cuenya, “Size Dependent Study of MeOH Decomposition Over Size-selected Pt Nanoparticles Synthesized via Micelle Encapsulation,” *Catal. Letters*, vol. 118, no. 1, pp. 1–7, 2007.

[56] H. Mistry, R. Reske, Z. Zeng, Z.-J. Zhao, J. Greeley, P. Strasser, and B. R. Cuenya, “Exceptional Size-Dependent Activity Enhancement in the Electroreduction of CO2 over Au Nanoparticles,” *J. Am. Chem. Soc.*, vol. 136, no. 47, pp. 16473–16476, Nov. 2014.

[57] R. Hou, M. D. Porosoff, J. G. Chen, and T. Wang, “Effect of oxide supports on Pd-Ni bimetallic catalysts for 1,3-butadiene hydrogenation,” *Appl. Catal. A Gen.*, vol. 490, pp. 17–23, 2015.

[58] Y. Guan and E. J. M. Hensen, “Ethanol dehydrogenation by gold catalysts: The effect of the gold particle size and the presence of oxygen,” *Appl. Catal. A Gen.*, vol. 361, no. 1, pp. 49–56, 2009.

[59] G. N. Vayssilov, Y. Lykhach, A. Migani, T. Staudt, G. P. Petrova, N. Tsud, T. Skála, A. Bruix, F. Illas, K. C. Prince, V. Matolín, K. M. Neyman, and J. Libuda, “Support nanostructure boosts oxygen transfer to catalytically active platinum nanoparticles,” *Nat. Mater.*, vol. 10, no. 4, pp. 310–315, 2011.

[60] X. Liu, M.-H. Liu, Y.-C. Luo, C.-Y. Mou, S. D. Lin, H. Cheng, J.-M. Chen, J.-F. Lee, and T.-S. Lin, “Strong Metal–Support Interactions between Gold Nanoparticles and ZnO Nanorods in CO Oxidation,” *J. Am. Chem. Soc.*, vol. 134, no. 24, pp. 10251–10258, Jun. 2012.

[61] W. Vervisch, C. Mottet, and J. Goniakowski, “Effect of epitaxial strain on theatomic structure of Pd clusters on MgO(100) substrate,” *Eur. Phys. J. D*, vol. 24, no. 1, pp. 311–314, 2003.

[62] C. Henry, “Size Effects on Structure and Morphology of Free or Supported Nanoparticles BT - Nanomaterials and Nanochemistry,” C. Bréchignac, P. Houdy, and M. Lahmani, Eds. Berlin, Heidelberg: Springer Berlin Heidelberg, 2007, pp. 3–34.

[63] M. Wilde, K. Fukutani, W. Ludwig, B. Brandt, J. H. Fischer, S. Schauermann, and H. J. Freund, “Influence of carbon deposition on the hydrogen distribution in Pd nanoparticles and their reactivity in olefin hydrogenation,” *Angew. Chemie - Int. Ed.*, vol. 47, no. 48, pp. 9289–9293, 2008.

[64] M. C. M. Daniel and D. Astruc, “Gold Nanoparticles: Assembly, Supramolecular Chemistry, Quantum-Size Related Properties and Applications toward Biology, Catalysis and Nanotechnology,” *Chem. Rev.*, vol. 104, no. 1, pp. 293–346, 2004.

[65] P. K. Jain, “Gold Nanoparticles for Physics, Chemistry, and Biology. Edited by Catherine Louis and Olivier Pluchery.,” *Angew. Chemie Int. Ed.*, vol. 53, no. 5, p. 1197, Jan. 2014.

[66] G. C. Bond, C. Louis, and D. T. Thompson, *Catalysis by Gold*, vol. 6. London: Imperial College Press, 2006.

[67] C. J. Murphy, “Nanocubes and Nanoboxes,” *Science (80-.).*, vol. 298, no. 5601, pp. 2139–2141, Dec. 2002.

[68] M. Faraday, “The Bakerian Lecture : Experimental Relations of Gold (and Other Metals) to Light,” *Phil. Trans. R. Soc. London*, no. January, pp. 145–181, 1857.

[69] J. T. Miller, A. J. Kropf, Y. Zha, J. R. Regalbuto, L. Delannoy, C. Louis, E.

Bus, and J. A. van Bokhoven, “The effect of gold particle size on AuAu bond length and reactivity toward oxygen in supported catalysts,” *J. Catal.*, vol. 240, no. 2, pp. 222–234, Jun. 2006.

[70] G. C. Schatz, “Electrodynamics of nonspherical noble metal nanoparticles and nanoparticle aggregates,” *J. Mol. Struct. THEOCHEM*, vol. 573, no. 1–3, pp. 73–80, Oct. 2001.

[71] J. Chen, Q. Zhang, Y. Wang, and H. Wan, “Size-Dependent Catalytic Activity of Supported Palladium Nanoparticles for Aerobic Oxidation of Alcohols,” *Adv. Synth. Catal.*, vol. 347, no. 10, p. 1356, 2008.

[72] N. Semagina, A. Renken, and L. Kiwi-Minsker, “Palladium Nanoparticle Size Effect in 1-Hexyne Selective Hydrogenation,” *J. Phys. Chem. C*, vol. 111, no. 37, pp. 13933–13937, 2007.

[73] B. Coq, A. Tijani, and F. Figuéras, “Particle size effect on the kinetics of p-chloronitrobenzene hydrogenation over platinum/alumina catalysts,” *J. Mol. Catal.*, vol. 68, no. 3, pp. 331–345, Sep. 1991.

[74] A. J. Plomp, H. Vuori, A. O. I. Krause, K. P. de Jong, and J. H. Bitter, “Particle size effects for carbon nanofiber supported platinum and ruthenium catalysts for the selective hydrogenation of cinnamaldehyde,” *Appl. Catal. A Gen.*, vol. 351, no. 1, pp. 9–15, Dec. 2008.

[75] A. S. K. Hashmi and G. J. Hutchings, “Gold Catalysis,” *Angew. Chemie - Int. Ed.*, vol. 45, no. 47, pp. 7896–7936, 2006.

[76] M. M. Schubert, S. Hackenberg, A. C. Van Veen, M. Muhler, V. Plzak, and R. J, “CO Oxidation over Supported Gold Catalysts —‘ Inert ’ and ‘ Active ’ Support Materials and Their Role for the Oxygen Supply during Reaction,” *J. Catal.*, vol. 122, pp. 113–122, 2001.

[77] M. Comotti, W. Li, B. Spliethoff, and F. Schu, “Support Effect in High Activity Gold Catalysts for CO Oxidation,” *J. Am. Chem. Soc.*, no. 15, pp. 917–924, 2006.

[78] A. Sandoval, A. Gómez-Cortés, R. Zanella, G. Díaz, and J. M. Saniger, “Gold nanoparticles: Support effects for the WGS reaction,” *J. Mol. Catal. A Chem.*,

vol. 278, no. 1, pp. 200–208, 2007.

[79] M. Shekhar, J. Wang, W.-S. Lee, W. D. Williams, S. M. Kim, E. a Stach, J. T. Miller, W. N. Delgass, and F. H. Ribeiro, “Size and support effects for the water-gas shift catalysis over gold nanoparticles supported on model Al2O3 and TiO2.,” *J. Am. Chem. Soc.*, vol. 134, pp. 4700–8, 2012.

[80] G. C. Bond and D. T. Thompson, “Gold-catalysed oxidation of carbon monoxide,” *Gold Bull.*, vol. 33, no. 2, pp. 41–50, 2000.

[81] X. Y. Liu, A. Wang, T. Zhang, and C. Y. Mou, “Catalysis by gold: New insights into the support effect,” *Nano Today*, vol. 8, no. 4, pp. 403–416, 2013.

[82] P. Concepción, S. Carrettin, and A. Corma, “Stabilization of cationic gold species on Au/CeO2 catalysts under working conditions,” *Appl. Catal. A Gen.*, vol. 307, no. 1, pp. 42–45, 2006.

[83] A. Abad, P. Concepción, A. Corma, and H. García, “A Collaborative Effect between Gold and a Support Induces the Selective Oxidation of Alcohols,” *Angew. Chemie Int. Ed.*, vol. 44, no. 26, pp. 4066–4069, Jun. 2005.

[84] F. Wang, W. Ueda, and J. Xu, “Detection and Measurement of Surface Electron Transfer on Reduced Molybdenum Oxides (MoO x) and Catalytic Activities of Au / MoO x ** Angewandte,” *Angew. Chemie - Int. Ed.*, vol. 51, pp. 3883–3887, 2012.

[85] V. R. Choudhary and D. K. Dumbre, “Supported Nano-Gold Catalysts for Epoxidation of Styrene and Oxidation of Benzyl Alcohol to Benzaldehyde,” *Top. Catal.*, vol. 52, no. 12, pp. 1677–1687, 2009.

[86] P. Forzatti, P. L. Villa, N. Ferlazzo, and D. Jones, “Multicomponent catalysts for the oxidation of propylene to acrolein: Fe2(MoO4)3 doped with Bi or Te,” *J. Catal.*, vol. 76, no. 1, pp. 188–207, 1982.

[87] A. Hugon, L. Delannoy, and C. Louis, “Influence of the reactant concentration in selective hydrogenation of 1,3-butadiene over supported gold catalysts under alkene rich conditions: A consideration of reaction mechanism,” *Gold Bull.*, vol. 42, no. 4, pp. 310–320, 2009.

[88] S. Schimpf, M. Lucas, C. Mohr, U. Rodemerck, A. Brückner, J. Radnik, H. Hofmeister, and P. Claus, “Supported gold nanoparticles: In-depth catalyst characterization and application in hydrogenation and oxidation reactions,” *Catal. Today*, vol. 72, no. 1–2, pp. 63–78, 2002.

[89] E. G. Allison and G. C. Bond, “The Structure and Catalytic Properties of Palladium-Silver and Palladium-Gold Alloys,” *Catal. Rev.*, vol. 7, no. 2, pp. 233–289, Jan. 1972.

[90] F. Gao and D. W. Goodmanz, “Pd – Au bimetallic catalysts : understanding alloy effects from planar models and (supported) nanoparticles,” *Chem. Soc. Rev.*, vol. 41, pp. 8009–8020, 2012.

[91] B. Zugic, S. Karakalos, K. J. Stowers, M. M. Biener, J. Biener, R. J. Madix, and C. M. Friend, “Continuous Catalytic Production of Methyl Acrylates from Unsaturated Alcohols by Gold: The Strong Effect of C=C Unsaturation on Reaction Selectivity,” *ACS Catal.*, vol. 6, pp. 1833–1839, 2016.

[92] X. Liu, M. Conte, D. Elias, L. Lu, D. J. Morgan, S. J. Freakley, P. Johnston, J. Kiely, and G. J. Hutchings, “Investigation of the active species in the carbon-supported gold catalyst for acetylene hydrochlorination,” *Catal. Sci. Technol.*, vol. 6, pp. 5144–5153, 2016.

[93] P. Johnston, N. Carthey, and G. J. Hutchings, “Discovery, Development, and Commercialization of Gold Catalysts for Acetylene Hydrochlorination,” *J. Am. Chem. Soc.*, vol. 137, no. 46, pp. 14548–14557, Nov. 2015.

[94] R. Ciriminna, E. Falletta, C. Della Pina, H. Teles, and M. Pagliaro, “Industrial Applications of Gold Catalysis Minireviews,” *Angew. Chemie - Int. Ed.*, vol. 8, pp. 14210–14217, 2016.

[95] C. H. Christensen and J. K. Nørskov, “Green Gold Catalysis,” *Science (80-.).*, vol. 327, no. 5963, pp. 278–279, Jan. 2010.

[96] A. Villa, G. M. Veith, and L. Prati, “Selective Oxidation of Glycerol under Acidic Conditions Using Gold Catalysts,” *Angew. Chemie*, vol. 122, no. 26, pp. 4601–4604, Jun. 2010.

[97] N. A. Afagh and A. K. Yudin, “Chemoselectivity and the Curious Reactivity

Preferences of Functional Groups Angewandte," *Angew. Chemie - Int. Ed.*, vol. 49, pp. 262–310, 2010.

[98] Z. Li, C. Brouwer, and C. He, "Gold-Catalyzed Organic Transformations," *Chem. Rev.*, vol. 108, pp. 3239–3265, 2008.

[99] A. Corma and P. Serna, "Chemoselective Hydrogenation of Nitro Compounds with Supported Gold Catalysts," *Science (80-.).*, vol. 313, no. 5785, p. 332 LP-334, Jul. 2006.

[100] K. Shimizu, Y. Miyamoto, T. Kawasaki, T. Tanji, Y. Tai, and A. Satsuma, "Chemoselective Hydrogenation of Nitroaromatics by Supported Gold Catalysts: Mechanistic Reasons of Size- and Support-Dependent Activity and Selectivity," *J. Phys. Chem. C*, vol. 113, no. 41, pp. 17803–17810, Oct. 2009.

[101] G. Bond and D. Thompson, "Formulation of mechanisms for gold-catalysed reactions *," *Gold Bull.*, vol. 42, no. 4, pp. 247–259, 2009.

[102] T. Thuening, J. Walker, H. Adams, O. Furlong, and W. T. Tysoe, "Surface Science Kinetics of low-temperature CO oxidation on Au (111)," *Surf. Sci.*, vol. 648, pp. 236–241, 2016.

[103] Q. He, S. J. Freakley, J. K. Edwards, A. F. Carley, A. Y. Borisevich, Y. Mineo, M. Haruta, G. J. Hutchings, and C. J. Kiely, "Population and hierarchy of active species in gold iron oxide catalysts for carbon monoxide oxidation," *Nat. Commun.*, vol. 7, pp. 1–8, 2016.

[104] L. Prati and M. Rossi, "Gold on Carbon as a New Catalyst for Selective Liquid Phase Oxidation of Diols," *J. Catal.*, vol. 176, no. 2, pp. 552–560, 1998.

[105] S. Carrettin, P. Mcmorn, P. Johnston, and G. J. Hutchings, "Selective oxidation of glycerol to glyceric acid using a gold catalyst in aqueous sodium hydroxide," *Chem. Commun.*, no. 7, pp. 696–697, 2002.

[106] G. C. Bond and P. A. Sermon, "Gold catalysts for olefin hydrogenation," *Gold Bull.*, vol. 6, no. 4, pp. 102–105, 1973.

[107] J. Jia, K. Haraki, J. N. Kondo, K. Domen, and K. Tamaru, "Selective Hydrogenation of Acetylene over Au/Al2O3 Catalyst," *J. Phys. Chem. B*, vol.

104, no. 47, pp. 11153–11156, Nov. 2000.

[108] M. Juliusa, S. Robertsa, and J. C. Q. Fletchera, “A review of the use of gold catalysts in selective hydrogenation reactions Lynsey McEwana,” *Gold Bull.*, vol. 43, no. 4, pp. 298–306, 2010.

[109] S. a Nikolaev, L. N. Zanaveskin, V. V Smirnov, V. a Averyanov, and K. L. Zanaveskin, “Catalytic hydrogenation of alkyne and alkadiene impurities from alkenes. Practical and theoretical aspects,” *Russ. Chem. Rev.*, vol. 78, no. 3, pp. 231–247, 2009.

[110] C. Mohr, H. Hofmeister, J. Radnik, and P. Claus, “Identification of Active Sites in Gold-Catalyzed Hydrogenation of Acrolein,” *J. Am. Chem. Soc.*, vol. 125, no. 7, pp. 1905–1911, Feb. 2003.

[111] C. Mohr, H. Hofmeister, and P. Claus, “The influence of real structure of gold catalysts in the partial hydrogenation of acrolein,” *J. Catal.*, vol. 213, no. 1, pp. 86–94, Jan. 2003.

[112] C. Kartusch and J. A. van Bokhoven, “Hydrogenation over gold catalysts: The interaction of gold with hydrogen,” *Gold Bull.*, vol. 42, no. 4, pp. 343–348, 2009.

[113] M. Boronat, P. Concepción, A. Corma, S. González, F. Illas, and P. Serna, “A Molecular Mechanism for the Chemoselective Hydrogenation of Substituted Nitroaromatics with Nanoparticles of Gold on TiO2 Catalysts: A Cooperative Effect between Gold and the Support,” *J. Am. Chem. Soc.*, vol. 129, no. 51, pp. 16230–16237, Dec. 2007.

[114] L. McEwan, M. Julius, S. Roberts, and J. Fletcher, “A review of the use of gold catalysts in selective hydrogenation reactions.,” *Gold Bull.*, vol. 43, no. 4, pp. 298–306, 2010.

[115] P. Claus, “Heterogeneously catalysed hydrogenation using gold catalysts,” *Appl. Catal. A Gen.*, vol. 291, no. 1–2, pp. 222–229, 2005.

[116] B. R. Cuenya, S.-H. Baeck, T. F. Jaramillo, and E. W. McFarland, “Size- and support-dependent electronic and catalytic properties of Au0/Au3+ nanoparticles synthesized from block copolymer micelles.,” *J. Am. Chem.*

Soc., vol. 125, no. 42, pp. 12928–12934, 2003.

[117] T. Fujitani, I. Nakamura, T. Akita, M. Okumura, and M. Haruta, "Hydrogen Dissociation by Gold Clusters," *Angew. Chemie*, vol. 121, no. 50, pp. 9679–9682, Dec. 2009.

[118] G. C. Bond, P. A. Sermon, G. Webb, D. A. Buchanan, and P. B. Wells, "Hydrogenation over supported gold catalysts," *J. Chem. Soc. Chem. Commun.*, no. 13, p. 444b–445, 1973.

[119] A. C. Gluhoi, J. W. Bakker, and B. E. Nieuwenhuys, "Gold, still a surprising catalyst: Selective hydrogenation of acetylene to ethylene over Au nanoparticles," *Catal. Today*, vol. 154, no. 1–2, pp. 13–20, Sep. 2010.

[120] T. Hayashi, K. Tanaka, and M. Haruta, "Selective Vapor-Phase Epoxidation of Propylene over Au / TiO 2 Catalysts in the Presence of Oxygen and Hydrogen," *J. Catal.*, vol. 575, pp. 566–575, 1998.

[121] MurdochM., W. I. N., N. A., M. B., K. A., H. F., LlorcaJ., and IdrissH., "The effect of gold loading and particle size on photocatalytic hydrogen production from ethanol over Au/TiO2 nanoparticles," *Nat Chem*, vol. 3, no. 6, pp. 489–492, Jun. 2011.

[122] A. Abad, A. Corma, and H. García, "Catalyst Parameters Determining Activity and Selectivity of Supported Gold Nanoparticles for the Aerobic Oxidation of Alcohols: The Molecular Reaction Mechanism," *Chem. – A Eur. J.*, vol. 14, no. 1, pp. 212–222, Jan. 2008.

[123] "History of Palladium," *http://www.bullion.com/palladium/historyofpalladium.html*. .

[124] I. Saldan, Y. Semenyuk, I. Marchuk, and O. Reshetnyak, "Chemical synthesis and application of palladium nanoparticles," *J. Mater. Sci.*, vol. 50, no. 6, pp. 2337–2354, 2015.

[125] "Palladium." [Online]. Available: http://www.unctad.org/infocomm/anglais/palladium/uses.htm.

[126] P. Colon, N. Pradelle-Plasse, and J. Galland, "Evaluation of the long-term corrosion behavior of dental amalgams: influence of palladium addition and

particle morphology," *Dent. Mater.*, vol. 19, no. 3, pp. 232–239, 2003.

[127] J. Kielhorn, C. Melber, D. Keller, and I. Mangelsdorf, "Palladium – A review of exposure and effects to human health," *Int. J. Hyg. Environ. Health*, vol. 205, no. 6, pp. 417–432, 2002.

[128] I. P. Beletskaya and A. V Cheprakov, "The Heck Reaction as a Sharpening Stone of Palladium Catalysis," *Chem. Rev.*, vol. 100, no. 8, pp. 3009–3066, 2000.

[129] N. T. S. Phan, M. Van Der Sluys, and C. W. Jones, "On the Nature of the Active Species in Palladium Catalyzed Mizoroki–Heck and Suzuki–Miyaura Couplings – Homogeneous or Heterogeneous Catalysis, A Critical Review," *Adv. Synth. Catal.*, vol. 348, no. 6, pp. 609–679, Apr. 2006.

[130] K. Roy, R. Jain, M. K. Ghosalya, K. Prabhakar Reddy, and C. S. Gopinath, "Three-way catalytic converter reactions aspects at near-ambient temperatures on modified Pd-surfaces," *Comptes Rendus Chim.*, vol. 19, no. 10, pp. 1363–1369, 2016.

[131] J. Wang, H. Chen, Z. Hu, M. Yao, Y. Li, J. Wang, H. Chen, Z. Hu, and M. Yao, "A Review on the Pd-Based Three-Way Catalyst A Review on the Pd-Based Three-Way Catalyst," *Catal. Rev. Sci. Eng.*, vol. 57, no. 1, pp. 79–144, 2017.

[132] F. Zeng and K. L. Hohn, "Modeling of three-way catalytic converter performance with exhaust mixture from natural gas-fueled engines," *Appl. Catal. B Environ.*, vol. 182, pp. 570–579, Mar. 2016.

[133] J. C. Summers, J. F. Skowron, and M. J. Miller, "Use of Light-Off Catalysts to Meet the California LEV/ULEV Standards," in *SAE Technical Paper 930386*, 1993.

[134] D. Lindner, E. S. Lox, R. van Yperen, K. Ostgathe, and T. Kreuzer, "Reduction of Exhaust Gas Emissions by Using Pd-based Three-way Catalysts," in *SAE Technical Paper 960802*, 1996.

[135] C. F. Cullis and B. M. Willatt, "Oxidation of methane over supported precious metal catalysts," *J. Catal.*, vol. 83, no. 2, pp. 267–285, 1983.

[136] Y.-F. Y. Yao, “The oxidation of CO and hydrocarbons over noble metal catalysts,” *J. Catal.*, vol. 87, no. 1, pp. 152–162, May 1984.

[137] L. Yang, S. Lin, X. Yang, W. Fang, and R. Zhou, “Promoting effect of alkaline earth metal doping on catalytic activity of HC and NOx conversion over Pd-only three-way catalyst,” *J. Hazard. Mater.*, vol. 279, pp. 226–235, Aug. 2014.

[138] X. Chen, Y. Cheng, C. Y. Seo, J. W. Schwank, and R. W. McCabe, “Aging, re-dispersion, and catalytic oxidation characteristics of model Pd/Al2O3 automotive three-way catalysts,” *Appl. Catal. B Environ.*, vol. 163, pp. 499–509, Feb. 2015.

[139] Yin and J. Liebscher, “Carbon−Carbon Coupling Reactions Catalyzed by Heterogeneous Palladium Catalysts,” *Chem. Rev.*, vol. 107, no. 1, pp. 133–173, 2007.

[140] Á. Molnár, “Efficient, Selective, and Recyclable Palladium Catalysts in Carbon−Carbon Coupling Reactions,” *Chem. Rev.*, vol. 111, no. 3, pp. 2251–2320, Mar. 2011.

[141] R. Narayanan and M. A. El-Sayed, “Effect of Catalysis on the Stability of Metallic Nanoparticles: Suzuki Reaction Catalyzed by PVP-Palladium Nanoparticles,” *J. Am. Chem. Soc.*, vol. 125, no. 27, pp. 8340–8347, Jul. 2003.

[142] N. T. S. Phan, D. H. Brown, and P. Styring, “A polymer-supported salen-type palladium complex as a catalyst for the Suzuki–Miyaura cross-coupling reaction,” *Tetrahedron Lett.*, vol. 45, no. 42, pp. 7915–7919, Oct. 2004.

[143] M. T. Reetz and E. Westermann, “Phosphane-Free Palladium-Catalyzed Coupling Reactions : The Decisive Role of Pd,” *Angew. Chemie - Int. Ed.*, vol. 39, no. 1, pp. 165–168, 2000.

[144] M. T. Reetz, E. Westermann, R. Lohmer, and G. Lohmer, “A highly active phosphine-free catalyst system for Heck reactions of aryl bromides,” *Tetrahedron Lett.*, vol. 39, no. 46, pp. 8449–8452, Nov. 1998.

[145] N. Lebrasseur and I. Larrosa, “Room Temperature and Phosphine Free

Palladium Catalyzed Direct C-2 Arylation of Indoles," *J. Am. Chem. Soc.*, vol. 130, no. 10, pp. 2926–2927, Mar. 2008.

[146] M. Pérez-Lorenzo, "Palladium Nanoparticles as Efficient Catalysts for Suzuki Cross-Coupling Reactions," *J. Phys. Chem. Lett.*, vol. 3, no. 2, pp. 167–174, Jan. 2012.

[147] B. J. Kestel, "Narrowing of the palladium-hydrogen miscibility gap in nanocrystalline palladium," *Phys. Rev. B*, vol. 48, no. 1, pp. 84–92, 1993.

[148] T. Mütschele and R. Kirchheim, "Hydrogen as a probe for the average thickness of a grain boundary," *Scr. Metall.*, vol. 21, no. 8, pp. 1101–1104, 1987.

[149] T. K. and W. A. O. and B. S. B. and T. B. Flanagan, "The partial excess thermodynamic properties of hydrogen in palladium," *J. Phys. F Met. Phys.*, vol. 13, no. 9, p. 1785, 1983.

[150] E. Wicke, H. Brodowsky, and H. Züchner, "Hydrogen in palladium and palladium alloys," in *Hydrogen in Metals II: Application-Oriented Properties*, G. Alefeld and J. Völkl, Eds. Berlin, Heidelberg: Springer Berlin Heidelberg, 1978, pp. 73–155.

[151] R. Lässer, "Isotope dependence of phase boundaries in the PdH, PdD, and PdT systems," *J. Phys. Chem. Solids*, vol. 46, no. 1, pp. 33–37, 1985.

[152] M. Johansson, E. Skúlason, G. Nielsen, S. Murphy, R. M. Nielsen, and I. Chorkendorff, "Hydrogen adsorption on palladium and palladium hydride at 1 bar," *Surf. Sci.*, vol. 604, no. 7–8, pp. 718–729, Apr. 2010.

[153] F. D. Manchester, A. San-Martin, and J. M. Pitre, "The H-Pd (hydrogen-palladium) System," *J. Phase Equilibria*, vol. 15, no. 1, pp. 62–83, 1994.

[154] I. Horiuti and M. Polanyi, "Exchange reactions of hydrogen on metallic catalysts," *Trans. Faraday Soc.*, vol. 30, no. 0, pp. 1164–1172, 1934.

[155] A. Borodziński and G. C. Bond, "Selective Hydrogenation of Ethyne in Ethene Rich Streams on Palladium Catalysts. Part 1. Effect of Changes to the Catalyst During Reaction," *Catal. Rev.*, vol. 48, no. 2, pp. 91–144, 2006.

[156] S. Hub, L. Hilaire, and R. Touroude, “Hydrogenation of But-1-yne and But-1-ene on Palladium Catalysts,” *Appl. Catal.*, vol. 36, pp. 307–322, 1988.

[157] G. Neri, M. G. Musolino, C. Milone, D. Pietropaolo, and S. Galvagno, “Particle size effect in the catalytic hydrogenation of 2,4-dinitrotoluene over Pd/C catalysts,” *Appl. Catal. A Gen.*, vol. 208, no. 1–2, pp. 307–316, Feb. 2001.

[158] C. E. Gigola, H. R. Aduriz, and P. Bodnariuk, “Particle size effect in the hydrogenation of acetylene under industrial conditions,” *Appl. Catal.*, vol. 27, no. 1, pp. 133–144, 1986.

[159] Y. Li, E. Boone, and M. A. El-Sayed, “Size Effects of PVP−Pd Nanoparticles on the Catalytic Suzuki Reactions in Aqueous Solution,” *Langmuir*, vol. 18, no. 12, pp. 4921–4925, Jun. 2002.

[160] J. Le Bars, U. Specht, J. S. Bradley, and D. G. Blackmond, “A Catalytic Probe of the Surface of Colloidal Palladium Particles Using Heck Coupling Reactions,” *Langmuir*, vol. 15, no. 22, pp. 7621–7625, Oct. 1999.

[161] O. M. Wilson, M. R. Knecht, J. C. Garcia-Martinez, and R. M. Crooks, “Effect of Pd Nanoparticle Size on the Catalytic Hydrogenation of Allyl Alcohol,” *J. Am. Chem. Soc.*, vol. 128, no. 14, pp. 4510–4511, Apr. 2006.

[162] M. Ruta, N. Semagina, and L. Kiwi-Minsker, “Monodispersed Pd nanoparticles for acetylene selective hydrogenation: Particle size and support effects,” *J. Phys. Chem. C*, vol. 112, no. 35, pp. 13635–13641, 2008.

[163] D. Teschner, E. Vass, M. Hävecker, S. Zafeiratos, P. Schnörch, H. Sauer, A. Knop-Gericke, R. Schlögl, M. Chamam, A. Wootsch, A. S. Canning, J. J. Gamman, S. D. Jackson, J. McGregor, and L. F. Gladden, “Alkyne hydrogenation over Pd catalysts: A new paradigm,” *J. Catal.*, vol. 242, no. 1, pp. 26–37, Aug. 2006.

[164] M. W. Tew, J. T. Miller, and J. A. van Bokhoven, “Particle Size Effect of Hydride Formation and Surface Hydrogen Adsorption of Nanosized Palladium Catalysts: L3 Edge vs K Edge X-ray Absorption Spectroscopy,” *J. Phys. Chem. C*, vol. 113, no. 34, pp. 15140–15147, Aug. 2009.

[165] C. Sachs, A. Pundt, and R. Kirchheim, “Solubility of hydrogen in single-sized palladium clusters,” *Phys. Rev. B*, vol. 64, p. 075408, 2001.

[166] D. Chartouni, G. Schmid, and L. Schlapbach, “Critical size and surface effect of the hydrogen interaction,” *Eur. Phys. J. D*, vol. 250, pp. 245–250, 2000.

[167] A. Hugon, L. Delannoy, J.-M. Krafft, and C. Louis, “Selective Hydrogenation of 1 , 3-Butadiene in the Presence of an Excess of Alkenes over Supported Bimetallic Gold - Palladium Catalysts,” *J. Phys. Chem. C*, vol. 4, no. i, pp. 10823–10835, 2010.

[168] B. K. Furlong, J. W. Hightower, T. Y. L. Chan, A. Sarkany, and L. Guczi, “1,3-Butadiene Selective Hydrogenation Over Pd/Alumina and Cupd/Alumina Catalysts,” *Appl. Catal. A, Gen.*, vol. 117, no. 1, pp. 41–51, 1994.

[169] X. F. Yang, A. Q. Wang, Y. L. Wang, T. Zhang, and J. Li, “Unusual Selectivity of Gold Catalysts for Hydrogenation of 1, 3-Butadiene toward cis-2-Butene: A joint experimental and theoretical investigation,” *J. Phys. Chem. C*, vol. 114, no. 7, pp. 3131–3139, 2010.

[170] B. Tardy, C. Noupa, C. Leclercq, J. C. Bertolini, A. Hoareau, M. Treilleux, J. P. Faure, and G. Nihoul, “Catalytic hydrogenation of 1,3-butadiene on Pd particles evaporated on carbonaceous supports: Particle size effect,” *J. Catal.*, vol. 129, no. 1, pp. 1–11, 1991.

[171] B. Tardy, C. Noupa, C. Leclercq, J. C. Bertolini, A. Hoareau, M. Treilleux, J. P. Faure, and G. Nihoul, “Catalytic hydrogenation of 1,3-butadiene on Pd particles evaporated on carbonaceous supports: Particle size effect,” *J. Catal.*, vol. 129, no. 1, pp. 1–11, 1991.

[172] J. Silvestre-Albero, G. Rupprechter, and H. J. Freund, “Atmospheric pressure studies of selective 1,3-butadiene hydrogenation on well-defined Pd/Al2O3/NiAl(110) model catalysts: Effect of Pd particle size,” *J. Catal.*, vol. 240, no. 1, pp. 58–65, 2006.

[173] J. Silvestre-Albero, G. Rupprechter, and H.-J. Freund, “From Pd nanoparticles to single crystals: 1,3-butadiene hydrogenation on well-defined model catalysts.,” *Chem. Commun. (Camb).*, no. 1, pp. 80–82, 2006.

[174] V. Dal Santo, A. Gallo, A. Naldoni, and L. Sordelli, “Selective butadiene hydrogenation by Pd nanoparticles deposed onto nano-sized oxide supports by CVD of Pd-hexafluoroacetylacetonate,” *Inorganica Chim. Acta*, vol. 380, pp. 216–222, Jan. 2012.

[175] D. C. Lee, J. H. Kim, and W. J. Kim, “Selective hydrogenation of 1 , 3-butadiene on TiO 2 -modified Pd / SiO 2 catalysts,” vol. 244, pp. 83–91, 2003.

[176] J. Goetz, M. A. Volpe, and R. Touroude, “Low-Loaded Pd / α -Al 2 O 3 Catalysts : Influence of Metal Particle Morphology on Hydrogenation of Buta-1 , 3-diene and Hydrogenation and Isomerization of But-1-ene,” vol. 377, no. 0393, pp. 369–377, 1996.

[177] W. Haiss, N. T. K. Thanh, J. Aveyard, and D. G. Fernig, “Determination of Size and Concentration of Gold Nanoparticles from UV−Vis Spectra,” *Anal. Chem.*, vol. 79, no. 11, pp. 4215–4221, Jun. 2007.

[178] R. Wojcieszak, M. J. Genet, P. Eloy, P. Ruiz, and E. M. Gaigneaux, “Determination of the Size of Supported Pd Nanoparticles by X-ray Photoelectron Spectroscopy. Comparison with X-ray Diffraction, Transmission Electron Microscopy, and H2 Chemisorption Methods,” *J. Phys. Chem. C*, vol. 114, no. 39, pp. 16677–16684, Oct. 2010.

[179] C. Prado-Burguete, A. Linares-Solano, F. Rodriguez-Reinoso, and C. S.-M. De Lecea, “Effect of carbon support and mean Pt particle size on hydrogen chemisorption by carbon-supported Pt ctalysts,” *J. Catal.*, vol. 128, no. 2, pp. 397–404, 1991.

[180] C. Amorim and M. A. Keane, “Palladium supported on structured and nonstructured carbon: A consideration of Pd particle size and the nature of reactive hydrogen,” *J. Colloid Interface Sci.*, vol. 322, no. 1, pp. 196–208, 2008.

[181] F. Boccuzzi, A. Chiorino, M. Manzoli, P. Lu, T. Akita, S. Ichikawa, and M. Haruta, “Au/TiO2 Nanosized Samples: A Catalytic, TEM, and FTIR Study of the Effect of Calcination Temperature on the CO Oxidation,” *J. Catal.*, vol. 202, no. 2, pp. 256–267, 2001.

[182] Z. L. Wang, “Transmission Electron Microscopy and Spectroscopy of Nanoparticles,” in *Characterization of Nanophase Materials*, Wiley-VCH Verlag GmbH, 1999, pp. 37–80.

[183] Z. L. Wang, “Nanomaterials for Nanoscience and Nanotechnology,” in *Characterization of Nanophase Materials*, Wiley-VCH Verlag GmbH, 1999, pp. 1–12.

[184] J. Liu, “Scanning Transmission Electron Microscopy of Nanoparticles,” in *Characterization of Nanophase Materials*, Wiley-VCH Verlag GmbH, 1999, pp. 81–132.

[185] D. Zanchet, B. D. Hall, and D. Ugarte, “X-ray Characterization of Nanoparticles,” in *Characterization of Nanophase Materials*, Wiley-VCH Verlag GmbH, 1999, pp. 13–36.

[186] H. Yoshida, Y. Kuwauchi, J. R. Jinschek, K. Sun, S. Tanaka, M. Kohyama, S. Shimada, M. Haruta, and S. Takeda, “Visualizing Gas Molecules Interacting with Supported Nanoparticulate Catalysts at Reaction Conditions,” *Science (80-.).*, vol. 335, no. 6066, p. 317 LP-319, Jan. 2012.

[187] R. Schlogl, “Heterogeneous Catalysis,” *Angew. Rev.*, no. 150, pp. 3465–3520, 2015.

[188] A. Gurlo and R. Riedel, “In Situ and Operando Spectroscopy for Assessing Mechanisms of Gas Sensing,” *Angew. Chemie Int. Ed.*, vol. 46, no. 21, pp. 3826–3848, May 2007.

[189] S. J. Tinnemans, J. G. Mesu, K. Kervinen, T. Visser, T. A. Nijhuis, A. M. Beale, D. E. Keller, A. M. J. Van Der Eerden, and B. M. Weckhuysen, “Combining operando techniques in one spectroscopic-reaction cell: New opportunities for elucidating the active site and related reaction mechanism in catalysis,” *Catal. Today*, vol. 113, no. 1–2, pp. 3–15, 2006.

[190] A. M. Beale and B. M. Weckhuysen, “EXAFS as a tool to interrogate the size and shape of mono and bimetallic catalyst nanoparticles,” *Phys. Chem. Chem. Phys.*, vol. 12, no. 21, pp. 5562–5574, 2010.

[191] E. J. Peterson, A. T. Delariva, S. Lin, R. S. Johnson, H. Guo, J. T. Miller, J. H.

Kwak, C. H. F. Peden, B. Kiefer, L. F. Allard, F. H. Ribeiro, and A. K. Datye, “Low-temperature carbon monoxide oxidation catalysed by regenerable atomically dispersed palladium on alumina,” *Nat. Commun.*, vol. 5, pp. 1–11, 2014.

[192] R. Frahm, “Quick scanning exafs: First experiments,” *Nucl. Instruments Methods Phys. Res. Sect. A Accel. Spectrometers, Detect. Assoc. Equip.*, vol. 270, no. 2, pp. 578–581, 1988.

[193] M. Nachtegaal, O. Müller, C. König, and R. Frahm, “QEXAFS: Techniques and Scientific Applications for Time-Resolved XAS,” in *X-Ray Absorption and X-Ray Emission Spectroscopy*, John Wiley & Sons, Ltd, 2016, pp. 155–183.

[194] B. S. Clausen, H. Topsøe, and R. Frahm, “Application of Combined X-Ray Diffraction and Absorption Techniques for in Situ Catalyst Characterization,” vol. Volume 42, W. O. H. D.D. Eley Bruce Gates and Helmut Knözinger BT - Advances in Catalysis, Ed. Academic Press, 1998, pp. 315–344.

[195] K. Paredis, L. K. Ono, F. Behafarid, Z. Zhang, J. C. Yang, A. I. Frenkel, and B. R. Cuenya, “Evolution of the Structure and Chemical State of Pd Nanoparticles during the in Situ Catalytic Reduction of NO with H2,” *J. Am. Chem. Soc.*, vol. 133, no. 34, pp. 13455–13464, Aug. 2011.

[196] J. Polte, T. T. Ahner, F. Delissen, S. Sokolov, F. Emmerling, A. F. Thünemann, and R. Kraehnert, “Mechanism of Gold Nanoparticle Formation in the Classical Citrate Synthesis Method Derived from Coupled In Situ XANES and SAXS Evaluation,” *J. Am. Chem. Soc.*, vol. 132, no. 4, pp. 1296–1301, Feb. 2010.

[197] D. Astruc, *Nanoparticles and Catalysis*. Weinheim: Wiley-VCH Verlag GmbH & Co. KGaA, 2007.

[198] F. Xu, S. Deng, J. Xu, W. Zhang, M. Wu, B. Wang, J. Huang, and G. Yu, “Highly Active and Stable Ni–Fe Bimetal Prepared by Ball Milling for Catalytic Hydrodechlorination of 4-Chlorophenol,” *Environ. Sci. Technol.*, vol. 46, no. 8, pp. 4576–4582, Apr. 2012.

[199] N. Hanada, T. Ichikawa, and H. Fujii, “Catalytic effect of niobium oxide on hydrogen storage properties of mechanically ball milled MgH2,” *Phys. B Condens. Matter*, vol. 383, no. 1, pp. 49–50, 2006.

[200] W. Su, J. Yu, Z. Li, and Z. Jiang, “Solvent-Free Cross-Dehydrogenative Coupling Reactions under High Speed Ball-Milling Conditions Applied to the Synthesis of Functionalized Tetrahydroisoquinolines,” *J. Org. Chem.*, vol. 76, no. 21, pp. 9144–9150, Nov. 2011.

[201] G. Liang, J. Huot, S. Boily, A. Van Neste, and R. Schulz, “Catalytic effect of transition metals on hydrogen sorption in nanocrystalline ball milled MgH2–Tm (Tm=Ti, V, Mn, Fe and Ni) systems,” *J. Alloys Compd.*, vol. 292, no. 1, pp. 247–252, 1999.

[202] N. Hanada, T. Ichikawa, and H. Fujii, “Catalytic Effect of Nanoparticle 3d-Transition Metals on Hydrogen Storage Properties in Magnesium Hydride MgH2 Prepared by Mechanical Milling,” *J. Phys. Chem. B*, vol. 109, no. 15, pp. 7188–7194, Apr. 2005.

[203] M. C. Denis, P. Gouérec, D. Guay, J. P. Dodelet, G. Lalande, and R. Schulz, “Improvement of the high energy ball-milling preparation procedure of CO tolerant Pt and Ru containing catalysts for polymer electrolyte fuel cells,” *J. Appl. Electrochem.*, vol. 30, no. 11, pp. 1243–1253, 2000.

[204] A. S. Edelstein and R. C. Cammarata, *Nanomaterials: Synthesis, properties and applications.*, vol. 9, no. 12. WILEY-VCH Verlag GmbH, 1997.

[205] J. Grunes, J. Zhu, E. A. Anderson, and G. A. Somorjai, “Ethylene hydrogenation over platinum nanoparticle array model catalysts fabricated by electron beam lithography: Determination of active metal surface area,” *J. Phys. Chem. B*, vol. 106, no. 44, pp. 11463–11468, 2002.

[206] P. M. Mendes, S. Jacke, K. Critchley, J. Plaza, Y. Chen, K. Nikitin, R. E. Palmer, J. A. Preece, S. D. Evans, and D. Fitzmaurice, “Gold Nanoparticle Patterning of Silicon Wafers Using Chemical e-Beam Lithography,” *Langmuir*, vol. 20, no. 9, pp. 3766–3768, Apr. 2004.

[207] M. M. Bellah, S. M. Christensen, and S. M. Iqbal, “Nanostructures for

medical diagnostics," *J. Nanomater.*, vol. 2012, 2012.

[208] C. Marichy, M. Bechelany, and N. Pinna, "Atomic Layer Deposition of Nanostructured Materials for Energy and Environmental Applications," *Adv. Mater.*, vol. 24, no. 8, pp. 1017–1032, Jan. 2012.

[209] S. Tomita, M. Hikita, M. Fujii, S. Hayashi, and K. Yamamoto, "A new and simple method for thin graphitic coating of magnetic-metal nanoparticles," *Chem. Phys. Lett.*, vol. 316, no. 5–6, pp. 361–364, Jan. 2000.

[210] T. Abe, M. Tanizawa, K. Watanabe, and A. Taguchi, "CO2 methanation property of Ru nanoparticle-loaded TiO2 prepared by a polygonal barrel-sputtering method," *Energy Environ. Sci.*, vol. 2, no. 3, pp. 315–321, 2009.

[211] J. He, I. Ichinose, T. Kunitake, and A. Nakao, "In Situ Synthesis of Noble Metal Nanoparticles in Ultrathin TiO2 − Gel Films by a Combination of Ion-Exchange and Reduction ... In Situ Synthesis of Noble Metal Nanoparticles in Ultrathin TiO 2 - Gel Films by a Combination of," *Langmuir*, vol. 18, no. November, pp. 10005–10010, 2002.

[212] J. Haber, J. H. Block, and B. Delmon, "Methods and Procedures for Catalyst Characterization," *Handbook of Heterogeneous Catalysis*. 15-Mar-2008.

[213] R. J. White, R. Luque, V. L. Budarin, J. H. Clark, and D. J. Macquarrie, "Supported metal nanoparticles on porous materials. Methods and applications," *Chem. Soc. Rev.*, vol. 38, no. 2, pp. 481–494, 2009.

[214] D. Andreeva, T. Tabakova, V. Idakiev, P. Christov, and R. Giovanoli, "Au/α-Fe2O3 catalyst for water–gas shift reaction prepared by deposition–precipitation," *Appl. Catal. A Gen.*, vol. 169, no. 1, pp. 9–14, 1998.

[215] R. Zanella, S. Giorgio, C.-H. Shin, C. R. Henry, and C. Louis, "Characterization and reactivity in CO oxidation of gold nanoparticles supported on TiO2 prepared by deposition-precipitation with NaOH and urea," *J. Catal.*, vol. 222, no. 2, pp. 357–367, 2004.

[216] Y. Il Kim, D. Kim, and C. S. Lee, "Synthesis and characterization of CoFe2O4 magnetic nanoparticles prepared by temperature-controlled coprecipitation method," *Phys. B Condens. Matter*, vol. 337, no. 1, pp. 42–51,

2003.

[217] D. Horváth, L. Toth, and L. Guczi, “Gold nanoparticles: effect of treatment on structure and catalytic activity of Au/Fe2O3 catalyst prepared by co-precipitation,” *Catal. Letters*, vol. 67, no. 2, pp. 117–128, 2000.

[218] A. P. Kumar, B. P. Kumar, A. B. V. K. Kumar, B. T. Huy, and Y.-I. Lee, “Preparation of palladium nanoparticles on alumina surface by chemical co-precipitation method and catalytic applications,” *Appl. Surf. Sci.*, vol. 265, pp. 500–509, Jan. 2013.

[219] G. R. Bamwenda, S. Tsubota, T. Nakamura, and M. Haruta, “The influence of the preparation methods on the catalytic activity of platinum and gold supported on TiO2 for CO oxidation,” *Catal. Letters*, vol. 44, no. 1, pp. 83–87, 1997.

[220] W.-C. Li, M. Comotti, and F. Schüth, “Highly reproducible syntheses of active Au/TiO2 catalysts for CO oxidation by deposition–precipitation or impregnation,” *J. Catal.*, vol. 237, no. 1, pp. 190–196, 2006.

[221] A. Eychmüller, U. Banin, S. Dehnen, A. Eichhöfer, J. F. Corrigan, and D. Fenske, “Syntheses and Characterizations: 3.1 Semiconductor Nanoparticles,” in *Nanoparticles*, Wiley-VCH Verlag GmbH & Co. KGaA, 2003, pp. 50–185.

[222] C. G. Blatchford, J. R. Campbell, and J. A. Creighton, “Plasma resonance — enhanced raman scattering by absorbates on gold colloids: The effects of aggregation,” *Surf. Sci.*, vol. 120, no. 2, pp. 435–455, 1982.

[223] R. Franke, J. Rothe, J. Pollmann, J. Hormes, H. Bönnemann, W. Brijoux, and T. Hindenburg, “A Study of the Electronic and Geometric Structure of Colloidal Ti0·0.5THF,” *J. Am. Chem. Soc.*, vol. 118, no. 48, pp. 12090–12097, Jan. 1996.

[224] J. Kimling, M. Maier, B. Okenve, V. Kotaidis, H. Ballot, and A. Plech, “Turkevich Method for Gold Nanoparticle Synthesis Revisited,” *J. Phys. Chem. B*, vol. 110, no. 32, pp. 15700–15707, Aug. 2006.

[225] X.-M. Li, M. R. de Jong, K. Inoue, S. Shinkai, J. Huskens, and D. N. Reinhoudt, “Formation of gold colloids using thioether derivatives as

stabilizing ligands," *J. Mater. Chem.*, vol. 11, no. 7, pp. 1919–1923, 2001.

[226] N. Zheng, J. Fan, and G. D. Stucky, "One-Step One-Phase Synthesis of Monodisperse Noble-Metallic Nanoparticles and Their Colloidal Crystals," *J. Am. Chem. Soc.*, vol. 128, no. 20, pp. 6550–6551, May 2006.

[227] H. Bönnemann and R. M. Richards, "Nanoscopic Metal Particles − Synthetic Methods and Potential Applications," *Eur. J. Inorg. Chem.*, vol. 2001, no. 10, pp. 2455–2480, Sep. 2001.

[228] S. Förster, "Colloids and polymers: Amphiphilic block copolymers," *Berichte der Bunsengesellschaft für Phys. Chemie*, vol. 101, no. 11, pp. 1671–1678, Nov. 1997.

[229] C. Petit and M. P. Pileni, "Synthesis of cadmium sulfide in situ in reverse micelles and in hydrocarbon gels," *J. Phys. Chem.*, vol. 92, no. 8, pp. 2282–2286, Apr. 1988.

[230] J. Tanori and M. P. Pileni, "Control of the Shape of Copper Metallic Particles by Using a Colloidal System as Template," *Langmuir*, vol. 13, no. 4, pp. 639–646, Feb. 1997.

[231] H. Bönnemann, W. Brijoux, R. Brinkmann, R. Fretzen, T. Joussen, R. Köppler, B. Korall, P. Neiteler, and J. Richter, "Preparation, characterization, and application of fine metal particles and metal colloids using hydrotriorganoborates," *J. Mol. Catal.*, vol. 86, no. 1, pp. 129–177, 1994.

[232] S.-W. Kim, S. Kim, J. B. Tracy, A. Jasanoff, and M. G. Bawendi, "Phosphine Oxide Polymer for Water-Soluble Nanoparticles," *J. Am. Chem. Soc.*, vol. 127, no. 13, pp. 4556–4557, Apr. 2005.

[233] Y. Li and M. A. El-Sayed, "The Effect of Stabilizers on the Catalytic Activity and Stability of Pd Colloidal Nanoparticles in the Suzuki Reactions in Aqueous Solution†," *J. Phys. Chem. B*, vol. 105, no. 37, pp. 8938–8943, Sep. 2001.

[234] M. Aslam, L. Fu, M. Su, K. Vijayamohanan, and V. P. Dravid, "Novel one-step synthesis of amine-stabilized aqueous colloidal gold nanoparticles," *J. Mater. Chem.*, vol. 14, no. 12, pp. 1795–1797, 2004.

[235] M. M. Maye, J. Luo, I.-I. S. Lim, L. Han, N. N. Kariuki, D. Rabinovich, Liu, and C.-J. Zhong, “Size-Controlled Assembly of Gold Nanoparticles Induced by a Tridentate Thioether Ligand,” *J. Am. Chem. Soc.*, vol. 125, no. 33, pp. 9906–9907, Aug. 2003.

[236] D. F. Evans, D. J. Mitchell, and B. W. Ninham, “Oil, water, and surfactant: properties and conjectured structure of simple microemulsions,” *J. Phys. Chem.*, vol. 90, no. 13, pp. 2817–2825, Jun. 1986.

[237] D. Ingert, “Colloidal Methods and Shape Anisotropy,” in *Nanomaterials and Nanochemistry*, C. Bréchignac, P. Houdy, and M. Lahmani, Eds. Berlin, Heidelberg: Springer Berlin Heidelberg, 2007, pp. 441–454.

[238] A. Riskin, “Study of the CSD process for the ordered deposition of metallic nanocrystals.,” 2012.

[239] A. S. Lee, V. Bütün, M. Vamvakaki, S. P. Armes, J. A. Pople, and A. P. Gast, “Structure of pH-Dependent Block Copolymer Micelles: Charge and Ionic Strength Dependence,” *Macromolecules*, vol. 35, no. 22, pp. 8540–8551, Oct. 2002.

[240] V. K. Aswal and P. S. Goyal, “Dependence of the size of micelles on the salt effect in ionic micellar solutions,” *Chem. Phys. Lett.*, vol. 364, no. 1, pp. 44–50, 2002.

[241] L. Zhang, R. J. Barlow, and A. Eisenberg, “Scaling Relations and Coronal Dimensions in Aqueous Block Polyelectrolyte Micelles,” *Macromolecules*, vol. 28, no. 18, pp. 6055–6066, Aug. 1995.

[242] S. Förster, M. Zisenis, E. Wenz, and M. Antonietti, “Micellization of strongly segregated block copolymers,” *J. Chem. Phys.*, vol. 104, no. 24, pp. 9956–9970, Jun. 1996.

[243] A. Taleb, C. Petit, and M. Pileni, “Synthesis of highly monodisperse silver nanoparticles from AOT reverse micelles: a way to 2D and 3D self-organization,” *Chem. Mater.*, vol. 9, no. 12, pp. 950–959, 1997.

[244] M. P. Pileni, “The role of soft colloidal templates in controlling the size and shape of inorganic nanocrystals,” *Nat Mater*, vol. 2, no. 3, pp. 145–150, Mar.

2003.

[245] R. Saito, S. Okamura, and K. Ishizu, “Introduction of colloidal silver into a poly(2-vinyl pyridine) microdomain of microphase separated poly(styrene-b-2-vinyl pyridine) film,” *Polymer (Guildf).*, vol. 33, no. 5, pp. 1099–1101, 1992.

[246] M. Antonietti and S. Heinz, “Supramolekulare Strukturen bei Polymeren: Ein Weg zu „Intelligenten” Materialien?,” *Nachrichten aus Chemie, Tech. und Lab.*, vol. 40, no. 3, pp. 308–314, Mar. 1992.

[247] J. P. Spatz, S. Sheiko, and M. Möller, “Ion-stabilized block copolymer micelles: film formation and intermicellar interaction,” *Macromolecules*, vol. 29, no. 9, pp. 3220–3226, 1996.

[248] J. P. Spatz, S. Mößmer, and M. Möller, “Mineralization of gold nanoparticles in a block copolymer microemulsion,” *Chem. - A Eur. J.*, vol. 2, no. 12, pp. 1552–1555, 1996.

[249] M. M. Vela, M. Valero, and F. Ortega, “Light Scattering and Electrical Conductivity Studies of the Aerosol OT Toluene Water - In - Oil Microemulsions,” *J. Phys. Chem. B*, vol. 105, pp. 10163–10168, 2001.

[250] C.-L. Chiang, “Controlled Growth of Gold Nanoparticles in AOT/C12E4/Isooctane Mixed Reverse Micelles,” *J. Colloid Interface Sci.*, vol. 239, no. 2, pp. 334–341, 2001.

[251] G. Kästle, H.-G. Boyen, F. Weigl, P. Ziemann, S. Riethmüller, C. H. Hartmann, J. P. Spatz, M. Möller, M. G. Garnier, and P. Oelhafen, “The Self-organization of Metal Loaded Micelles - An Approach to Prepare Ordered Arrays of Metallic Nanoislands,” *Phase Transitions*, vol. 76, no. 4–5, pp. 307–313, 2003.

[252] J. P. Spatz, A. Roescher, and M. Moeller, “Gold nanoparticles in micellar poly(styrene)-b-poly(ethylene oxide) films - size and interparticle distance control in monoparticulate films,” *Am. Chem. Soc. Polym. Prepr. Div. Polym. Chem.*, vol. 37, no. 1, p. 409, 1996.

[253] J. R. Croy, S. Mostafa, H. Heinrich, and B. R. Cuenya, “Size-selected pt

nanoparticles synthesized via micelle encapsulation: Effect of pretreatment and oxidation state on the activity for methanol decomposition and oxidation," *Catal. Letters*, vol. 131, no. 1–2, pp. 21–32, 2009.

[254] S. Mostafa, F. Behafarid, J. R. Croy, L. K. Ono, L. Li, J. C. Yang, A. I. Frenkel, and B. R. Cuenya, "Shape-dependent catalytic properties of Pt nanoparticles," *J. Am. Chem. Soc.*, vol. 132, no. 44, pp. 15714–15719, 2010.

[255] F. Behafarid, L. K. Ono, S. Mostafa, J. R. Croy, G. Shafai, S. Hong, T. S. Rahman, S. R. Bare, and B. Roldan Cuenya, "Electronic properties and charge transfer phenomena in Pt nanoparticles on γ-Al2O3: size, shape, support, and adsorbate effects," *Phys. Chem. Chem. Phys.*, vol. 14, p. 11766, 2012.

[256] B. Roldan Cuenya, J. R. Croy, S. Mostafa, F. Behafarid, L. Li, Z. Zhang, J. C. Yang, Q. Wang, and A. I. Frenkel, "Solving the structure of size-selected Pt nanocatalysts synthesized by inverse micelle encapsulation," *J. Am. Chem. Soc.*, vol. 132, no. 25, pp. 8747–8756, 2010.

[257] B. Roldan Cuenya, M. Alcántara Ortigoza, L. K. Ono, F. Behafarid, S. Mostafa, J. R. Croy, K. Paredis, G. Shafai, T. S. Rahman, L. Li, Z. Zhang, and J. C. Yang, "Thermodynamic properties of Pt nanoparticles: Size, shape, support, and adsorbate effects," *Phys. Rev. B - Condens. Matter Mater. Phys.*, vol. 84, no. 24, pp. 1–14, 2011.

[258] D. J. Martin, D. Decarolis, R. Tucoulou, G. Martínez-Criado, and A. M. Beale, "Towards the interrogation of the behaviour of a single nanoparticle under realistic catalytic reaction conditions," *Catal. Struct. React.*, vol. 3, no. 1–2, pp. 63–70, Apr. 2017.

[259] D. James Martin, D. Decarolis, Y. I. Odarchenko, J. J. Herbert, T. Arnold, J. Rawle, C. Nicklin, H.-G. Boyen, and A. M. Beale, "Reversible restructuring of supported Au nanoparticles during butadiene hydrogenation revealed by operando GISAXS/GIWAXS," *Chem. Commun.*, vol. 53, pp. 5159–5162, 2017.

[260] E. K. Gibson, A. M. Beale, C. R. A. Catlow, A. Chutia, D. Gianolio, A. Gould, A. Kroner, K. M. H. Mohammed, M. Perdjon, and S. M. Rogers, "Restructuring of AuPd nanoparticles studied by a combined XAFS/DRIFTS

approach," *Chem. Mater.*, 2015.

[261] T. Cukic, R. Kraehnert, M. Holena, D. Herein, D. Linke, and U. Dingerdissen, "The influence of preparation variables on the performance of Pd/Al2O3 catalyst in the hydrogenation of 1,3-butadiene: Building a basis for reproducible catalyst synthesis," *Appl. Catal. A Gen.*, vol. 323, pp. 25–37, 2007.

[262] B. R. Cuenya, "Metal nanoparticle catalysts beginning to shape-up," *Acc. Chem. Res.*, vol. 46, no. 8, pp. 1682–1691, 2013.

[263] D. B. Williams and C. B. Carter, "The Transmission Electron Microscope," in *Transmission Electron Microscopy: A Textbook for Materials Science*, Boston, MA: Springer US, 2009, pp. 3–22.

[264] D. R. G. Mitchell and B. Schaffer, "Scripting-customised microscopy tools for Digital Micrograph™," *Ultramicroscopy*, vol. 103, no. 4, pp. 319–332, 2005.

[265] K. W. Schneider, C. A.; Rasband, W. S. & Eliceiri, "NIH Image to ImageJ: 25 years of image analysis," *Nat. Methods*, vol. 9, no. 7, p. 671, 2012.

[266] K.-S. Lee and M. A. El-Sayed, "Gold and Silver Nanoparticles in Sensing and Imaging: Sensitivity of Plasmon Response to Size, Shape, and Metal Composition," *J. Phys. Chem. B*, vol. 110, no. 39, pp. 19220–19225, Oct. 2006.

[267] K. L. Kelly, E. Coronado, L. L. Zhao, and G. C. Schatz, "The Optical Properties of Metal Nanoparticles: The Influence of Size, Shape, and Dielectric Environment," *J. Phys. Chem. B*, vol. 107, no. 3, pp. 668–677, Jan. 2003.

[268] S. Link and M. A. El-Sayed, "Size and Temperature Dependence of the Plasmon Absorption of Colloidal Gold Nanoparticles," *J. Phys. Chem. B*, vol. 103, no. 21, pp. 4212–4217, May 1999.

[269] S. Underwood and P. Mulvaney, "Effect of the Solution Refractive Index on the Color of Gold Colloids," *Langmuir*, vol. 10, no. 10, pp. 3427–3430, Oct. 1994.

[270] J. J. Mock, D. R. Smith, and S. Schultz, "Local Refractive Index Dependence

of Plasmon Resonance Spectra from Individual Nanoparticles," *Nano Lett.*, vol. 3, no. 4, pp. 485–491, Apr. 2003.

[271] J. Klaas, G. Schulz-Ekloff, and N. I. Jaeger, "UV−Visible Diffuse Reflectance Spectroscopy of Zeolite-Hosted Mononuclear Titanium Oxide Species," *J. Phys. Chem. B*, vol. 101, no. 8, pp. 1305–1311, 1997.

[272] T. Hida, "Brownian Motion BT - Brownian Motion," T. Hida, Ed. New York, NY: Springer US, 1980, pp. 44–113.

[273] M. Sartor, *Dynamic light scattering*. University of California San Diego.

[274] R. Pecora, "Dynamic Light Scattering Measurement of Nanometer Particles in Liquids," *J. Nanoparticle Res.*, vol. 2, no. 2, pp. 123–131, 2000.

[275] S. Bordiga, E. Groppo, G. Agostini, J. A. Van Bokhoven, and C. Lamberti, "Reactivity of surface species in heterogeneous catalysts probed by in situ x-ray absorption techniques," *Chem. Rev.*, vol. 113, no. 3, pp. 1736–1850, 2013.

[276] S. Bordiga, E. Groppo, G. Agostini, J. A. van Bokhoven, and C. Lamberti, "Reactivity of Surface Species in Heterogeneous Catalysts Probed by In Situ X-ray Absorption Techniques," *Chem. Rev.*, vol. 113, no. 3, pp. 1736–1850, Mar. 2013.

[277] R. A. Van Nordsthand, "The Use of X-Ray K-Absorption Edges in the Study of Catalytically Active Solids," *Adv. Catal.*, vol. 12, pp. 149–187, 1960.

[278] D. C. Koningsberger, B. L. Mojet, G. E. Van Dorssen, and D. E. Ramaker, "XAFS spectroscopy ; fundamental principles and data analysis," *Top. Catal.*, vol. 10, pp. 143–155, 2000.

[279] A. G. McKale, G. S. Knapp, and S.-K. Chan, "Practical method for full curved-wave theory analysis of experimental extended x-ray-absorption fine structure," *Phys. Rev. B*, vol. 33, no. 2, pp. 841–846, Jan. 1986.

[280] B. Ravel and M. Newville, "ATHENA, ARTEMIS, HEPHAESTUS: data analysis for X-ray absorption spectroscopy using IFEFFIT," *J. Synchrotron Radiat.*, vol. 12, no. 4, pp. 537–541, 2005.

[281] M. Newville, "IFEFFIT: interactive XAFS analysis and FEFF fitting," *J.*

Synchrotron Radiat., vol. 8, p. 322, 2001.

[282] B. B. He, "Small-Angle X-Ray Scattering," in *Two-Dimensional X-Ray Diffraction*, John Wiley & Sons, Inc., 2009, pp. 329–350.

[283] R. Hilfiker, H.-F. Eicke, W. Sager, C. Steeb, U. Hofmeier, and R. Gehrke, "Form and Structure Factors of Water/AOT/Oil Microemulsions from Synchrotron SAXS," *Berichte der Bunsengesellschaft für Phys. Chemie*, vol. 94, no. 6, pp. 677–683, Jun. 1990.

[284] S. R. Kline, "Reduction and analysis of SANS and USANS data using IGOR Pro," *J. Appl. Crystallogr.*, vol. 39, pp. 895–900, 2006.

[285] M. Kotlarchyk, R. B. Stephens, and J. S. Huang, "Study of Schultz distribution to model polydispersity of microemulsion droplets," *J. Phys. Chem.*, vol. 92, no. 6, pp. 1533–1538, 1988.

[286] O. Glatter and O. Kratky, *Small Angle X-ray Scattering*. London: Academic Press, 1982.

[287] P. Ghosh, G. Han, M. De, C. K. Kim, and V. M. Rotello, "Gold nanoparticles in delivery applications," *Adv. Drug Deliv. Rev.*, vol. 60, no. 11, pp. 1307–1315, Aug. 2008.

[288] R. Elghanian, J. J. Storhoff, R. C. Mucic, R. L. Letsinger, and C. A. Mirkin, "Selective Colorimetric Detection of Polynucleotides Based on the Distance-Dependent Optical Properties of Gold Nanoparticles," *Science (80-.).*, vol. 277, no. 5329, p. 1078 LP-1081, Aug. 1997.

[289] M. Moritz and M. Geszke-Moritz, "The newest achievements in synthesis, immobilization and practical applications of antibacterial nanoparticles," *Chem. Eng. J.*, vol. 228, pp. 596–613, Jul. 2013.

[290] G. Cao, *Nanastructures and Nanomaterials - Synthesis, Properties and Applications*, vol. 2. London: Imperial College Press, 2004.

[291] A. S. Edelstein and R. C. Cammarata, *Nanomaterials : synthesis, properties, and applications*. Abingdon: Taylor & Francis, 1998.

[292] P. A. Schaal, A. Besmehn, E. Maynicke, M. Noyong, B. Beschoten, and U.

Simon, “Electrically Conducting Nanopatterns Formed by Chemical e-Beam Lithography via Gold Nanoparticle Seeds,” *Langmuir*, vol. 28, no. 5, pp. 2448–2454, Feb. 2012.

[293] W. Karim, A. Kleibert, U. Hartfelder, A. Balan, J. Gobrecht, J. A. van Bokhoven, and Y. Ekinci, “Size-dependent redox behavior of iron observed by in-situ single nanoparticle spectro-microscopy on well-defined model systems,” *Sci. Rep.*, vol. 6, no. 1, p. 18818, 2016.

[294] B. Yin, H. Ma, S. Wang, and S. Chen, “Electrochemical Synthesis of Silver Nanoparticles under Protection of Poly(N-vinylpyrrolidone),” *J. Phys. Chem. B*, vol. 107, no. 34, pp. 8898–8904, Aug. 2003.

[295] A. Nemamcha, J.-L. Rehspringer, and D. Khatmi, “Synthesis of Palladium Nanoparticles by Sonochemical Reduction of Palladium(II) Nitrate in Aqueous Solution,” *J. Phys. Chem. B*, vol. 110, no. 1, pp. 383–387, Jan. 2006.

[296] M. C. Saint-Lager, I. Laoufi, A. Bailly, O. Robach, S. Garaudee, and P. Dolle, “Catalytic properties of supported gold nanoparticles: new insights into the size-activity relationship gained from in operando measurements,” *Faraday Discuss.*, vol. 152, pp. 253–265, 2011.

[297] I. Laoufi, M. C. Saint-Lager, R. Lazzari, J. Jupille, O. Robach, S. Garaudée, G. Cabailh, P. Dolle, H. Cruguel, and A. Bailly, “Size and catalytic activity of supported gold nanoparticles: An in operando study during CO oxidation,” *J. Phys. Chem. C*, vol. 115, no. 11, pp. 4673–4679, 2011.

[298] A. Kabelitz, A. Guilherme, M. Joester, U. Reinholz, M. Radtke, R. Bienert, K. Schulz, R. Schmack, R. Kraehnert, and F. Emmerling, “Time-resolved in situ studies on the formation mechanism of iron oxide nanoparticles using combined fast-XANES and SAXS,” *CrystEngComm*, vol. 17, no. 44, pp. 8463–8470, 2015.

[299] J. Polte, X. Tuaev, M. Wuithschick, A. Fischer, A. F. Thuenemann, K. Rademann, R. Kraehnert, and F. Emmerling, “Formation Mechanism of Colloidal Silver Nanoparticles : Analogies and Di ff erences to the Growth of Gold Nanoparticles,” *ACS Nano*, vol. 7, no. 7, pp. 5791–5802, 2012.

[300] N. T. K. Thanh, N. Maclean, and S. Mahiddine, “Mechanisms of Nucleation and Growth of Nanoparticles in Solution,” *Chem. Rev.*, vol. 114, no. 15, pp. 7610–7630, Aug. 2014.

[301] T. Sakai and P. Alexandridis, “Single-step synthesis and stabilization of metal nanoparticles in aqueous pluronic block copolymer solutions at ambient temperature,” *Langmuir*, vol. 20, no. 20, pp. 8426–8430, 2004.

[302] D. J. Martin, D. Decarolis, R. Tucoulou, G. Martínez-Criado, and A. M. Beale, “Towards the interrogation of the behaviour of a single nanoparticle under realistic catalytic reaction conditions,” *Catal. Struct. React.*, vol. 3, no. 1–2, pp. 63–70, Apr. 2017.

[303] U. Wiedwald, L. Han, J. Biskupek, U. Kaiser, and P. Ziemann, “Preparation and characterization of supported magnetic nanoparticles prepared by reverse micelles,” *Beilstein J. Nanotechnol.*, vol. 1, no. 1, pp. 24–47, 2010.

[304] M. Harada and Y. Kamigaito, “Nucleation and Aggregative Growth Process of Platinum Nanoparticles Studied by in Situ Quick XAFS Spectroscopy,” *Langmuir*, vol. 28, no. 5, pp. 2415–2428, Feb. 2012.

[305] Z. Zhang and Y. Wu, “Investigation of the NaBH4-Induced Aggregation of Au Nanoparticles,” *Langmuir*, vol. 26, no. 12, pp. 9214–9223, Jun. 2010.

[306] L. Bronstein, M. Antonietti, and P. Valetsky, “Metal Colloids in Block Copolymer Micelles: Formation and Material Properties,” in *Nanoparticles and Nanostructured Films*, Wiley-VCH Verlag GmbH, 1998, pp. 145–171.

[307] J.-M. Yun, J.-S. Yeo, J. Kim, H.-G. Jeong, D.-Y. Kim, Y.-J. Noh, S.-S. Kim, B.-C. Ku, and S.-I. Na, “Solution-Processable Reduced Graphene Oxide as a Novel Alternative to PEDOT:PSS Hole Transport Layers for Highly Efficient and Stable Polymer Solar Cells,” *Adv. Mater.*, vol. 23, no. 42, pp. 4923–4928, Nov. 2011.

[308] H. B. Bohidar and M. Behboudnia, “Characterization of reverse micelles by dynamic light scattering,” *Colloids Surfaces A Physicochem. Eng. Asp.*, vol. 178, no. 1–3, pp. 313–323, Mar. 2001.

[309] R. D. Falcone, J. J. Silber, and N. M. Correa, “What are the factors that

control non-aqueous/AOT/n-heptane reverse micelle sizes? A dynamic light scattering study," *Phys. Chem. Chem. Phys.*, vol. 11, no. 47, p. 11096, 2009.

[310] D. Voulgaris, C. Tsitsilianis, V. Grayer, F. J. Esselink, and G. Hadziioannou, "Amphiphile micelles formed by polystyrene/poly(2-vinyl pyridine) heteroarm star copolymers in toluene," *Polymer (Guildf).*, vol. 40, no. 21, pp. 5879–5889, Oct. 1999.

[311] B. N. Khlebtsov and N. G. Khlebtsov, "On the measurement of gold nanoparticle sizes by the dynamic light scattering method," *Colloid J.*, vol. 73, no. 1, pp. 118–127, 2011.

[312] C. M. Hoo, N. Starostin, P. West, and M. L. Mecartney, "A comparison of atomic force microscopy (AFM) and dynamic light scattering (DLS) methods to characterize nanoparticle size distributions," *J. Nanoparticle Res.*, vol. 10, no. 1, pp. 89–96, 2008.

[313] S. Mössmer, J. P. Spatz, M. Möller, T. Aberle, J. Schmidt, and W. Burchard, "Solution Behavior of Poly(styrene)- b lock -poly(2-vinylpyridine) Micelles Containing Gold Nanoparticles," *Macromolecules*, vol. 33, no. 13, pp. 4791–4798, 2000.

[314] P. Zhang and T. K. Sham, "Tuning the electronic behavior of Au nanoparticles with capping molecules," *Appl. Phys. Lett.*, vol. 81, no. 4, pp. 736–738, Jul. 2002.

[315] G. S. Pokrovski, B. R. Tagirov, J. Schott, E. F. Bazarkina, J.-L. Hazemann, and O. Proux, "An in situ X-ray absorption spectroscopy study of gold-chloride complexing in hydrothermal fluids," *Chem. Geol.*, vol. 259, no. 1, pp. 17–29, 2009.

[316] T. M. Salama, T. Shido, R. Ohnishi, and M. Ichikawa, "EXAFS/XANES, XRD, and UV−Vis Characterization of Intrazeolitic Gold(I) Prepared by Monolayer Dispersion of AuCl3 inside Na−Y Zeolite," *J. Phys. Chem.*, vol. 100, no. 9, pp. 3688–3694, Jan. 1996.

[317] M. Hargittai, A. Schulz, B. Réffy, and M. Kolonits, "Molecular Structure, Bonding, and Jahn−Teller Effect in Gold Chlorides: Quantum Chemical

Study of AuCl3, Au2Cl6, AuCl4-, AuCl, and Au2Cl2 and Electron Diffraction Study of Au2Cl6," *J. Am. Chem. Soc.*, vol. 123, no. 7, pp. 1449–1458, Feb. 2001.

[318] S. N. Reifsnyder, H. H. Lamb, and N. Carolina, "Characterization of Silica-Supported Pd - Au Clusters by X-ray Absorption Spectroscopy," *J. Phys. Chem. B*, vol. 2, no. 3, pp. 321–329, 1999.

[319] A. Riskin, A. M. Beale, H.-G. Boyen, A. Vantomme, A. Hardy, and M. K. Van Bael, "The use of XAFS to determine the nature of interaction of iron and molybdenum metal salts within PS-b-P2VP micelles.," *Phys. Chem. Chem. Phys.*, vol. 15, no. 5, pp. 1675–81, 2013.

[320] H. Shi, N. Xu, D. Zhao, and B.-Q. Xu, "Immobilized PVA-stabilized gold nanoparticles on silica show an unusual selectivity in the hydrogenation of cinnamaldehyde," *Catal. Commun.*, vol. 9, no. 10, pp. 1949–1954, 2008.

[321] A. B. Kroner, K. M. H. Mohammed, M. Gilbert, G. Duller, L. Cahill, P. Leicester, E. J. Shotton, A. B. Kroner, K. M. H. Mohammed, M. Gilbert, G. Duller, L. Cahill, P. Leicester, R. Woolliscroft, and E. J. Shotton, "A flexible gas flow reaction cell for in situ X-ray Absorption Spectroscopy studies," *AIP Conf. Proc.*, vol. 1741, pp. 10–14, 2016.

[322] S. Eustis and M. A. El-Sayed, "Why gold nanoparticles are more precious than pretty gold: Noble metal surface plasmon resonance and its enhancement of the radiative and nonradiative properties of nanocrystals of different shapes," *Chem. Soc. Rev.*, vol. 35, no. 3, pp. 209–217, 2006.

[323] O. Varnavski, G. Ramakrishna, J. Kim, D. Lee, and T. Goodson, "Critical Size for the Observation of Quantum Confinement in Optically Excited Gold Clusters," *J. Am. Chem. Soc.*, vol. 132, no. 1, pp. 16–17, Jan. 2010.

[324] E. Bus, J. T. Miller, and J. A. van Bokhoven, "Hydrogen Chemisorption on Al2O3-Supported Gold Catalysts," *J. Phys. Chem. B*, vol. 109, no. 30, pp. 14581–14587, Aug. 2005.

[325] E. Bus, D. E. Ramaker, and J. A. van Bokhoven, "Structure of Ethene Adsorption Sites on Supported Metal Catalysts from in Situ XANES

Analysis," *J. Am. Chem. Soc.*, vol. 129, no. 26, pp. 8094–8102, Jul. 2007.

[326] N. Weiher, E. Bus, L. Delannoy, C. Louis, D. E. Ramaker, J. T. Miller, and J. A. van Bokhoven, "Structure and oxidation state of gold on different supports under various CO oxidation conditions," *J. Catal.*, vol. 240, no. 2, pp. 100–107, 2006.

[327] T. A. Nijhuis, E. Sacaliuc, A. M. Beale, A. M. J. van der Eerden, J. C. Schouten, and B. M. Weckhuysen, "Spectroscopic evidence for the adsorption of propene on gold nanoparticles during the hydro-epoxidation of propene," *J. Catal.*, vol. 258, no. 1, pp. 256–264, 2008.

[328] A. L. Bugaev, A. A. Guda, A. Lazzarini, K. A. Lomachenko, E. Groppo, R. Pellegrini, A. Piovano, H. Emerich, A. V. Soldatov, L. A. Bugaev, V. P. Dmitriev, J. A. van Bokhoven, and C. Lamberti, "In situ formation of hydrides and carbides in palladium catalyst: When XANES is better than EXAFS and XRD," *Catal. Today*, vol. 283, no. 1, pp. 119–126, 2017.

[329] R. H. R. Castro and D. V Quach, "Analysis of Anhydrous and Hydrated Surface Energies of gamma-Al2O3 by Water Adsorption Microcalorimetry," *J. Phys. Chem. C*, vol. 116, no. 46, pp. 24726–24733, Nov. 2012.

[330] B. Lönnberg, "Characterization of milled Si3N4 powder using X-ray peak broadening and surface area analysis," *J. Mater. Sci.*, vol. 29, no. 12, pp. 3224–3230, 1994.

[331] J. Mizele, J. L. Dandurand, and J. Schott, "Determination of the surface energy of amorphous silica from solubility measurements in micropores," *Surf. Sci.*, vol. 162, no. 1, pp. 830–837, 1985.

[332] G. Guenther and O. Guillon, "Models of size-dependent nanoparticle melting tested on gold," *J. Mater. Sci.*, vol. 49, no. 23, pp. 7915–7932, 2014.

[333] J. A. Moulijn, A. E. van Diepen, and F. Kapteijn, "Catalyst deactivation: is it predictable?," *Appl. Catal. A Gen.*, vol. 212, no. 1, pp. 3–16, 2001.

[334] B. K. Furlong, J. W. Hightower, T. Y.-L. Chan, A. Sarkany, and L. Guczi, "1,3-Butadiene selective hydrogenation over Pd/alumina and CuPd/alumina catalysts," *Appl. Catal. A Gen.*, vol. 117, no. 1, pp. 41–51, 1994.

[335] J. Gaube and H. F. Klein, “Kinetics and mechanism of butene isomerization/hydrogenation and of 1,3-butadiene hydrogenation on palladium,” *Appl. Catal. A Gen.*, vol. 470, pp. 361–368, 2014.

[336] G. Garcia Cervantes, F. J. Cadete Santos Aires, and J. C. Bertolini, “Compared properties of Pd on thermo-conductor supports (SiC, Si 3N4) and Pd on oxide supports (Al2O 3, SiO2) for the 1,3-butadiene hydrogenation reaction,” *J. Catal.*, vol. 214, no. 1, pp. 26–32, 2003.

[337] A. Sarkany, “Effect of Hydrocarbonaceous Deposits on Competitive Hydrogenation of 1,3-Butadiene and Propene over Pd Catalyst,” *J. Catal.*, vol. 180, no. 2, pp. 149–152, 1998.

[338] A. Sarkany, “Hydrocarbonaceous deposit assisted n-butane formation in hydrogenation of 1,3-butadiene over Pd catalysts,” *Appl. Catal. A Gen.*, vol. 175, no. 1, pp. 245–253, 1998.

[339] E. M. Crabb and R. Marshall, “Properties of alumina supported Pd-Fe and Pt-Fe catalysts prepared using surface organometallic chemistry,” *Appl. Catal. A Gen.*, vol. 217, no. 1, pp. 41–53, 2001.

8 Appendix

8.1 Chapter 2

8.1.1 TGA measurement

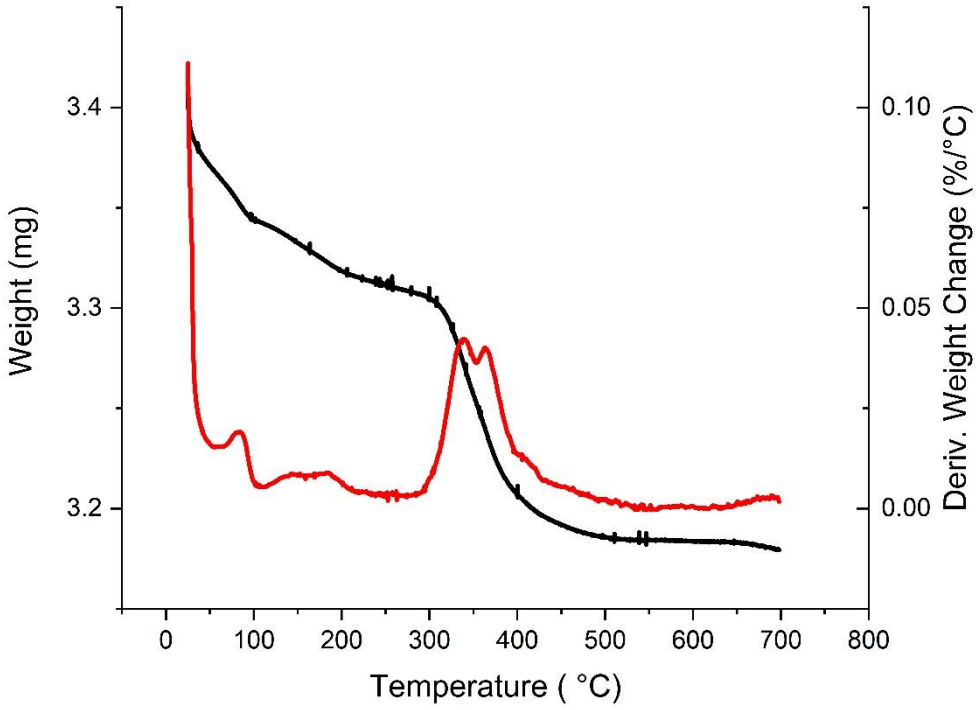

Figure S.2.1. TGA of Au/SiO_2 30-8.5 before calcination process

8.2 Chapter 3

8.2.1 SAXS Fit

In this section is shown the fit of the SAXS data obtained during the experiment shown in chapter 3

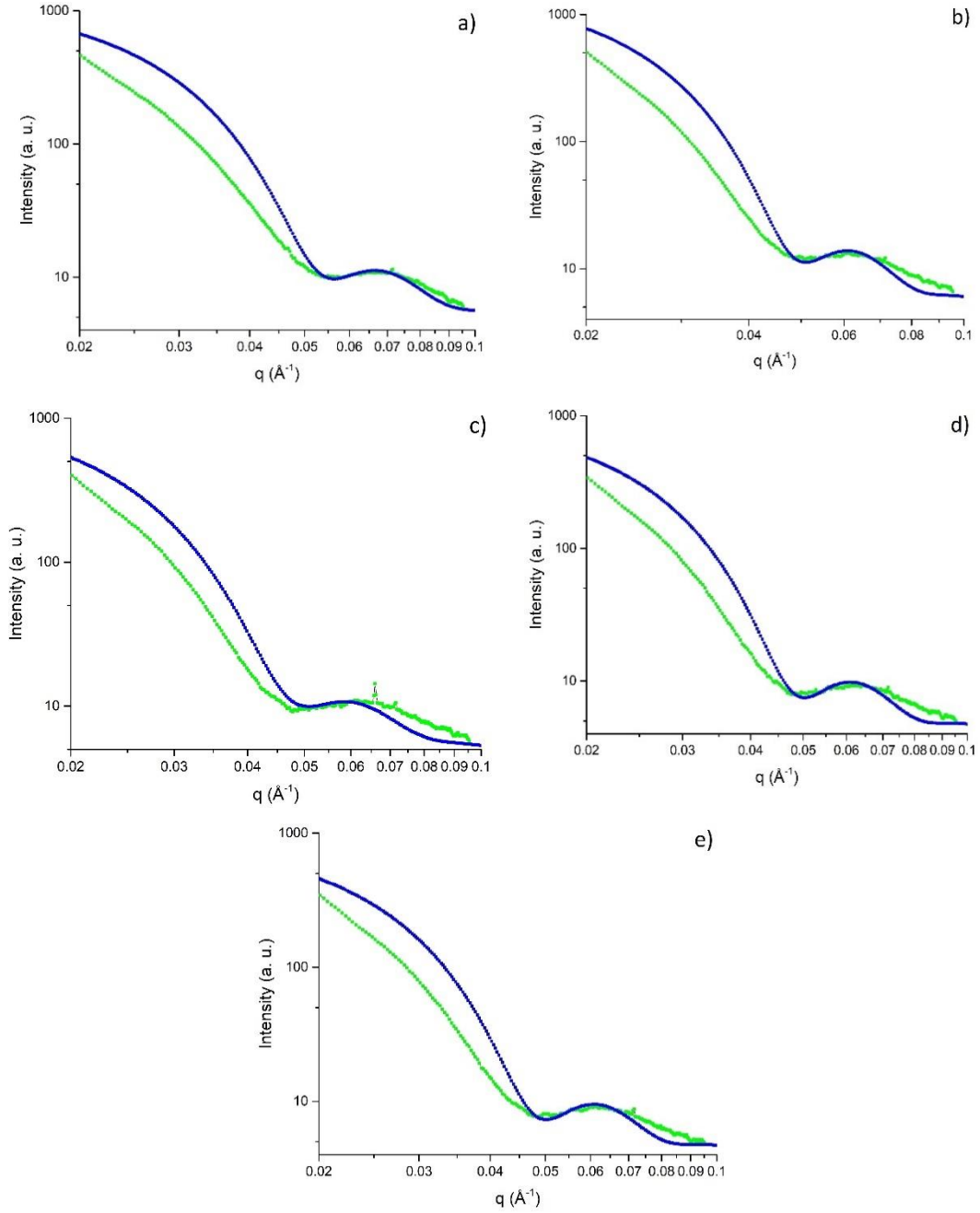

Figure S3.3.1. 1D SAXS curves (in green) and corresponding fitted curves (in blue) for sample A-HCl, after a) 0h; b)20 min; c) 1h 15 min; d) 2h 15 min; e) 6h 15 min

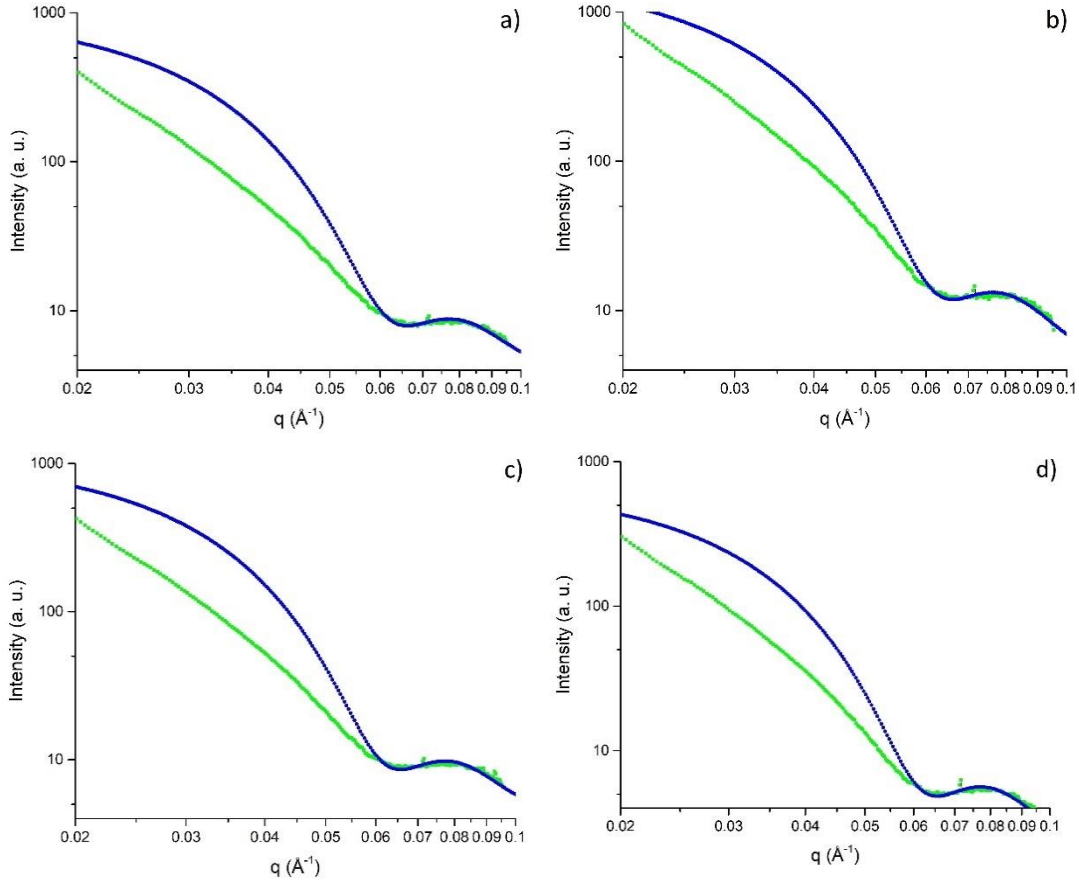

Figure S3.3.2. 1D SAXS curves (in green) and corresponding fitted curves (in blue) for sample A, after a) 0h; b) 1h 15 min; c) 2h 15 min; d) 6h 15 min

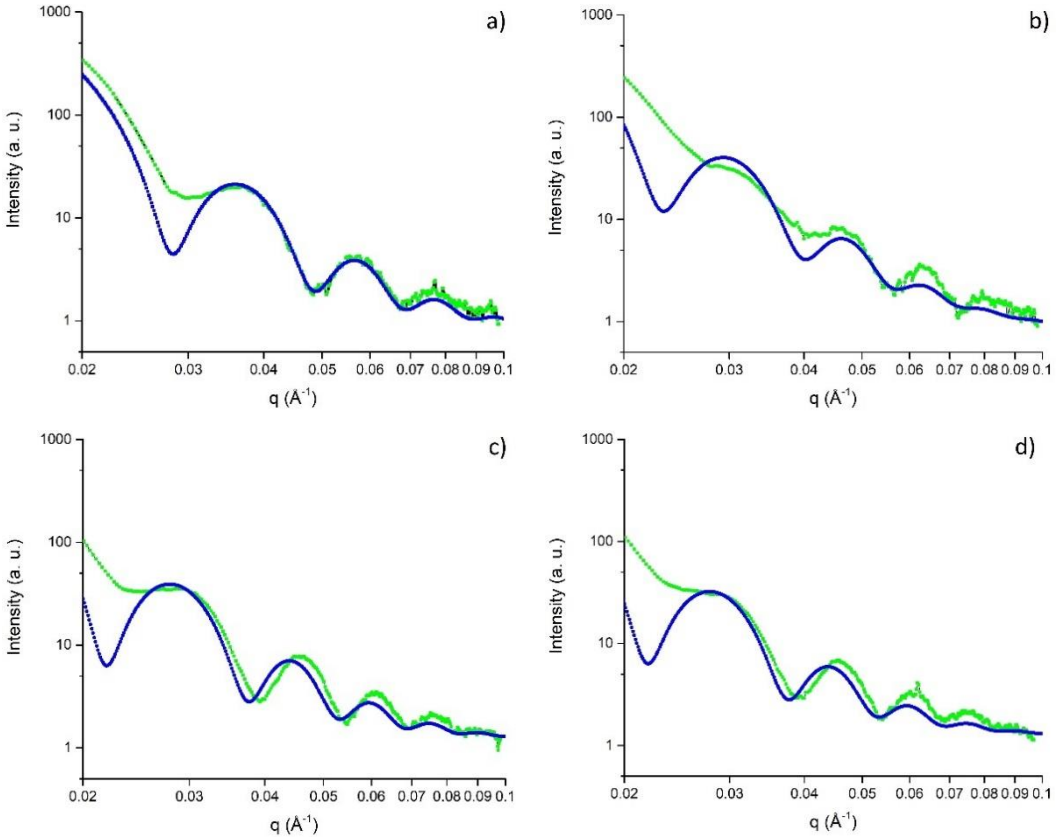

Figure S3.3.3. 1D SAXS curves (in green) and corresponding fitted curves (in blue) for sample B-HCl, after a) 0h; b)20 min; c) 1h 15 min; d) 6h 15 min

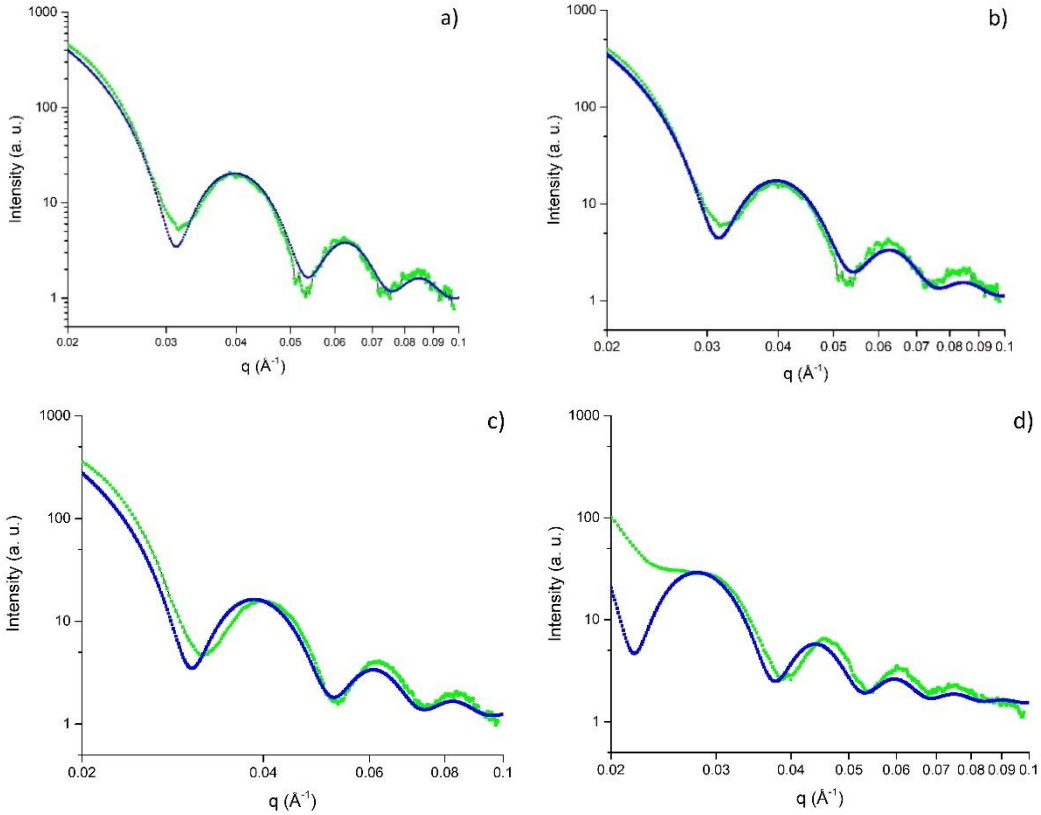

Figure S3.3.4. 1D SAXS curves (in green) and corresponding fitted curves (in blue) for sample B, after a) 0h; b)20 min; c) 1h 15 min; d) 6h 15 min

8.2.2 UV-Vis

Figure S3.3.5. Photograph of the UV-Vis cuvette with sample A-HCl showing precipitated Au nanoparticles formed after 24 hours of the reduction.

8.3 Chapter 4

In this section are shown the results from the fit on XAFS data for Au nanoparticles

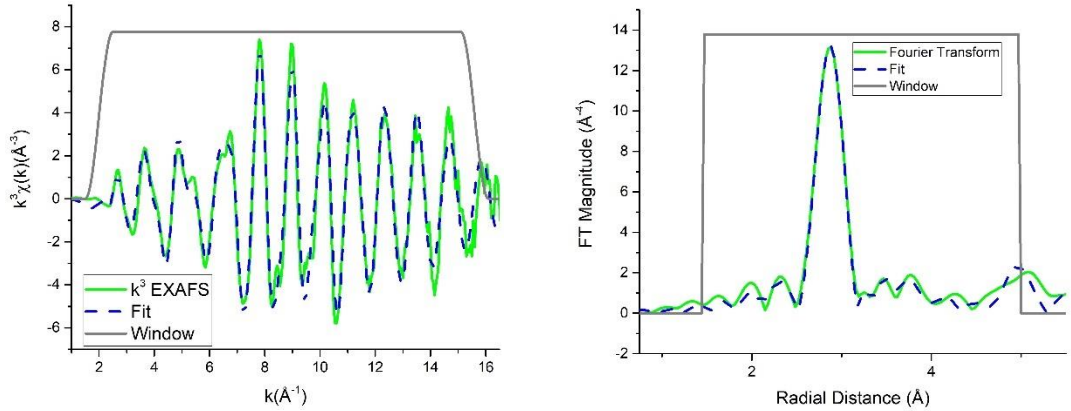

Figure S4.1. k^3-weighted EXAFS fit in k (on the left) and R (on the right) space of Au/SiO_2 16-3.5

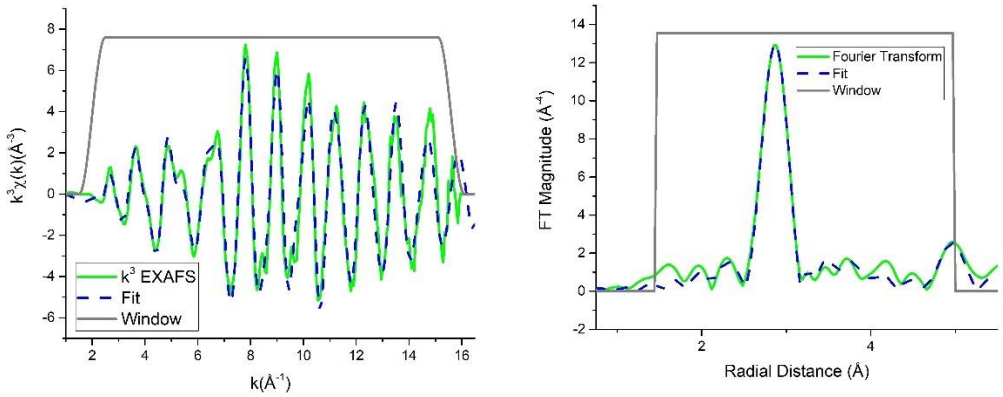

Figure S4.2. k^3-weighted EXAFS fit in k (on the left) and R (on the right) space of Au/SiO_2 175-70

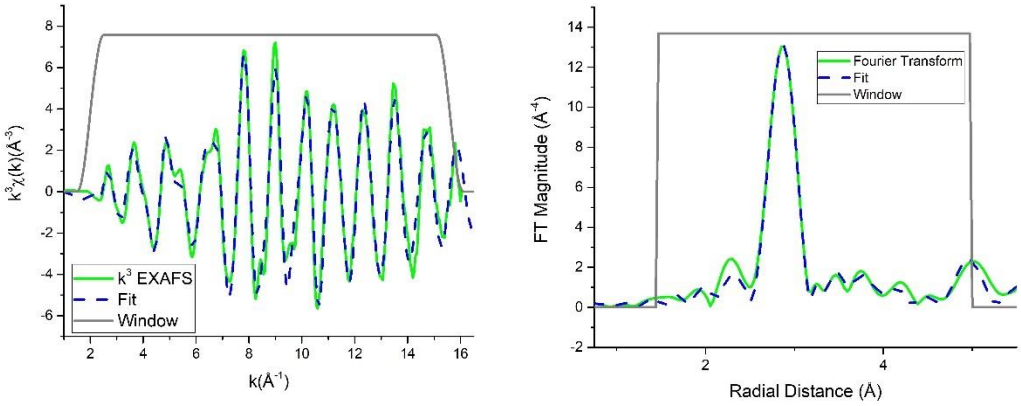

Figure S4.3. k^3-weighted EXAFS fit in k (on the left) and R (on the right) space of Au/Al_2O_3 175-70

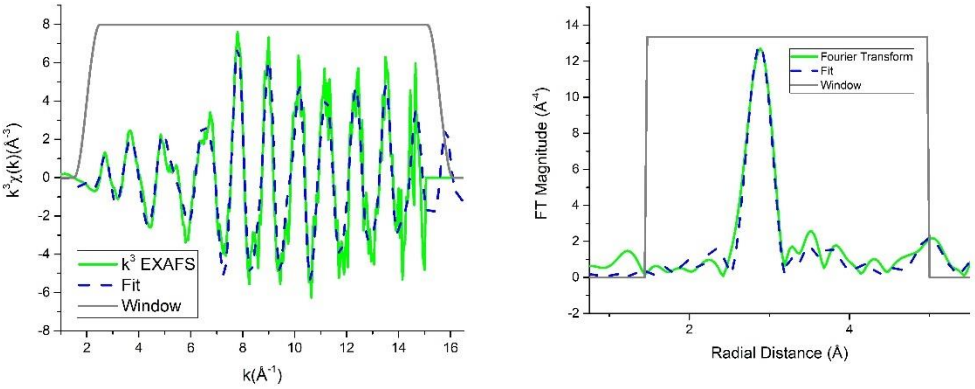

Figure S4.4. k^3-weighted EXAFS fit in k (on the left) and R (on the right) space of Au/Si_3N_4 175-70

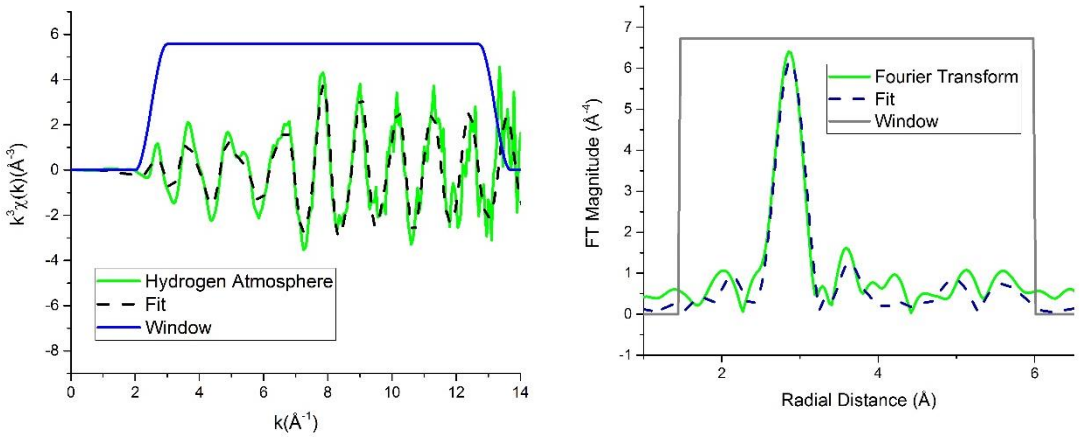

Figure S4.5. k^3-weighted EXAFS fit in k (on the left) and R (on the right) space of Au/SiO_2 175-70 under H_2 atmosphere

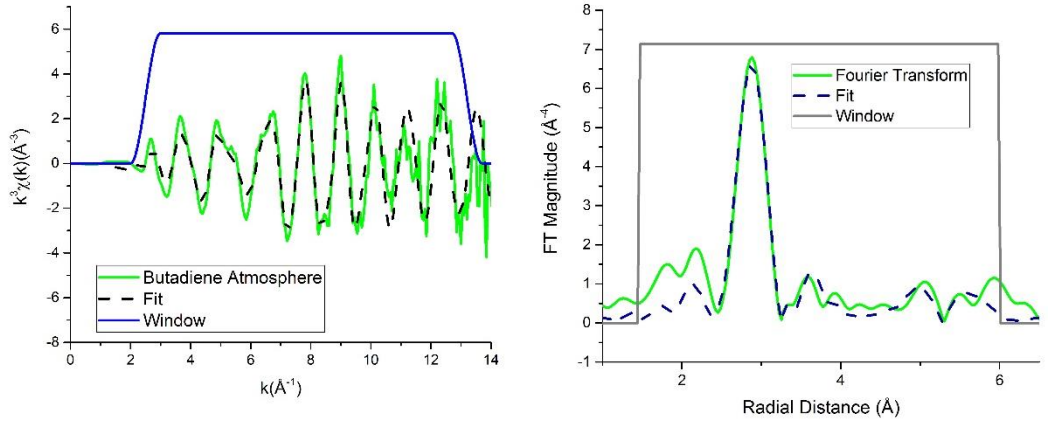

Figure S4.6. k^3-weighted EXAFS fit in k (on the left) and R (on the right) space of Au/SiO_2 175-70 under 1,3-butadiene atmosphere

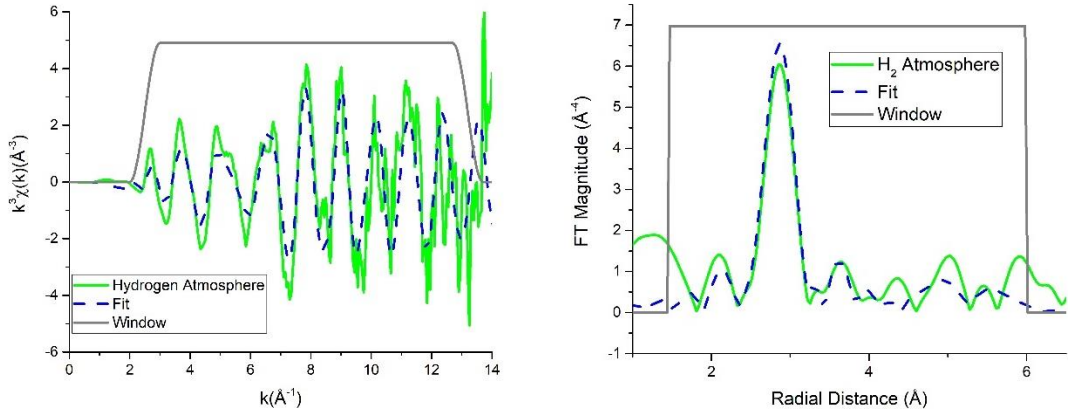

Figure S4.7. k^3-weighted EXAFS fit in k (on the left) and R (on the right) space of Au/SiO_2 16-3.5 under H_2 atmosphere

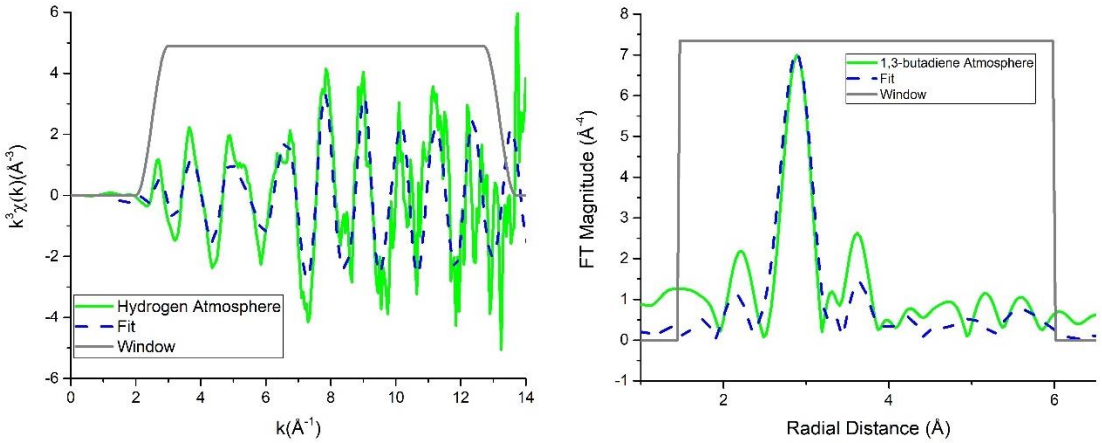

Figure S4.8. k^3-weighted EXAFS fit in k (on the left) and R (on the right) space of Au/SiO_2 16-3.5 under 1,3-butadiene

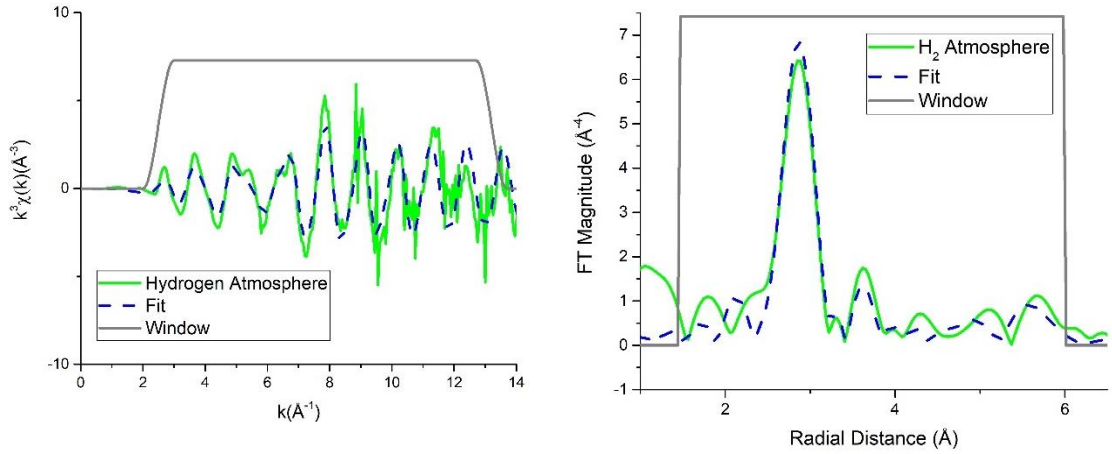

Figure S4.9. k^3-weighted EXAFS fit in k (on the left) and R (on the right) space of Au/Al_2O_3 175-70 under H_2 atmosphere

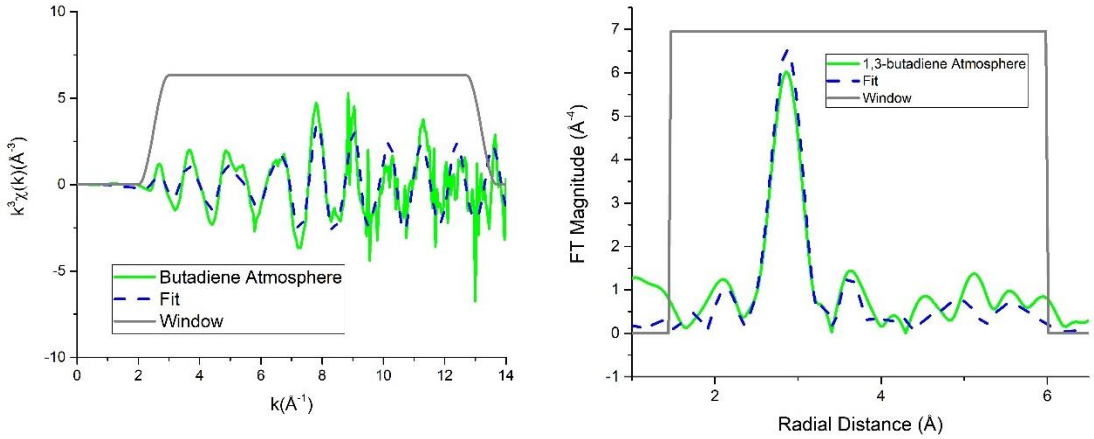

Figure S4.10. k^3-weighted EXAFS fit in k (on the left) and R (on the right) space of Au/Al_2O_3 175-70 under 1,3-butadiene

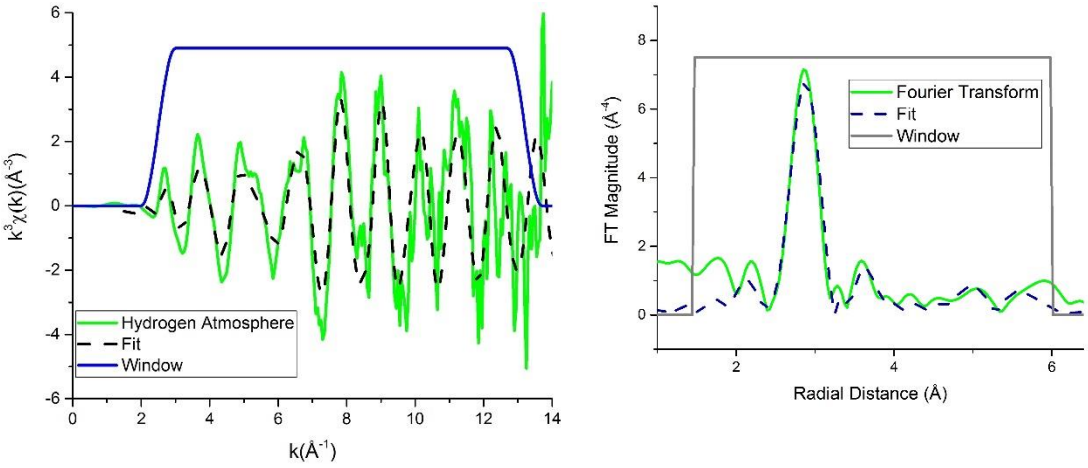

Figure S4.11. k^3-weighted EXAFS fit in k (on the left) and R (on the right) space of Au/Si_3N_4 175-70 under H_2 atmosphere

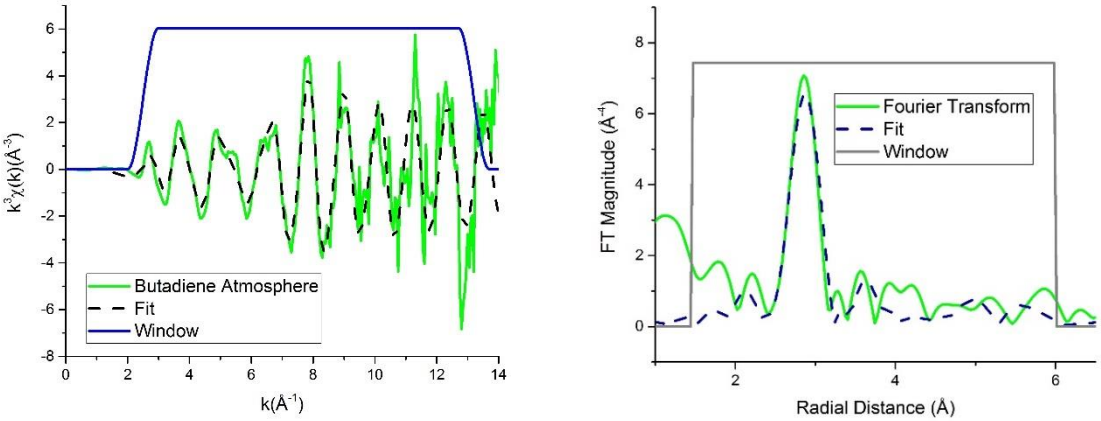

Figure S4.12. k^3-weighted EXAFS fit in k (on the left) and R (on the right) space of Au/Si_3N_4 175-70 under 1,3-butadiene atmosphere

Table S4.1. EXAFS fit results obtained from Au/SiO_2 30-8.5, using a constant Debye-Waller factor, as a function of the gas composition

Gas composition	2CN	2nd shell radius (Å)	3CN	3rd shell radius (Å)	4CN	4th shell radius (Å)
Helium	1.27 ± 3.18	4.04 ± 0.01	12.08 ± 6.16	4.949 ± 0.02	9.72 ± 6.2	5.71 ± 0.02
Hydrogen	1.66 ± 4.05	4.02 ± 0.02	11.06 ± 7.81	4.92 ± 0.02	11.21 ± 8.41	5.68 ± 0.03
1,3-Butadiene	0.0015 ±3.2	4.02 ± 0.01	13.66 ± 6.29	4.92 ± 0.02	8.9 ± 5.27	5.69 ± 0.02
Hydrogen/ 1,3-Butadiene	1.79 ± 3.15	4.04 ± 0.01	10.41 ± 6.19	4.95 ± 0.02	7.98 ± 5.6	5.71 ± 0.02
Hydrogen (After reaction)	1.86 ± 3.04	4.03 ± 0.01	10.28 ± 5.98	4.94 ± 0.02	9.14 ± 6.2	5.70 ± 0.02

Table S4.2. EXAFS fit results obtained from Au/SiO_2 16-3.5, using a constant Debye-Waller factor, as a function of the gas composition

Gas composition	2CN	2nd shell radius (Å)	3CN	3rd shell radius (Å)	4CN	4th shell radius (Å)
Helium	-4.1 ± 6.42	3.99 ± 0.02	13.25 ± 10.72	4.90 ± 0.03	6.76 ± 10.73	5.66 ± 0.04
Hydrogen	-0.5 ± 5.29	4.03 ± 0.02	7.71 ± 8.77	4.93 ± 0.03	3.6 ± 9.86	5.69 ± 0.03
1,3-Butadiene	2.44 ± 5.16	4.04 ± 0.02	3.23 ± 8.73	4.95 ± 0.02	6.69 ± 8.1	5.72 ± 0.03
Hydrogen/ 1,3-Butadiene	0.8 ± 4.1	4.01 ± 0.02	7.144 ± 6.84	4.92 ± 0.02	6.92 ± 6.83	5.68 ± 0.02
Hydrogen (After reaction)	3.12 ± 4.36	4.00 ± 0.02	7.14 ± 7.36	4.90 ± 0.02	4.66 ± 6.62	5.66 ± 0.02

Table S4.3. EXAFS fit results obtained from Au/SiO_2 175-70, using a constant Debye-Waller factor, as a function of the gas composition

Gas composition	2CN	2nd shell radius (Å)	3CN	3rd shell radius (Å)	4CN	4th shell radius (Å)
Helium	2.35 ± 3.79	4.03 ± 0.02	6.13 ± 6.33	4.94 ± 0.02	4.074 ± 6.745	5.70 ± 0.02
Hydrogen	2.31 ± 3.35	4.02 ± 0.02	6.59 ± 5.59	4.92 ± 0.02	8.73 ± 5.89	5.68 ± 0.02
1,3-Butadiene	0.14 ± 3.6	4.04 ± 0.02	8.27 ± 6.02	4.95 ± 0.02	6.78 ± 5.91	5.71 ± 0.02
Hydrogen/ 1,3-Butadiene	1.62 ± 3.47	4.04 ± 0.02	10.21 ± 5.84	4.95 ± 0.02	10.8 ± 5.82	5.71 ± 0.02

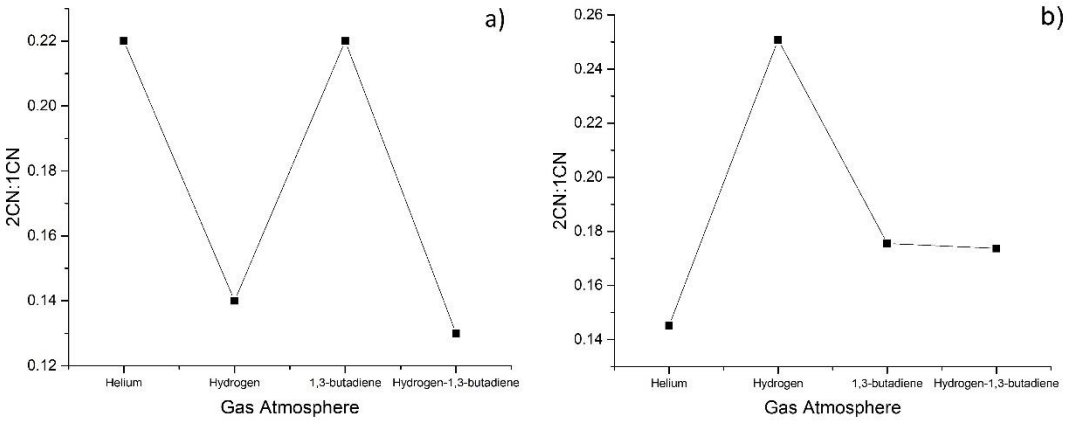

Figure S4.13. Variation of 2CN:1CN ratio as function of the gas atmosphere for a) Au/Si_3N_4 175-70; b) Au/SiO_2 175-70

Table S4.5. EXAFS fit results obtained from Au/Si_3N_4 170-70, using a constant Debye-Waller factor, as a function of the gas composition

Gas composition	2CN		3CN		4CN	
Helium	2.11 ± 4.23	4.03 ± 0.02	6.89 ± 7.14	4.94 ± 0.02	5.48 ± 6.6	5.70 ± 0.02
Hydrogen	1.74 ± 4.2	4.02 ± 0.02	4.95 ± 7.05	4.92 ± 0.02	5.19 ± 6.74	5.68 ± 0.02
1,3-Butadiene	0.9 ± 5.82	4.02 ± 0.03	4.4 ± 9.8	4.93 ± 0.03	2.99 ± 9.37	5.69 ± 0.02
Hydrogen/ 1,3-Butadiene	2.17 ± 4.17	4.03 ± 0.02	3.82 ± 7.04	4.93 ± 0.02	2.5 ± 6.52	5.69 ± 0.02
Hydrogen (After reaction)	2.04 ± 7.8	4.03 ± 0.04	6 ±13.22	4.93 ± 0.03	6.09 ± 11.62	5.70 ± 0.03

Table S4.4. EXAFS fit results obtained from Au/Al_2O_3 170-70, using a constant Debye-Waller factor, as a function of the gas composition

Gas composition	2CN	2nd shell radius (Å)	3CN	3rd shell radius (Å)	4CN	4th shell radius (Å)
Helium	1.71 ± 4.5	4.02 ± 0.02	6.12 ± 7.54	4.92 ± 0.02	4.0221 ± 8.0036	5.69 ± 0.03
Hydrogen	1.34 ± 4.99	4.02 ± 0.02	5.39 ± 8.33	4.93 ± 0.02	9.6 ± 8.845	5.69 ± 0.03
1,3-Butadiene	2.07 ± 4.92	4.02 ± 0.02	6.56 ± 8.16	4.93 ± 0.03	6.92 ± 9.2	5.69 ± 0.03
Hydrogen/ 1,3-Butadiene	-0.53 ± 5.47	4.01 ± 0.02	7.73 ± 9.08	4.91 ± 0.03	5.2 ± 9.6	5.67 ± 0.03
Hydrogen (After reaction)	1.99 ± 7.14	4.03 ± 0.03	6.09 ± 12.09	4.94± 0.03	6.12 ± 10.77	5.69 ± 0.04

8.4 Chapter 5

In this section are shown the results from the fit on XAFS data for Pd nanoparticles

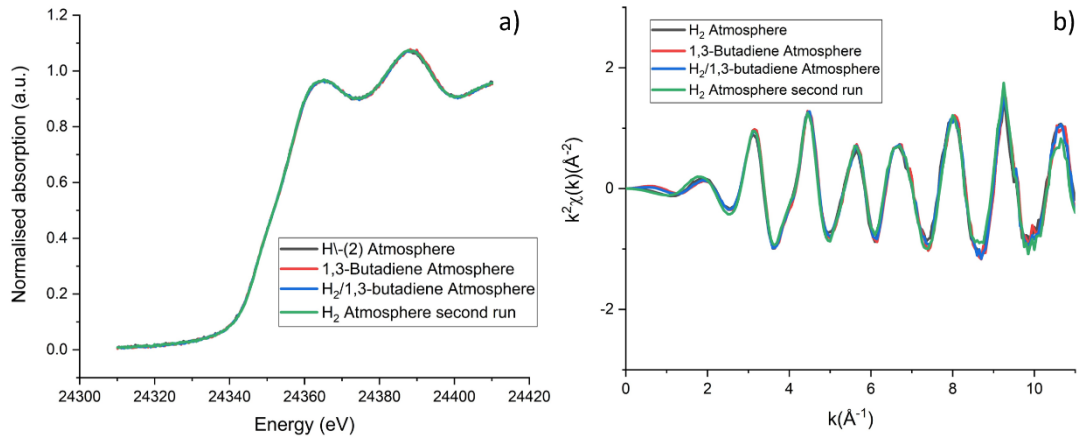

Figure S5.1. XANES data and k^2-EXAFS data of Pd/SiO_2 30-8.5

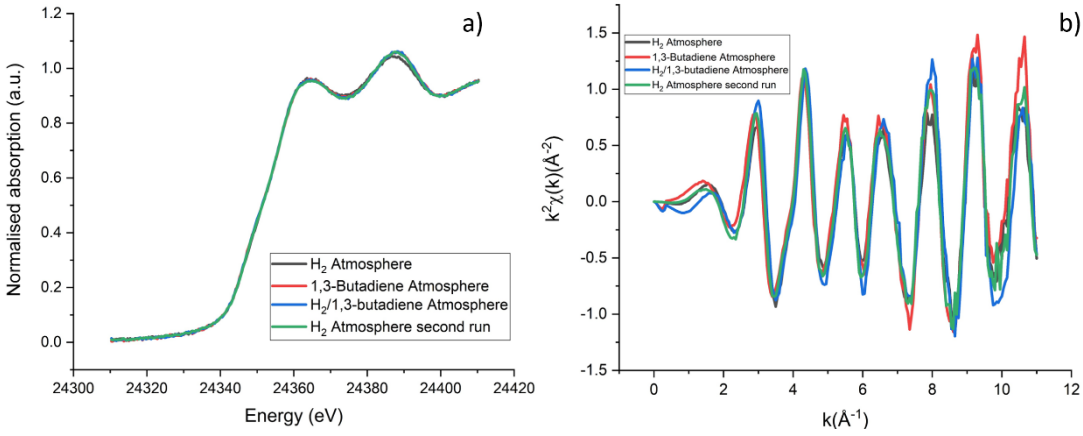

Figure S5.2. XANES data and k^2-EXAFS data of Pd/SiO_2 16-3.5

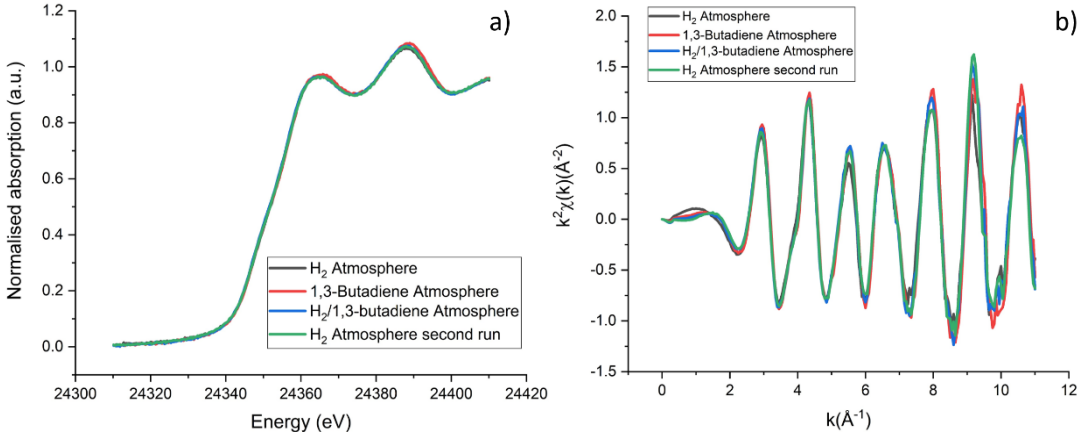

Figure S5.3. XANES data and k^2-EXAFS data of Pd/SiO_2 175-70

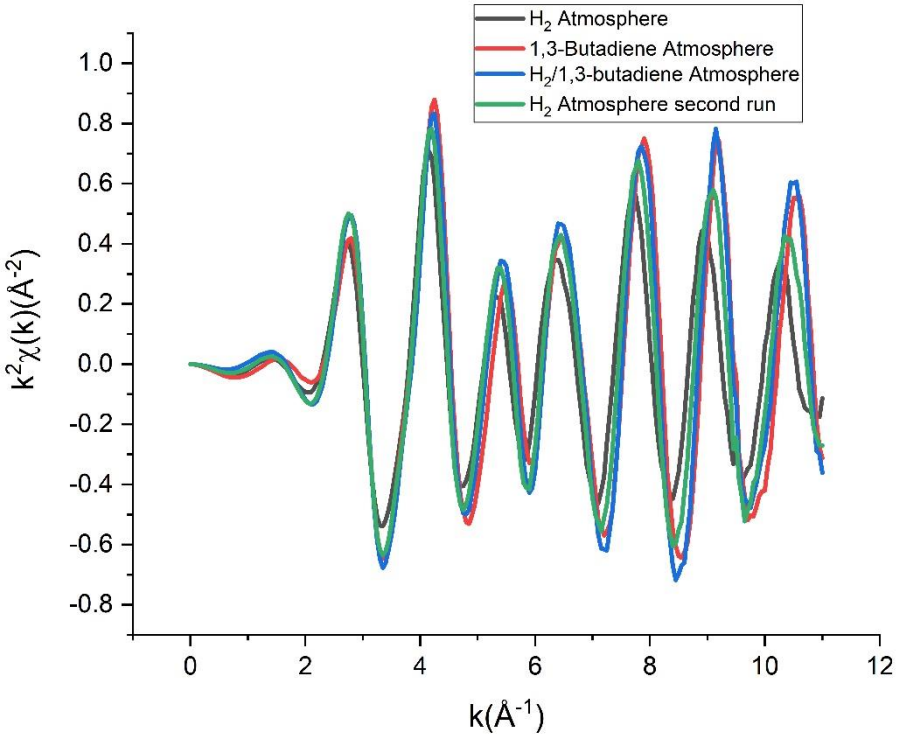

Figure S5.4. k^2-EXAFS data of Pd/Al_2O_3 30-8.5

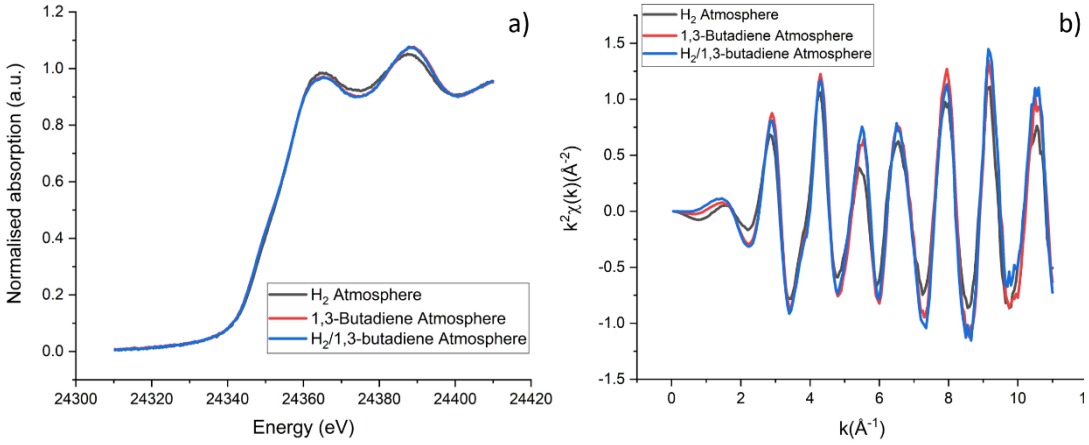

Figure S5.5. XANES data and k^2-EXAFS data of Pd/Si_3N_4 30-8.5

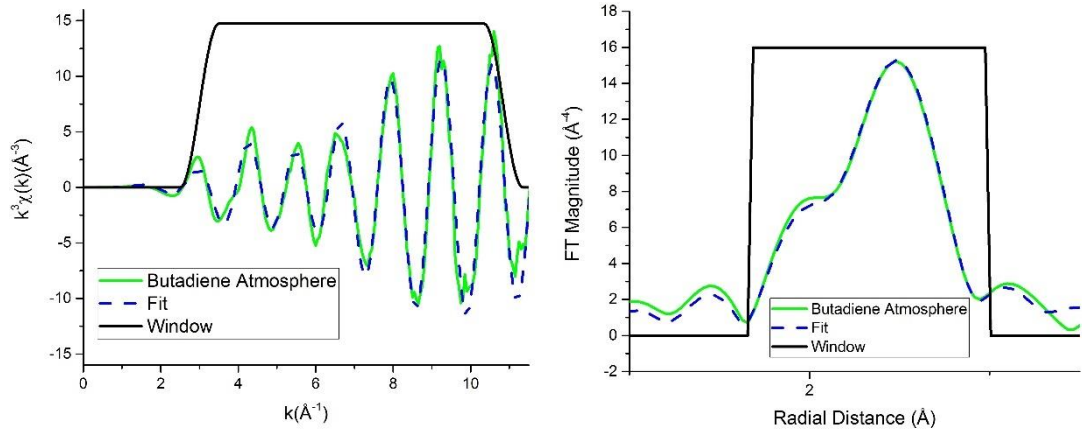

Figure S5.6. k^3-weighted EXAFS fit in k (on the left) and R (on the right) space of Pd/SiO_2 175-70 under 1,3-butadiene atmosphere

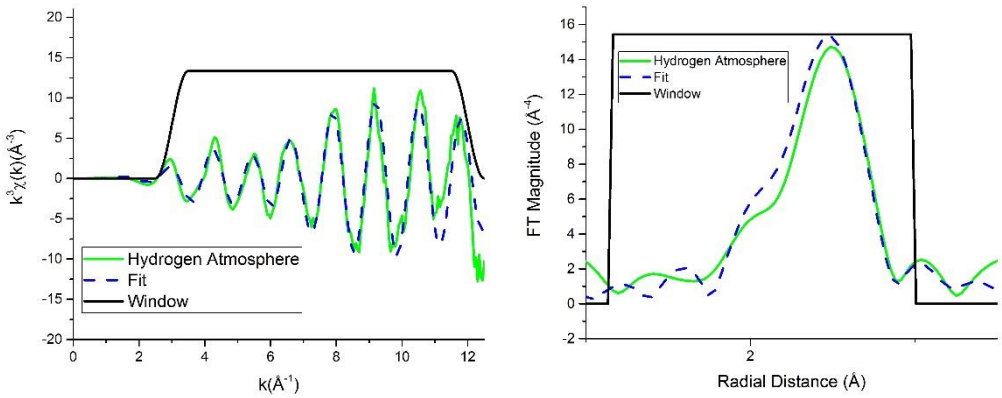

Figure S5.7. k^3-weighted EXAFS fit in k (on the left) and R (on the right) space of Pd/SiO_2 175-70 under H_2 atmosphere

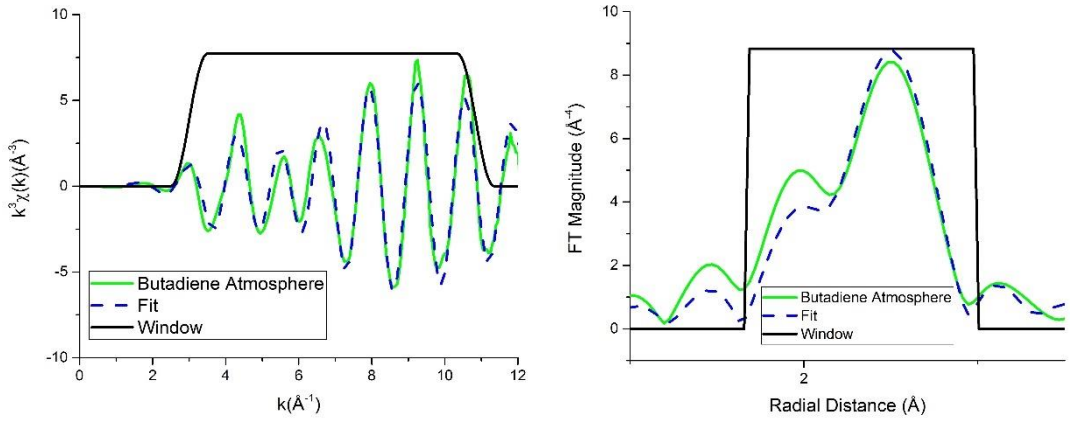

Figure S5.8. k^3-weighted EXAFS fit in k (on the left) and R (on the right) space of Pd/Al_2O_3 30-8.5 under 1,3-butadiene atmosphere

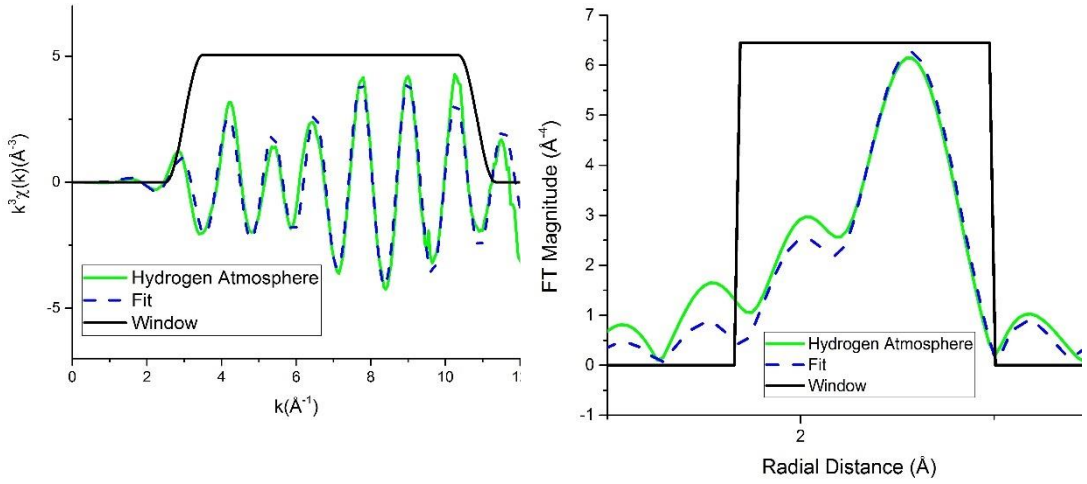

Figure S5.9. k^3-weighted EXAFS fit in k (on the left) and R (on the right) space of Pd/Al_2O_3 30-8.5 under H_2 atmosphere

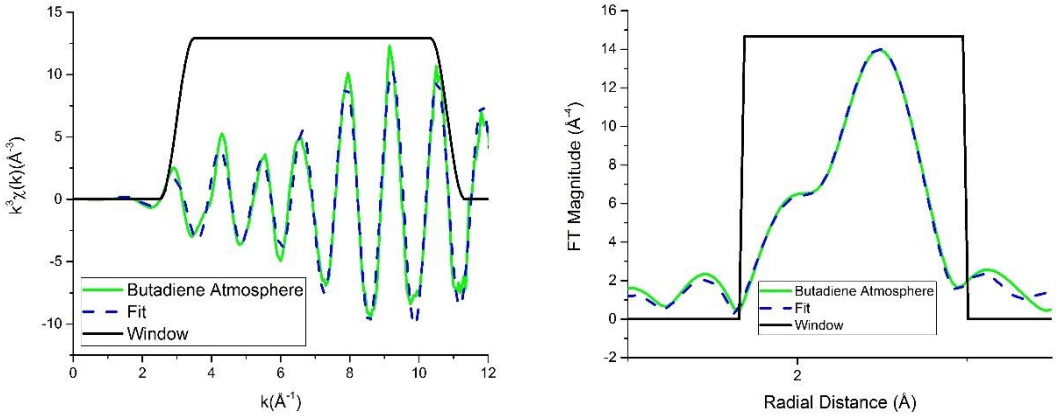

Figure S5.10. k^3-weighted EXAFS fit in k (on the left) and R (on the right) space of Pd/Si_3N_4 30-8.5 under 1,3-butadiene atmosphere

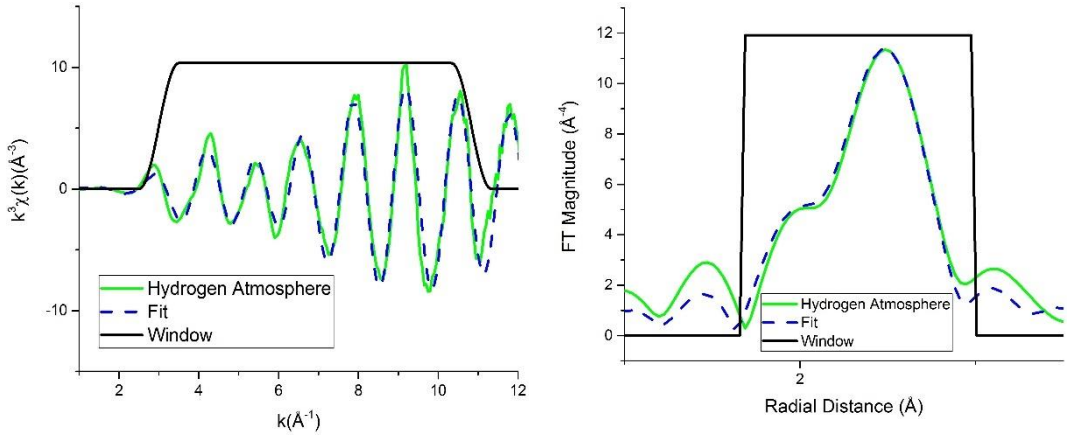

Figure S5.11. k^3-weighted EXAFS fit in k (on the left) and R (on the right) space of Pd/Si_3N_4 30-8.5 under H_2 atmosphere

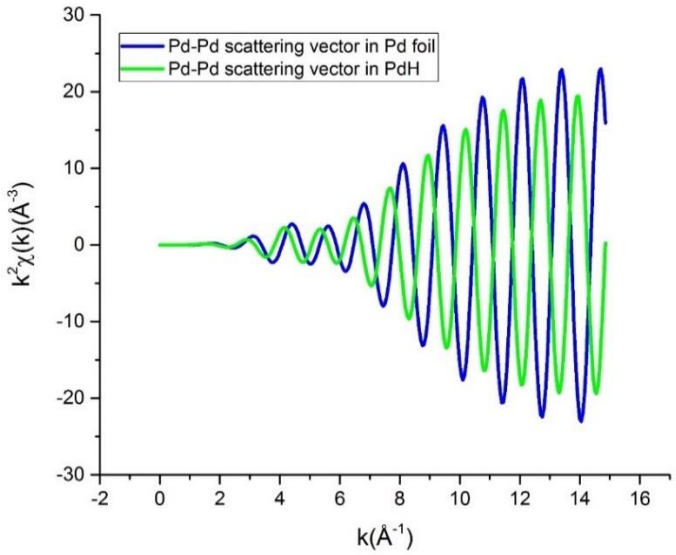

Figure S5.12. k^2-EXAFS for Pd-Pd scattering vector in a Pd foil and in PdH calculated from structural parameter through IEFFIT. The two scattering vector are out of phase, leading to phase cancellation.